frontiers | Research Topics

Responsive biomaterials for controlled release and cancer theranostics

Edited by
Xiaowei Zeng, Zhongjian Xie, Guojun Chen,
Hongzhong Chen and Guoqing Pan

Published in
Frontiers in Bioengineering and Biotechnology

ISSN 1664-8714
ISBN 978-2-8325-3069-6
DOI 10.3389/978-2-8325-3069-6

About Frontiers

Frontiers is more than just an open access publisher of scholarly articles: it is a pioneering approach to the world of academia, radically improving the way scholarly research is managed. The grand vision of Frontiers is a world where all people have an equal opportunity to seek, share and generate knowledge. Frontiers provides immediate and permanent online open access to all its publications, but this alone is not enough to realize our grand goals.

Frontiers journal series

The Frontiers journal series is a multi-tier and interdisciplinary set of open-access, online journals, promising a paradigm shift from the current review, selection and dissemination processes in academic publishing. All Frontiers journals are driven by researchers for researchers; therefore, they constitute a service to the scholarly community. At the same time, the *Frontiers journal series* operates on a revolutionary invention, the tiered publishing system, initially addressing specific communities of scholars, and gradually climbing up to broader public understanding, thus serving the interests of the lay society, too.

Dedication to quality

Each Frontiers article is a landmark of the highest quality, thanks to genuinely collaborative interactions between authors and review editors, who include some of the world's best academicians. Research must be certified by peers before entering a stream of knowledge that may eventually reach the public - and shape society; therefore, Frontiers only applies the most rigorous and unbiased reviews. Frontiers revolutionizes research publishing by freely delivering the most outstanding research, evaluated with no bias from both the academic and social point of view. By applying the most advanced information technologies, Frontiers is catapulting scholarly publishing into a new generation.

What are Frontiers Research Topics?

Frontiers Research Topics are very popular trademarks of the *Frontiers journals series*: they are collections of at least ten articles, all centered on a particular subject. With their unique mix of varied contributions from Original Research to Review Articles, Frontiers Research Topics unify the most influential researchers, the latest key findings and historical advances in a hot research area.

Find out more on how to host your own Frontiers Research Topic or contribute to one as an author by contacting the Frontiers editorial office: frontiersin.org/about/contact

Responsive biomaterials for controlled release and cancer theranostics

Topic editors

Xiaowei Zeng — Sun Yat-sen University, China
Zhongjian Xie — Shenzhen University, China
Guojun Chen — McGill University, Canada
Hongzhong Chen — Sun Yat-sen University, China
Guoqing Pan — Jiangsu University, China

Citation

Zeng, X., Xie, Z., Chen, G., Chen, H., Pan, G., eds. (2023). *Responsive biomaterials for controlled release and cancer theranostics*. Lausanne: Frontiers Media SA.
doi: 10.3389/978-2-8325-3069-6

Table of contents

frontiers | Frontiers in Bioengineering and Biotechnology

TYPE Editorial
PUBLISHED 19 July 2023
DOI 10.3389/fbioe.2023.1255293

OPEN ACCESS

EDITED AND REVIEWED BY
Hasan Uludag,
University of Alberta, Canada

*CORRESPONDENCE
Xiaowei Zeng,
zengxw23@mail.sysu.edu.cn
Hongzhong Chen,
chenhzh58@mail.sysu.edu.cn
Guoqing Pan,
panguoqing@ujs.edu.cn
Guojun Chen,
guojun.chen@mcgill.ca
Zhongjian Xie,
zjxie2011@163.com

RECEIVED 08 July 2023
ACCEPTED 13 July 2023
PUBLISHED 19 July 2023

CITATION
Gao N, Zeng X, Chen H, Pan G, Chen G and Xie Z (2023), Editorial: Responsive biomaterials for controlled release and cancer theranostics.
Front. Bioeng. Biotechnol. 11:1255293.
doi: 10.3389/fbioe.2023.1255293

Editorial: Responsive biomaterials for controlled release and cancer theranostics

Nansha Gao[1], Xiaowei Zeng[2]*, Hongzhong Chen[2]*, Guoqing Pan[3]*, Guojun Chen[4]* and Zhongjian Xie[1]*

[1]Shenzhen Children's Hospital, Clinical Medical College of Southern University of Science and Technology, Shenzhen, Guangdong, China, [2]School of Pharmaceuticals Sciences, Sun Yat-sen University, Shenzhen, Guangdong, China, [3]Institute for Advanced Materials, School of Materials Science and Engineering, Jiangsu University, Zhenjiang, Jiangsu, China, [4]Department of Biomedical Engineering, McGill University, Montreal, QC, Canada

KEYWORDS

responsive biomaterials, controlled release, drug delivery, cancer theranostics, cancer nanotechnology, personalized medicine

Editorial on the Research Topic
Responsive biomaterials for controlled release and cancer theranostics

Nowadays, cancer has become a major public health problem worldwide. Responsive biomaterials undergo changes specifically in response to specific environmental induction, providing potential clinical applications for controlled release, cancer therapeutics diagnostics and personalized medicine. The microenvironment of tumor site is significantly different from that of normal site, such as higher temperature, lower pH value or secretion of certain specific enzymes. Recently, a great quantity of stimuli-responsive biomaterials have been engineered for biomedical applications using different environment stimulus, which could be chemicals such as pH, glucose, enzymes, or physicals such as ultrasound, light, temperature, radiation, or their combinations.

In this Research Topic, we consisted of 10 articles, including six articles, two review articles and two mini reviews, contributed by 67 researchers worldwide. The original research articles involved multiple delivery systems: nanohybrid hydrogels, nanoemulsions, microcapsules and other nanoparticles or nanosheets. These nanosystems were rationally designed and synthesized of novel responsive nanomaterials for controlled release and cancer theranostics or other disease treatments, providing enormous references for their clinical applications.

There are two review articles on this Research Topic. In a review article, Ding et al. provided a systematic summary of photothermal nano hydrogels and discussed their biomedical applications. They noted that the preparation of photothermal nanohydrogels should focus on the photothermal nanomaterials, and summarized the most commonly used photothermal agents including nanomaterials made of metal, carbon based, metal sulfide/oxide, polymer, black phosphorus, MXenes, organic dye and other composite nanomaterials. The authors highlighted the applications of photothermal nanocomposite hydrogel in drug release, photothermal anti-bacterial and wound repair, photothermal inhibition of cancer, bone tissue regeneration, and other aspects such as hydrogel eye piece or electric response hydrogel. In another review article, Qian et al. summarized the advantages and disadvantages of several widely used nanomaterials including mesoporous silica nanoparticles (MSNs),

quantum dots (QDs), gold nanoparticles (AuNPs), liposomes, carbon nanotubes (CNTs), and magnetic nanoparticles (MNPs) for the treatment of urinary tract tumor in the areas of controlled drug release, biosensing, tumor imaging and treatment therapy. They pointed out that more clinical studies would be needed to confirm the safety and efficacy of nanoparticles in tumor diagnosis and therapy.

The two mini reviews summarized the graphene-based nanomaterials and chitosan-based hydrogels for stimuli-responsive drug-delivery systems, respectively. Khakpour et al. first introduced the crystal structure and excellent optical, electrical, and thermal properties of graphene-based nanomaterials including graphene oxide (GO) and graphene quantum dots (GQDs). Then, the derivative modification for drug delivery with polymers, biomacromolecules and nanoparticles were discussed. In the end, the authors listed the potential and progress of stimuli-responsive drug delivery from six aspects: pH-sensitive, redox-responsive, ROS-responsive, NIR-responsive, thermo-responsive, and electro-responsive. Garshasbi et al. indicated that injectable chitosan-based hydrogels could offer tremendous potential for drug delivery and tissue engineering due to their better biocompatibility, strong adhesion and hemostatic activity. They dedicated the applications and advantages of injectable chitosan-based hydrogels in cartilage healing, bone tissue engineering, dental pulp stem cells, and anti-cancer drug delivery system. By utilizing the carrier capacity and handling flexibility of *in situ* gelation, they suggested to regulate the dosage of a hydrogel formulation, since the injectable gel must undergo a sol-gel transition near or at the intended insertion site.

In this Research Topic, all of the original studies presented crucial aspects regarding the preparation, modification, and potential clinical translation of responsive biomaterials. pH-sensitive biomaterials take advantage of the lower pH of tumor microenvironment to achieve tumor drug targeting, improving anticancer therapeutic efficacy when combined with photodynamic or photothermal therapy. Combined chemo-photodynamic therapy (chemo-PDT) is always impeded by macrophage clearance and nonspecific distribution in healthy tissues, so extracellular acidity (pH_e ~6.5–6.8) in the tumor matrix is a promising stimulus. Zhang et al. constructed a mixed polymeric micelle ($^{DA}NP_{CT}$) that encapsulates chlorin e6 (Ce6) as the photosensitizer and hypoxia-induced prodrug tirapazamine (TPZ), finally achieved controlled photodynamic therapy and hypoxia-activating chemotherapy through pH_e-induced TAT presentation in the tumor matrix. In an original study, Yin et al. developed a novel drug delivery system using surface modification of polydopamine (PDA) and a folate-targeting ligand, which achieves pH-responsive, long-term circulation *in vivo*, active targeting functions and provides a promising chemotherapy strategy for improving the treatment of oral cancer. The PDA membranes exhibited pH sensitivity and photothermal effect, which facilitated drug release in the acidic tumor microenvironment under laser irradiation, demonstrating remarkable chemotherapeutic-photothermal synergy. In another work, Sun et al. designed a paclitaxel loaded, hyaluronan-conjugated polypyrrole-baced nanoparticle with a cystine dihydrochloride connecting arm for reduction response. It exhibited favorable photothermal effects and enhanced drug release through a combined response to temperature and redox, indicating promising potential for synergistic chemo-photothermal therapy.

One article has been published related to imaging-guided cell tracking. Imaging technologies for tracking cells *in vivo* may provide non-invasive, real-time, quantitative, and multi-dimensional information about the cells. Tang et al. fabricated a partially fluorinated paramagnetic nanoemulsions using perfluoro-tert-butyl benzyl ether, a partially fluorinated agent, for ^{19}F MRI-fluorescence imaging (FLI) dual-modal cell tracking, showing improved physicochemical properties while maintaining high ^{19}F MRI sensitivity for dual imaging cancer cells tracking.

In addition to improving the anti-tumor therapeutic effect as drug delivery carriers, some progressive response biomaterials also exhibit great potential in the treatment of other diseases. Wang et al. encapsulated magnolol that extracted from magnolia plants to construct poly (DL-lactide-co-glycolide)–poly (ethylene glycol) (PLGA-PEG) nanoparticles, and investigated their preventive and therapeutic effects on OVA-induced chronic asthma in mice. In another article, Xu et al. focused on a lidocaine-embedded polylactic acid-glycolic acid (Lidocaine@PLGA) ultrasonic-responsive microcapsule for relieving sciatica nerve pain. They indicated that the use of ultrasound as a trigger switch could achieve ultrasound-triggered rapid release of lidocaine from the microcapsule.

In conclusion, the current Research Topic reports different types of responsive biomaterials and their broad applications in controlled release, cancer theranostics and other personalized medicine, providing new chances for developing advanced drug delivery systems towards clinical translation.

Author contributions

All authors listed have made a substantial, direct, and intellectual contribution to the work and approved it for publication.

Funding

This work was supported by the Natural Science Foundation of Guangdong Province (2022A1515110271 and 2022B1515020093) and Guangdong High-level Hospital Construction Fund.

Conflict of interest

The authors declare that the research was conducted in the absence of any commercial or financial relationships that could be construed as a potential conflict of interest.

Publisher's note

frontiers | Frontiers in Bioengineering and Biotechnology

TYPE Original Research
PUBLISHED 24 October 2022
DOI 10.3389/fbioe.2022.1049437

OPEN ACCESS

EDITED BY
Shige Wang,
University of Shanghai for Science and Technology, China

REVIEWED BY
Hui Liu,
Southwest University, China
Chaoyi Yao,
Queen's University Belfast, United Kingdom

*CORRESPONDENCE
Jingjun Sun,
sunjingjun1984@163.com
Guoqin Jiang,
jiang_guoqin@163.com

†These authors have contributed equally to this work

SPECIALTY SECTION
This article was submitted to Biomaterials, a section of the journal Frontiers in Bioengineering and Biotechnology

RECEIVED 20 September 2022
ACCEPTED 11 October 2022
PUBLISHED 24 October 2022

CITATION
Sun J, Zhu S, Xu W and Jiang G (2022), Redox-responsive hyaluronan-conjugated polypyrrole nanoparticles targeting chemo-photothermal therapy for breast cancer.
Front. Bioeng. Biotechnol. 10:1049437.
doi: 10.3389/fbioe.2022.1049437

Redox-responsive hyaluronan-conjugated polypyrrole nanoparticles targeting chemo-photothermal therapy for breast cancer

Jingjun Sun[1,2*†], Shuangjiu Zhu[1,3†], Weixuan Xu[2,4] and Guoqin Jiang[1*]

[1]Department of Surgery, The Second Affiliated Hospital of Soochow University, Suzhou, China, [2]Department of Breast Surgery, Affiliated Maternity and Child Health Care Hospital of Nantong University, Nantong, Jiangsu, China, [3]Department of Thyroid and Breast Surgery, The Second People's Hospital of Lianyungang City, Lianyungang, China, [4]School of Medicine, Nantong University, Nantong, Jiangsu, China

The combination of chemo-photothermal therapy has a wide application prospect in the intensive treatment of cancer. In this study, we developed a complex nanoparticle consist of polypyrrole, cystine dihydrochloride and hyaluronan. The polypyrrole nanoparticles loaded with paclitaxel exhibited good photothermal effects, and the drug release can be triggered by combined response of temperature and redox. *In vitro* biological studies indicated the nanoparticles could effectively induced apoptosis of MDA-MB-231 breast cancer cells involved in the potential mechanism of inhibition of biological expression of heat shock proteins and JAK-STAT signaling pathway. In addition, the nanoparticles have a significant inhibitory effect on cancer growth in breast tumor-bearing mice model, indicating that they have great potential for synergistic chemo-photothermal therapy.

KEYWORDS

polypyrrole, redox responsive, hyaluronan, photothermal effects, chemophotothermal therapy

Introduction

Breast cancer has the highest mortality and morbidity among women and poses a serious threat to women's health (Bray et al., 2018). Cancer cells can be effectively killed by photothermal therapy through the thermal effect of photothermal agents under near-infrared irradiation (NIR) (de Melo-Diogo et al., 2017; Liu et al., 2019; Li and Pu, 2020; Luo et al., 2021; Zhang et al., 2021). Because NIR-II laser (1,000–1,350 nm) can penetrate tissue deeper and have better biocompatibility than NIR-I lights (650–950 nm), NIR-II-responsive photothermal agents have recently received much attention (Geng et al., 2020; Yu et al., 2021; Xu et al., 2022). Polypyrrole (PPy) is one of the commonly reported NIR-II-responsive photothermal agents, and it shows many advantages, such as facile

preparation, good biocompatibility, and high photothermal conversion efficiency (Song et al., 2015; Mi et al., 2017; Guo et al., 2019; Xu et al., 2022). However, the researches on PPy-based nanoparticles with distinct absorbance in the NIR-II bio-window are limited.

The stimulatory-responsive drug delivery system has gained a lot of attention, which can promote the release of intracellular drugs and further enhance the killing effect of tumor. With the further understanding of cancer and the microenvironment of cancer tissue, scientists have confirmed that the proliferation, invasion and metastasis of cancer cell are highly related to the abnormal changes of cancer tissue microenvironment (Zhang et al., 2019). Through exploring the features of cancer tissue microenvironment, drug delivery system can be correspondingly designed to release drugs at specific sites or respond to specific stimuli, which will improve the delivery efficiency, enhance the bioavailability of drugs, as well as reduce toxic and side effects (Hossen et al., 2019). Glutathione (GSH) is a powerful antioxidant. There is higher concentration of GSH in cancer tissues than that in normal tissues. Therefore, redox properties can serve as potential stimuli to control drug release. It has been reported that the overexpression of CD44 receptor of hyaluronan (HA) existing in many different types of tumor cells (Misra et al., 2011). Therefore, HA is a potential tool to enhance the tumor targeting effect of drug carriers.

Herein, we aim to design a multi-functional PPy based nanoparticles that can be used in synergistic chemo-photothermal therapy. The multifunctional PPy based nanoparticles (PCH) consists of PPy, cystine dihydrochloride (Cys) and HA. Cys connecting arm can endow the nanoparticles with the characteristics of reduction response. Thus, this system can not only ablate tumors through photothermal effect, but also trigger drug release in tumor microenvironment by reduction-responsive stimuli. Structures, photothermal effect, and redox/temperature dependent drug release pattern of the PPy based complex nanoparticles were studied. In addition, cytostatic experiments and mechanisms were performed on MDA-MB-231 cells. The anti-tumor effects of paclitaxel (PTX) loaded PCH nanoparticles breast tumor-bearing mice were also evaluated.

Materials and methods

Materials

Pyrrole (Py) was obtained from Rhawn (Shanghai, China). Pyrrole-1-propionic acid (Py-COOH), polyvinyl alcohol (PVA, Mw: 89,000–98,000), 1-ethyl-3-(3-dimethylaminopropyl) carbodiimide hydrochloride (EDC), N-hydroxysuccinimide (NHS) and Ferric chloride hexahydrate ($FeCl_3$) were purchased from Macklin (Shanghai, China). Hyaluronic acid

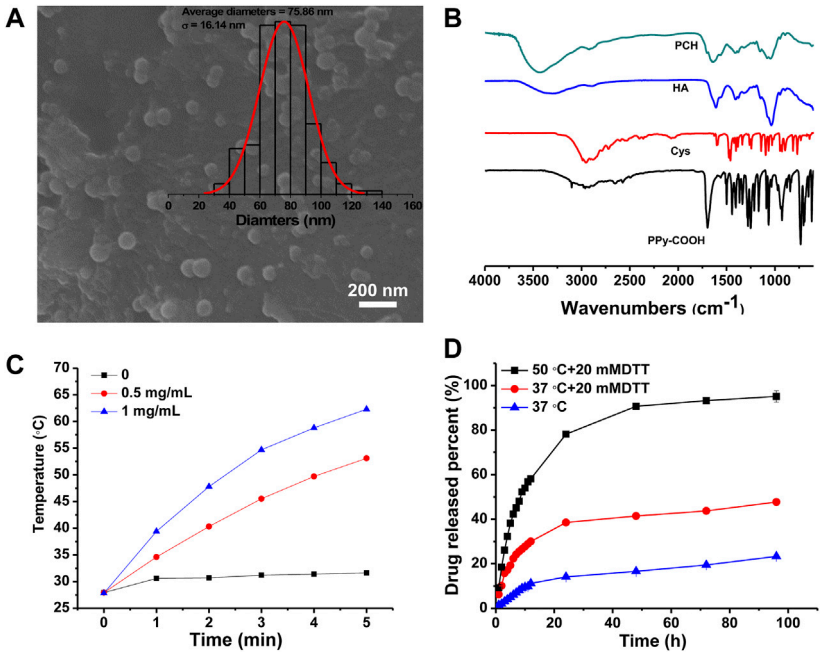

FIGURE 1
(A) SEM micrographs and diameter distribution histograms of PCH nanoparticles. **(B)** FTIR spectrum of PPy-COOH, Cys, HA, and PCH. **(C)** Temperature curves of PCH aqueous solutions (0, 0.5, 1 mg/ml) under laser irradiation of 1,064 nm laser at the power density of 1 W/cm^2. **(D)** Cumulative release curve of PTX/PCH nanoparticles in different media and temperature.

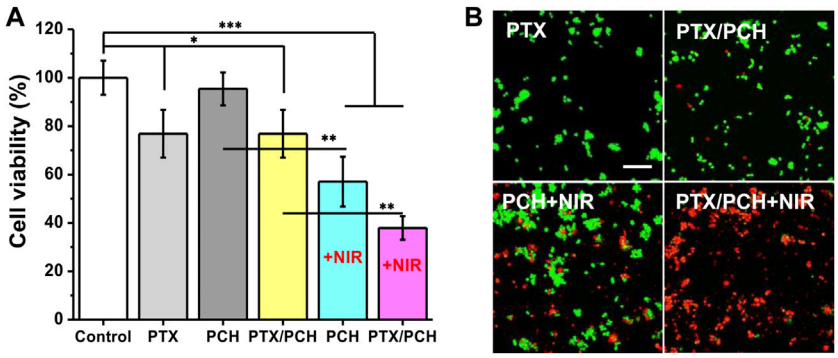

FIGURE 2
(A) *In-vitro* combined tumor photothermal therapy of PCH; **(B)** Morphology of dead/live staining of MDA-MB-231 cells corresponding to **(A)**. Scare bar = 50 μm.

[HA, MDMW: 22 × 105 Da)] was supplied by Nantong Feiyu Biotechnology Co., Ltd., Paclitaxel (PTX) was obtained from Yangtze Pharmaceutical Group Co., Ltd., Cystine dihydrochloride (Cys) from Shanghai Aladdin Biotechnology Co., Ltd.

Synthesis and characterization of nanoparticles

PPy-COOH nanoparticles were firstly prepared according to previous work. Briefly, $FeCl_3$ (0.6 g) was added to 10 ml 8% PVA solution and stirred for 1 h. Then, Py and Py-COOH (0.376 g) was added into the solution at 4°C, the mass ratio of Py to Py-COOH was set as 1:1. The chemical oxidation polymerization of Py/Py-COOH monomer was carried out for 4 h at 4°C. 0.24 mg EDC and 0.192 mg NHS were dissolved in 20 ml water, and then added into the PPy-COOH nanoparticles solution for 2 h. After that, 0.6 g Cys was added into above activated PPy-COOH nanoparticles solution and stirred for 24 h at room temperature. PPy-Cys nanoparticles were obtained through centrifugation and purification. 12 mg EDC and 9 mg NHS was added in to 2 ml HA solution for 0.5 h. Then, it was added into 18 ml above PPy-Cys nanoparticles solution and stirred for 12 h at room temperature. Finally, PPy-Cys-HA (PCH) nanoparticles were collected through centrifugation and purification.

Chemical analysis of the nanoparticles was characterized using a FTIR (TENSOR 27, Bruker, Germany). Samples were scanned at resolution of 2 cm^{-1} in transmission mode. Scanning range is from 4,000 to 400 cm^{-1}. Morphological information of the nanoparticles was collected using a

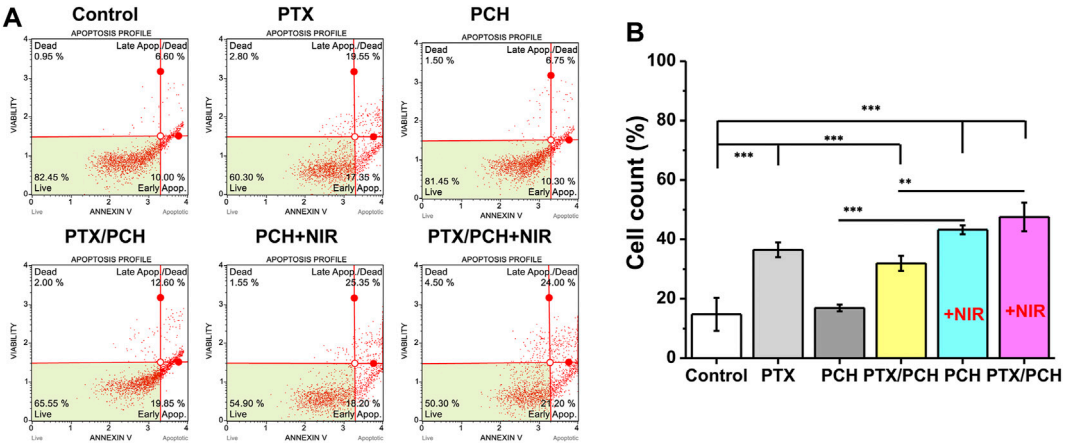

FIGURE 3
(A) Annexin V and Dead Cell analysis method for the apoptosis of MDA-MB-231 cells. **(B)** Apoptosis of MDA-MB-231 cells.

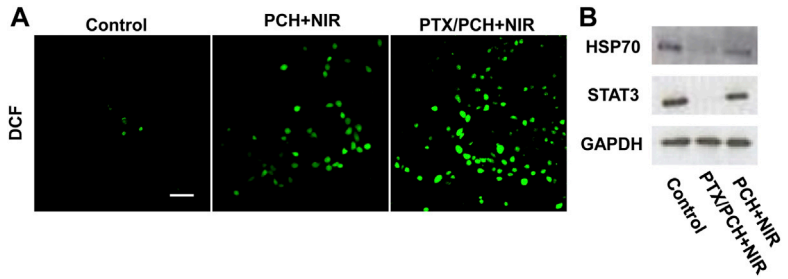

FIGURE 4
(A) ROS production detection after distinct treatments. **(B)** HSP70 and STAT3 expression evaluation. Scare bar = 50 μm.

scanning electron microscopy (SEM, ZEISS Gemini SEM 300, Germany). Diameter of the nanoparticles were measured using an ImageJ 1.40 G software.

Near-infrared irradiation-photothermal effect

Aqueous solutions of PCH nanoparticles at different concentrations (0, 0.5, and 1 mg/ml) were irradiated with a 1,064 nm laser (1.0 W/cm^2) for 5 min. Photothermal images were caught every 1 min using a thermal imaging camera (FLIR C3, Fluke, United States).

Drug loading and release

PTX-loaded PCH (PTX/PCH) nanoparticles were also prepared as described above. The *in vitro* release of PTX (initial concentration: 50 μg/ml) from PTX/PCH nanoparticles (0.5 ml) was investigated using a dialysis bag at 37°C in 25 ml PBS (10 mM, pH 7.4) either in the presence or absence of 20 mM DTT (to simulate a highly reduced tumor microenvironment). At

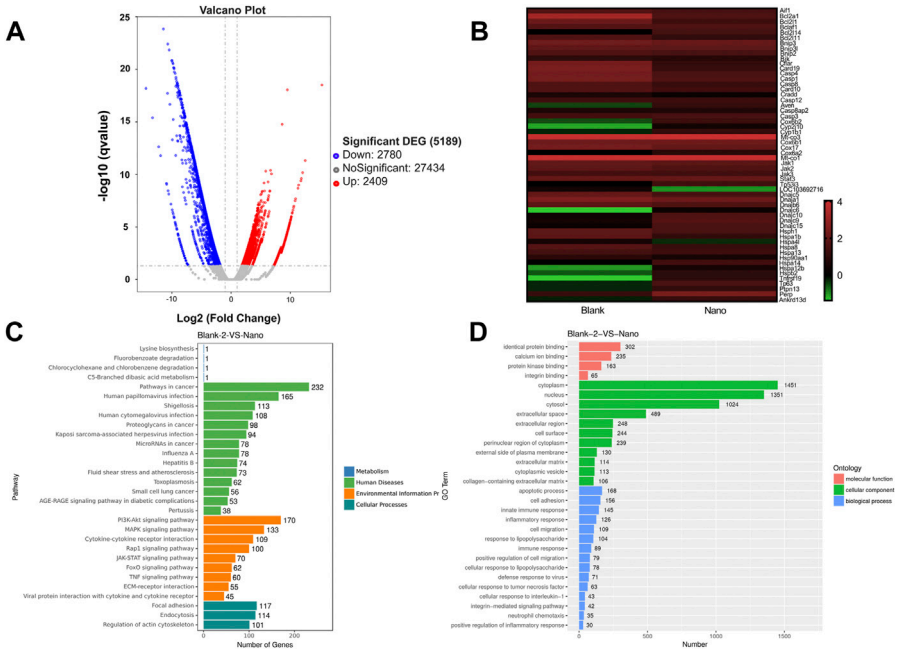

FIGURE 5
Transcriptomic sequence. **(A)** Volcano map of TCP and PTX/PCH + NIR. **(B)** Heatmap of differentially expressed genes in TCP and PTX/PCH + NIR groups. **(C)** KEGG pathway enrichment. **(D)** GO terms.

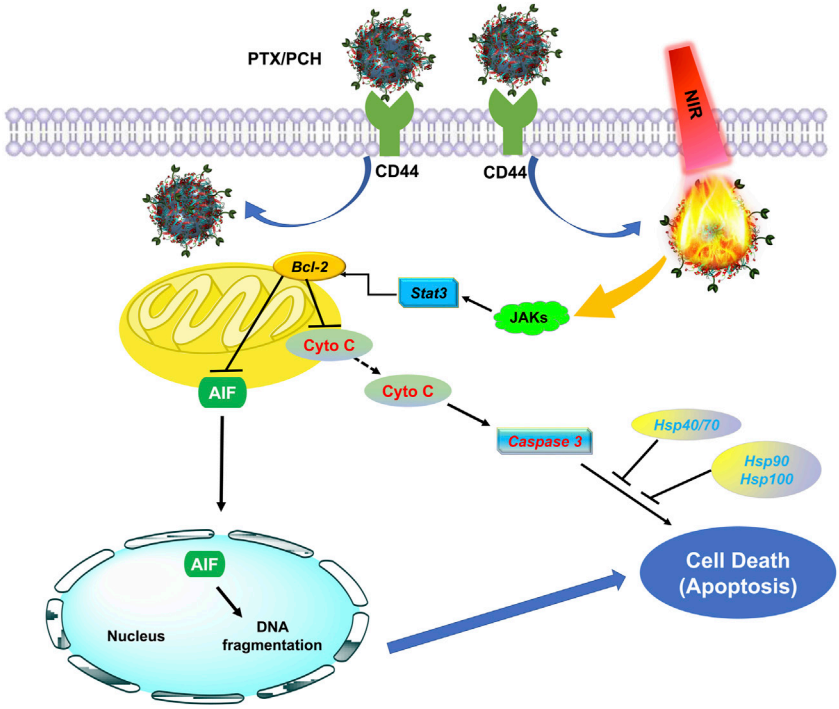

FIGURE 6
Schematic illustration for the mechanism of PTX/PCH + NIRs induced apoptosis.

predetermined time intervals, 5 ml of release buffer was sucked out and supplemented with an equal volume of fresh buffer. The amount of released PTX was measured by high performance liquid chromatography (HPLC).

Cytotoxicity study

MDA-MB-231 cells were seeded into 96-well plates (8×10^3 cells/well) and incubated with 0.5 mg/ml PCH and PTX/PCH nanoparticles for 24 h. Cells treated with PBS were served as control. In addition, MDA-MB-231 cells were laser-irradiated with PCH and PTX/PCH nanoparticle groups for 5 min and further incubated for 24 h. CCK-8 assay was used to determine the viability. Cells were stained with dead/live kit for 15 min. Then, cells were washed with PBS and observed by fluorescence microscope (Nikon Ti-DH).

Cell apoptosis assay

MDA-MB-231 cells were seeded into 12-well plates (5×10^5 cell/ml) and incubated for 24 h. Cells were washed twice with PBS and medium containing 0.5 mg/ml PCH and PTX/PCH nanoparticles were added, respectively. After being cultured for 12 h, the cells were washed twice with PBS and 1 ml fresh medium was added. NIR groups were irradiated with a 1,064 nm laser at a power of 1 W/cm^2 for 1 min and non-NIR groups were not treated. After incubation of another 6 h, the cells were washed twice with PBS and digested with trypsin. The cells were centrifuged and collected. Finally, the cells were processed according to the instructions in the MuseTM Annexin V and Dead Cell Kit (Merck, Germany). The result was recorded using Muse Cell Analyer (Merck, Germany).

Intracellular reactive oxygen species detection

To detect the amount of ROS, MDA-MB-231 cells were incubated with different samples and then the probe DCFH-DA (10 μM) was added to each well. 30 min later, the medium was removed, and the cells were washed with PBS and observed under a fluorescence microscope (Nikon Ti-DH).

Western blot analysis

MDA-MB-231 cells were seeded on a 6-well plate and cultured for 12 h. After different treatments, cells were

harvested and washed three times with PBS. The cells were then collected and further lysed for Western blot analysis.

High-throughput RNA-seq

For transcriptomic sequencing, MDA-MB-231 were seeded onto a 6-well plate and cultured overnight. After distinct treatments, the cells were harvested, and TRIzol was used for total RNA isolation. The isolated total RNA was stored in liquid nitrogen ready for use. RNA concentration was determined and total RNA quality inspection was performed. RNA libraries were then prepared by PCR amplification. Finally, sequencing was performed on the RNA-seq platform according to the manufacturer's instruction, and the data obtained were processed by Genewiz Co. Ltd.

In-vivo antitumor efficacy

Therapeutic effect of PTX-loaded PCH nanoparticles was evaluated in nude mice bearing MDA-MB-231 breast cancer xenografts. All the animal experimental procedures were approved by the ethical committee of Soochow University. When the volume of the tumor was in the range of 30–40 mm^3, the treatments were initiated (day 0). The mice were randomly divided into two groups, and there are six in each group. All mice were injected with PTX/PCH nanoparticles (5 mg PTX equiv./kg) *via* tail vein. The samples were continuously irradiated with a 1,064 nm laser (1 W/cm^2) for 5 min. The temperature elevation and photothermal images of mice were recorded by using a thermal imaging camera (FLIR C3, Fluke, United States). The treatment was repeated every 3 days for 5 times. The tumor volume was calculated according to the formula $V = 0.5 \times L \times W \times H$, where L, W, and H are the tumor dimensions at the length, width and height, respectively. At the end of the treatment, the tumor, liver, heart and kidney tissues were removed from mice. The tissues were fixed with 4% paraformaldehyde for 24 h and dehydrated with 30% sucrose solution for 48 h. The tissues were frozen at −80°C and sectioned with 8 μm thickness. The sliced organ tissues were stained by hematoxylin and eosin (H&E) and observed.

Statistical analysis

All data are presented as the mean ± standard deviation (SD). One-way analysis of variance (ANOVA) of Origin 8.0 was used to determine significance among groups. When p value was less than 0.5, the difference was significant. $^*p < 0.05$, $^{**}p < 0.01$, $^{***}p < 0.001$.

Results and discussion

Synthesis and characterization of nanoparticles

The synthetic procedure of PCH nanoparticles consisted of three steps. The first step was to prepare PPy-COOH nanoparticles by a one-step aqueous dispersion polymerization of Py and Py-COOH. The second step was the grafting of Cys onto PPy-COOH nanoparticles. The third step was to prepare HA derived PPy nanoparticles. As shown in Figure 1A, PCH nanoparticles were in a spherical shape with a nearly uniform size of 75.86 ± 16.14 nm. This is consistent with previously reported (Guo et al., 2019).

To verify that whether HA molecules were successfully modified onto the surface of PPy nanoparticles, PCH, PPy-COOH and Cys were characterized by FTIR (Figure 1B). PPy-COOH exhibit a peak at 1,690 cm^{-1}, attributing to –C=O. Weak peaks at 1,595 cm^{-1} and 1,030–1,230 cm^{-1} are caused by the bending vibration of –NH and the tensile vibration of the Cys C–N bond. In addition, because of the low detection sensitivity limit for the S–S bond strength, no stretching vibration of the disulfide bond (S–S) appears in the FTIR spectra (Rao et al., 2018). For HA, the peaks at about 3,300 cm^{-1} and 2,900 cm^{-1} are owing to the stretching vibrations of O–H/N–H bond and C–H bonds, respectively. The FTIR spectra show peaks at about 1,610 cm^{-1} and 1,405 cm^{-1} and could be ascribed to the stretching vibrations of the C=O and C–O bonds of the –COO– group, while the characteristic peak of C–O–C showed asymmetrical and symmetrical stretching frequencies at 1,145 and 1,040 cm^{-1} (Das et al., 2018). The peaks at 1,560 cm^{-1} are owing to the –NH stretching frequencies in HA. A new absorption peak at 1707 cm^{-1} amide (C=O stretching) appears in the FTIR spectra of the PCH, indicating that the modification caused the formation of amide bonds. All in all, these clearly suggested that HA has been successfully grafted to the surface of PPy nanoparticles.

Previous study has demonstrated that PPy based nanoparticles can absorb the spectrum in the NIR-II range very well (Xu et al., 2022). As shown in Figure 1C, when the solution was irradiated with a NIR-II laser at 1,064 nm, its temperature increased, and the temperature was positively correlated with the PCH concentration. For 1 mg/ml case, the temperature of the solution can reach up to 62.3°C within 5 min of irradiation, confirming the excellent photothermal conversion ability of PPy. Based on Korgel's method (Xie et al., 2022; Zhang et al., 2022), the photothermal conversion

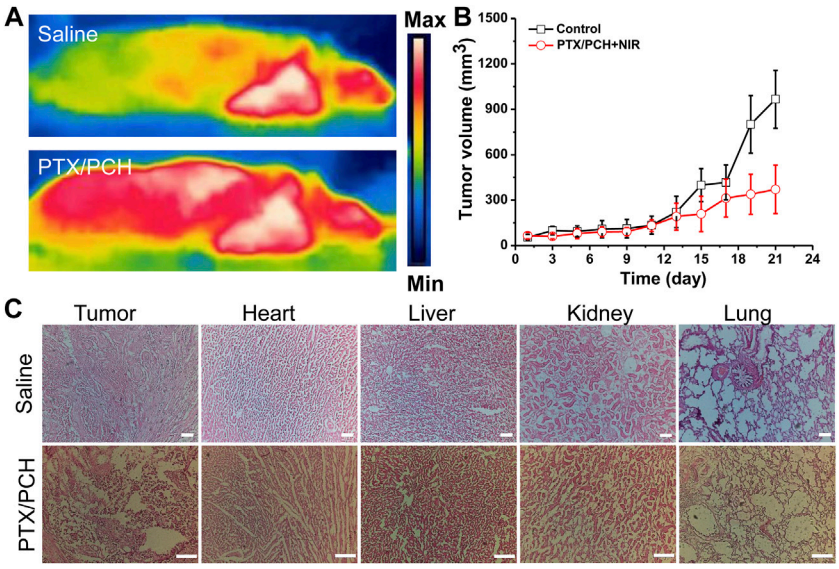

FIGURE 7
(A) Thermal images of the animals treated with saline (NIR) or PTX/PCH (NIR). **(B)** Tumor volume changes. **(C)** The H&E assay indicates themorphological change of the organs (PBS-NIR treated group and PTX/PCH-NIR treated group). Scare bar = 100 μm.

efficiency of the PCH nanoparticle was determined to be 33.48% (Supplementary Figures S1A,B). In the three lasers' on-off cycles, the maximum temperature of the PCH nanoparticles could remain stable; therefore, the PCH nanoparticle has acceptable photothermal stability (Supplementary Figure S1C).

The release of PTX from PTX/PCH nanoparticles was measured at 37°C or 50°C for 96 h (Figure 1D). 20 mM DTT were used to simulate the high reducing tumor microenvironment. It was found that the cumulative release amount of PTX from PTX/PCH nanoparticles within 96 h was 23.3%, 47.7%, and 95.1% at T = 37°C, T = 37°C/20 mM, T = 50°C/20 mM DTT, respectively. This suggested that the PTX release increased with the temperature rising and in the presence of 20 mM DTT. The increased PTX release rate might be attributed to DTT triggered disulfide bond cleavage and inverse cross-linking of the PCH. Therefore, drug release can be accelerated in an intracellular reducing environment (Zhu et al., 2016), and this controlled drug release is beneficial to the improvement of tumor treatment.

In-vitro cell assay

The *in vitro* combined cancer therapy of PTX/PCH nanoparticles was also investigated. As shown in Figure 2A, cells treated with saline remained healthy, while the viability of cells treated with pure PTX and PTX/PCH was significantly reduced (PTX: 76.85%, $p < 0.05$, versus saline; PTX/PCH: 79.25%, $p < 0.05$, versus saline) due to the cell killing effect of PTX. Besides, the proliferation of PCH-treated cells was significantly inhibited after NIR irradiation (57.03%, $p < 0.001$, compared to saline), suggesting the excellent *in vitro* photothermal therapeutic efficiency. In addition, due to the NIR triggered photothermal ablation and PTX induced chromosomal instability (Scribano et al., 2021), cancer cells treated with PTX/PCH NIR were mostly killed with a viability of 37.86% ($p < 0.001$, versus saline), which was significantly lower than that treated with PTX/PCH ($p < 0.01$), pure PTX ($p < 0.001$) and PCH + NIR ($p < 0.01$). Moreover, CCK-8 and dead/live staining results further demonstrated the synergistic chemotherapy and photothermal efficiency of PTX/PCH nanoparticles (Figure 2B).

In Annexin V and Dead Cell analysis, the four regions represent dead cells, late apoptosis, early apoptosis, and live cells, respectively, and late + early apoptosis represents total apoptosis. As presented in Figures 3A,B, the total apoptosis rate of cells treated with pure PTX and PTX/PCH was significantly increased (PTX: 36.5%, $p < 0.001$, versus control; PTX/PCH: 31.95%, $p < 0.001$, versus control) suggesting that chemotherapy caused the total apoptosis. PCH + NIR and PTX/PCH was 43.25 ± 1.47% and 47.53 ± 4.80%, respectively, with significant difference from no NIR groups ($p < 0.001$), indicating that NIR led to more apoptosis of cells and the combined treatment group had the best therapeutic effect.

Reactive oxygen species (ROS) sensitive probe DCFH-DA was applied to investigate the production of ·OH in cells. The fluorescence intensity increased from PCH + NIR and PTX/PCH + NIR to the control group. The strongest fluorescence was observed in PTX/PCH + NIR group, indicating its strong ability to produce ·OH and cause cell necrosis (Figure 4A). As shown in Figure 4B, the expression of heat shock protein 70 (HSP70) was inhibited both in the PCH + NIR

and PTX/PCH + NIR groups. It was reported that the suppression of HSPs functions can disrupt the cell homeostasis and interfere with the integrity of protein interaction, thereby reducing the cell thermotolerance and improving the efficacy of photothermal therapy (Wang et al., 2016). STAT3 is an oncogene, and the activation and overexpression of STAT3 are relevant with the malignant transformation of cells (Qiao et al., 2016). The expression of STAT3 was suppressed in the PTX/PCH + NIR groups, which will reduce the resistance of tumor cells and promote the therapeutic effect.

Transcriptomic sequencing generated a volcanic map showing 2,780 downregulated and 2,409 upregulated differentially expressed genes in the PTX/PCH + NIR group (Figure 5A). A total of 56 upregulated and downregulated differentially expressed apoptosis related genes were identified. Using the FPKM values of differentially expressed genes under different experimental conditions as expression levels, hierarchical clustering analysis was performed to create a heat map (Figure 5B). Specially, Hsps genes (Hsp40/70 family, Hsp90 family and Hsp100), JAKs genes, Stat3 genes and Bcl-2 genes were downregulated. Bcl-2 is an anti-apoptotic protein and a downstream target gene of START3 (Edmonds et al., 2012). The Kyoto Encyclopedia of Genes and Genomes (KEGG) diagram showed that six pathways were enriched in the PTX/PCH + NIR group, and the higher expression level of the JAK-STAT signaling pathway was also clearly observed (Figure 5C). The gene ontology (GO) analysis showed that enriched GO biological process terms of the PTX/PCH + NIR group were related to associated with apoptotic processes, cell adhesion, and innate immune responses, respectively (Figure 5D).

Through western blot analysis and transcriptome sequencing, the possible mechanism by which the PTX/PCH + NIRs induced apoptosis of MDA-MB-231 cells is summarized in Figure 6. PTX/PCH + NIRs induced Hsps impaired, heat shock causes the down expression of JAKs, Stat3 and Bcl-2, and the conformational changes of outer membrane of the mitochondria that allows the release of cytochrome c (Cyto C) and apoptosis inducing factor (AIF) (Choi et al., 2011). In turn, apoptotic bodies are formed and apoptosis downstream is carried out by activated Caspase 3. The released AIF enters into the nucleus and causes cell death (Fu et al., 1987).

In-vivo tumor therapy

Figure 7A are thermal images of the tumor *in vivo* 2 days after the first administration of NPs and irradiation with NIR for 5 min. Temperatures of the tumors were around 52°C (PTX/PCH + NIRs), and 32°C (NIR plus saline), indicating that a large number of NIR-responsive PTX/PCH NPs may accumulate at the tumor sites after administration. The group that received saline + NIR showed a negligible antitumor efficacy. The group that received PTX/PCH + NIR showed the high antitumor efficacy (Figure 7B) (Feng et al., 2018). Figure 7C shows the histological results. It can be found that the developed PCH administered through local intratumoral delivery into tumor are beneficial because they avoid toxicity to various treatments of surrounding healthy organs (heart, liver, kidney, and lung), they maximize preservation of functional tissue near the tumor. Histological results also revealed that a large number of tumorous cells were mixed with small connective tissue stroma (Figure 7C). Nevertheless, tumor eradication with a luminal structure was observed in the PTX/PCH + NIR treated group, indicating that the PTX/PCH provided a synergistic effect significantly enhanced breast cancer cell death (Figure 7C) (Gao et al., 2014).

Conclusion

Overall, we reported the synthesis of redox PCH nanoparticles for structural and physicochemical property control for efficient PTT and chemotherapy in breast cancer. The physicochemical and photothermal properties, drug release characteristic, and *in-vitro* and *in-vivo* antitumor therapy efficiency of the devised PCH nanoparticles were studied, and it was found that PTX/PCH nanoparticles induced apoptosis of breast cancer cells through JAK-STAT signaling pathway. The results of this study may provide a new pathway for designing conjugated polymer nanoparticles for breast cancer treatment and other clinical applications.

Data availability statement

The original contributions presented in the study are included in the article/Supplementary Material, further inquiries can be directed to the corresponding authors.

Ethics statement

The animal study was reviewed and approved by Soochow University.

Author contributions

JS, WX, and SZ carried out the concepts, design, experiment, analysis data and manuscript preparation. JS and GJ reviewed and edited the manuscript. All authors have read and confirmed the content of the manuscript.

Funding

This work was supported by National Natural Science Foundation of China (Grant No.:81873730), the medical scientific research project of Jiangsu Commission of Health (Grant No.: Z2020076), and the Preponderant Clinic Discipline Group Project of the Second Affiliated Hospital of Soochow University (Grant No.: XKTJ-XK202009).

Conflict of interest

The authors declare that the research was conducted in the absence of any commercial or financial relationships that could be construed as a potential conflict of interest.

Publisher's note

Supplementary material

The Supplementary Material for this article can be found online at: https://www.frontiersin.org/articles/10.3389/fbioe.2022.1049437/full#supplementary-material

References

Bray, F., Ferlay, J., Soerjomataram, I., Siegel, R. L., Torre, L. A., and Jemal, A. (2018). Global cancer statistics 2018: GLOBOCAN estimates of incidence and mortality worldwide for 36 cancers in 185 countries. *CA A Cancer J. Clin.* 68 (6), 394–424. doi:10.3322/caac.21492

Choi, J., Yang, J., Jang, E., Suh, J.-S., Huh, Y.-M., Lee, K., et al. (2011). Gold nanostructures as photothermal therapy agent for cancer. *Anticancer. Agents Med. Chem.* 11 (10), 953–964. doi:10.2174/187152011797927599

Das, D., Thi Thu Hien, P., and Noh, I. (2018). Characterizations of hyaluronate-based terpolymeric hydrogel synthesized via free radical polymerization mechanism for biomedical applications. *Colloids Surfaces B Biointerfaces* 170, 64–75. doi:10.1016/j.colsurfb.2018.05.059

De Melo-Diogo, D., Pais-Silva, C., Dias, D. R., Moreira, A. F., and Correia, I. J. (2017). Strategies to improve cancer photothermal therapy mediated by nanomaterials. *Adv. Healthc. Mat.* 6 (10), 1700073. doi:10.1002/adhm.201700073

Edmonds, C., Hagan, S., Gallagher-Colombo, S. M., Busch, T. M., and Cengel, K. A. (2012). Photodynamic therapy activated signaling from epidermal growth factor receptor and STAT3 targeting survival pathways to increase PDT efficacy in ovarian and lung cancer. *Cancer Biol. Ther.* 13 (14), 1463–1470. doi:10.4161/cbt.22256

Feng, Q., Liu, Y., Huang, J., Chen, K., Huang, J., and Xiao, K. (2018). Uptake, distribution, clearance, and toxicity of iron oxide nanoparticles with different sizes and coatings. *Sci. Rep.* 8 (1), 2082. doi:10.1038/s41598-018-19628-z

Fu, K. K., Phillips, T. L., Silverberg, I. J., Jacobs, C., Goffinet, D. R., Chun, C., et al. (1987). Combined radiotherapy and chemotherapy with bleomycin and methotrexate for advanced inoperable head and neck cancer: Update of a northern California oncology group randomized trial. *J. Clin. Oncol.* 5 (9), 1410–1418. doi:10.1200/JCO.1987.5.9.1410

Gao, M., Xu, H., Zhang, C., Liu, K., Bao, X., Chu, Q., et al. (2014). Preparation and characterization of curcumin thermosensitive hydrogels for intratumoral injection treatment. *Drug Dev. Ind. Pharm.* 40 (11), 1557–1564. doi:10.3109/03639045.2013.838579

Geng, B., Qin, H., Shen, W., Li, P., Fang, F., Li, X., et al. (2020). Carbon dot/WS2 heterojunctions for NIR-II enhanced photothermal therapy of osteosarcoma and bone regeneration. *Chem. Eng. J.* 383, 123102. doi:10.1016/j.cej.2019.123102

Guo, B., Zhao, J., Wu, C., Zheng, Y., Ye, C., Huang, M., et al. (2019). One-pot synthesis of polypyrrole nanoparticles with tunable photothermal conversion and drug loading capacity. *Colloids Surfaces B Biointerfaces* 177, 346–355. doi:10.1016/j.colsurfb.2019.02.016

Hossen, S., Hossain, M. K., Basher, M. K., Mia, M. N. H., Rahman, M. T., and Uddin, M. J. (2019). Smart nanocarrier-based drug delivery systems for cancer therapy and toxicity studies: A review. *J. Adv. Res.* 15, 1–18. doi:10.1016/j.jare.2018.06.005

Li, J., and Pu, K. (2020). Semiconducting polymer nanomaterials as near-infrared photoactivatable protherapeutics for cancer. *Acc. Chem. Res.* 53 (4), 752–762. doi:10.1021/acs.accounts.9b00569

Liu, Y., Bhattarai, P., Dai, Z., and Chen, X. (2019). Photothermal therapy and photoacoustic imaging via nanotheranostics in fighting cancer. *Chem. Soc. Rev.* 48 (7), 2053–2108. doi:10.1039/c8cs00618k

Luo, K., Wu, H., Chen, Y., Li, J., Zhou, L., Yang, F., et al. (2021). Preparation of Bi-based hydrogel for multi-modal tumor therapy. *Colloids Surfaces B Biointerfaces* 200, 111591. doi:10.1016/j.colsurfb.2021.111591

Mi, F.-L., Burnouf, T., Lu, S.-Y., Lu, Y.-J., Lu, K.-Y., Ho, Y.-C., et al. (2017). Self-targeting, immune transparent plasma protein coated nanocomplex for noninvasive photothermal anticancer therapy. *Adv. Healthc. Mat.* 6 (14), 1700181. doi:10.1002/adhm.201700181

Misra, S., Heldin, P., Hascall, V. C., Karamanos, N. K., Skandalis, S. S., Markwald, R. R., et al. (2011). Hyaluronan-CD44 interactions as potential targets for cancer therapy. *FEBS J.* 278 (9), 1429–1443. doi:10.1111/j.1742-4658.2011.08071.x

Qiao, L., Mei, Z., Yang, Z., Li, X., Cai, H., and Liu, W. (2016). ALA-PDT inhibits proliferation and promotes apoptosis of SCC cells through STAT3 signal pathway. *Photodiagnosis Photodyn. Ther.* 14, 66–73. doi:10.1016/j.pdpdt.2016.01.008

Rao, K. M., Parambadath, S., Kumar, A., Ha, C.-S., and Han, S. S. (2018). Tunable intracellular degradable periodic mesoporous organosilica hybrid nanoparticles for doxorubicin drug delivery in cancer cells. *ACS Biomater. Sci. Eng.* 4 (1), 175–183. doi:10.1021/acsbiomaterials.7b00558

Scribano, C. M., Wan, J., Esbona, K., Tucker, J. B., Lasek, A., Zhou, A. S., et al. (2021). Chromosomal instability sensitizes patient breast tumors to multipolar divisions induced by paclitaxel. *Sci. Transl. Med.* 13 (610), eabd4811. doi:10.1126/scitranslmed.abd4811

Song, X., Liang, C., Gong, H., Chen, Q., Wang, C., and Liu, Z. (2015). Photosensitizer-conjugated albumin-polypyrrole nanoparticles for imaging-guided *in vivo* photodynamic/photothermal therapy. *Small* 11 (32), 3932–3941. doi:10.1002/smll.201500550

Wang, S., Tian, Y., Tian, W., Sun, J., Zhao, S., Liu, Y., et al. (2016). Selectively sensitizing malignant cells to photothermal therapy using a CD44-targeting heat shock protein 72 depletion nanosystem. *ACS Nano* 10 (9), 8578–8590. doi:10.1021/acsnano.6b03874

Xie, M., Liu, X., and Wang, S. (2022). Degradation of methylene blue through Fenton-like reaction catalyzed by MoS2-doped sodium alginate/Fe hydrogel. *Colloids Surfaces B Biointerfaces* 214, 112443. doi:10.1016/j.colsurfb.2022.112443

Xu, L., Wang, J., Wang, J., Lu, S.-Y., Yang, Q., Chen, C., et al. (2022). Polypyrrole-iron phosphate-glucose oxidase-based nanocomposite with cascade catalytic capacity for tumor synergistic apoptosis-ferroptosis therapy. *Chem. Eng. J.* 427, 131671. doi:10.1016/j.cej.2021.131671

Yu, Z., Chan, W. K., Zhang, Y., and Tan, T. T. Y. (2021). Near-infrared-II activated inorganic photothermal nanomedicines. *Biomaterials* 269, 120459. doi:10.1016/j.biomaterials.2020.120459

Zhang, C., Zeng, Z., Cui, D., He, S., Jiang, Y., Li, J., et al. (2021). Semiconducting polymer nano-PROTACs for activatable photo-immunometabolic cancer therapy. *Nat. Commun.* 12 (1), 2934. doi:10.1038/s41467-021-23194-w

Zhang, L., He, G., Yu, Y., Zhang, Y., Li, X., and Wang, S. (2022). Design of biocompatible chitosan/polyaniline/laponite hydrogel with photothermal conversion capability. *Biomolecules* 12 (8), 1089. doi:10.3390/biom12081089

Zhang, Z.-T., Huang-Fu, M.-Y., Xu, W.-H., and Han, M. (2019). Stimulus-responsive nanoscale delivery systems triggered by the enzymes in the tumor microenvironment. *Eur. J. Pharm. Biopharm.* 137, 122–130. doi:10.1016/j.ejpb.2019.02.009

Zhu, Y., Wang, X., Chen, J., Zhang, J., Meng, F., Deng, C., et al. (2016). Bioresponsive and fluorescent hyaluronic acid-iodixanol nanogels for targeted X-ray computed tomography imaging and chemotherapy of breast tumors. *J. Control. Release* 244, 229–239. doi:10.1016/j.jconrel.2016.08.027

frontiers | Frontiers in Bioengineering and Biotechnology

TYPE Review
PUBLISHED 03 November 2022
DOI 10.3389/fbioe.2022.1066617

OPEN ACCESS

EDITED BY
Xiaowei Zeng,
Sun Yat-sen University, China

REVIEWED BY
Tongkai Chen,
Guangzhou University of Chinese Medicine, China
Yifeng Lei,
Wuhan University, China

*CORRESPONDENCE
Miao Wang,
wangmiao@ujs.edu.cn
Li Ni,
nili@suda.edu.cn

†These authors have contributed equally to this work

SPECIALTY SECTION
This article was submitted to Biomaterials, a section of the journal Frontiers in Bioengineering and Biotechnology

RECEIVED 11 October 2022
ACCEPTED 21 October 2022
PUBLISHED 03 November 2022

CITATION
Ding F, Zhang L, Chen X, Yin W, Ni L and Wang M (2022), Photothermal nanohybrid hydrogels for biomedical applications. *Front. Bioeng. Biotechnol.* 10:1066617. doi: 10.3389/fbioe.2022.1066617

Photothermal nanohybrid hydrogels for biomedical applications

Fan Ding[1†], Linlin Zhang[2†], Xu Chen[1], Weiling Yin[1], Li Ni[2*] and Miao Wang[1*]

[1]Institute for Advanced Materials, School of Materials Science and Engineering, Jiangsu University, Zhenjiang, Jiangsu, China, [2]Department of Orthopaedic Surgery, Orthopedic Institute, The First Affiliated Hospital, Suzhou Medical College, Soochow University, Suzhou, Jiangsu, China

In the past decades, diseases such as wound infection, cancer, bone defect and osteoarthritis have constantly threatened the public health. However, the traditional treatment has many insufficiencies, such as high cost, easy recurrence and high biological toxicity. Hydrogel is a material with three-dimensional network structure, which has a series of advantages, such as injectability, self-heal ability, easy loading and controllability of drug release, and excellent biocompatibility. Therefore, it is extensively used in drug delivery, antibacterial, anti-cancer and other fields. However, the traditional hydrogels have the single performance, and therapeutic efficacy is often rely on the drugs loaded on them to cure diseases, which cannot achieve sustainable therapeutic effect. In order to solve this problem, photothermal nano hydrogel with photothermal agent (PTA) has become an ideal material due to its excellent physical and chemical properties. Photothermal nano hydrogels used in photothermal therapy (PTT) can exploit the photothermal effect of photothermal agent to increase local temperature and control the sol-gel phase transition behavior of hydrogels, so they are widely used in drug release, photothermal sterilization, photothermal inhibition of cancer cells and enhancement of bone repair. To sum up, this paper introduces the preparation of hydrogels with photothermal nanomaterials, and discusses their applications in the fields of drug release, photothermal sterilization, photothermal cancer cell inhibition and enhanced bone repair.

KEYWORDS

biomedical hydrogel, photothermal therapy, photothermal antibacterial, photothermal cancer suppressor, photo-controlled drug release

Introduction

Hydrogel is a kind of soft material with a three-dimensional network structure, which is made up of networks with hydrophilic polymers, and is crosslinked by physical or chemical bonds between strong water absorption. By simulating the composition, physical and chemical properties of the natural extracellular matrix (ECM), the hydrogel performs good biodegradability and biocompatibility. (Cao et al., 2021; Pei et al., 2021). And the hydrogels exhibit stimulus response and self-healing properties under the stimulation of

external environment can meet the needs of hydrogels in medical materials, which has attracted extensive attention of researchers (Ou & Tian, 2021; Xie et al., 2021; Zhang & Lucia, 2021). In recent years, hydrogels have been widely used in biomedical fields, such as drug delivery, antibacterial therapy, biosensors and cancer cell inhibition (Xu et al., 2022a; Xu et al., 2022b; Zhang et al., 2022).

Photothermal nano hydrogel is a kind of hydrogel with photothermal nano materials added during the preparation of hydrogel. Photothermal therapy (PTT) generated by photothermal nano hydrogel is a typical photon triggered therapy method. It can use the photothermal effect of photothermal agent (PTA) to extract energy from visible light/near-infrared light, convert it into heat, increase the temperature of the surrounding environment, and achieve the effect of ablating of tumor cells and killing bacteria. (Chen et al., 2021; Guedes et al., 2021). It is highly necessary to choose the appropriate photothermal agent. The ideal photothermal agents with appropriate NIR band gap and high response to near-infrared light irradiation can effectively convert light energy into heat energy under near-infrared light irradiation, and improve the therapeutic effect (Lu Y. et al., 2021). Photothermal treatment has many advantages. It can reduce the pain of patients during treatment. Secondly, it has short processing time and obvious therapeutic effect. More importantly, the materials used for photothermal treatment are of low toxicity or even non-toxic, causing less harm to the human body. So far, many forms of photothermal therapy have been studied and applied to the field of anti-cancer and antibacterial (Yu et al., 2019; Zhao et al., 2022).

Photothermal agent (PTA) is an crucial factor of photothermal therapy and the selection of appropriate photothermal agent is very important to the success of photothermal therapy (Guedes et al., 2021; Zhang et al., 2021). PTA should have high photothermal conversion efficiency, easy to prepare and good biocompatibility. However, many photothermal agents with high thermal efficiency have certain toxicity, which is not suitable for medical application. Hydrogels made by combining materials with photothermal agents with high biocompatibility can not only retain the high photothermal conversion effect, but also reduce biological toxicity and make them more biocompatible. In this paper, several typical photothermal nanohydrogels are reviewed and their applications in biomedical fields are also discussed.

Photothermal nanomaterials for hydrogel fabrication

The preparation of photothermal nanohydrogels mainly relies on the photothermal nanomaterials. The most widely used ones mainly include Metal nanomaterials, Carbon based nanomaterials, Metal sulfide/oxide nanomaterials, Black phosphorus nanomaterials, MXenes nanomaterials, Polymer nanomaterials, Organic dye nanomaterials, etc. In the following, the development of different photothermal materials for the preparation of photothermal nanohydrogels will be discussed in detail.

Metal nanomaterials

The properties of metal nanomaterials are very excellent. It has a strong surface plasmon resonance (LSPR) effect. When the incident photon frequency matches the overall vibration frequency of the metal nano material, the nano material will have a strong absorption effect on the photon energy, and a strong resonance absorption peak will appear in the spectrum. (Ai et al., 2021). Moreover, metal nanomaterials have excellent thermal properties, high absorption cross section and high field conversion efficiency in the near infrared region. Metal nanomaterials combine with peptides, antibodies, biocompatible polymers, chemical drugs and immune factors, and have great potential in the field of biomedicine (Park et al., 2018). The metal nanomaterials most explored and studied in PTT are gold nanomaterials, silver nanomaterials and copper nanomaterials, All of them have the advantages of strong absorption, excellent adjustable physical properties, optical properties and biocompatibility (Xu H. et al., 2020; Lu X. et al., 2021).

At present, various configurations of nanostructures based on gold have been developed. Among them, gold nanorods (GNR) have attracted much attention because of their simple biological coupling, strong and adjustable plasma absorption. In particular, there are two plasmon resonance surfaces on the surface of GNR, the transverse band represented in the visible region (650 nm–950 nm) and the longitudinal band represented in the near infrared region (1000 nm–1350 nm), so the radiation can penetrate tissues to the maximum extent, making it an ideal material for biomedical applications (Zhang Y. et al., 2020; Gupta & Malviya, 2021). GNR have biofilm activity and are an attractive therapeutic method for photothermal therapy. The hydrogel added with gold nanoparticles (GNP) shows certain advantages in biomedical applications. On the one hand, the hydrogel has good biocompatibility and degradability. On the other hand, the GNP are used as light absorbers, making the hydrogel well used in photothermal therapy. Bermudez-Jimenez et al. prepared gold nanorod hydrogels by embedding GNR into a non-toxic, biocompatible and biodegradable chitosan hydrogel (Bermudez-Jimenez et al., 2020). Combined with PTT treatment, it can effectively control the pathogenic bacteria in the mouth. In another study, Liu et al. modified gold nanorods by a two-block copolymer, an injectable nanocomposite hydrogel was prepared by the interaction of α-cyclodextrin (Figure 1A)(Liu M. et al., 2019). The hydrogel can not only improve the

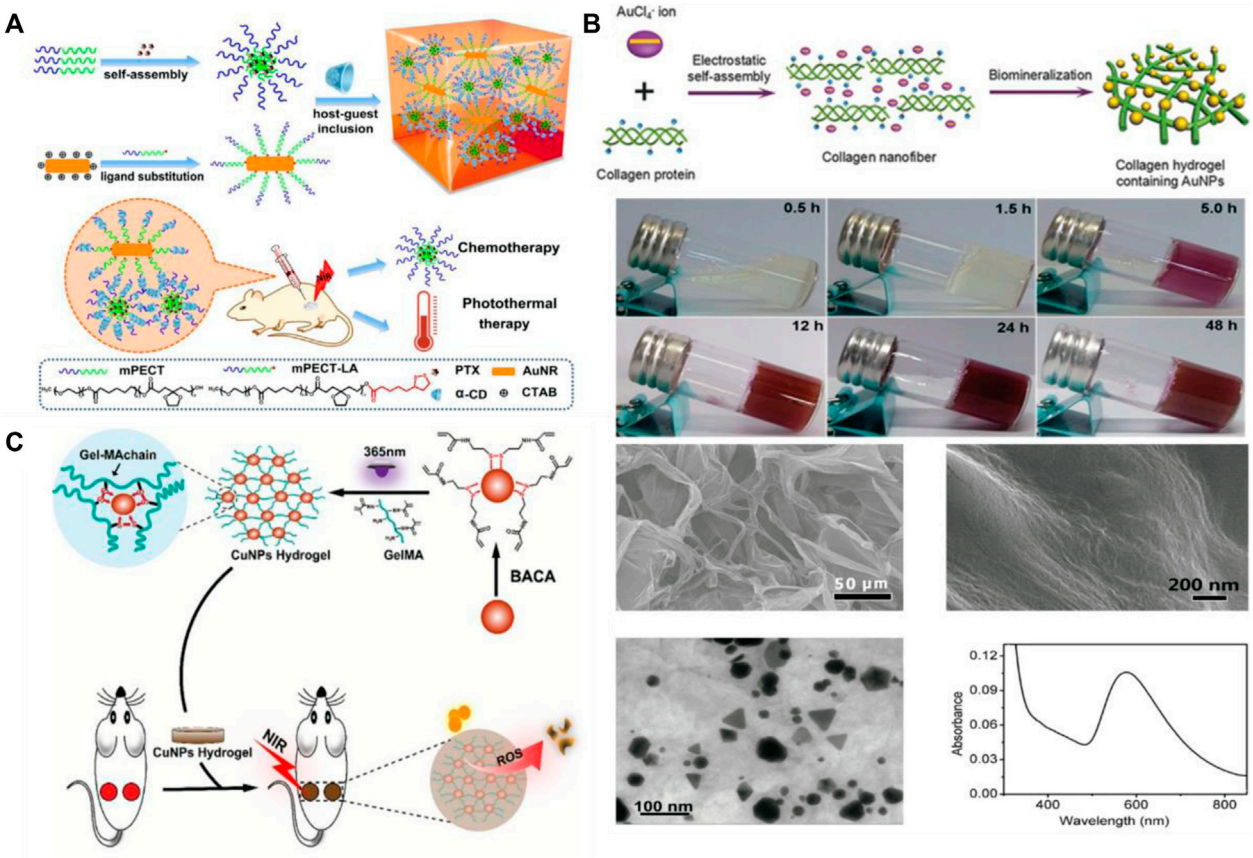

FIGURE 1
(A) Preparation of gold nano hydrogel and its application in chemotherapy-assisted photothermal therapy. Reproduced from ref.49 with permission from 2019 Royal Society of Chemistry. **(B)** Synthesis and characterization of injectable and self-healing collagen hydrogels containing gold nanoparticles. Reproduced from ref. 87 with permission from 2016 WILEY-VCH. **(C)** Preparation of copper nano hydrogel and schematic diagram of antibacterial principle of photothermal therapy. Reproduced from ref. 75 with permission from 2019 Royal Society of Chemistry.

biocompatibility of AuNR, but also realize local photothermal treatment. Moorcroft et al. co loaded IRIKIRIKCONH$_2$ (IK8) and GNR into polyethylene glycol (PEG) hydrogels, and achieved the bactericidal effect on *Staphylococcus aureus* by photothermal triggering the release of IK8 (Moorcroft et al., 2020). At the same time, relevant experiments further confirmed that the hydrogels loaded with GNR had certain photothermal damage to the biofilms. At present, photothermal ablation (PTA) based on nanotechnology, as a highly effective treatment method for solid tumors, has been widely explored. Gold nanoparticles, as strong light absorbers, can absorb NIR and achieve local fever through photothermal conversion effect, which can reduce the damage to tissues around the wound to the maximum extent while treating the wound (Zhang R. et al., 2020). Xing et al. proposed a method based on biomineralization trigger for the first time to prepare collagen hydrogels with adjustable mechanical properties (Figure 1B) (Xing et al., 2016). Through electrostatic bonding between collagen chains (positively charged) and inorganic anion clusters, GNP were formed, which were controlled as cross-linking agents for mechanical properties, to prepare hydrogels with advantages of *in vivo* injection. When the stress relaxation of the hydrogel is caused by the non-covalent interaction between GNP and collagen chains, the hydrogel can recover rapidly under the condition of applied stress. This study expands the application of GNP hydrogel.

Silver nanoparticles (Ag NP$_s$) have similar photothermal properties to GNP. Because of their photothermal effects, toxicity of silver, and wide applicability in the pharmaceutical field, they have always attracted the attention of researchers. (Awasthi et al., 2020; Ren et al., 2021). Silver nanoparticles have become a good photothermal agent because of their high photo thermal conversion efficiency, easy synthesis and multifunctional adjustability of their surface properties (de Oliveira Lima et al., 2022). Recently, Amatya et al. prepared hydrogel films with good photothermal activity through bovine serum protein (BSA) and Ag NPs and applied them *in vivo* (Amatya et al., 2021). Under 0.6 W low laser power, the temperature can be reached 45 °C which is ample for tumor ablation.

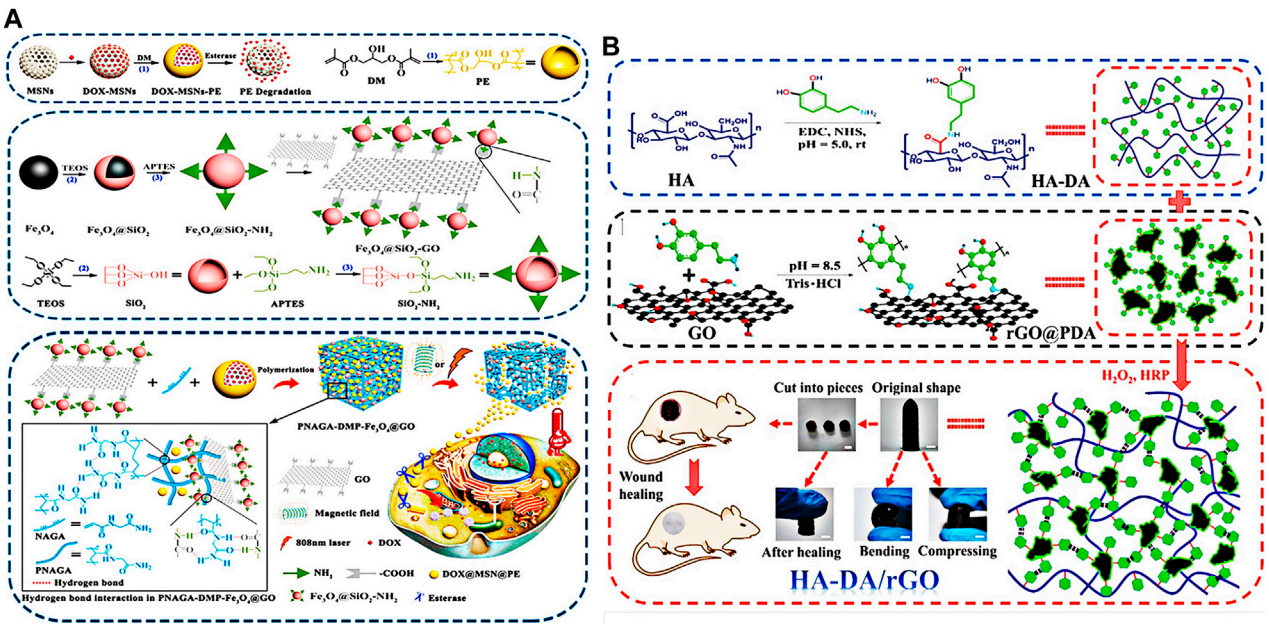

FIGURE 2
(A) Schematic diagram of the preparation of nanocomposite hydrogel and its mechanism in tumor therapy. Reproduced from ref. 101 with permission from 2020 Elsevier ltd. **(B)** Diagrammatic sketch of HA-DA/rGO hydrogel preparation. Reproduced from ref. 42 with permission from 2019 WILEY-VCH.

Due to local surface plasmon resonance, copper nanoparticles show strong light absorption in visible and near infrared, similar to that of silver and gold nanoparticles. Nano copper has been widely used in wound healing due to its high redox potential, low production cost and broad-spectrum antibacterial activity. Chen et al. successfully embedded nanoparticles into guar gum hydrogel to form copper nanoparticle hydrogel (Chen et al., 2017). The copper nanoparticles embedded in the hydrogel have a good photo thermal conversion rate. After 10 min of laser irradiation, the temperature of the hydrogel can rise to 67°C. This rapidly rise in temperature contributes to the high antibacterial performance of copper on irradiated nanoparticle hydrogels. Tao et al. reported a MA modified copper nanoparticle hydrogel (Figure 1C) (Tao et al., 2019). In combination with 808 nm NIR radiation, copper NPs embedded in the hydrogel can produce reactive oxygen species (ROS), and effectively convert NIR laser energy into local heat. It can eradicate *Escherichia coli* and *Staphylococcus aureus* bacteria *in vitro* antibacterial experiments. Most importantly, the hydrogel can also promote wound healing and realize multi-functional application of hydrogel.

Carbon-based nanomaterials

Graphene is a new material with a single-layer two-dimensional honeycomb lattice structure, which is closely packed with sp^2 hybrid connected carbon atoms (Deng X. et al., 2020). The sp^2 hybrid carbon atoms of Graphene oxide in the hexagonal lattice structure allows to absorb light of different wavelengths, and its photothermal capacity can be enhanced with the increase of photoabsorption, which make it a good photothermal heating material (Falke et al., 2020; Huang, 2022). Lee et al. used graphene oxide and modified it with polyethylene glycol to develop a wavelength independent hydrogel system, to improve the dispersion of graphene oxide in aqueous solution (Lee et al., 2020). Under the irradiation of 532 nm, 785 nm and 980 nm lasers, the temperature of graphene oxide polyethylene glycol solution can reach 43°C, and free radical polymerization can be triggered at this temperature. Yuan et al. prepared a magnet and light double response hydrogel by introduced Fe_3O_4-GO nanocomposite as a magneto photothermal agent. Fe_3O_4-GO nanocomposite can convert the external magnetic field and near-infrared (NIR) light into heat, which can effectively improve the local temperature in the hydrogel (Figure 2A) (Yuan et al., 2020). Li et al. modified graphene oxide with polyethyleneimine, an amine terminal polymer branch, and prepared a hydrogel (Li et al., 2019). The hydrogel is not only structurally stable, but also can provide continuous drug delivery and near-infrared photothermal effect. Also many researchers studied the reduction of graphene oxide to improve the photothermal properties of graphene oxide. Liang and his colleagues prepared a series of hyaluronic acid grafted dopamine and

reduced graphene oxide (rGO) hydrogels using the H_2O_2/HPR (horseradish peroxidase) system (Figure 2B) (Liang et al., 2019). The hydrogels have good self-healing properties, antioxidant activity and tissue adhesion. And most importantly, the enhanced antibacterial properties of the hydrogels through near-infrared (NIR) radiation, make them a good wound dressing. Liu and his colleagues prepared the hydrogel by functionalizing and reducing graphene oxide with pH responsive carboxymethyl chitosan (Liu W. et al., 2019). The hydrogel not only has excellent degradability and biocompatibility, but also has better photothermal conversion efficiency than many other photosensitizers, reaching 86.7%.

Metal sulfide/oxide nanomaterials

Metal sulfides/oxides which cost less than precious metals are also use in PTT. Copper sulfide nanostructures have excellent photothermal properties. Unlike the infrared absorption of gold nanostructures, the infrared absorption of copper sulfide nanoparticles comes from the energy band transition (Sun et al., 2019; Xie et al., 2022). Fu and his colleagues reported an injectable and thermosensitive hydrogel encapsulating copper sulfide nanoparticles (Fu et al., 2018). Nanodots are uniformly distributed in the hydrogel matrix, and their particle size remains unchanged. The hydrogel not only shows the ability of forming *in-situ* gel with thermal response, and the chemical toxicity of copper sulfide was reduced by "composing" nano dots in the matrix. In another study, Lin et al. incorporated copper sulfide nanoparticles (CuS NPs) into hyaluronic acid (HA) to construct hydrogels (Lin et al., 2021). By combining the photothermal characteristics of CuS NPs, the sterilization of low temperature photothermal therapy is realized, also the improvement of the antibacterial efficiency and minimization of the damage to normal tissues. The team combined the photothermal effect and antibacterial effect provides a new idea for the new type of wound bandage.

Silver sulfide quantum dots are semiconductor materials with strong light stability and high biocompatibility. Because of their unique properties such as broadband absorption, convenient preparation, good chemical stability and low toxicity, they have attracted extensive attention. Recently, Hou et al. encapsulated the near-infrared silver sulfide quantum dots as photosensitizers in the hydrophobic cavity by self-assembly of polypeptide hydrogels, and then integrated the drugs DOX and Bestin into the hydrogels, thus prepared a multifunctional gene engineering polypeptide hydrogel encapsulating silver sulfide quantum dots (Hou et al., 2020). Due to the photothermal properties of silver sulfide quantum dots, the release of DOX from hydrogels is promoted, thus the overall therapeutic effect is improved.

Bismuth sulfide (Bi_2S_3) is a promising PTT agent with a narrow direct band gap (E ≈ 1.3 eV). Bi_2S_3 nanostructures have been used as CT contrast agents, its cost is much lower than other metal elements (such as gold, platinum and tantalum). Bi_2S_3 nanoparticles also have biocompatibility and metabolism, and have low toxicity. Different types of Bi_2S_3 nanoparticles, such as Bi_2S_3 nanorods, nano porous bladder and nanodots are more commonly used. Smaller Bi_2S_3 nanoparticles are thought to have better light absorption and can be excreted from the bladder. Wu et al. embedded the ultra-small (less than 3 nm) Bi_2S_3 nano point into the hydrogel to improve the stability of the Bi_2S_3 nano point and endow the injectability of hydrogel (Figure 3A) (Wu et al., 2021). The hydrogel can maintain the same photothermal performance after being stored for 3 months. In another study, Wu et al. designed and synthesized MoS_2/Bi_2S_3-PEG (MBP) nano sheets (Figure 3B). And they dispersed them together with DOX into agar solution to build a hydrogel system with photothermal conversion performance, and achieve tumor PTT and chemotherapy under the guidance of computer tomography (CT)/photoacoustic (PA) dual model imaging (Wu et al., 2018).

MoS_2 is another representative sulfide. Jin et al. designed to load positively charged DOX and negatively charged PC10A onto the surface of molybdenum disulfide nano sheets to prepare mixed PC10A/DOX/MoS_2 nano particles and dispersed them in hydrogels (Jin et al., 2020). Molybdenum disulfide nano sheets were used as both photothermic agent and photodynamic agent in hydrogels. The production of hot oxygen and reactive oxygen can cause immune response and promote photothermal therapy on tumors. Zhou et al. reported a simple method to prepare sodium alginate (ALG) - Fe^{3+}(MAF) hydrogel containing molybdenum disulfide and glucose oxidase (GOx) (Zhou L. et al., 2020). The hydrogel has high photothermal conversion capacity of molybdenum disulfide, and an enzymatic reaction could occur in the hydrogel, which provides an effective way for the use of enzymes in cancer treatment.

Black phosphorus nanomaterials

Black phosphorus nanomaterials (BP) nano sheet is a kind of two-dimensional nano material with unique properties such as adjustable band gap, high NIR absorption and high photo thermal conversion efficiency (Eswaraiah et al., 2016; Ren et al., 2017). BP nano sheet has the characteristics of highly efficient single oxygen generation, and has extensive NIR absorption and photothermal conversion characteristic under whole visible light region, and is extensively used in photothermal therapy. As an inorganic nano agent, BP nano tablets are attractive due to their biocompatibility. Because phosphorus is an important element in human bones, accounting for about 1% of human body weight. Qin et al. used the biocompatible copolymer F127 as the matrix to construct the thermosensitive hydrogel together with the photothermal therapeutic agent BP nano sheet (Qin et al., 2019). The hydrogel has the characteristics of near infrared

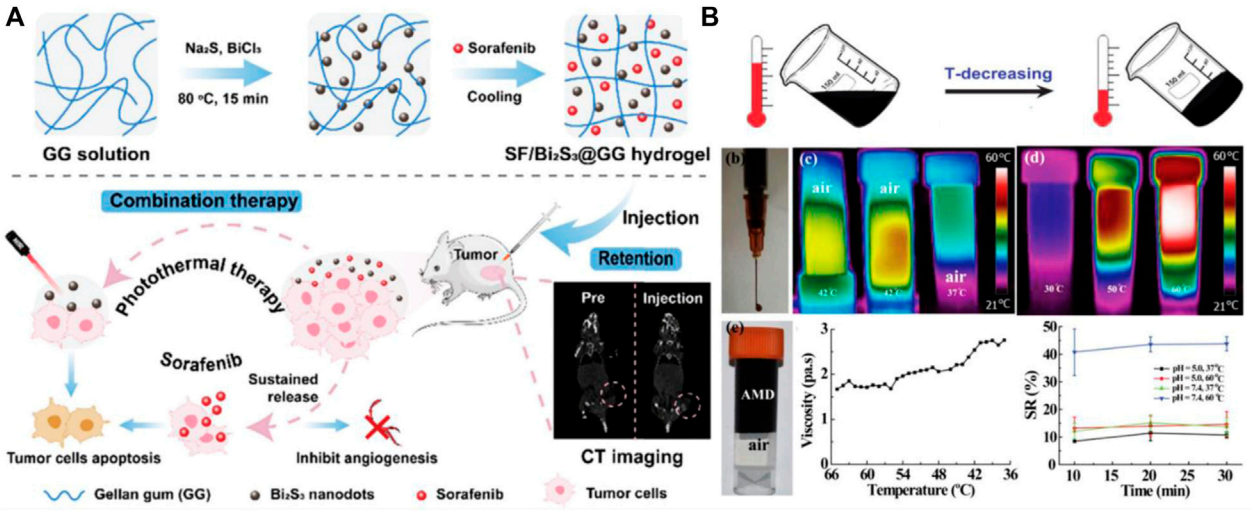

FIGURE 3
(A) Preparation of SF/ Bi2S3@GG photothermal nanohydrogel and its application in tumor therapy. Reproduced from ref. 83 with permission from 2021 Royal Society of Chemistry. **(B)** The formation principle of AMD hydrogel and its photothermal performance test. Reproduced from ref. 81 with permission from 2017 Published by Elsevier Ltd.

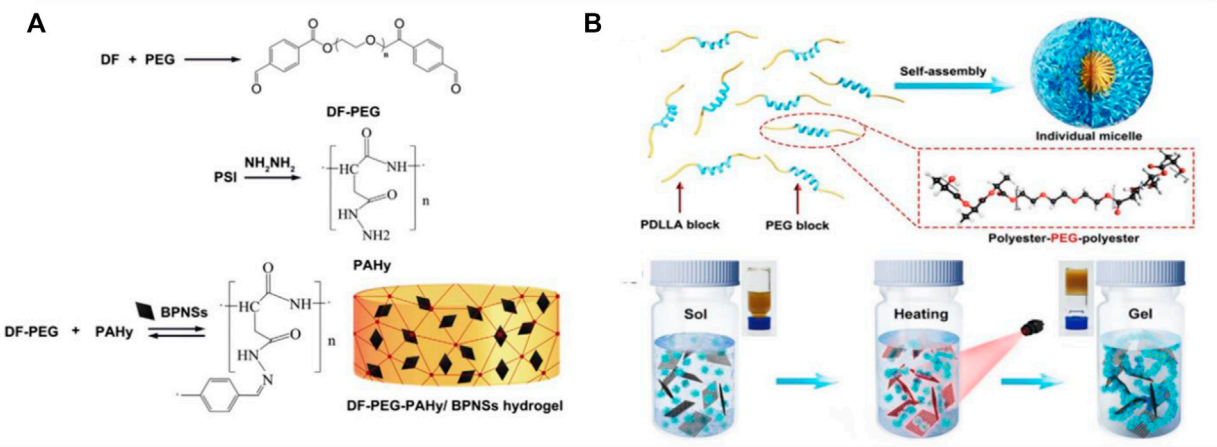

FIGURE 4
(A) Schematic diagram of preparation of black photothermal nanohybrid hydrogels. Reproduced from ref. 82 with permission from 2019 Published by Elsevier Inc. **(B)** Preparation of black phosphorus nano hydrogel and its schematic diagram of gel sol transition under infrared light irradiation. Reproduced from ref. 70 with permission from 2018 The Authors. Published by WILEY-VCH.

photothermal conversion, photothermal stability and biodegradability. Wu et al. prepared a pH sensitive DF-PEG-PAHy/BPNSs hydrogel by adding black phosphorus nanoparticles (BPNSs) into the hydrogel formed by diphenylaldehyde functionalized polymer and polyaspartic hydrazine polymer (Figure 4A) (Wu et al., 2019). This study shows that the hydrogel has good gel characteristics, pH sensitivity and near-infrared response. Due to the photothermal effect of BP NPs, NIR accelerates the release of drugs in the hydrogel. In addition, BP nano tablets are naturally degraded in the physiological environment, in the form of harmless PO_4^{3-} as the final degradation product. Shao and his colleagues combined BP nano tablets with thermosensitive hydrogels to prepare hydrogels for photothermal therapy after cancer surgery (Figure 4B) (Shao et al., 2018). The research shows that the hydrogel has excellent NIR PTT performance, good biodegradability and biocompatibility. It can promote the rapid transformation of sol gel under NIR irradiation safely. A gel film

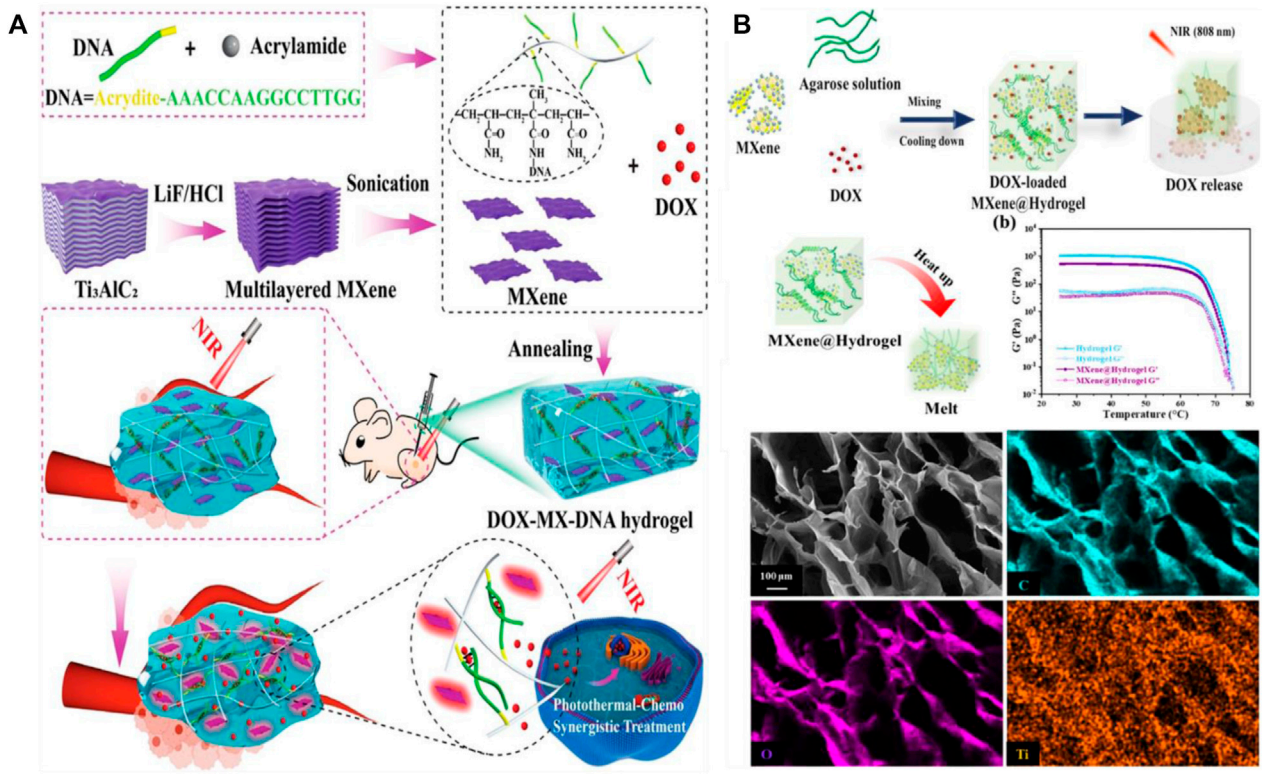

FIGURE 5
(A) Schematic diagram of the principle of MXene-DNA hydrogel loaded drugs in cancer treatment. Reproduced from ref. 29 with permission from 2022 Wiley-VCH GmbH. **(B)** Schematic diagram of synthesis and melting after heating of MXene based photothermal hydrogel. Reproduced from ref. 16 with permission from 2021 Published by Elsevier B.V.

can quickly form by spraying the hydrogel under NIR irradiation on the wound, which performed a high PTT effect and can eliminate the residual tumor tissue.

MXenes nanomaterials

After the discovery of titanium carbide ($Ti_3C_2T_x$) by Naguib et al., in 2011, transition metal carbides, nitrides, and carbon nitrides (often referred to as MXene) have attracted widely attention because of their unique planar structures, excellent physicochemical properties, and chemical diversity (Naguib et al., 2011). The general formula for these materials is $M_{n+1}X_nT_x$ (n = 1, 2, or 3), where M is an early transition metal, X is carbon and/or nitrogen, and T is the surface end inherited from the synthesis process, like -OH, -O, and -F (Xu D. et al., 2020). As a photothermal agent, MXene nanosheets exhibit strong light absorption in the near infrared range, high specific surface area and negative charge, which make abundant anchoring position of the therapeutic agent, so MXene nanosheets are widely used in photothermal therapy (Lin et al., 2017; Lin et al., 2018). He and his colleagues used MXene as photothermal agent and doxorubicin as loading chemotherapy agent, and combined it with DNA hydrogel to establish a photothermal-chemical synergistic therapy system for highly effective local cancer treatment (Figure 5A) (He et al., 2022). Under local near-infrared light irradiation, the MXene nanosheet converts light energy into heat energy and triggers the reversible transformation of hydrogel from gel to solution, releasing DOX therapeutic agent. The experimental results showed that the hydrogel had excellent biocompatibility and showed effective local cancer treatment. Dong and colleagues prepared a drug-loaded MXene/ agarose hydrogel (Dong et al., 2021). They first prepared a two-dimensional MXene nanosheet with high photothermal conversion efficiency and photothermal stability, then introduced the MXene nanosheet into the low melting point agarose gel skeleton. The temperature of the loaded hydrogel can rapidly rise to 60°C under near-infrared light and hydrolyze to release the encapsulated drug (Figure 5B). The kinetics of drug release can be regulated by agarose concentration, MXene concentration, irradiation intensity and irradiation

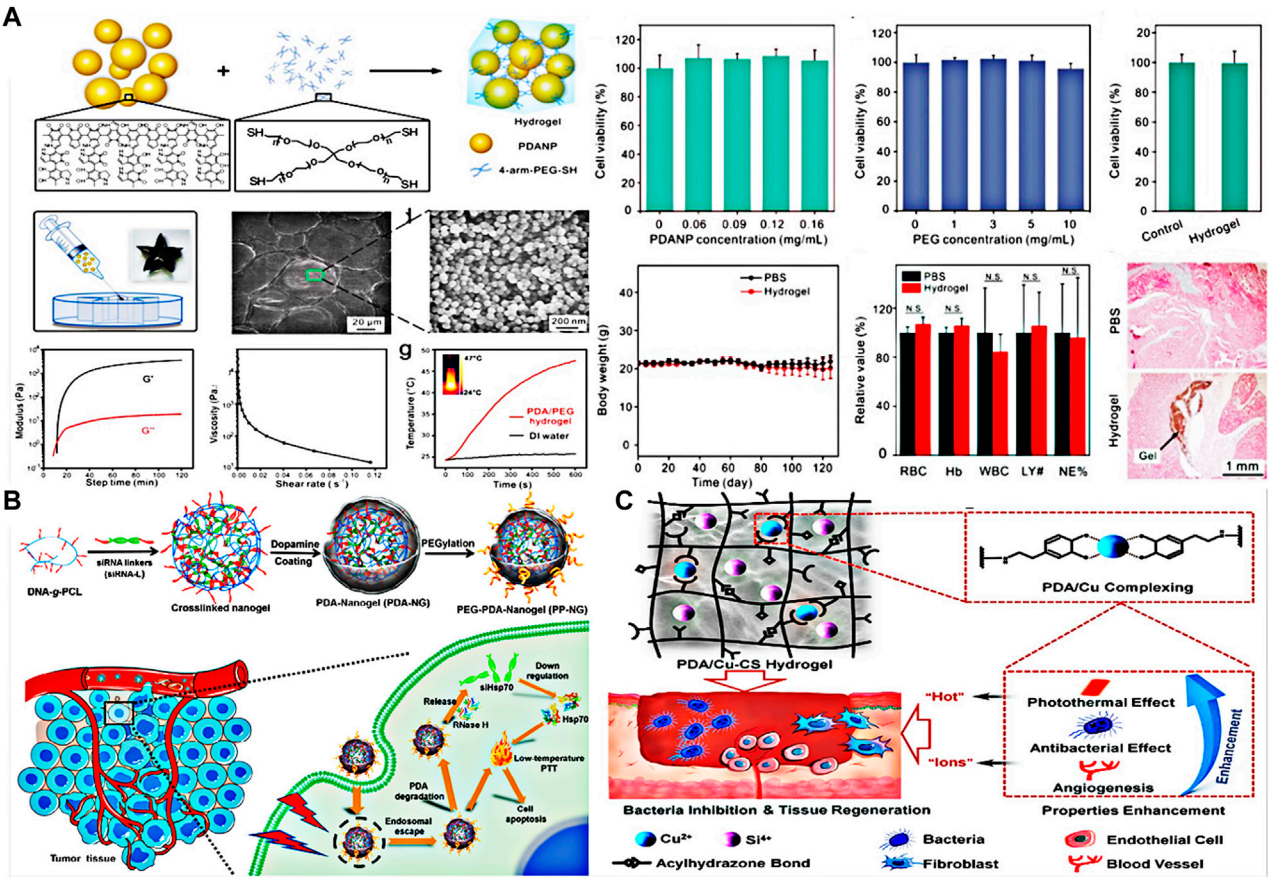

FIGURE 6
(A) Preparation and performance test of PDA-PEG hybrid hydrogels. Reproduced from ref. 80 with permission from 2017, American Chemical Society. **(B)** Preparation of polydopamine coated nucleic acid hydrogels. Reproduced from ref. 15 with permission from 2020 Elsevier Ltd. **(C)** Preparation of polydopamine combined Cu-CS hydrogel and its application in antibacterial. Reproduced from ref. 92 with permission from 2020, American Chemical Society.

time. This research provides a new way to develop smart hydrogel-based drug delivery systems for local cancer treatment. Li et al. prepared an anisotropic MXene@PVA hydrogel by directed cryoassisted salting-out. (Li Y. et al., 2022). Because of the good photothermal properties of MXene, the hydrogel can be used in local hyperthermia treatment of the infected site under near-infrared laser (808 nm) irradiation. In addition, the hydrogel has excellent mechanical properties, with stress up to 0.5 MPa and strain up to 800%. Bacterial experiments showed that the hydrogel had broad spectrum antibacterial activity against both Gram-positive and Gram-negative bacteria. Li and colleagues designed a hydrogel film with MXene nanosheets embedded with heat-responsive gelatin (Li Y. et al., 2022). They used an epithelial cell adhesion molecule antibody to modify the hydrogel membrane so that it could specifically recognize and isolate CTCS from whole blood. The captured CTCS can be released without damage through temperature responsive release and photothermal site release.

Polymeric nanomaterials

Dopamine (DA) is a biocompatible neurotransmitter in human body. It can synthesize polydopamine (PDA) by oxidative self-polymerization, and has different photothermal properties. Biologically inspired poly (dopamine) (PDA) based hydrogels have attracted great attention because of their well-known adhesion and biocompatibility (Han et al., 2017; Zhou D. et al., 2020). Wang et al. described a polydopamine nanoparticle conjugated polyethylene glycol hydrogel that could be used for on-demand drug delivery and combined chemotherapy-photothermal therapy under near-infrared irradiation (Figure 6A) (Wang et al., 2017). Most importantly, the hydrogel had good biocompatibility and would not cause

inflammation *in vivo*, and the hydrogel-mediated chemophotothermal therapy could effectively inhibit tumor growth. Zheng et al. designed a new injectable thermosensitive nano hydrogel by loading PDA NP and chemotherapy drugs (Zheng et al., 2020). The hydrogel has anti protein adsorption and photothermal effects, and the injectable amphoteric ion thermosensitive hydrogel has the advantage of low pollution. Ding et al. designed a nucleic acid nanogel coated with polydopamine (PDA) (Figure 6B) (Ding et al., 2020). After being coated with a layer of polydopamine, the nanogel not only protects the nanogel from enzymatic degradation, but also enables the nanogel to have good photothermal conversion ability under near-infrared (NIR) light irradiation. The study shows that the surface temperature of medical implants coated with PDA can be increased under NIR irradiation, which can effectively kill the adhering microorganisms on the implant surface. In addition, Xu et al. synthesized multifunctional composite hydrogels with PDA and Cu-doped calcium silicate ceramics (Cu-CS) as the main components(Figure 6C) (Xu Q. et al., 2020). Copper doped calcium silicate bioceramics have unique biological activity. The composition of PDA and Cu-CS enhanced the antibacterial performance through the "thermionic effect" of copper ions and photothermal materials synergetic antibacterial function.

Organic dye nanomaterials

Organic dye nanomaterials are also a common photothermal nanomaterials. Indocyanine green (ICG) is a water-soluble anionic tricarbocyanine dye with NIR absorption properties of 808 nm laser irradiation (Lee & Chang, 2017; Ma et al., 2019). Because of its low toxicity, it is widely used. In one study, Pan et al. prepared an ICG alginate gel with good photothermal treatment and good biocompatibility. Most importantly, hydrogels have a strong ICG fixation ability, which facilitates the accumulation of photothermal agents (Pan et al., 2019). This fixation can also reduce the potential side effects of ICG spread to surrounding tissues and improve biocompatibility.

Prussian blue (PB) is also a common organic dye nanomaterial. It was called a pigment in history. PB can be prepared in colloidal form by direct synthesis method. It has a strong charge transfer centered at~700 nm and a large tail in the near-infrared range. The radiation of this band will lead to thermal relaxation, and local hyperthermia can be generated by irradiating in the so-called bio transparent near-infrared window. PB nanoparticles have complete biocompatibility (PB has been approved by FDA) and biodegradability. Fu et al. established an injectable hydrogel containing Prussian blue nanospheres for cancer photothermal therapy (Fu J. et al., 2019). The hydrogel showed satisfactory serum stability and photothermal conversion ability. In addition, the hydrogel containing the photosensitizer nanospheres has better photothermal conversion efficiency than the nanospheres.

Biliflavin is a dark green bile pigment that is a by-product of the breakdown of hemoglobin. In recent years, the endogenous metabolite biliverin has been shown to have high photothermal conversion properties, as well as cell-protective effects with antioxidant and anti-inflammatory properties. Yao et al. designed a bioinspired green hydrogel (BVSF) (Yao et al., 2020). They incorporated biliverdin into a naturally derived silk fibroin matrix and the resultant hydrogel could be used for anti-glioma, photothermal therapy and wound healing. In the presence of biligreen, the temperature of the hydrogels can rapidly increase to higher than 45°C under NIR irradiation. Meanwhile, BVSF hydrogels can stimulate cell proliferation, migration and adhesion, and perform anti-inflammatory properties, and significantly accelerate wound repair and regeneration.

Composite nanomaterials

During the construction of hydrogel, in addition to the single photosensitive material, two kinds of composite hybrid materials may play a better effect. Liu et al. prepared a hybrid hydrogel by electrostatic complexation of DNA with upconverted rare-earth Au hybrid nanoparticles (Figure 7A) (Liu et al., 2020). The hybrid hydrogel had a higher photothermal efficiency (42.7%) due to the network formed between DNA and rare-earth Au hybrid nanoparticles. Local administration under 808 nm laser irradiation can achieve tumor eradication without recurrence. Xu and his colleagues prepared AG-PC hybrid hydrogels without antibiotics (Figure 7B) (Xu M.-L. et al., 2019). The hydrogel prepared by doping polyvinyl alcohol (PVA)/chitosan (CS) is highly stable. Because AuNR@G has the photothermal conversion characteristics. Therefore, the hybridized hydrogel showed a highly effective inhibition against both gram-negative *Escherichia coli* and gram-positive *Staphylococcus aureus* under 808 nm laser irradiation. Xing and his colleagues synthesized a collagen hydrogel using self-assembly initiated by gold biomineralization (Xing et al., 2016). Due to the reversible weak interaction between collagen chains and gold nanoparticles, the hydrogel has shear thinning and self-healing functions. This hybrid hydrogel of gold nanoparticles and collagen chains can be used in local drug delivery and sustained release, and provides novel strategy for a wide range of biomedical applications such as drug delivery and tissue engineering. Wang and colleagues synthesized a carrageenan based hybrid hydrogel functionalized with ZR-Fc MOF nanosheets using COOH-PEG-COOH as a carrier (Figure 7C) (Wang X. et al., 2021). The hybrid hydrogel can trap Gram-negative and Gram-positive bacteria by destroying ROS. The hybrid hydrogel can synergistically kill bacteria by decomposing H_2O_2 into toxic hydroxyl radicals and photothermal effects.

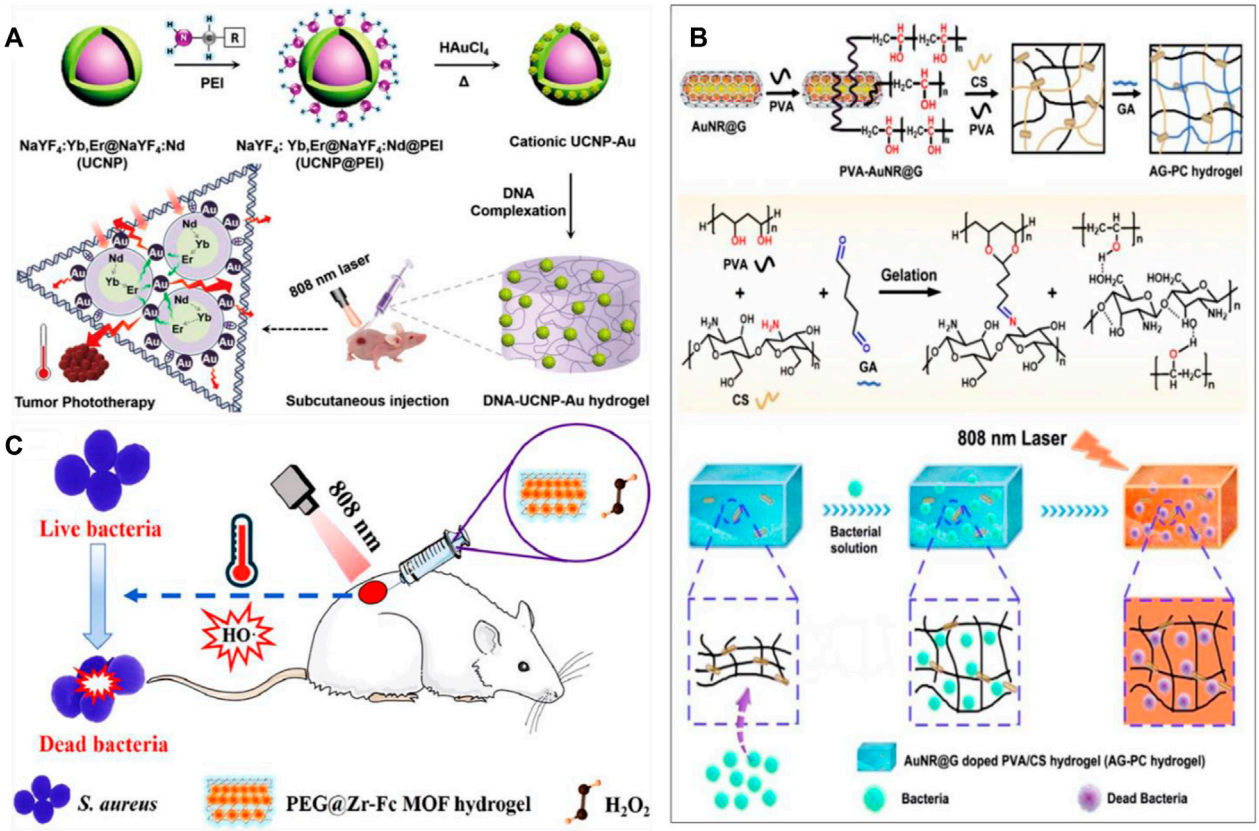

FIGURE 7
(A) Preparation and application of DNA-inorganic hybrid hydrogels. Reproduced from ref. 47 with permission from 2020 Wiley-VCH GmbH. **(B)** Schematic diagram of the procedure for preparation of AG-PC hydrogel and the suggested mechanism and its application in antimicrobial field. Reproduced from ref. 91 with permission from 2019 Royal Society of Chemistry. **(C)** Diagram of the action mechanism of hybrid hydrogels. Reproduced from ref. 79 with permission from Acta Materialia Inc. Published by Elsevier Ltd.

Other nanomaterials

In addition to the above eight photothermal nano-hydrogel materials, there are some other photothermal nano-materials for hydrogel preparation. Ma et al. synthesized a multifunctional Nd Ca Si silicate glass and glass/alginate composite hydrogel (Ma et al., 2020). The hydrogel has fluorescence temperature monitoring performance. Most importantly, due to the addition of bioactive silicate components, the hydrogel has the ability to repair the thermal damage caused by PTT. Therefore, the hydrogel can not only obtain the appropriate PTT temperature for effective treatment of tumors, but also minimize the damage to normal tissues. Han and his colleagues synthesized a new type of photosensitive antibacterial hydrogel (Figure 8A) (Han et al., 2020). The hydrogel can capture bacteria by electrostatic adsorption, and then kill a large number of adsorbed bacteria by high temperature generated by Russel blue MOF particles under near-infrared light. The inhibition rate of *Staphylococcus aureus* and *Escherichia coli* could reach 99.97% and 99.93%, respectively. Sheng and his colleagues synthesized a novel bioactive photothermal nanohybrid hydrogel using Fe-bauxite (Fe_2SiO_4) bioceramics and N, O-carboxymethyl chitosan as matrix (Figure 8B) (Sheng et al., 2021). The photothermal nanohybrid hydrogel has good Fe^{2+}/SiO_4^{4-} release and photothermal properties, which can simulate the therapeutic effect of hot spring. Animal Experiments have proved that hydrogels can promote angiogenesis and have great application potential in the field of wound repair materials.

Biomedical applications of photothermal nanocomposite hydrogels

The application of photothermal nanocomposite hydrogel in biology mainly depends on the photothermal effect of hydrogel itself and the special role of drug loading. Photothermal

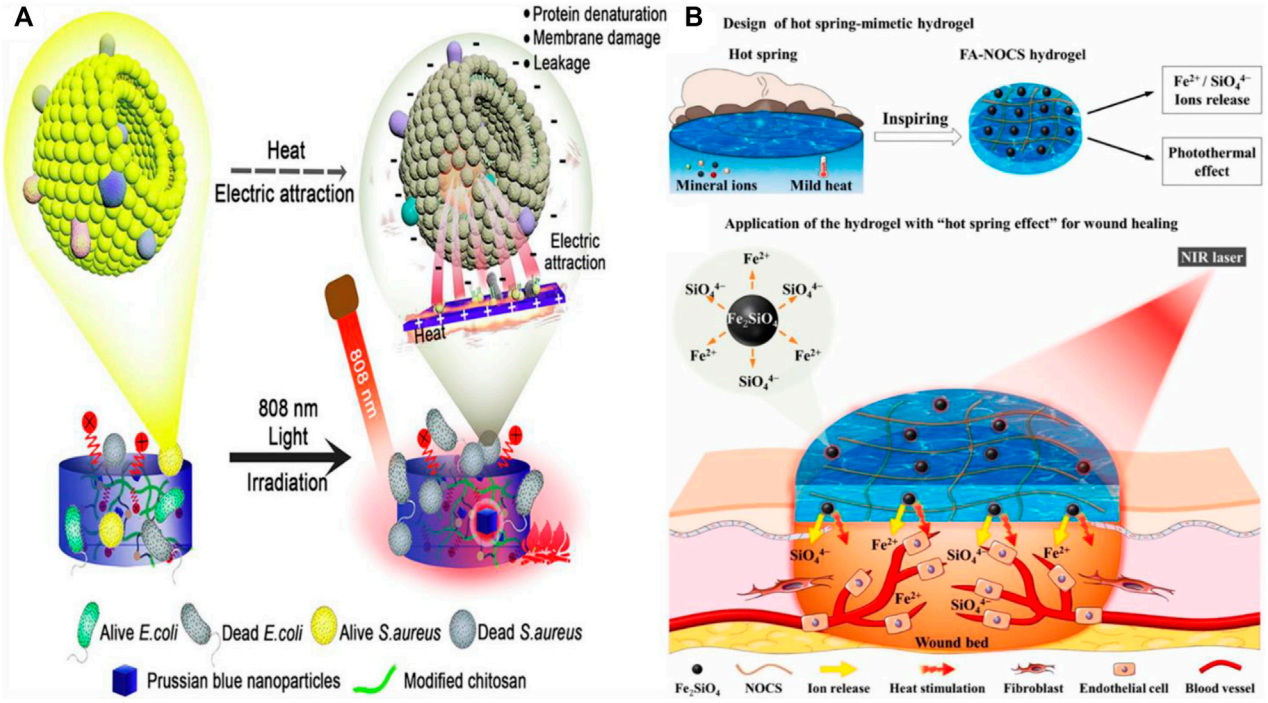

FIGURE 8
(A) Schematic of bactericidal action of hydrogel. Reproduced from ref. 26 with permission from 2020 Elsevier B.V. **(B)** Schematic diagram of application of bioactive photothermal hydrogel in wound healing. Reproduced from ref. 71 with permission from 2020 Elsevier Ltd.

nanocomposite hydrogels can kill bacteria, inhibit tumor and control drug release through photothermal effect. Drugs released through the photothermal effect can further enhance the killing effect on bacteria and tumors. In addition, the photothermal nanocomposite hydrogel can also enhance the repair of bone tissue. These are described in detail below.

Photothermal-controlled drug delivery

One of the main applications of photothermal nanohydrogels is to control the release of drugs by their photothermal properties (Liu C. et al., 2019; Dong et al., 2021). The synergistic treatment of light and heat promotes drugs has better therapeutic effect on diseases. Sun and colleagues combined 5′-guanosine monophosphoric acid, indocyanine green, hemin, and metformin to construct a hydrogel HMI@GEL for breast cancer treatment (Figure 9A) (Sun et al., 2022). Due to the photothermal effect of ICG, the hydrogel has good NIR photo-triggering and continuous drug delivery characteristics. Most importantly, the loading concentration of metformin on the hydrogel was as high as 300 mg ml^{-1}. This is the highest reported in the literature. The combination of metformin and catalase mimic Hemin@mil88 can not only significantly inhibit mitochondrial respiration in tumors, but also achieve high oxygen production *in situ*. The hydrogel successfully achieves the synchronization of drug synergistic therapy and photo-controlled release under 808 nm laser irradiation, which provides a more reliable direction for the treatment of breast cancer. Zheng and his colleagues prepared a temperature sensitive injectable hydrogel of poly (N-isopropylacrylamide-co-sulfonamide methacrylate) (PNS) in the zwitterionic structure (Zheng et al., 2020). The aqueous dispersion of the nano gel is colloidal at room temperature, and the hydrogel is formed due to thermal sensitivity at 36°C. After the chemotherapeutic drug DOX and photothermal agent PDA nanoparticles are loaded on the hydrogel, DOX can be continuously released from the hydrogel, and the drug release can be accelerated by near-infrared laser irradiation. The synergistic effect of photothermal therapy and local chemotherapy shows a better anti-cancer effect. Geng and his colleagues prepared polyacrylic acid-B-N-isopropylamid-B-acrylic acid/polypyrrole the temperature sensitive composite polymer nanogel through redox polymerization in PNA micelles dissolved in pyrrole (PPy@PNA) (Figure 9B) (Geng et al., 2020). The hydrogel has sensitive sol-gel phase transition behavior, shear dilution characteristics and excellent photothermal properties. It can induce drug release through NIR, and promote drug penetration in tumors. Hou et al. synthesized a powerful injectable agarose hydrogel containing sodium humate and doxorubicin (Figure 9C) (Hou et al., 2018). Under near-infrared

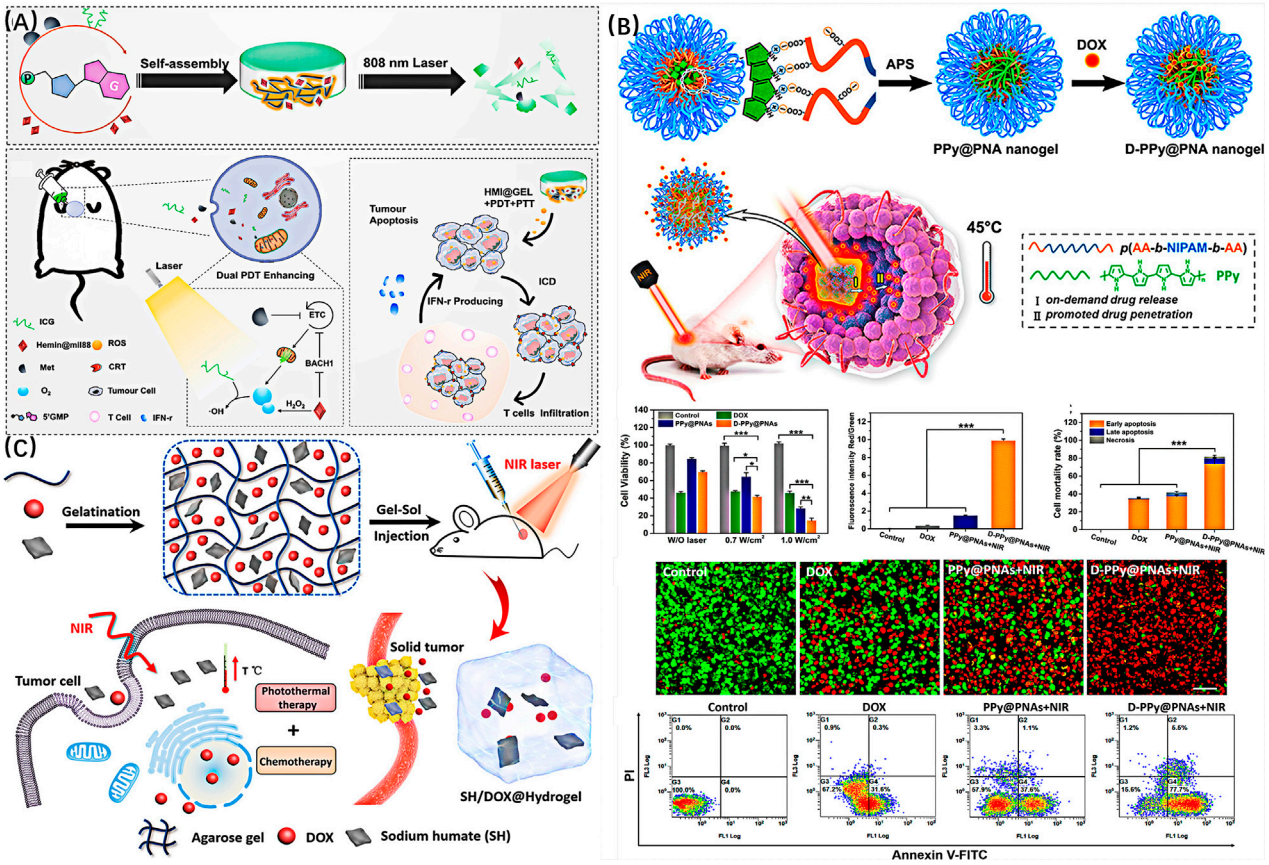

FIGURE 9
(A) Schematic illustration of HMI@GEL. Reproduced from ref. 72 with permission from 2022 Elsevier Ltd. **(B)** Schematic diagram of preparation of temperature sensitive nano hydrogel and its application in temperature controlled drug release for tumor treatment. Reproduced from ref. 22 with permission from 2020, American Chemical Society. **(C)** Schematic diagram of the principle of SH/DOX @ hydrogel controlling drug release and tumor ablation by using photothermal effect. Reproduced from ref. 31 with permission from 2018, American Chemical Society.

light irradiation, SH can effectively convert light energy into heat energy, thereby inducing local high temperature, and continuously release drugs through typical gel sol transition. The drug release rate can be controlled by changing the concentration of agarose, SH and DOX, or the laser power density and irradiation time. Animal experiments show that this light triggered drug release and local hyperthermia combined with chemotherapy photothermal therapy have excellent tumor inhibition.

Photothermal bacterial killing and wound repair

The harm caused by bacterial infection has been puzzling people. Antibiotics can be used for wound healing to avoid bacterial infection. Long term use of antibiotics may lead to drug resistance. The commonly used gold ion antibacterial is reduced because of its toxicity. Therefore, photothermal therapy has been introduced into the field of antibacterial, it provides an effective treatment strategy for wound infection (Xu J.-W. et al., 2019; Chen et al., 2020).

Wang et al. combined pH sensitive bromothymol blue and near-infrared absorption conjugated polymer into heat sensitive chitosan hydrogel (Figure 10A) (Wang et al., 2020b). Diagnose of the biofilm of *Staphylococcus aureus* (*Staphylococcus aureus*) and the acidic microenvironment of infected wounds were carried out by visible color changes in hydrogels. After rapid diagnosis, hydrogels can be used to treat infect sites, even stubborn biofilms that are difficult to eradicate, by hyperthermia under the irradiation of NIR laser (808 nm). Through thermotherapy, it has broad-spectrum antibacterial activity against gram positive, gram negative and drug-resistant bacteria. Han and his colleagues prepared a GelDA/PGO hydrogel through dopamine grafted gelatin (GelDA) and polydopamine coated graphene oxide (PGO). The introduction of graphene oxide makes hydrogels have excellent photothermal antibacterial

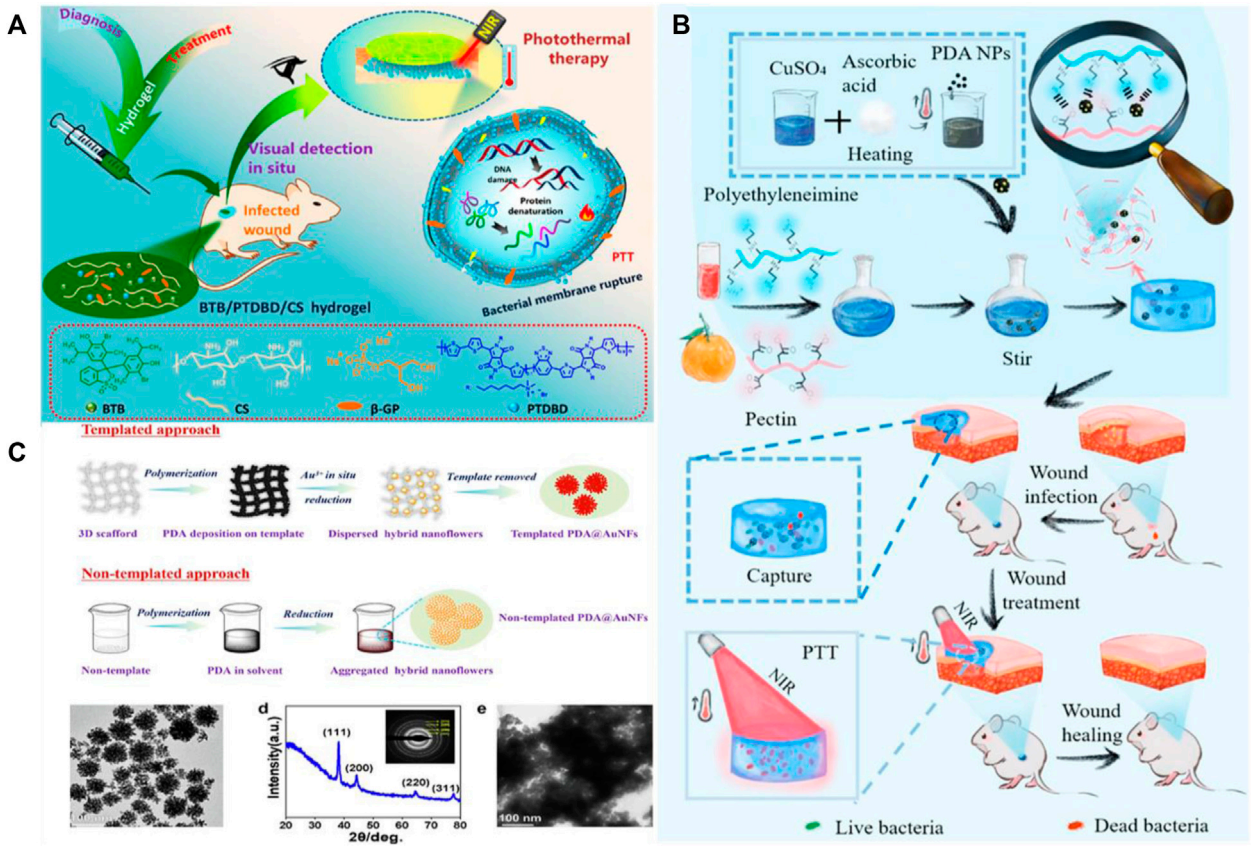

FIGURE 10
(A) Preparation of thermosensitive chitosan hydrogel and its application in the diagnosis and photothermal treatment of bacterial infection. Reproduced from ref. 78 with permission from 2020, American Chemical Society. **(B)** Synthesis and antimicrobial representation of CPAP/PDA@Cu hydrogels. Reproduced from ref. 41 with permission from 2022 The Authors. Published by Elsevier Ltd. **(C)** Preparation diagram and performance characterization of PDA@AuNFs. Reproduced from ref. 30 with permission from 2022 Elsevier B.V.

properties and is beneficial to enhance wound healing *in vivo* (Han et al., 2022). Deng et al. put single fatty acid Fe (III) (TA Fe) nanoparticles in agarose (AG) hydrogel (Deng H. et al., 2020). When the NIR was irradiated for 10 min, the temperature sharply increased to 58°C, indicating that the nanocomposite hydrogel produced had significant photothermal effects. Through *in vitro* antibacterial test, the hydrogel can effectively kill nearly 99% of bacteria under 10min NIR irradiation. Li and his colleagues prepared a hydrogel with photothermal properties by *in-situ* culturing Cu NPs on the surface of polydopamine and introducing an electrolyte hydrogel precursor (Figure 10B) (Li Z. et al., 2022). Its photothermal properties are better than those of pure polydopamine nanoparticles, and it also can capture and kill bacteria through electrostatic adsorption, which helps to improve the antibacterial performance. In addition, You and others also put forward their own views. They prepared a multifunctional hydrogel wound dressing using copper/tannic acid nanosheets (You et al., 2022). In addition to absorption exudate, the dressing has adjustable photothermal antibacterial and reactive oxygen species scavenging properties. These properties can not only play the role of hemostasis, antibacterial and anti-inflammatory, but also achieve wound repair and restore skin physiological function by reducing inflammation. Hong et al. selected the bacterial cellulose scaffold as the template platform for polydopamine deposition, controlled the growth of mixed polydopamine and gold nanoparticles through *in situ* deposition and reduction technology, and controlled the template platform within 100 nm (Figure 10C) (Hong et al., 2022). Under the irradiation of NIR, the template showed good photothermal performance, and the photothermal temperature could rise from 45°C to 55°C, with good antibacterial effect. Yin et al. used the photothermal properties of copper disulfide nanoparticles to prepare hydrogels through metal coordination (Yin et al., 2022). The photothermal antibacterial efficiency of hydrogels against *Staphylococcus aureus* and *Escherichia coli* can reach 99%. At the same time, it can reduce inflammation and promote skin tissue.

Photothermal cancer cell inhibition

In today's society, tumors threaten people's life and health, but the effect of traditional surgical resection and chemotherapy is not very ideal. People began to care about other effective treatments to treat tumors. The application of photothermal nanomaterials in disease therapy has attracted great attention (Ruhi et al., 2018; Yan et al., 2022). Yang and his colleagues developed a methylcellulose hydrogel platform with photothermal properties and injectable properties (Yang et al., 2021). The hydrogel can be rapidly heated to more than 50.0°C under near-infrared irradiation to achieve the goal of killing tumor cells and preventing tumor recurrence after surgery *in vivo*. The addition of MP in hydrogels can not only improve the strength of hydrogels, but also facilitate the attachment of normal breast cells and adipocytes to promote breast reconstruction. Liu et al. developed a bio-inorganic hybrid hydrogel with near-infrared light response (Liu et al., 2020). The addition of DNA in the NIR response system makes the hydrogel a porous interconnected structure. The interaction between adjacent DNA strands and UCNP-Au nanoparticles makes the photothermal efficiency of the hydrogel as high as 42.7%, and the tumor can be eradicated under 808 nm laser irradiation. Zhou and his colleagues reported an injectable self-healing hydrogel system based on CuS nanoparticles (Zhou et al., 2021). Hydrogels were constructed by forming a 3D network of polyethylene glycol functionalized CuS nanoparticles with surface amino groups with oxidized dextran and PEG with amino terminal groups. The introduction of CuS NPs endows hydrogels with excellent photothermal properties and can inhibit tumor growth in a subcutaneous skin-tumor model. Interestingly, the hydrogel also continuously releases Cu^{2+}, which can promote the proliferation of fibroblasts and vascular endothelial cells. Lee and his colleagues synthesized a biodegradable hemoglobin hydrogel (Lee et al., 2019). The hydrogel was constructed by the rapid formation of PEG linkage between hemoglobin and polyethylene glycol *in situ*. The hemoglobin hydrogel was heated to 60°C under near-infrared laser irradiation, which could effectively inhibit A549 lung cancer cells. Most importantly, the hemoglobin has good biocompatibility and can be completely degraded in 21 days after implantation.

Photothermal-enhanced bone tissue regeneration

The number of patients with bone defects and osteoarthritis is increasing. It not only brings pain to patients, but also is a major problem in clinical treatment. The main reason for the failure of bone defect and osteoarthritis repair is the loss of osteoblasts and chondrocytes. (Marchev et al., 2017). The biomineralization of calcium and phosphorus ions in extracellular matrix is the key to bone regeneration. (de Melo Pereira & Habibovic, 2018; Cheng et al., 2020). At present, many scholars have introduced photothermal therapy into orthopedic repair, providing a new strategy for this field (Wang et al., 2020a; Chang et al., 2022). Wu et al. prepared hydrogels by using the photothermal properties of polydopamine nanoparticles and methacryloyl gelatin (Wu et al., 2022). Animal studies have shown that, hydrogels can promote the alkaline ALP activity and the formation of extracellular calcified nodules. Polydopamine nanoparticles can provide mild photothermal treatment and have better bone repair ability. Liu et al. synthesized a new NIR hydrogel with high photoresponse and mechanical strength using rare-earth gold hybrid nanoparticles and alginate molecules (Figure 11A) (Liu et al., 2021). The hydrogel can not only eradicate tumors by local photothermal therapy, but also effectively promote bone repair as an internal matrix.

Miao and his colleagues prepared nanocomposite hydrogels through BP nano sheets (Miao et al., 2019). Under near-infrared radiation, nanocomposite hydrogels have effective photothermal antibacterial properties. In the absence of bone induction factors, hydrogel matrix could enhance mineralization and bone regeneration, and promote bone formation *in vitro*. Tan et al. prepared EMC simulated hydrogel through BP nano sheet coated by MSC membrane (Figure 11B) (Tan et al., 2022). Under NIR irradiation, they activated heat shock proteins mediated matrix metalloproteinases (MMPs) to induce mild photothermal effect and stimulate the recruitment of osteoblasts. At the same time, the thermal decomposition of BP will release phosphate ions into the surrounding medium and attract calcium ions to form hydroxyapatite in the ECM, which is conducive to the migration and differentiation of osteoblasts and achieves the effect of bone repair.

In addition, Qing et al. added MgO nanoparticles and black phosphorus nanoparticles into poly (vinyl alcohol)/chitosan hydrogels (Qing et al., 2022). The hydrogel can kill more than 99.9% of *Staphylococcus aureus* and *Escherichia coli* under NIR irradiation. The released Mg ions stimulate mesenchymal stem cells to migrate to the hydrogel, and cooperate with the released phosphate to promote osteogenic differentiation, then synergistic photothermal antibacterial and bone regeneration can be achieved. Luo et al. successfully synthesized hydrogels containing cisplatin and dopamine-modified nanohydroxyapatite by Schiff base reaction between aldehyde group on sodium alginate and amino group on chitosan (Figure 11C) (Luo et al., 2019). The results show that the photothermal properties of hydrogels under near-infrared laser (808 nm) irradiation can effectively ablate tumor cells *in vitro* and inhibit tumor growth *in vivo*. Most importantly, because of the abundant functional groups on dopamine, hydrogels can also promote the adhesion and proliferation of bone marrow mesenchymal stem cells, further promote the formation of bone tissue.

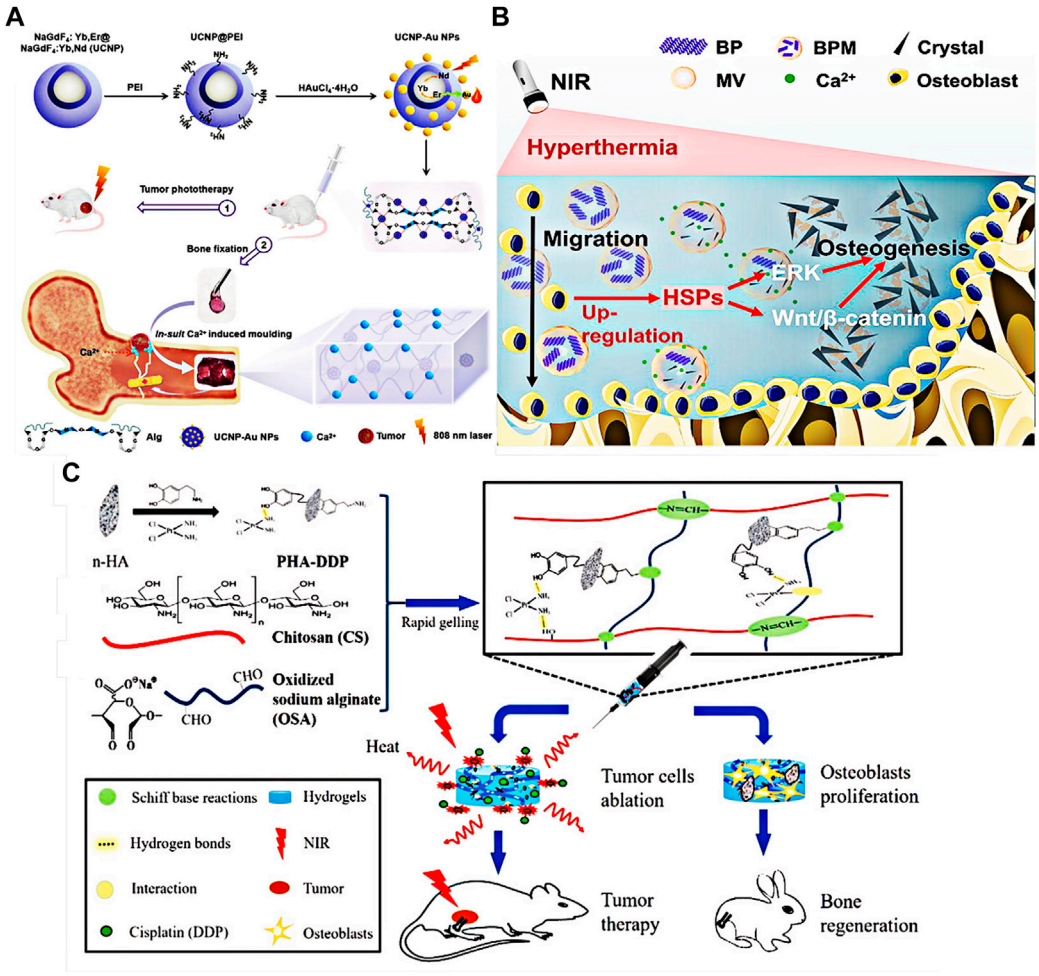

FIGURE 11
(A) Schematic diagram of preparation and principle of near-infrared hydrogel that can promote bone healing. Reproduced from ref. 46 with permission from 2021 Wiley-VCH GmbH. **(B)** Schematic diagram of the principle of photothermal nanohydrogel promoting bone regeneration. Reproduced from ref. 74 with permission from 2021 Elsevier B.V. **(C)** Preparation of cisplatin and dopamine-modified nanohydroxyapatite hydrogel and its application in cancer therapy. Reproduced from ref. 53 with permission from 2019 WILEY-VCH.

Other biomedical applications

The eye is an important and special organ of the human body, with unique physiological and anatomical characteristics. If eye diseases occur, it is difficult to cure. With the frequent use of lighting screens, eye diseases have become an increasingly serious phenomenon (Li et al., 2021). Although there are many drugs for relieving or treating eye in drops, powders and ointments on the market, there are many deficiencies in their use, such as low permeability, low bioavailability, short stay time, frequent administration, etc. The intraocular bioavailability of these drugs is very low, usually only 1–5% (Wang F. et al., 2021). At present, some non-traditional ocular drug delivery systems have been extensively studied, such as nano carriers, hydrogels, liposomes, etc. Researchers began to introduce photothermal nano hydrogels into ocular drug delivery systems. Pang et al. developed a mini eye patch based on photothermal conversion hydrogel (Pang et al., 2019). The hydrogel eye piece was prepared by cross-linking gelatin and gold nanoparticles. The heating performance of eye piece was obtained through infrared temperature profile and cycling temperature experiments. The results show that the eye system can perceive a variety of visible

light and react through spontaneous heating. Through the hydrogel patch, it can convert all kinds of light into heat, stimulate the lacrimal gland to produce more tears to alleviate dry eye.

Microfluidics refers to the science and technology involved in the system of using micro pipes (tens to hundreds of microns in size) to process or manipulate micro fluids (nano liters to a liter in volume). Through electrical stimulation to regulate and transfer plasma nanomaterials, photosensitive materials are introduced to prepare a hydrogel based microfluidic platform with photothermal response, which can effectively provide photothermal therapy in tumor treatment. Ha and his colleagues developed one microfluidic platform based on electric response hydrogel for brain tumor targeting and photothermal therapy (Ha et al., 2020). Electroresponsive hydrogels are composed of silver nanowires (Ag NWs) with high conductivity and biocompatible collagen type I gels. The electroresponsive hydrogel based microfluidic actuator platform can deliver the electroresponsive smart nanomaterials, while the vasopeptide coupled gold nanorods provide photothermal therapy. The combination of electric response and photothermal therapy can promote the release of tumor drugs and effectively improve the therapeutic effect. Fu et al. introduced the principle of photothermal sensor into the analysis device based on microfluidic paper (μ PADs), a photothermal microfluidic sensing platform with multi-channel dual-mode quantitative readout driven by a NIR laser is developed (Fu G. et al., 2019). Prussian blue was used as an analyte related photothermal agent, which was synthesized *in situ* in the thermal reaction poly (n-isopropylacrylamide) hydrogel as a photothermal sensor on the chip. The photothermal effect driven by the NIR laser not only triggered the dose dependent heat generation on the chip, but also triggered the phase change induced release of hydrogel dye, and enabled the dual-mode vision based on thermal image and distance to read the analyte concentration quantitatively in a multi-channel manner. The elevated temperature of the hydrogel on the tablet and the moving distance of the dye solution released are directly proportional to the concentration of PB.

Conclusion and perspectives

The application and development of metal nanomaterials, carbon-based nanomaterials, metal sulfide/oxide nanoparticles, black phosphorus nanomaterials, MXenes nanomaterials, polymer nanomaterials and organic dye materials in the preparation of photothermal nano hydrogels are reviewed in this paper. The applications of photothermal nano hydrogels in drug release, photothermal sterilization, photothermal cancer cell inhibition and bone repair enhancement were introduced in detail. Photothermal nano hydrogels can inhibit the growth of bacteria and tumor cells through the high temperature generated by the photothermal effect, and control the sol-gel transition behavior of hydrogels through the photothermal characteristics, thus control the drug release. The synergistic effect of photothermal therapy and chemotherapy can greatly enhance the therapeutic effect and reduce the drug toxicity. There is no doubt that the photothermal therapy of local hyperthermia combined with chemotherapy will have further applications in medical engineering.

Author contributions

FD: Investigation, Conceptualization, Writing-original draft. LZ: Investigation, Writing-original draft. XC: Investigation, Review and editing. WY: Investigation, Review and editing. LN: Investigation, Review and editing. MW: Conceptualization, Supervision, Writing-review and editing.

Acknowledgments

We acknowledge the National Natural Science Foundation of China (32222041, 81902248 and 21875092), the National Natural Science Foundation of Jiangsu Province (BK20220059), the National Key Research and Development Program of China (2019YFA0112000), the Innovation and Entrepreneurship Program of Jiangsu Province, the “Six Talent Peaks” program of Jiangsu Province (2018-XCL-013), the China Postdoctoral Science Foundation funded project (2021M702393), and the “Jiangsu Specially-Appointed Professor” Program.

Conflict of interest

The authors declare that the research was conducted in the absence of any commercial or financial relationships that could be construed as a potential conflict of interest.

Publisher’s note

References

Ai, K., Huang, J., Xiao, Z., Yang, Y., Bai, Y., and Peng, J. (2021). Localized surface plasmon resonance properties and biomedical applications of copper selenide nanomaterials. *Mater. Today Chem.* 20, 100402. doi:10.1016/j.mtchem.2020.100402

Amatya, R., Hwang, S., Park, T., Chung, Y. J., Ryu, S., Lee, J., et al. (2021). BSA/Silver nanoparticle-loaded hydrogel film for local photothermal treatment of skin cancer. *Pharm. Res.* 38, 873–883. doi:10.1007/s11095-021-03038-4

Awasthi, P., An, X., Xiang, J., Kalva, N., Shen, Y., and Li, C. (2020). Facile synthesis of noncytotoxic PEGylated dendrimer encapsulated silver sulfide quantum dots for NIR-II biological imaging. *Nanoscale* 12, 5678–5684. doi:10.1039/c9nr10918h

Bermudez-Jimenez, C., Nino-Martinez, N., Patino-Marin, N., Martinez-Gutierrez, F., Ruiz, F., Bach, H., et al. (2020). Effective control of biofilms by photothermal therapy using a gold nanorod hydrogel. *J. Biomed. Mat. Res.* 108, 333–342. doi:10.1002/jbm.b.34392

Cao, H., Duan, L., Zhang, Y., Cao, J., and Zhang, K. (2021). Current hydrogel advances in physicochemical and biological response-driven biomedical application diversity. *Signal Transduct. Target. Ther.* 6, 426–431. doi:10.1038/s41392-021-00830-x

Chang, L., Liu, X., Zhu, J., Rao, Y., Chen, D., Wang, Y., et al. (2022). Cellulose-based thermo-responsive hydrogel with NIR photothermal enhanced DOX released property for anti-tumor chemotherapy. *Colloids Surfaces B Biointerfaces* 218, 112747. doi:10.1016/j.colsurfb.2022.112747

Chen, S., Tang, F., Tang, L., and Li, L. (2017). Synthesis of Cu-nanoparticle hydrogel with self-healing and photothermal properties. *ACS Appl. Mat. Interfaces* 9, 20895–20903. doi:10.1021/acsami.7b04956

Chen, T., Yao, T., Peng, H., Whittaker, A. K., Li, Y., Zhu, S., et al. (2021). An injectable hydrogel for simultaneous photothermal therapy and photodynamic therapy with ultrahigh efficiency based on carbon dots and modified cellulose nanocrystals. *Adv. Funct. Mat.* 31, 2106079. doi:10.1002/adfm.202106079

Chen, Y., Gao, Y., Chen, Y., Liu, L., Mo, A., and Peng, Q. (2020). Nanomaterials-based photothermal therapy and its potentials in antibacterial treatment. *J. Control. Release* 328, 251–262. doi:10.1016/j.jconrel.2020.08.055

Cheng, L., Chen, Z., Cai, Z., Zhao, J., Lu, M., Liang, J., et al. (2020). Bioinspired functional black phosphorus electrospun fibers achieving recruitment and biomineralization for staged bone regeneration. *Small* 16, 2005433. doi:10.1002/smll.202005433

de Melo Pereira, D., and Habibovic, P. (2018). Biomineralization-inspired material design for bone regeneration. *Adv. Healthc. Mat.* 7, 1800700. doi:10.1002/adhm.201800700

de Oliveira Lima, A. M., Fragal, E. H., Caldas, B. S., Nakamura, T. U., Rubira, A. F., and Silva, R. (2022). Functional mesoporous silica decorated with Ag nanoparticles as chemo-photothermal agents. *Microporous Mesoporous Mater.* 341, 112097. doi:10.1016/j.micromeso.2022.112097

Deng, H., Yu, Z., Chen, S., Fei, L., Sha, Q., Zhou, N., et al. (2020a). Facile and eco-friendly fabrication of polysaccharides-based nanocomposite hydrogel for photothermal treatment of wound infection. *Carbohydr. Polym.* 230, 115565. doi:10.1016/j.carbpol.2019.115565

Deng, X., Liang, H., Yang, W., and Shao, Z. (2020b). Polarization and function of tumor-associated macrophages mediate graphene oxide-induced photothermal cancer therapy. *J. Photochem. Photobiol. B Biol.* 208, 111913. doi:10.1016/j.jphotobiol.2020.111913

Ding, F., Gao, X., Huang, X., Ge, H., Xie, M., Qian, J., et al. (2020). Polydopamine-coated nucleic acid nanogel for siRNA-mediated low-temperature photothermal therapy. *Biomaterials* 245, 119976. doi:10.1016/j.biomaterials.2020.119976

Dong, Y., Li, S., Li, X., and Wang, X. (2021). Smart MXene/agarose hydrogel with photothermal property for controlled drug release. *Int. J. Biol. Macromol.* 190, 693–699. doi:10.1016/j.ijbiomac.2021.09.037

Eswaraiah, V., Zeng, Q., Long, Y., and Liu, Z. (2016). Black phosphorus nanosheets: Synthesis, characterization and applications. *Small* 12, 3480–3502. doi:10.1002/smll.201600032

Falke, Y., Senkovskiy, B. V., Ehlen, N., Wysocki, L., Marangoni, T., Durr, R. A., et al. (2020). Photothermal bottom-up graphene nanoribbon growth kinetics. *Nano Lett.* 20, 4761–4767. doi:10.1021/acs.nanolett.0c00317

Fu, G., Zhu, Y., Xu, K., Wang, W., Hou, R., and Li, X. (2019a). Photothermal microfluidic sensing platform using near-infrared laser-driven multiplexed dual-mode visual quantitative readout. *Anal. Chem.* 91, 13290–13296. doi:10.1021/acs.analchem.9b04059

Fu, J. J., Zhang, J. Y., Li, S. P., Zhang, L. M., Lin, Z. X., Liang, L., et al. (2018). CuS nanodot-loaded thermosensitive hydrogel for anticancer photothermal therapy. *Mol. Pharm.* 15, 4621–4631. doi:10.1021/acs.molpharmaceut.8b00624

Fu, J., Wu, B., Wei, M., Huang, Y., Zhou, Y., Zhang, Q., et al. (2019b). Prussian blue nanosphere-embedded *in situ* hydrogel for photothermal therapy by peritumoral administration. *Acta Pharm. Sin. B* 9, 604–614. doi:10.1016/j.apsb.2018.12.005

Geng, S., Zhao, H., Zhan, G., Zhao, Y., and Yang, X. (2020). Injectable *in situ* forming hydrogels of thermosensitive polypyrrole nanoplatforms for precisely synergistic photothermo-chemotherapy. *ACS Appl. Mat. Interfaces* 12, 7995–8005. doi:10.1021/acsami.9b22654

Guedes, G., Wang, S., Fontana, F., Figueiredo, P., Lindén, J., Correia, A., et al. (2021). Dual-crosslinked dynamic hydrogel incorporating {Mo154} with pH and NIR responsiveness for chemo-photothermal therapy. *Adv. Mater.* 33, 2007761. doi:10.1002/adma.202007761

Gupta, N., and Malviya, R. (2021). Understanding and advancement in gold nanoparticle targeted photothermal therapy of cancer. *Biochimica Biophysica Acta - Rev. Cancer* 1875, 188532. doi:10.1016/j.bbcan.2021.188532

Ha, J. H., Shin, H. H., Choi, H. W., Lim, J. H., Mo, S. J., Ahrberg, C. D., et al. (2020). Electro-responsive hydrogel-based microfluidic actuator platform for photothermal therapy. *Lab. Chip* 20, 3354–3364. doi:10.1039/d0lc00458h

Han, D., Li, Y., Liu, X., Li, B., Han, Y., Zheng, Y., et al. (2020). Rapid bacteria trapping and killing of metal-organic frameworks strengthened photo-responsive hydrogel for rapid tissue repair of bacterial infected wounds. *Chem. Eng. J.* 396, 125194. doi:10.1016/j.cej.2020.125194

Han, K., Bai, Q., Zeng, Q., Sun, N., Zheng, C., Wu, W., et al. (2022). A multifunctional mussel-inspired hydrogel with antioxidant, electrical conductivity and photothermal activity loaded with mupirocin for burn healing. *Mater. Des.* 217, 110598. doi:10.1016/j.matdes.2022.110598

Han, L., Lu, X., Liu, K., Wang, K., Fang, L., Weng, L.-T., et al. (2017). Mussel-inspired adhesive and tough hydrogel based on nanoclay confined dopamine polymerization. *ACS Nano* 11, 2561–2574. doi:10.1021/acsnano.6b05318

He, P. P., Du, X., Cheng, Y., Gao, Q., Liu, C., Wang, X., et al. (2022). Thermal-responsive MXene-DNA hydrogel for near-infrared light triggered localized photothermal-chemo synergistic cancer therapy. *Small* 18, 2200263. doi:10.1002/smll.202200263

Hong, J., Chen, M., Xian, J., Li, C., Zheng, X., Deng, Q., et al. (2022). Preparation of Au-based hybrid nanoflowers as efficient photothermal agents for antibacterial application. *Mater. Lett.* 317, 132034. doi:10.1016/j.matlet.2022.132034

Hou, M., Yang, R., Zhang, L., Zhang, L., Liu, G., Xu, Z., et al. (2018). Injectable and natural humic acid/agarose hybrid hydrogel for localized light-driven photothermal ablation and chemotherapy of cancer. *ACS Biomater. Sci. Eng.* 4, 4266–4277. doi:10.1021/acsbiomaterials.8b01147

Hou, X. L., Dai, X., Yang, J., Zhang, B., Zhao, D. H., Li, C. Q., et al. (2020). Injectable polypeptide-engineered hydrogel depot for amplifying the anti-tumor immune effect induced by chemo-photothermal therapy. *J. Mat. Chem. B* 8, 8623–8633. doi:10.1039/d0tb01370f

Huang, F. G. (2020). Nanovehicles with nitric oxide release and photothermal activity-based hydrogels for bacteria-infected wound healing. *ACS Appl. Mat. Interfaces* 12 (26), 28952–28964. doi:10.1021/acsami.0c04080

Jin, R., Yang, J., Ding, P., Li, C., Zhang, B., Chen, W., et al. (2020). Antitumor immunity triggered by photothermal therapy and photodynamic therapy of a 2D MoS_2 nanosheet-incorporated injectable polypeptide-engineered hydrogel combinated with chemotherapy for 4T1 breast tumor therapy. *Nanotechnology* 31, 205102. doi:10.1088/1361-6528/ab72b9

Lee, C., Lim, K., Kim, S. S., Lee, E. S., Oh, K. T., Choi, H.-G., et al. (2019). Near infrared light-responsive heat-emitting hemoglobin hydrogels for photothermal cancer therapy. *Colloids Surfaces B Biointerfaces* 176, 156–166. doi:10.1016/j.colsurfb.2018.12.070

Lee, H., Kim, S., Ryu, C., and Lee, J. Y. (2020). Photothermal polymerization using graphene oxide for robust hydrogelation with various light sources. *ACS Biomater. Sci. Eng.* 6, 1931–1939. doi:10.1021/acsbiomaterials.0c00161

Lee, Y.-H., and Chang, D.-S. (2017). Fabrication, characterization, and biological evaluation of anti-HER2 indocyanine green-doxorubicin-encapsulated PEG-b-PLGA copolymeric nanoparticles for targeted photochemotherapy of breast cancer cells. *Sci. Rep.* 7, 46688–46713. doi:10.1038/srep46688

Li, Q., Wen, J., Liu, C., Jia, Y., Wu, Y., Shan, Y., et al. (2019). Graphene-nanoparticle-based self-healing hydrogel in preventing postoperative recurrence of breast cancer. *ACS Biomater. Sci. Eng.* 5, 768–779. doi:10.1021/acsbiomaterials.8b01475

Li, Y., Han, M., Cai, Y., Jiang, B., Zhang, Y., Yuan, B., et al. (2022a). Muscle-inspired MXene/PVA hydrogel with high toughness and photothermal therapy for promoting bacteria-infected wound healing. *Biomater. Sci.* 10, 1068–1082. doi:10.1039/d1bm01604k

Li, Z., Cheng, H., Ke, L., Liu, M., Wang, C. G., Jun Loh, X., et al. (2021). Recent advances in new copolymer hydrogel-formed contact lenses for ophthalmic drug delivery. *ChemNanoMat* 7, 564–579. doi:10.1002/cnma.202100008

Li, Z., You, S., Mao, R., Xiang, Y., Cai, E., Deng, H., et al. (2022b). Architecting polyelectrolyte hydrogels with Cu-assisted polydopamine nanoparticles for photothermal antibacterial therapy. *Mater. Today Bio* 15, 100264. doi:10.1016/j.mtbio.2022.100264

Liang, Y., Zhao, X., Hu, T., Chen, B., Yin, Z., Ma, P. X., et al. (2019). Adhesive hemostatic conducting injectable composite hydrogels with sustained drug release and photothermal antibacterial activity to promote full-thickness skin regeneration during wound healing. *Small* 15, e1900046. doi:10.1002/smll.201900046

Lin, H., Chen, Y., and Shi, J. (2018). Insights into 2D MXenes for versatile biomedical applications: Current advances and challenges ahead. *Adv. Sci. (Weinh).* 5, 1800518. doi:10.1002/advs.201800518

Lin, H., Wang, X., Yu, L., Chen, Y., and Shi, J. (2017). Two-dimensional ultrathin MXene ceramic nanosheets for photothermal conversion. *Nano Lett.* 17, 384–391. doi:10.1021/acs.nanolett.6b04339

Lin, X., Fang, Y., Hao, Z., Wu, H., Zhao, M., Wang, S., et al. (2021). Bacteria-triggered multifunctional hydrogel for localized chemodynamic and low-temperature photothermal sterilization. *Small* 17, e2103303. doi:10.1002/smll.202103303

Liu, B., Gu, X., Sun, Q., Jiang, S., Sun, J., Liu, K., et al. (2021). Injectable *in situ* induced robust hydrogel for photothermal therapy and bone fracture repair. *Adv. Funct. Mat.* 31, 2010779. doi:10.1002/adfm.202010779

Liu, B., Sun, J., Zhu, J., Li, B., Ma, C., Gu, X., et al. (2020). Injectable and NIR-responsive DNA–inorganic hybrid hydrogels with outstanding photothermal therapy. *Adv. Mat.* 32, 2004460. doi:10.1002/adma.202004460

Liu, C., Guo, X., Ruan, C., Hu, H., Jiang, B.-P., Liang, H., et al. (2019a). An injectable thermosensitive photothermal-network hydrogel for near-infrared-triggered drug delivery and synergistic photothermal-chemotherapy. *Acta biomater.* 96, 281–294. doi:10.1016/j.actbio.2019.07.024

Liu, M., Huang, P., Wang, W., Feng, Z., Zhang, J., Deng, L., et al. (2019b). An injectable nanocomposite hydrogel co-constructed with gold nanorods and paclitaxel-loaded nanoparticles for local chemo-photothermal synergetic cancer therapy. *J. Mat. Chem. B* 7, 2667–2677. doi:10.1039/c9tb00120d

Liu, W., Zhang, X., Zhou, L., Shang, L., and Su, Z. (2019c). Reduced graphene oxide (rGO) hybridized hydrogel as a near-infrared (NIR)/pH dual-responsive platform for combined chemo-photothermal therapy. *J. Colloid Interface Sci.* 536, 160–170. doi:10.1016/j.jcis.2018.10.050

Lu, X., Hou, J., Yang, K., Zhu, L., Xing, B., and Lin, D. (2021a). Binding force and site-determined desorption and fragmentation of antibiotic resistance genes from metallic nanomaterials. *Environ. Sci. Technol.* 55, 9305–9316. doi:10.1021/acs.est.1c02047

Lu, Y., Fan, D., Wang, Y., Xu, H., Lu, C., and Yang, X. (2021b). Surface patterning of two-dimensional nanostructure-embedded photothermal hydrogels for high-yield solar steam generation. *ACS Nano* 15, 10366–10376. doi:10.1021/acsnano.1c02578

Luo, S., Wu, J., Jia, Z., Tang, P., Sheng, J., Xie, C., et al. (2019). An injectable, bifunctional hydrogel with photothermal effects for tumor therapy and bone regeneration. *Macromol. Biosci.* 19, 1900047. doi:10.1002/mabi.201900047

Ma, H., Zhou, Q., Chang, J., and Wu, C. (2019). Grape seed-inspired smart hydrogel scaffolds for melanoma therapy and wound healing. *ACS Nano* 13, 4302–4311. doi:10.1021/acsnano.8b09496

Ma, L., Zhou, Y., Zhang, Z., Liu, Y., Zhai, D., Zhuang, H., et al. (2020). Multifunctional bioactive Nd-Ca-Si glasses for fluorescence thermometry, photothermal therapy, and burn tissue repair. *Sci. Adv.* 6, eabb1311. doi:10.1126/sciadv.abb1311

Marchev, A. S., Dimitrova, P. A., Burns, A. J., Kostov, R. V., Dinkova-Kostova, A. T., and Georgiev, M. I. (2017). Oxidative stress and chronic inflammation in osteoarthritis: Can NRF2 counteract these partners in crime? *Ann. N. Y. Acad. Sci.* 1401, 114–135. doi:10.1111/nyas.13407

Miao, Y., Shi, X., Li, Q., Hao, L., Liu, L., Liu, X., et al. (2019). Engineering natural matrices with black phosphorus nanosheets to generate multi-functional therapeutic nanocomposite hydrogels. *Biomater. Sci.* 7, 4046–4059. doi:10.1039/c9bm01072f

Moorcroft, S. C. T., Roach, L., Jayne, D. G., Ong, Z. Y., and Evans, S. D. (2020). Nanoparticle-loaded hydrogel for the light-activated release and photothermal enhancement of antimicrobial peptides. *ACS Appl. Mat. Interfaces* 12, 24544–24554. doi:10.1021/acsami.9b22587

Naguib, M., Kurtoglu, M., Presser, V., Lu, J., Niu, J., Heon, M., et al. (2011). Two-dimensional nanocrystals produced by exfoliation of Ti_3AlC_2. *Adv. Mat.* 23, 4248–4253. doi:10.1002/adma.201102306

Ou, Y., and Tian, M. (2021). Advances in multifunctional chitosan-based self-healing hydrogels for biomedical applications. *J. Mat. Chem. B* 9, 7955–7971. doi:10.1039/d1tb01363g

Pan, H., Zhang, C., Wang, T., Chen, J., and Sun, S. K. (2019). *In situ* fabrication of intelligent photothermal indocyanine green-alginate hydrogel for localized tumor ablation. *ACS Appl. Mat. Interfaces* 11, 2782–2789. doi:10.1021/acsami.8b16517

Pang, Y., Wei, C., Li, R., Wu, Y., Liu, W., Wang, F., et al. (2019). <p>Photothermal conversion hydrogel based mini-eye patch for relieving dry eye with long-term use of the light-emitting screen</p>. *Int. J. Nanomedicine* 14, 5125–5133. doi:10.2147/ijn.s192407

Park, H. H., Srisombat, L.-o., Jamison, A. C., Liu, T., Marquez, M. D., Park, H., et al. (2018). Temperature-responsive hydrogel-coated gold nanoshells. *Gels* 4, 28. doi:10.3390/gels4020028

Pei, X., Wang, J., Cong, Y., and Fu, J. (2021). Recent progress in polymer hydrogel bioadhesives. *J. Polym. Sci.* 59, 1312–1337. doi:10.1002/pol.20210249

Qin, L., Ling, G., Peng, F., Zhang, F., Jiang, S., He, H., et al. (2019). Black phosphorus nanosheets and gemcitabine encapsulated thermo-sensitive hydrogel for synergistic photothermal-chemotherapy. *J. Colloid Interface Sci.* 556, 232–238. doi:10.1016/j.jcis.2019.08.058

Qing, Y., Wang, H., Lou, Y., Fang, X., Li, S., Wang, X., et al. (2022). Chemotactic ion-releasing hydrogel for synergistic antibacterial and bone regeneration. *Mater. Today Chem.* 24, 100894. doi:10.1016/j.mtchem.2022.100894

Ren, Q., Ma, Y., Zhang, S., Ga, L., and Ai, J. (2021). One-step synthesis of water-soluble silver sulfide quantum dots and their application to bioimaging. *ACS omega* 6, 6361–6367. doi:10.1021/acsomega.0c06276

Ren, X., Li, Z., Huang, Z., Sang, D., Qiao, H., Qi, X., et al. (2017). Environmentally robust black phosphorus nanosheets in solution: Application for self-powered photodetector. *Adv. Funct. Mat.* 27, 1606834. doi:10.1002/adfm.201606834

Ruhi, M. K., Ayse, A. K., and Gülsoy, M. (2018). Dose-dependent photochemical/photothermal toxicity of indocyanine green-based therapy on three different cancer cell lines. *Photodiagnosis Photodyn. Ther.* 21, 334–343. doi:10.1016/j.pdpdt.2018.01.008

Shao, J., Ruan, C., Xie, H., Li, Z., Wang, H., Chu, P. K., et al. (2018). Black-phosphorus-incorporated hydrogel as a sprayable and biodegradable photothermal platform for postsurgical treatment of cancer. *Adv. Sci. (Weinh).* 5, 1700848. doi:10.1002/advs.201700848

Sheng, L., Zhang, Z., Zhang, Y., Wang, E., Ma, B., Xu, Q., et al. (2021). A novel "hot spring"-mimetic hydrogel with excellent angiogenic properties for chronic wound healing. *Biomaterials* 264, 120414. doi:10.1016/j.biomaterials.2020.120414

Sun, Y., Fang, K., Hu, X., Yang, J., Jiang, Z., Feng, L., et al. (2022). NIR-light-controlled G-quadruplex hydrogel for synergistically enhancing photodynamic therapy via sustained delivery of metformin and catalase-like activity in breast cancer. *Mater. Today Bio* 16, 100375. doi:10.1016/j.mtbio.2022.100375

Sun, Y., Gao, J., Liu, Y., Kang, H., Xie, M., Wu, F., et al. (2019). Copper sulfide-macroporous polyacrylamide hydrogel for solar steam generation. *Chem. Eng. Sci.* 207, 516–526. doi:10.1016/j.ces.2019.06.044

Tan, L., Hu, Y., Li, M., Zhang, Y., Xue, C., Chen, M., et al. (2022). Remotely-activatable extracellular matrix-mimetic hydrogel promotes physiological bone mineralization for enhanced cranial defect healing. *Chem. Eng. J.* 431, 133382. doi:10.1016/j.cej.2021.133382

Tao, B., Lin, C., Deng, Y., Yuan, Z., Shen, X., Chen, M., et al. (2019). Copper-nanoparticle-embedded hydrogel for killing bacteria and promoting wound healing with photothermal therapy. *J. Mat. Chem. B* 7, 2534–2548. doi:10.1039/c8tb03272f

Wang, F., Song, Y., Huang, J., Wu, B., Wang, Y., Pang, Y., et al. (2021a). Lollipop-inspired multilayered drug delivery hydrogel for dual effective, long-term, and NIR-defined glaucoma treatment. *Macromol. Biosci.* 21, 2100202. doi:10.1002/mabi.202100202

Wang, H., Zeng, X., Pang, L., Wang, H., Lin, B., Deng, Z., et al. (2020a). Integrative treatment of anti-tumor/bone repair by combination of MoS_2 nanosheets with 3D printed bioactive borosilicate glass scaffolds. *Chem. Eng. J.* 396, 125081. doi:10.1016/j.cej.2020.125081

Wang, H., Zhou, S., Guo, L., Wang, Y., and Feng, L. (2020b). Intelligent hybrid hydrogels for rapid *in situ* detection and photothermal therapy of bacterial infection. *ACS Appl. Mat. Interfaces* 12, 39685–39694. doi:10.1021/acsami.0c12355

Wang, X., Sun, X., Bu, T., Wang, Q., Zhang, H., Jia, P., et al. (2021b). Construction of a photothermal hydrogel platform with two-dimensional PEG@ zirconium-ferrocene MOF nanozymes for rapid tissue repair of bacteria-infected wounds. *Acta Biomater.* 135, 342–355. doi:10.1016/j.actbio.2021.08.022

Wang, X., Wang, C., Wang, X., Wang, Y., Zhang, Q., and Cheng, Y. (2017). A polydopamine nanoparticle-knotted poly(ethylene glycol) hydrogel for on-demand drug delivery and chemo-photothermal therapy. *Chem. Mat.* 29, 1370–1376. doi:10.1021/acs.chemmater.6b05192

Wu, C., Zhao, J., Hu, F., Zheng, Y., Yang, H., Pan, S., et al. (2018). Design of injectable agar-based composite hydrogel for multi-mode tumor therapy. *Carbohydr. Polym.* 180, 112–121. doi:10.1016/j.carbpol.2017.10.024

Wu, R. S., Lin, J., Xing, Y. M., Dai, Z. L., Wang, L. W., and Zhang, X. P. (2019). pH-sensitive black phosphorous-incorporated hydrogel as novel implant for cancer treatment. *J. Pharm. Sci.* 108, 2542–2551. doi:10.1016/j.xphs.2019.03.003

Wu, Y., Liang, Y., Liu, Y., Hao, Y., Tao, N., Li, J., et al. (2021). A Bi_2S_3-embedded gellan gum hydrogel for localized tumor photothermal/antiangiogenic therapy. *J. Mat. Chem. B* 9, 3224–3234. doi:10.1039/d1tb00257k

Wu, Y., Zhang, X., Tan, B., Shan, Y., Zhao, X., and Liao, J. (2022). Near-infrared light control of GelMA/PMMA/PDA hydrogel with mild photothermal therapy for skull regeneration. *Biomater. Adv.* 133, 112641. doi:10.1016/j.msec.2022.112641

Xie, S., Chen, Y., Guo, Z., Luo, Y., Tan, H., Xu, L., et al. (2021). Agar/carbon dot crosslinked polyacrylamide double-network hydrogels with robustness, self-healing, and stimulus-response fluorescence for smart anti-counterfeiting. *Mat. Chem. Front.* 5, 5418–5428. doi:10.1039/d1qm00338k

Xie, Y., Gan, C., Li, Z., Liu, W., Yang, D., and Qiu, X. (2022). Fabrication of a lignin-copper sulfide-incorporated PVA hydrogel with near-infrared-activated photothermal/photodynamic/peroxidase-like performance for combating bacteria and biofilms. *ACS Biomater. Sci. Eng.* 8, 560–569. doi:10.1021/acsbiomaterials.1c01406

Xing, R., Liu, K., Jiao, T., Zhang, N., Ma, K., Zhang, R., et al. (2016). An injectable self-assembling collagen-gold hybrid hydrogel for combinatorial antitumor photothermal/photodynamic therapy. *Adv. Mat.* 28, 3669–3676. doi:10.1002/adma.201600284

Xu, D., Li, Z., Li, L., and Wang, J. (2020a). 2D MXene nanomaterials: Insights into the photothermal conversion of 2D MXene nanomaterials: Synthesis, mechanism, and applications (adv. Funct. Mater. 47/2020). *Adv. Funct. Mat.* 30, 2070314. doi:10.1002/adfm.202070314

Xu, H., Shang, H., Wang, C., and Du, Y. (2020b). Low-dimensional metallic nanomaterials for advanced electrocatalysis. *Adv. Funct. Mat.* 30, 2006317. doi:10.1002/adfm.202006317

Xu, J.-W., Yao, K., and Xu, Z.-K. (2019a). Nanomaterials with a photothermal effect for antibacterial activities: An overview. *Nanoscale* 11, 8680–8691. doi:10.1039/c9nr01833f

Xu, M.-L., Guan, L.-Y., Li, S.-K., Chen, L., and Chen, Z. (2019b). Stable gold graphitic nanocapsule doped hydrogels for efficient photothermal antibacterial applications. *Chem. Commun.* 55, 5359–5362. doi:10.1039/c9cc01933b

Xu, Q., Chang, M., Zhang, Y., Wang, E., Xing, M., Gao, L., et al. (2020c). PDA/Cu bioactive hydrogel with "hot ions effect" for inhibition of drug-resistant bacteria and enhancement of infectious skin wound healing. *ACS Appl. Mat. Interfaces* 12, 31255–31269. doi:10.1021/acsami.0c08890

Xu, T., Liu, K., Sheng, N., Zhang, M., Liu, W., Liu, H., et al. (2022a). Biopolymer-based hydrogel electrolytes for advanced energy storage/conversion devices: Properties, applications, and perspectives. *Energy Storage Mater.* 48, 244–262. doi:10.1016/j.ensm.2022.03.013

Xu, Y., Chen, H., Fang, Y., and Wu, J. (2022b2200494). Hydrogel combined with phototherapy in wound healing. *Adv. Healthc. Mat.* 11, 2200494. doi:10.1002/adhm.202200494

Yan, J., Zhang, Y., Zheng, L., Wu, Y., Wang, T., Jiang, T., et al. (2022). Let-7i miRNA and platinum loaded nano-graphene oxide platform for detection/reversion of drug resistance and synergetic chemical-photothermal inhibition of cancer cell. *Chin. Chem. Lett.* 33, 767–772. doi:10.1016/j.cclet.2021.08.018

Yang, X., Gao, L., Wei, Y., Tan, B., Wu, Y., Yi, C., et al. (2021). Photothermal hydrogel platform for prevention of post-surgical tumor recurrence and improving breast reconstruction. *J. Nanobiotechnology* 19, 307–313. doi:10.1186/s12951-021-01041-w

Yao, Q., Lan, Q. H., Jiang, X., Du, C. C., Zhai, Y. Y., Shen, X., et al. (2020). Bioinspired biliverdin/silk fibroin hydrogel for antiglioma photothermal therapy and wound healing. *Theranostics* 10, 11719–11736. doi:10.7150/thno.47682

Yin, W., Wang, Q., Zhang, J., Chen, X., Wang, Y., Jiang, Z., et al. (2022). A dynamic nano-coordination protein hydrogel for photothermal treatment and repair of infected skin injury. *J. Mat. Chem. B* 10, 8181–8185. doi:10.1039/d2tb01146h

You, S., Xiang, Y., Qi, X., Mao, R., Cai, E., Lan, Y., et al. (2022). Harnessing a biopolymer hydrogel reinforced by copper/tannic acid nanosheets for treating bacteria-infected diabetic wounds. *Mater. Today Adv.* 15, 100271. doi:10.1016/j.mtadv.2022.100271

Yu, Y.-T., Shi, S.-W., Wang, Y., Zhang, Q.-L., Gao, S.-H., Yang, S.-P., et al. (2019). A ruthenium nitrosyl-functionalized magnetic nanoplatform with near-infrared light-controlled nitric oxide delivery and photothermal effect for enhanced antitumor and antibacterial therapy. *ACS Appl. Mat. Interfaces* 12, 312–321. doi:10.1021/acsami.9b18865

Yuan, P., Yang, T., Liu, T., Yu, X., Bai, Y., Zhang, Y., et al. (2020). Nanocomposite hydrogel with NIR/magnet/enzyme multiple responsiveness to accurately manipulate local drugs for on-demand tumor therapy. *Biomaterials* 262, 120357. doi:10.1016/j.biomaterials.2020.120357

Zhang, R., Wang, L., Wang, X., Jia, Q., Chen, Z., Yang, Z., et al. (2020a). Acid-induced *in vivo* assembly of gold nanoparticles for enhanced photoacoustic imaging-guided photothermal therapy of tumors. *Adv. Healthc. Mat.* 9, 2000394. doi:10.1002/adhm.202000394

Zhang, X., Tan, B., Wu, Y., Zhang, M., and Liao, J. (2021). A review on hydrogels with photothermal effect in wound healing and bone tissue engineering. *Polymers* 13, 2100. doi:10.3390/polym13132100

Zhang, Y., Liu, J., Yu, Y., Chen, S., Huang, F., Yang, C., et al. (2020b). Enhanced radiotherapy using photothermal therapy based on dual-sensitizer of gold nanoparticles with acid-induced aggregation. *Nanomedicine Nanotechnol. Biol. Med.* 29, 102241. doi:10.1016/j.nano.2020.102241

Zhang, Y., Tian, S., Huang, L., Li, Y., Lu, Y., Li, H., et al. (2022). Reactive oxygen species-responsive and Raman-traceable hydrogel combining photodynamic and immune therapy for postsurgical cancer treatment. *Nat. Commun.* 13, 4553–4615. doi:10.1038/s41467-022-32160-z

Zhang, Z., and Lucia, L. (2021). Toward synergistic reinforced graphene nanoplatelets composite hydrogels with self-healing and multi-stimuli responses. *Polymer* 234, 124228. doi:10.1016/j.polymer.2021.124228

Zhao, J., Xu, W., Zhao, Z., Ling, G., and Zhang, P. (2022). Intelligent nanocomposite hydrogels with simultaneous photothermal antitumor and antibacterial efficacy for cutaneous melanoma treatment. *Compos. Part B Eng.* 243, 110130. doi:10.1016/j.compositesb.2022.110130

Zheng, A., Wu, D., Fan, M., Wang, H., Liao, Y., Wang, Q., et al. (2020). Injectable zwitterionic thermosensitive hydrogels with low-protein adsorption and combined effect of photothermal-chemotherapy. *J. Mat. Chem. B* 8, 10637–10649. doi:10.1039/d0tb01763a

Zhou, D., Li, S., Pei, M., Yang, H., Gu, S., Tao, Y., et al. (2020a). Dopamine-modified hyaluronic acid hydrogel adhesives with fast-forming and high tissue adhesion. *ACS Appl. Mat. Interfaces* 12, 18225–18234. doi:10.1021/acsami.9b22120

Zhou, L., Chen, F., Hou, Z., Chen, Y., and Luo, X. (2021). Injectable self-healing CuS nanoparticle complex hydrogels with antibacterial, anti-cancer, and wound healing properties. *Chem. Eng. J.* 409, 128224. doi:10.1016/j.cej.2020.128224

Zhou, L., Zhao, J., Chen, Y., Zheng, Y., Li, J., Zhao, J., et al. (2020b). MoS_2-ALG-Fe/GOx hydrogel with Fenton catalytic activity for combined cancer photothermal, starvation, and chemodynamic therapy. *Colloids Surfaces B Biointerfaces* 195, 111243. doi:10.1016/j.colsurfb.2020.111243

frontiers | Frontiers in Bioengineering and Biotechnology

TYPE Original Research
PUBLISHED 03 November 2022
DOI 10.3389/fbioe.2022.1049750

OPEN ACCESS

EDITED BY
Shige Wang,
University of Shanghai for Science and Technology, China

REVIEWED BY
Xiang Li,
Fourth Affiliated Hospital of Nanjing Medical University, China
Shaowei Bo,
Jinan University, China
Juan Mou,
Shanghai Normal University, China

*CORRESPONDENCE
ShiZhen Chen,
chenshizhen@apm.ac.cn
Zitong Zheng,
nhzzt@163.com
Zhong-Xing Jiang,
zxjiang@apm.ac.cn

†These authors have contributed equally to this work

SPECIALTY SECTION
This article was submitted to Biomaterials, a section of the journal Frontiers in Bioengineering and Biotechnology

RECEIVED 21 September 2022
ACCEPTED 17 October 2022
PUBLISHED 03 November 2022

CITATION
Tang T, Zhu Q, Liu S, Dai H, Li Y, Tang C, Chen K, Jiang M, Zhu L, Zhou X, Chen S, Zheng Z and Jiang Z-X (2022), ^{19}F MRI-fluorescence imaging dual-modal cell tracking with partially fluorinated nanoemulsions. *Front. Bioeng. Biotechnol.* 10:1049750. doi: 10.3389/fbioe.2022.1049750

^{19}F MRI-fluorescence imaging dual-modal cell tracking with partially fluorinated nanoemulsions

Ting Tang[1,2†], Qiang Zhu[1,2†], Shuang Liu[3], Hailong Dai[1,2], Yu Li[2], Caihong Tang[1], Kexin Chen[1,2], Mou Jiang[2], Lijun Zhu[2], Xin Zhou[2], ShiZhen Chen[2*], Zitong Zheng[1*] and Zhong-Xing Jiang[2*]

[1]Hunan Provincial Key Laboratory of Tumor Microenvironment Responsive Drug Research, Department of Pharmacy, Hengyang Medicinal School, The Second Affiliated Hospital, University of South China, Hengyang, Hunan, China, [2]State Key Laboratory of Magnetic Resonance and Atomic and Molecular Physics, National Center for Magnetic Resonance in Wuhan, Wuhan Institute of Physics and Mathematics, Innovation Academy for Precision Measurement Science and Technology, Chinese Academy of Sciences, Wuhan, China, [3]Department of Pediatrics, Affiliated Hospital of Changchun University of Traditional Chinese Medicine, Changchun, China

As a noninvasive "hot-spot" imaging technology, fluorine-19 magnetic resonance imaging (^{19}F MRI) has been extensively used in cell tracking. However, the peculiar physicochemical properties of perfluorocarbons (PFCs), the most commonly used ^{19}F MRI agents, sometimes cause low sensitivity, poor cell uptake, and misleading results. In this study, a partially fluorinated agent, perfluoro-*tert*-butyl benzyl ether, was used to formulate a ^{19}F MRI-fluorescence imaging (FLI) dual-modal nanoemulsion for cell tracking. Compared with PFCs, the partially fluorinated agent showed considerably improved physicochemical properties, such as lower density, shorter longitudinal relaxation times, and higher solubility to fluorophores, while maintaining high ^{19}F MRI sensitivity. After being formulated into stable, monodisperse, and paramagnetic Fe^{3+}-promoted nanoemulsions, the partially fluorinated agent was used in ^{19}F MRI-FLI dual imaging tracking of lung cancer A549 cells and macrophages in an inflammation mouse model.

KEYWORDS

^{19}F MRI, fluorescence, cell tracking, partially fluorinated, nanoemulsions

Introduction

Tracking cells *in vivo* with imaging technologies is highly important for biology, pathology, and medicine (Hong et al., 2011; Kircher et al., 2011; Bulte and Daldrup-Link, 2018). Such imaging technologies may provide real-time, noninvasive, quantitative, and multidimensional information about the cells for a better understanding of the biological and pathological processes on a cellular level, thus promoting accurate diagnosis and effective therapy. For example, tracking the circulating cancer cells *in vivo* with imaging

technology may shed light on cancer metastasis mechanisms and therapeutic strategies (Xia et al., 2012; Nedosekin et al., 2013; Lee et al., 2018; Dutta et al., 2019; Deán-Ben et al., 2020), while monitoring macrophages may help visualize the immune response to inflammation (Stoll et al., 2012; Bouvain et al., 2019).

In recent years, considerable attention has been given to developing novel imaging technologies for cell tracking. Among the imaging technologies, fluorescent protein-based fluorescence imaging (FLI) (Chudakov et al., 2003; Sun et al., 2009; Ghosh et al., 2019), fluorescence dye-based FLI (Bulte et al., 2004; Maška et al., 2013; Tian et al., 2020), paramagnetic nanoparticle-based ^{1}H MRI (Cromer Berman et al., 2011; Ahrens and Zhong, 2013; Li et al., 2013), and fluorinated nanoemulsion-based ^{19}F MRI (Ferreira et al., 2008; Bulte, 2009; Wang et al., 2013) are among the most used ones. Since each imaging technology has its strengths and weaknesses, tracking cells with multimodal imaging is highly preferred, which takes advantage of each imaging technology and provides accurate, detailed, and multidimensional information. During cell tracking, the cells are usually labeled *in vitro* and tracked *in vivo*, and some special cells, such as macrophages, may also be labeled and tracked *in vivo*. FLI is advantageous for *in vitro* cellular study due to its convenience, high sensitivity, and resolution. Meanwhile, ^{19}F MRI perfectly overcomes the tissue-depth limit of FLI during the *in vivo* animal study and provides noninvasive, quantitative, and background-free "hot-spot" cell images without ionizing radiation. Thus, ^{19}F MRI-FLI dual imaging systems have shown significant potential for clinical application.

Although some ^{19}F MRI-FLI dual imaging systems have recently been developed for cell tracking (Ahrens et al., 2005; Gaudet et al., 2017; Peng et al., 2018), many issues remain unaddressed. On the one hand, the low sensitivity of ^{19}F MRI requires high ^{19}F MRI agent-loading per cell and a large number of ^{19}F-labeled cells to achieve clear cell images (Ahrens et al., 2005; Gaudet et al., 2017; Peng et al., 2018). Furthermore, the non-symmetric allocation of fluorine atoms in most perfluorocarbon (PFC)-based imaging agents leads to severe signal splitting, low ^{19}F MRI sensitivity, and chemical shift imaging artifacts. On the other hand, the peculiar physicochemical properties of PFCs, such as high hydrophobicity, low polarity, and low solubility in hydrocarbons, usually result in complex formulation and severe internal organ retention (Meyer et al., 1992; Kimura et al., 2004; Janjic et al., 2008). Notably, the extremely low solubility and interaction of fluorescent dyes in PFCs may cause aggregation-induced quenching (ACQ) of fluorescence, difficulties in encapsulation, and early release of fluorescent dyes (Würthner et al., 2011; Battistelli et al., 2016). Moreover, the high density of PFCs and their nanoemulsions may cause low cell uptake, cell damage, and misleading results (Patel et al., 2013). To address these issues, we recently used partially fluorinated agents, hydrofluorocarbons (HFCs), as alternatives for PFCs (Chen et al., 2022; Wu et al., 2022). These commercially available HFCs had a unified ^{19}F NMR peak, considerable solubility toward fluorescent dyes and functional agents, relatively low density and high ^{19}F MRI sensitivity, and efficient cell uptake. However, significant cytotoxicity was found in the HFC nanoemulsions, which promoted the synthesis of highly sensitive and biocompatible HFC agents.

Herein, we have developed novel partially fluorinated nanoemulsions for efficient ^{19}F MRI cell tracking through synthesizing, screening, and formulating a series of HFCs. Because of their high ^{19}F MRI sensitivity, biocompatibility, and stability (Wu et al., 2021), perfluoro-*tert*-butyl benzyl ethers 1–7 were designed as HFCs (Figure 1). Three strategies have been used to improve the ^{19}F MRI sensitivity. First, 1–6 symmetrical PFTB groups were introduced into the benzyl cores to generate an intense unified singlet ^{19}F NMR peak from 9 to 54 equivalent ^{19}F atoms in HFCs 1–7, that is, the utility of every ^{19}F atom for sensitive ^{19}F MRI. Second, the π–π interactions among the benzene cores of HFCs 1–7 may slow their movements and thus shorten the longitudinal relaxation time (T_1), which would shorten the data collection time during ^{19}F MRI and thus improve the signal-to-noise ratio per unit time for sensitive ^{19}F MRI. Third, perfluoro-*tert*-butoxylated diketone chelators 8 and 9 may capture paramagnetic ions into the HFCs and further shorten T_1 through the paramagnetic relaxation enhancement (PRE) effect for highly sensitive ^{19}F MRI. Due to their similar hydrofluorocarbon structures, chelators 8 and 9 may be highly soluble in HFCs 1–7 and provide a unified ^{19}F NMR peak from the mixture. In these ways, a unified ^{19}F NMR peak with an ultrashort T_1 would be generated for highly sensitive ^{19}F MRI cell tracking. The near-infrared fluorescence of the resulting fluorinated nanoemulsion may be realized by aza-BODIPY 11. Compared to highly fluorinated PFCs, HFCs 1–7 with a benzene core and lower fluorine content may have much higher solubility toward aza-BODIPY 11 and thus improve the FLI capability. Moreover, the co-solubility and improved interactions among HFCs 1–7, chelators 8 and 9, and aza-BODIPY 11 may stabilize the nanoemulsion for high biocompatibility. Perfluoro-15-crown-5 10, a widely used PFC in ^{19}F MRI, was employed as a control to illustrate the impact of π–π interactions and enhanced solubility.

Materials and methods

General information

^{1}H, ^{13}C, and ^{19}F NMR spectra were recorded on a Bruker 400 MHz or 500 MHz. Chemical shifts and coupling constants (*J*) were provided in ppm and Hertz (Hz), respectively. ^{1}H NMR spectra were referenced to tetramethylsilane (d, 0.00 ppm) using $CDCl_3$ (s, 7.26 ppm) or acetone-d_6 (m, 2.05 ppm) as the solvent. ^{13}C NMR spectra were referenced to solvent carbons (77.2 ppm for $CDCl_3$ and 29.8 ppm for acetone-d_6). ^{19}F NMR spectra were

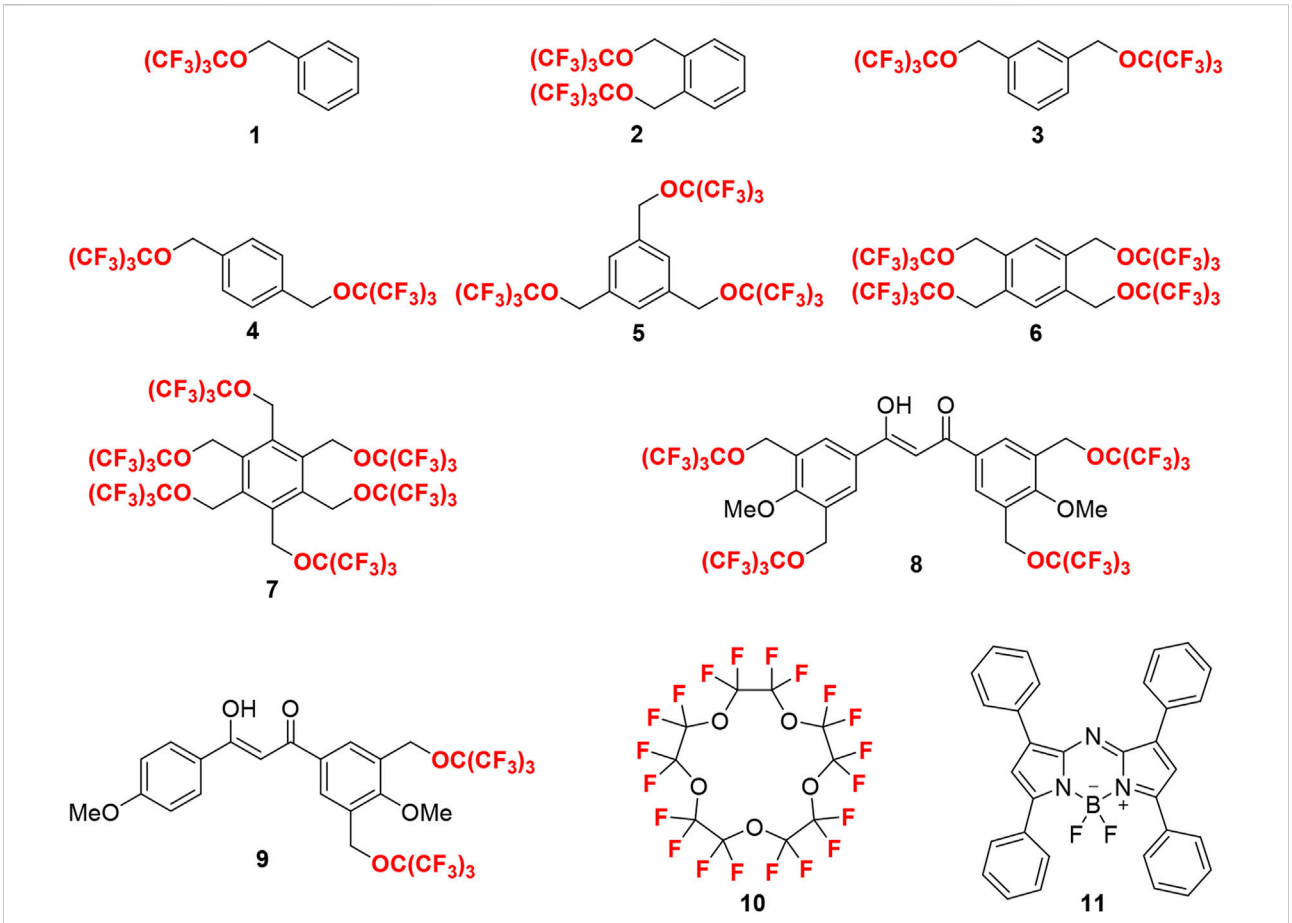

FIGURE 1
Structures of HFCs 1–7, chelators 8 and 9, perfluoro-15-crown-5 10, and aza-BODIPY 11.

referenced to 2% hexafluorobenzene (s, −164.90 ppm) in $CDCl_3$. The splitting patterns for ^1H NMR and ^{19}F NMR spectra were denoted as follows: s = singlet, d = doublet, t = triplet, q = quartet, and m = multiplet.

Phospholipid S75 was purchased from Lipoid GmbH (Ludwigshafen, Germany). Pluronic F68 (average MW = 8,350) was obtained from Adamas (Shanghai, China). Medicinal-grade soybean oil was acquired from Aladdin (Shanghai, China). Aza-BODIPY was synthesized in this lab according to the method used by Jokic et al. (2012). Human breast cancer MCF-7 cells and human triple-negative breast cancer MDA-MB-231 cells were purchased from the Cell Bank of the Chinese Academy of Sciences (Shanghai, China). The human lung adenocarcinoma cell line A549 was purchased from Beyotime (Shanghai, China). BALB/c mice (female, 5–6 weeks old) and BALB/c nude mice (female, 5–6 weeks old) were purchased from Hubei BIONT Biotechnology Co., Ltd. Unless otherwise indicated, all reagents were obtained from a commercial supplier and used without prior purification. All solvents were either analytical or HPLC grade. Deionized water was used unless otherwise indicated. THF was dried and freshly distilled before use. Column flash chromatography was performed on silica gel (200–300 mesh) with the eluent as indicated in the procedures. All animal studies were conducted according to the experimental practices and standards approved by the Animal Welfare and Research Ethics Committee at the Innovation Academy for Precision Measurement Science and Technology, Chinese Academy of Sciences.

The size distribution and polymer dispersion index (PDI) of nanoparticles were determined by a dynamic light-scattering (DLS) instrument (Malvern, Nano ZS 90, United Kingdom). UV-Vis and fluorescence emission spectra were obtained using a UV-2600 UV-Vis spectrophotometer (Shimadzu, Japan) and a FluoroMax-4 spectrofluorometer (HORIBA Scientific, America), respectively. Aza-BODIPY encapsulation efficiency (EE%) and drug loading efficiency (DLE%) were determined using an LC20-AT reversed-phase high-performance liquid chromatograph (Shimadzu, Japan). *In vitro* cellular uptake was determined by a Leica-TCS-SP8-STED CLMS (Leica,

Germany). Cell viability (%) was determined using an ELx800 light-absorption microplate reader (BioTek, America). *In vivo* fluorescence imaging was determined using an IVIS Spectrum *in vivo* imaging system (PerkinElmer, America).

Synthesis of HFCs 1–7 and chelators 8 and 9

HFC 1: Under an argon atmosphere, a solution of potassium perfluoro-*tert*-butoxide (15.0 g, 54.7 mmol) in anhydrous *N,N*-dimethylformamide (DMF, 100 ml) was added to a reaction flask containing benzyl bromide 12 (7.8 ml, 65.6 mmol). The reaction mixture was stirred at 40°C for 12 h until thin-layer chromatography (TLC) analysis showed that benzyl bromide was consumed completely. Then, the reaction mixture was quenched with water, and the lower phase was collected as a yellowish oil, which was washed with water thrice to give HFC 1 as a colorless oil (15.9 g, 89% yield). ^{1}H NMR (400 MHz, $CDCl_3$) δ 7.39–7.31 (m, 5H) and 5.02 (s, 2H). ^{19}F NMR (376 MHz, $CDCl_3$) δ −73.11 (s).

General synthetic procedures for HFCs 2–6 using the synthesis of HFC 2 as an example: Under an argon atmosphere, a solution of potassium perfluoro-*tert*-butoxide (6.2 g, 22.6 mmol) in anhydrous DMF (25 ml) was added to a reaction flask containing bromide 13 (2.0 g, 7.6 mmol). The reaction mixture was stirred at room temperature for 24 h until TLC showed that the starting material was consumed completely. The reaction mixture was quenched with water, and the white precipitate was collected and washed with water several times to give HFC 2 (Zhao et al., 2012) as a white powder (3.0 g, 69% yield). ^{1}H NMR (400 MHz, $CDCl_3$) δ 7.43–7.39 (m, 1H), 7.34–7.32 (m, 3H), and 5.05 (s, 4H).^{19}F NMR (376 MHz, $CDCl_3$) δ −73.27 (s).

HFC 3 (Zhao et al., 2012) was prepared as a white powder (5.5 g, 84% yield) from 14 (3.0 g, 11.4 mmol) using the same procedure as that for compound 2, with an increased amount of potassium perfluoro-*tert*-butoxide (9.3 g, 33.9 mmol). ^{1}H NMR (400 MHz, $CDCl_3$) δ 7.42 (s, 4H) and 5.12 (s, 4H). ^{19}F NMR (376 MHz, $CDCl_3$) δ −73.31 (s).

HFC 4 (Zhao et al., 2012) was prepared as a white powder (0.9 g, 83% yield) from 15 (0.5 g, 1.9 mmol) using the same procedure as that for compound 2, with an increased amount of potassium perfluoro-*tert*-butoxide (2.1 g, 7.7 mmol). ^{1}H NMR (400 MHz, acetone-d_6) δ 7.38 (s, 4H) and 5.08 (s, 4H). ^{19}F NMR (376 MHz, acetone-d_6) δ −71.18 (s).

HFC 5 (Zhao et al., 2012) was prepared as a white powder (4.6 g, 89% yield) from 16 (2.0 g, 5.6 mmol) using the same procedure as that for compound 2, with an increased amount of potassium perfluoro-*tert*-butoxide (6.1 g, 22.3 mmol). ^{1}H NMR (400 MHz, $CDCl_3$) δ 7.32 (s, 3H) and 5.07 (s, 6H). ^{19}F NMR (376 MHz, $CDCl_3$) δ −73.36 (s).

HFC 6 was prepared as a white powder (1.0 g, 80% yield) from 17 (0.5 g, 1.1 mmol) using the same procedure as that for compound 2, with an increased amount of potassium perfluoro-*tert*-butoxide (1.8 g, 6.6 mmol). ^{1}H NMR (400 MHz, acetone-d_6) δ 7.67 (s, 2H) and 5.28 (s, 8H). ^{19}F NMR (376 MHz, acetone-d_6) δ −71.24. ^{13}C NMR (101 MHz, acetone-d_6) δ 135.3, 129.9, 121.3 (q, J = 292.9 Hz), 81.2–80.3 (m), and 69.5. HRMS (ESI) calculated for $C_{26}H_{10}F_{36}O_4K^+$ ([M + K]$^+$) 1108.9636 found 1108.9628.

Compound 20: Under an argon atmosphere, anhydrous methanol (300 ml) and concentrated sulfuric acid (6.1 ml) were added to a reaction flask containing acid 19 (10.0 g, 55.5 mmol). The resulting mixture was refluxed for 8 h. Then, the reaction was quenched with water and extracted with dichloromethane (DCM, 300 ml, three times). The combined organic layers were dried over anhydrous Na_2SO_4 and concentrated under vacuum, and the residue was purified by silica gel column chromatography (PE/EA = 100/1) to give compound 20 (Grimster et al., 2013) as a yellowish oil (11.8 g, 99% yield). ^{1}H NMR (400 MHz, $CDCl_3$) δ 7.71 (s, 2H), 3.88 (s, 3H), 3.74 (s, 3H), and 2.31 (s, 6H).

Compound 21: Under an argon atmosphere, compound 20 (11.0 g, 56.7 mmol), *N*-bromosuccinimide (NBS, 22.4 g, 125.8 mmol), and azobisisobutyronitrile (AIBN, 58.3 mg, 0.35 mmol) were dissolved in CCl_4 (230 ml). The resulting mixture was refluxed for 3 h. Then, the reaction was quenched with water and extracted with dichloromethane (DCM, 300 ml, three times). The combined organic layers were dried over anhydrous Na_2SO_4 and concentrated under vacuum, and the residue was purified by silica gel column chromatography (PE/EA = 250/1) to give compound 21 as a white powder (11.8 g, 59% yield). ^{1}H NMR (400 MHz, $CDCl_3$) δ 8.07 (s, 2H), 4.56 (s, 4H), 4.08 (s, 3H), and 3.92 (s, 3H). ^{13}C NMR (101 MHz, $CDCl_3$) δ 165.7, 160.4, 133. 7, 132.5, 127.0, 62.6 (d, J = 1.7 Hz), 52.5 (d, J = 1.8 Hz), and 26.9. HRMS (ESI) calculated for $C_{11}H_{12}Br_2O_3Na^+$ ([M + Na]$^+$ 347.9025 found 347.9020.

Compound 22: Under an argon atmosphere, a solution of potassium perfluoro-*tert*-butoxide (10.9 g, 39.8 mmol) in anhydrous DMF (60 ml) was added to a reaction flask containing compound 21 (4.0 g, 11.4 mmol). The reaction mixture was stirred at 40°C for 12 h. The mixture was quenched with water. The precipitate was collected and washed with water three times. After dissolving in diethyl ether, the precipitate was dried over anhydrous Na_2SO_4. Then, the solution was filtered and concentrated to give a residue, which was purified by rapidly flushing the silica gel column with low-boiling petroleum ether to give compound 22 as a white powder (4.7 g, 62% yield). ^{1}H NMR (400 MHz, acetone-d_6) δ 8.04 (s, 2H), 5.18 (s, 4H), 3.82 (s, 3H), and 3.77 (s, 3H). ^{19}F NMR (376 MHz, acetone-d_6) δ −71.01 (s). ^{13}C NMR (101 MHz, $CDCl_3$) δ 165.9, 161.6, 133.7, 129.0, 127.1, 120.5 (q, J = 292.8 Hz), 80.4–79.5 (m), 66.3, 63.8, and 52.6. HRMS (ESI)

calculated for $C_{19}H_{12}F_{18}O_5Na^+$ ([M + Na]$^+$ 658.0290 found 658.0291.

Compound 24: Under an argon atmosphere, compound 23 (1.0 g, 5.6 mmol, in 20 ml CCl_4) was added to the reaction flask containing NBS (2.2 g, 12.4 mmol) and AIBN (5.5 mg, 0.033 mmol). After being refluxed at 85°C for 3.5 h, the reaction mixture was quenched with water and extracted with DCM (300 ml, three times). The combined organic layers were dried over anhydrous Na_2SO_4, concentrated under vacuum, and purified by silica gel column chromatography (PE/EA = 150/1) to give compound 24 as a white powder (0.96 g, 51% yield). ^{1}H NMR (400 MHz, $CDCl_3$) δ 7.98 (s, 2H), 4.57 (s, 4H), 4.08 (s, 3H), and 2.60 (s, 3H). ^{13}C NMR (101 MHz, $CDCl_3$) δ 196.2, 160.6, 134.0, 132.6, 132.5, 62.6, 27.0, and 26.7. HRMS (ESI) calculated for $C_{11}H_{12}Br_2O_2Na^+$ ([M + Na]$^+$) 358.9076 found 358.9075.

Compound 25: Under an argon atmosphere, a solution of potassium perfluoro-*tert*-butoxide (0.7 g, 2.6 mmol) in anhydrous DMF (15 ml) was added to a reaction flask containing compound 24 (0.3 g, 0.9 mmol). After being stirred at room temperature for 24 h, the reaction mixture was quenched with water. The white precipitate was collected, dissolved in petroleum ether, and dried over anhydrous Na_2SO_4. Then, the solution was filtered and concentrated to give a residue, which was purified by rapidly flushing the silica gel column with low-boiling petroleum ether to give compound 25 as a white solid (0.4 g, 72% yield). ^{1}H NMR (400 MHz, acetone-d_6) δ 8.06 (s, 2H), 5.18 (s, 4H), 3.82 (s, 3H), and 2.46 (s, 3H). ^{19}F NMR (376 MHz, acetone-d_6) δ −70.99. ^{13}C NMR (101 MHz, $CDCl_3$) δ 196.3, 161.4, 134.0, 132.1, 129.2, 120.5 (q, J = 293.2 Hz), 80.4–79.3 (m), 66.3, 63.7, and 26.5. HRMS (ESI) calculated for $C_{19}H_{12}F_{18}O_4$ Na$^+$ ([M + Na]$^+$) 669.0340 found 669.0342.

Compound 9: In a glove box, anhydrous tetrahydrofuran (THF, 4 ml) was added to the reaction flask containing compound 22 (441 mg, 0.7 mmol) and *p*-methoxy acetophenone (50 mg, 0.3 mmol). Then, potassium *tert*-butoxide (111 mg, 1.0 mmol) was added. The mixture was stirred at room temperature for 2 h and further stirred at 50°C for 24 h. Subsequently, a 2-N HCl solution was added to neutralize the reaction mixture. After that, the mixture was extracted with diethyl ether (60 ml, three times). The combined organic layers were dried over anhydrous Na_2SO_4, concentrated under vacuum, and purified by silica gel column chromatography (PE/EA = 100/1) to give compound 9 as a white solid (55.5 mg, 24% yield). ^{1}H NMR (500 MHz, $CDCl_3$) δ 8.02–7.94 (m, 4H), 7.00–6.98 (m, 2H), 6.71 (s, 1H), 5.15 (s, 4H), and 3.88 (d, J = 3.0 Hz, 6H). ^{19}F NMR (376 MHz, $CDCl_3$) δ −72.98. ^{13}C NMR (101 MHz, $CDCl_3$) δ 185.9, 182.9, 163. 6, 160.7, 132.6, 130.7, 129.4, 129.2, 127.9, 120.5 (q, J = 293.6 Hz), 114.2, 92.2, 80.5–79.9 (m), 66.4, 63.7, and 55.7. HRMS (ESI) calculated for $C_{27}H_{18}F_{18}O_6Na^+$ ([M + Na]$^+$) 803.0708 and found 803.0706.

Formulation and characterization of partially fluorinated nanoemulsions

The typical procedure for formulating partially fluorinated nanoemulsion using nanoemulsion E1 as an example: The optimized formulation is composed of 36% Lipoid S75, 4.5% soybean oil, 0.5% aza-BODIPY 11, 1% chelator 9, and 58% HFC 1. Briefly, Lipoid S75 and aza-BODIPY 11 were each dissolved in DCM. Chelator 9 (2 mg) was dissolved in HFC 1 (130 mg), and the aza-BODIPY 11 (1 mg, 2.7 mM) solution was added. Then, the solution of Lipoid S75 (80 mg, 20% w/v) was added to the mixture. The resulting mixture was transferred to a 100-ml round-bottom flask and subjected to solvent removal under vacuum at a rotation speed of 50 rpm for 5 min at 37°C, thus forming a thin film. The deionized water (4 ml) was added to the reaction flask under ultrasound. The crude nanoemulsion was sonicated in a water bath for 10 min and in a cell disruptor for 5 min, followed by filtration through a 0.2-μm syringe filter.

Determination of aza-BODIPY encapsulation efficiency (EE %) and drug loading content (DLC%): Different concentrations of aza-BODIPY standard solutions (5 μg/ml, 10 μg/ml, 20 μg/ml, 25 μg/ml, 30 μg/ml, 40 μg/ml, and 50 μg/ml) were prepared with analytical acetonitrile as the solvent, and the standard curve of aza-BODIPY was drawn with high-performance liquid chromatography (HPLC). The chromatographic conditions of HPLC are as follows: column: RP C18 column, 5 μm, 4.6 mm × 100 mm; mobile phase: A as H_2O and B as CH_3CN; gradient: B of 70%–100% (30 min); wavelength: 650 nm; injection volume: 20 μl; flow rate: 0.7 ml/min.

Nanoemulsions E1–E4 were centrifuged at 11,000 rpm for 30 min, the concentration of free aza-BODIPY in the supernatant was measured by HPLC, and the mass of free aza-BODIPY (W_f) was calculated based on the standard curve measured earlier. The total weight of dried nanoemulsions (W_d) and the total content of aza-BODIPY in nanoemulsions (W_t) were calculated, and EE% and DLC% were calculated using Equations 1 and 2.

$$EE\% = (W_t - W_f)/W_t \times 100\%, \quad (1)$$

$$DLC\% = (W_t - W_f)/W_d \times 100\%. \quad (2)$$

In vitro cellular uptake study

A549 cells were cultured in DMEM high-glucose medium with 10% fetal bovine serum and 1% penicillin–streptomycin. All cells were cultured at 37°C in a humidified atmosphere containing 5% CO_2. About 2 × 10^6 A549 cells were seeded into culture flasks overnight. A culture medium containing nanoemulsions (E1–E4) with 18 mM ^{19}F was added. After

12 h incubation at 37°C, the medium was removed, and the cells were washed with PBS thrice. Trypsin was added to detach cells, and the cells were resuspended in PBS for counting. Subsequently, the cells were centrifuged, and the supernatant was removed; 400 μl of cell lysis solution was added and then transferred to a 5-mm NMR tube, and a capillary tube containing 100 μl of sodium trifluomethanesulfonate solution was added to measure the content of ^{19}F.

About 2×10^5 A549 cells were seeded on 2-cm cell culture dishes for 12 h. A culture medium containing the BODIPY (10 μg/ml)-labeled nanoemulsions (E1–E4) was added. After 12 h of incubation, the medium was removed, and the cells were washed with PBS and fixed with 4% paraformaldehyde for 15 min. Then, fixed cells were stained with 200 μl of 4,6-diamino-2-phenylindole (DAPI) for 10 min and washed with PBS at least three times. Finally, cells were imaged using a confocal laser scanning microscope (CLSM).

In vitro cellular cytotoxicity assay

A549 cells, MCF-7 cells, and MDA-MB-231 cells were cultured in DMEM high-glucose medium with 10% fetal bovine serum and 1% penicillin–streptomycin. All cells were cultured at 37°C in a humidified atmosphere containing 5% CO_2.

In vitro cell cytotoxicity was evaluated using a cell counting (CCK-8) assay. About 1×10^4 cells (A549, MCF-7, and MDA-MB-231, respectively) were seeded per well in 96-well plates (n = 3) and cultured for 24 h. Nanoemulsions (E1–E4) were diluted with the medium to a specific concentration and added to each well, respectively. After incubation for 12 h, cells were washed with PBS (pH 7.4) twice. Then, 100 μl of CCK-8 (10% v/v) solution was added to each well and incubated for another 2 h. Finally, the absorbance at 450 nm was measured with a microplate reader.

Cell viability (%) was calculated using the following formula:

$$\text{Cell viability}\,(\%) = [(A_{\text{Test}} - A_{\text{Blank}})/(A_{\text{Control}} - A_{\text{Blank}})] \times 100\%,$$

where A_{Test}, A_{Control}, and A_{Blank} represented the absorbance of cells with different treatments, untreated cells, and PBS buffer solution, respectively.

In vitro nanoemulsion ^{19}F MRI study

All ^{19}F MRI phantom experiments in the *in vitro* nanoemulsion ^{19}F MRI study were performed on a 400-MHz Bruker BioSpec MRI system at 25°C. Nanoemulsions E1–E4 were serially diluted with water to give a series of ^{19}F concentrations of 40 mM, 20 mM, 10 mM, 5 mM, and 2.5 mM, respectively.

For E1–E4, the ^{19}F density-weighted ^{19}F MRI phantom images were acquired by using a gradient-echo (GRE) pulse sequence with the following parameters: method = RARE, matrix size = 32 × 32, SI = 20 mm, FOV = 3.0 cm × 3.0 cm, TR = 4,000 ms, TE = 3 ms, NS = 12, and scan time = 384 s. For T_1-weighted ^{19}F MRI phantom images, a gradient-echo (GRE) pulse sequence with the following parameters was used: method = RARE, matrix size = 32 × 32, SI = 20 mm, FOV = 3.0 cm × 3.0 cm, TR = 180 ms, TE = 3 ms, NS = 135, and scan time = 389 s.

In vitro cellular ^{19}F MRI study

About 1×10^7 A549 cells were seeded on 10-cm cell culture dishes for 24 h. A culture medium containing nanoemulsions (E1–E4) with 18 mM of ^{19}F was added. After 12 h of incubation at 37°C, the medium was removed, and the cells were washed with PBS twice. Trypsin was added to digest the cells, and the cell suspension was transferred into a centrifuge tube. After centrifuging at 2,000 r/min for 5 min, the supernatant was removed, and the cell pellet was resuspended in PBS. The suspension was transferred to a 0.5-ml tube and centrifuged again to pellet the cells. Finally, the 0.5-ml tube was placed in a 10-mm NMR tube for imaging.

All ^{19}F MRI phantom experiments in the *in vitro* cellular ^{19}F MRI study were performed on a 400-MHz Bruker BioSpec MRI system at 25°C.

The ^{19}F density-weighted ^{19}F MRI phantom images were acquired by using a gradient-echo (GRE) pulse sequence with the following parameters: method = RARE, matrix size = 32 × 32, SI = 20 mm, FOV = 2.0 cm × 2.0 cm, TR = 4,000 ms, TE = 3 ms, NS = 12, and scan time = 384 s. For T_1-weighted ^{19}F MRI phantom images, a gradient-echo (GRE) pulse sequence with the following parameters was used: method = RARE, matrix size = 32 × 32, SI = 20 mm, FOV = 2.0 cm × 2.0 cm, TR = 180 ms, TE = 3 ms, NS = 135, and scan time = 389 s.

In vivo ^{19}F MRI and fluorescence imaging

Tracking A549 cancer cells in mice

About 1×10^7 A549 cells were seeded on 10-cm cell culture dishes for 24 h. A culture medium containing nanoemulsions (E1–E2) with 36 mM of ^{19}F was added. After 12 h of incubation at 37°C, the medium was removed, and the cells were washed with PBS twice. Trypsin was added to digest the cells; then, the cell suspension was transferred into a centrifuge tube. The suspension was centrifuged at 2,000 r/min for 5 min. The supernatant was discarded, and the pellet was resuspended in PBS; 0.1 ml of PBS (containing about 1 × 107 E1- or E2-labeled cells) was injected subcutaneously into the left and right backs of BALB/c nude mice (n = 3), respectively. *In vivo* ^{19}F MR images were captured using a 9.4-T nuclear magnetic resonance, in which the mice were anesthetized with 5% chloral hydrate.

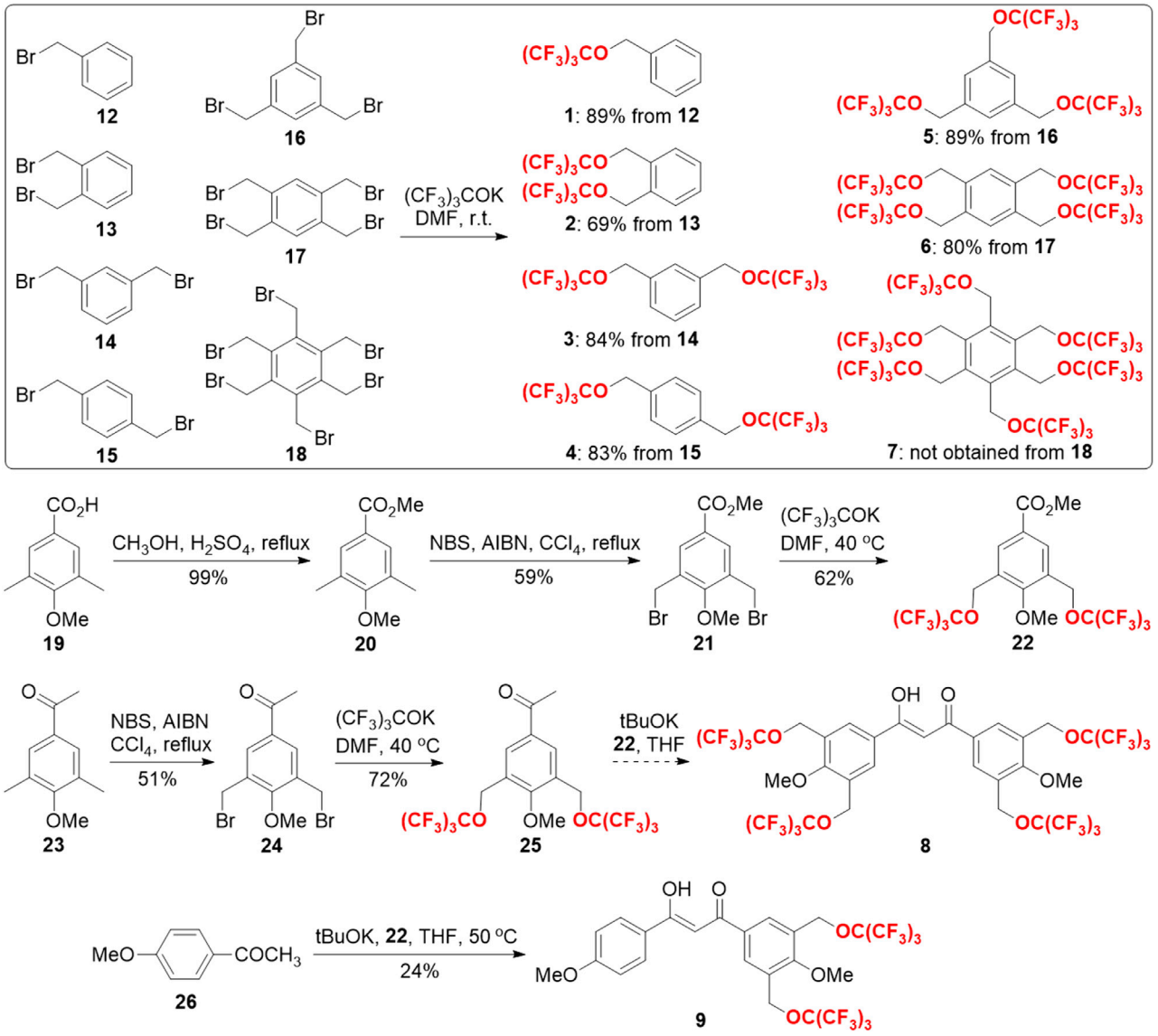

SCHEME 1
Synthesis of HFCs 1–7 and chelators 8 and 9.

The ^{19}F density-weighted ^{19}F MRI phantom images of mice were acquired using the RARE sequence with the following parameters: TR = 2.5 s, TE = 4.6 ms, RARE factor = 8, number of averages = 130, number of repetitions = 1, matrix size = 48 × 48, FOV = 50 mm × 40 mm, number of slices = 1, slice thickness = 15 mm, and total acquisition time = 32.5 min. T_1-weighted ^{19}F MRI phantom images of mice were acquired using the RARE sequence with the following parameters: TR = 200 ms, TE = 4.6 ms, RARE factor = 8, number of averages = 1,630, number of repetitions = 1, matrix size = 48 × 48, FOV = 50 mm × 40 mm, number of slices = 1, slice thickness = 15 mm, and total acquisition time = 32.6 min.

In vivo fluorescence images were determined using an IVIS imaging system (PerkinElmer) (excitation/emission, 640/680 nm), in which the mice were anesthetized with 1%–2% isoflurane in O_2.

Tracking macrophages in an inflammation mouse model

Three BALB/c mice were given footpad injections in their right paw, each containing 1% carrageenan solution (CAS# 9,064–57-7, Sigma) in 0.9% saline. After 1 h, the mice received 100 µl of E1 or E2 (C_F = 0.36 mmol/kg) through intravenous injection *via* the tail vein. For *in vivo* fluorescence imaging, all

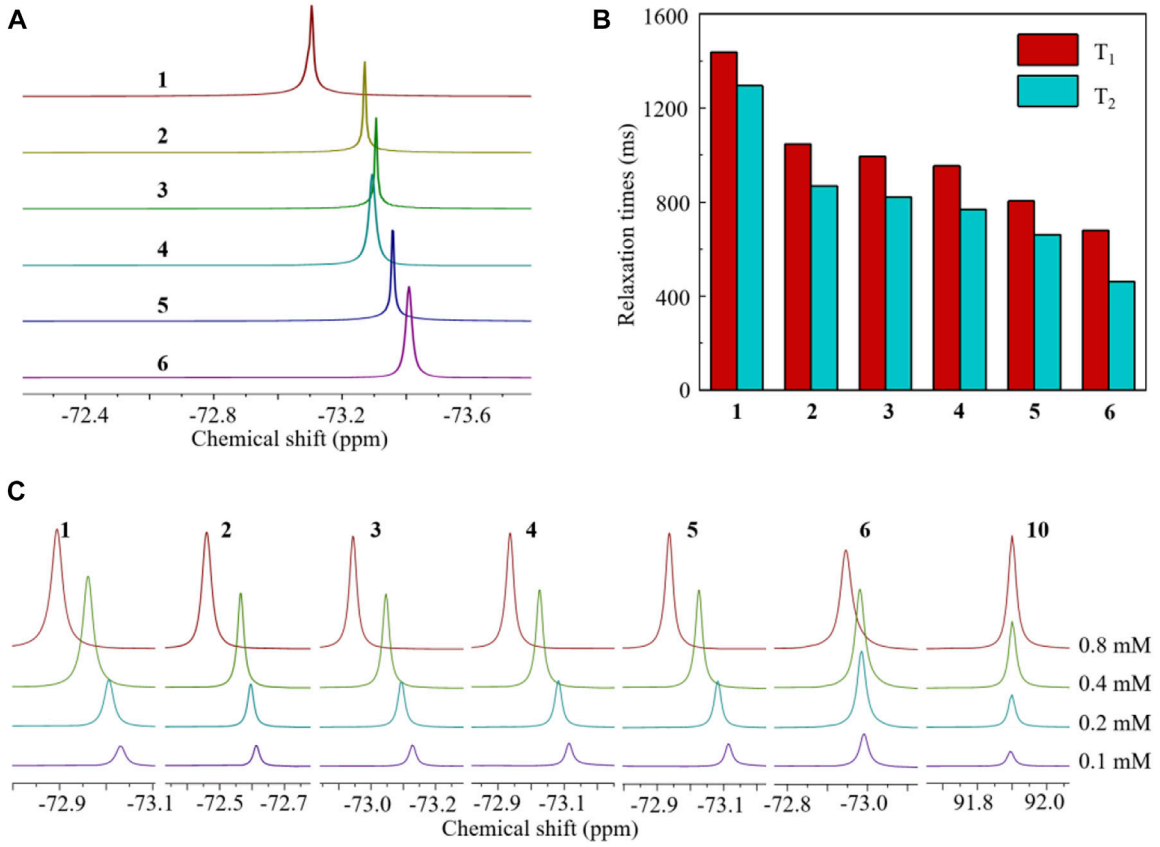

FIGURE 2
Partial ^{19}F NMR spectra [**(A)**, in $CDCl_3$], ^{19}F relaxation times [**(B)**, 0.4 mM in PFMCH], and concentration-dependent ^{19}F NMR spectra [**(C)**, in PFMCH, with perfluoro-20-crown-5 10 as a control] of HFCs 1–6. All ^{19}F NMR experiments were performed at 500 MHz at room temperature. Hexafluorobene was used as the internal standard.

mice underwent serial fluorescence imaging (IVIS, PerkinElmer, America) (excitation/emission, 640/680 nm) at 2 h, 4 h, 6 h, 8 h, and 12 h after receiving E1 or E2, during which the mice were anesthetized with 1%–2% isoflurane in O_2. A quantitative analysis of the total radiance (photons/s) was performed with Living Image software (PerkinElmer) by defining identical regions of interest covering the left (control) and right paws. *In vivo* ^{19}F MR images were captured using a 9.4-T nuclear magnetic resonance, during which the mice were anesthetized with 5% chloral hydrate.

Results and discussion

With these ideas in mind, the synthesis of HFCs 1–7 and fluorinated chelators 8 and 9 was then carried out (Scheme 1). First, from a series of commercially available benzyl bromides 12–18, HFCs 1–6 were synthesized in just one step by nucleophilic substitution of the bromides with potassium perfluoro-*tert*-butoxide in *N, N*-dimethylformaldehyde (DMF). Under the optimized conditions, HFCs 1–6 were prepared in good yields on multi-gram scales. Notably, pure HFC 1 was conveniently obtained by collecting the lower phase of the water-quenched reaction mixture, and HFCs 2–6 were obtained by filtration from the mixture, followed by washing with water. Because of the high steric hindrance, many attempts failed to synthesize HFC 7 with 6 perfluoro-*tert*-butoxyl groups, which delivered complex mixtures. Second, the synthesis of fluorinated chelator 8 commenced with the construction of fluorinated ester 22 and ketone 25. The commercially available benzoic acid derivative 19 was first transformed into the corresponding methyl ester 20, which was then radically di-brominated into bromide 21. Through the potassium perfluoro-*tert*-butoxide substitution reaction mentioned earlier, fluorinated ester 22 was prepared on a gram scale with a 36% yield over three steps. Similarly, commercially available ketone 23 was di-brominated and then substituted with potassium perfluoro-*tert*-butoxide to give fluorinated ketone 25 with a 37% yield over two steps. However, the Claisen condensation between the fluorinated ester 22 and ketone 25 led to a complex mixture,

TABLE 1 Ingredients, particle sizes, and PDIs of partially fluorinated nanoemulsions.

Entry	Ingredients[a]	Size[b] (PDI)
1	1, 9, 11, and S75	127 (0.23)
2	1, 9, 11, lecithin, and F68	113 (0.32)
3	1, 9, 11, S75, and soybean oil (E1)	143 (0.14)
4	1, 9, 11, S75, soybean oil, and $FeCl_3$ (E2)	145 (0.14)
5	1, 9, 11, lecithin, F68, and soybean oil (E3)	189 (0.19)
6	1, 9, 11, lecithin, F68, soybean oil, and $FeCl_3$ (E4)	189 (0.21)

[a]Amount of ingredients in 4 ml water: 130 mg 1, 2 mg 9, 1 mg 11, and 10 mg soybean oil.
[b]Particle sizes were measured by DLS, as nm of the diameter.

probably due to the high steric hindrance and peculiar fluorous properties in the reactants. To address these issues, we replaced the fluorinated ketone 25 with commercially available 1-(4-methoxyphenyl)ethan-1-one 26 and successfully prepared partially fluorinated chelator 9 under anhydrous conditions.

The structures of HFCs 1–6 and chelator 9 were confirmed by their $^{1}H/^{13}C/^{19}F$ NMR and mass spectra (see Supplementary Material). The structures of known compounds 1–5 were further confirmed by comparing their ^{1}H NMR spectra with those of Zhao et al. (2012). As expected, all the fluorinated compounds gave a sharp singlet ^{19}F NMR peak from their multiple symmetrical fluorines, respectively (Figure 2A). HFCs 2–6 are clear solids at room temperature. Notably, solid fluorinated agents usually have an ultra-short transverse relaxation time (T_2) and a quenched ^{19}F signal. Thus, it is necessary to disperse solid HFCs 2–6 in surfactants or liquid agents to extend the T_2 for sensitive ^{19}F MRI. Interestingly, solid HFCs 2–6 showed high solubility in liquid HFC 1 due to their similar chemical structures, delivering fluorinated solutions with a pseudo singlet ^{19}F NMR peak and tunable fluorine content (F %). HFCs 5 and 6, with the highest fluorine contents, showed heavy fluorous properties, for example, low solubility in most hydrocarbon solvents but high solubility in fluorous solvents like perfluoro(methylcyclohexane) (PFMCH). Thus, the ^{19}F relaxation times of HFCs 1–6 were measured in PFMCH (Figure 2B). A molecular weight (MW)-dependent pattern of ^{19}F relaxation time was observed from HFCs 1–6, that is, the larger the MW, the shorter the relaxation times. Compared to many perfluorocarbons, HFCs 1–6 had relatively short relaxation times and small T_1/T_2 ratios. During ^{19}F MRI, short T_1 and long T_2, that is, a small T_1/T_2 ratio, are beneficial for rapid data collection and thus sensitive ^{19}F MRI. It was noteworthy that the π–π interactions among the benzene cores were successfully observed in the concentration-dependent ^{19}F NMR spectra of HFCs 1–6 in PFMCH (Figure 2C). When increasing the concentrations, the ^{19}F NMR peaks of HFCs 1–6 were shifted to the low field as far as 0.184 ppm in HFC 3. In contrast, neglectable apparent chemical shift changes, about 0.005 ppm, were observed in the corresponding solutions of perfluoro-20-crown-5 10, which has no benzene structure. Furthermore, HFC 6 with four bulky PFTB groups gave a minimal ^{19}F chemical shift change of 0.045 ppm among the HFCs, in which the high steric hindrance severely reduced the π–π interactions. In pure HFC 1 and its HFC 2–6 solutions, the π–π interactions were supposed to reduce the T_1 for sensitive ^{19}F MRI. Therefore, HFCs 1–6 were conveniently synthesized on relatively large scales as valuable and sensitive ^{19}F MRI agents with a high F%, a sharp singlet ^{19}F NMR peak, significant π–π interactions among the benzene cores, and relatively short relaxation times.

Because of its liquid form, very cheap precursor, and convenient multigram-scale synthesis, HFC 1 was selected to formulate partially fluorinated nanoemulsions for ^{19}F MRI cell tracking. Due to their similar chemical structures, fluorinated chelator 9 was quite soluble in HFC 1, dramatically simplifying the formulation of paramagnetic nanoemulsions. S75 and egg yolk lecithin together with F68 were, respectively, identified as the optimal surfactants for the formulation, providing nanoemulsions of HFC 1, chelator 9, and aza-BODIPY 11 using a thin-film dispersion method (Table 1, Entries 1 and 2). Interestingly, adding a small amount of soybean oil delivered highly monodisperse nanoemulsions E1 and E3 (Table 1, Entries 3 and 5). After adding $FeCl_3$ to the nanoemulsion solution, the apparent color change indicated the chelation of Fe^{3+} by fluorinated chelator 9, providing a paramagnetic nanoemulsion with negligible particle size and PDI changes. After the removal of unchelated Fe^{3+} in the solutions by dialysis, paramagnetic nanoemulsions E2 and E4 were prepared with high monodispersity (Table 1, Entries 4 and 6).

The high monodispersity of nanoemulsions E1–E4 was confirmed by dynamic light scattering (DLS) with low polydispersity indexes (PDI, Figure 3A). Furthermore, DLS detected only slight changes in the particle size and PDI of E1 solutions during 14 days (Figure 3B), indicating its high stability. In contrast, a considerable increase in the PDI of E3 between day 8 and day 14 showed less efficacy of lecithin and F68 in formulating HFC 1. NIR dye aza-BODIPY 11 was successfully encapsulated into the nanoemulsions with high efficiency (E1: 93%, E2: 96%, E3: 93%, and E4: 97%) and a loading content of about 0.45%. Compared to aza-BODIPY 11, the nanoemulsions gave slightly red-shifted maximum UV-Vis absorption peaks around 653 nm (Figure 3C) and a maximum FL emission peak around 682 nm (Figure 3D). Moreover, the encapsulation did not compromise the fluorescence intensity of aza-BODIPY (Supplementary Figure S3). It was found that the Fe^{3+} in nanoemulsions E2 and E4 considerably lowered the maximum UV-Vis absorption and FL emission intensities, probably due to the photoinduced electron transfer between aza-BODIPY and Fe^{3+} (El-Khouly et al., 2004; Doose et al., 2009; Fukuzumi et al., 2012). Each fluorinated nanoemulsion gave a singlet ^{19}F NMR peak of around −72.4 ppm (Figure 3E).

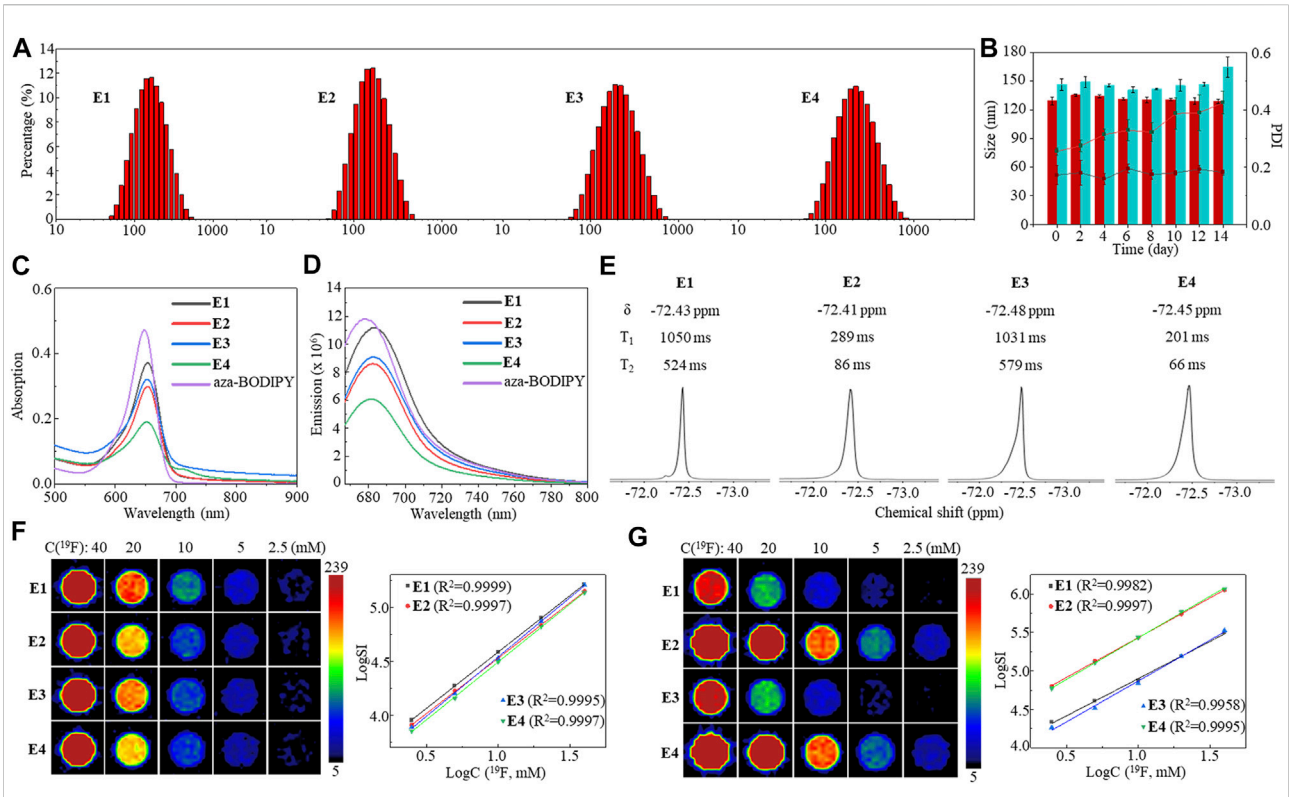

FIGURE 3
DLS **(A)**, stability monitored by DLS over 14 days **(B)**, UV-Vis absorption spectra **(C)**, FL emission spectra **(D)**, partial ^{19}F NMR spectra and ^{19}F relaxation times **(E)**, ^{19}F density-dependent phantom images and the logarithm plot of SI versus ^{19}F concentration **(F)**, and ^{19}F T_1-dependent phantom images and the logarithm plot of SI versus ^{19}F concentration **(G)** of nanoemulsions E1–E4.

The nanoemulsions E1 and E3 had relatively long ^{19}F T_1, while the Fe^{3+} in nanoemulsions E2 and E4 significantly shortened the ^{19}F T_1 by 3.6 and 5.1 folds, respectively, through the PRE effect (Figure 3E). The short T_1 facilitated a fast ^{19}F T_1-dependent ^{19}F MRI scan for high-quality images. The nanoemulsions E1–E4 were imaged by ^{19}F MRI at a ^{19}F concentration as low as 5 mM using a ^{19}F density-dependent MRI method with a data collection time of 384 s (Figure 3F). As expected, the ^{19}F MRI sensitivity was significantly improved by the encapsulated Fe^{3+} using a ^{19}F T_1-dependent MRI method, in which paramagnetic nanoemulsions were imaged at a low concentration of 2.5 mM with a data collection time of 389 s (Figure 3G). Notably, the logarithm of ^{19}F signal intensity (SI) was proportional to the ^{19}F concentration in both density-dependent ^{19}F MRI and T_1-dependent ^{19}F MRI (Figures 3F, G), which facilitates the quantification of ^{19}F concentration with ^{19}F SI. Thus, fluorinated nanoemulsions E1–E4 with high monodispersity, stability, and unified and paramagnetic-enhanced ^{19}F signals were formulated as sensitive and quantitative ^{19}F MRI-FLI dual imaging agents.

Next, nanoemulsions E1–E4 were investigated in cells. First, the biocompatibility of nanoemulsions E1–E4 was investigated in human lung cancer A549 cells, human breast cancer MCF-7 cells, and human triple-negative breast cancer MDA-MB-231 cells using the CCK-8 cytotoxicity assay. High cell viabilities were observed in the nanoemulsion-treated cells with a ^{19}F dose as high as 45 mM after 12 h of incubation (Figures 4A–C), far beyond the ^{19}F MRI-detectable concentrations mentioned earlier. Second, due to their relatively high stability, a quantitative ^{19}F NMR study was carried out on the nanoemulsion E1- and E2-treated A549 cells. After incubating 1×10^7 A549 cells with nanoemulsions E1 and E2 at a ^{19}F concentration of 18 mM for 12 h, the cell lysates were quantitatively analyzed with ^{19}F NMR, which gave a strong ^{19}F NMR peak of around −71.3 ppm, respectively (Figure 4D). After calibrating the ^{19}F NMR SI with an internal standard of sodium triflate, each cell was found to take up 10^{11} fluorine atoms (Figure 4E). Interestingly, A549 cell lines showed significantly higher uptake of paramagnetic nanoemulsion E2 than diamagnetic nanoemulsion E1, while the reason for this phenomenon is still unclear. Third, the cell uptakes of nanoemulsions E1 and E2 were studied with confocal microscopy in A549 cells (Figure 4F). After 12 h of incubation, the red fluorescence of aza-BODIPY was visible in the cytoplasm around the nucleus dyed with blue-fluorescent DAPI, indicating the successful uptake of nanoemulsions E1 and E2. Notably, the Fe^{3+}

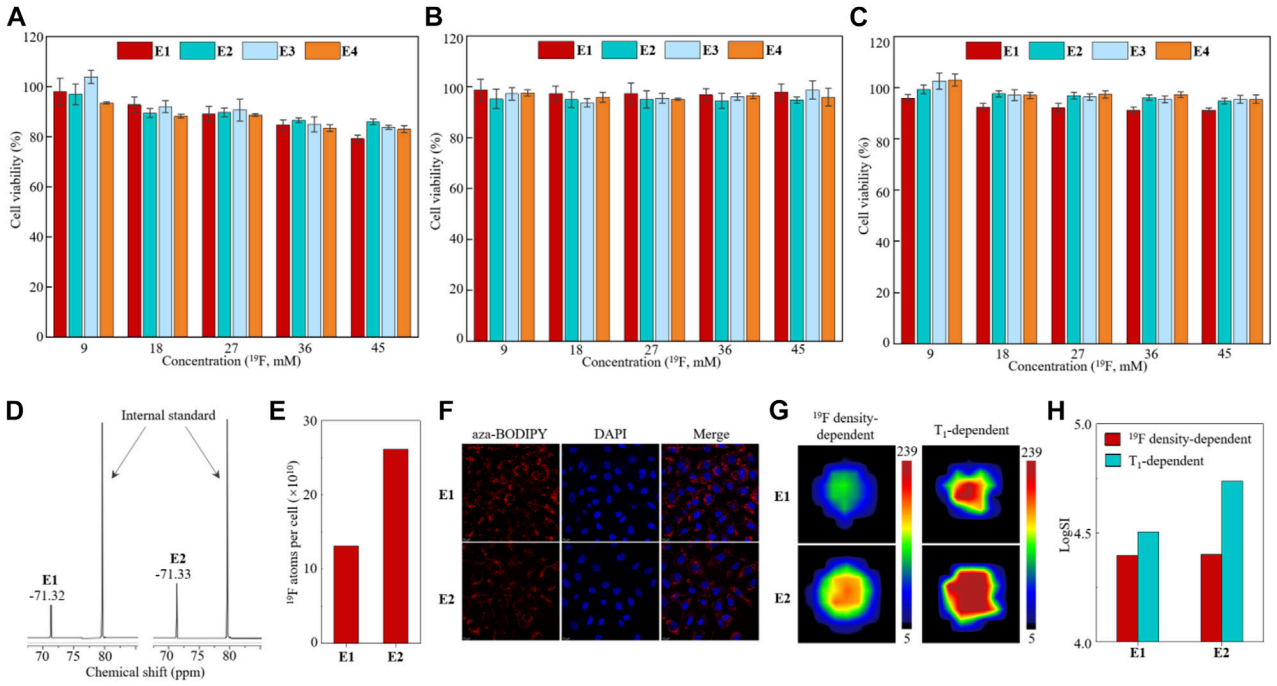

FIGURE 4
Cytotoxicity assay of nanoemulsions E1–E4 in A549 cells **(A)**, MCF-7 cells **(B)**, and MDA-MB-231 cells **(C)**. Partial ^{19}F NMR spectra **(D)** and quantitative analysis of ^{19}F atoms' uptake in each cell **(E)** of nanoemulsion E1- and E2-treated A549 cell lysates. Confocal microscopy images of A549 cells treated with nanoemulsion E1 and E2 after 12 h of incubation **(F)**. ^{19}F MRI images **(G)** and quantitative analysis of ^{19}F SI **(H)** of nanoemulsion E1- and E2-treated A549 cells.

partially quenched the FL of aza-BODIPY in nanoemulsion E2, resulting in a weaker FL intensity of E2-treated cells than that of E1-treated cells. In addition, no notable hemolysis was observed for nanoemulsions E1 and E2 in the blood (Supplementary Figure S2), and no death of BALB/c mice was observed after intravenous injection of nanoemulsion (100 μl, ^{19}F concentration of 450 mM) in an acute toxicity test, indicating the good biocompatibility of nanoemulsions E1 and E2. Finally, ^{19}F MRI was carried out on the E1- and E2-treated A549 cells. About 1×10^7 A549 cells were clearly imaged by both ^{19}F density-dependent and T_1-dependent ^{19}F MRI with short data collection times of 384 s and 389 s, respectively (Figure 4G). Moreover, due to the PRE effect of Fe^{3+}, the SI of T_1-dependent ^{19}F MRI was 2.2-fold higher than that of ^{19}F density-dependent ^{19}F MRI in the mice injected with paramagnetic nanoemulsion E2-treated A549 cells (Figure 4H). Therefore, the partially fluorinated nanoemulsions E1 and E2 had high biocompatibility, quantifiable ^{19}F NMR, efficient cell uptake, and high ^{19}F MRI sensitivity, which were suitable for quantitative ^{19}F MRI-FLI dual imaging cell tracking.

Finally, *in vivo* ^{19}F MRI-FLI dual-modal cell tracking with partially fluorinated nanoemulsions E1 and E2 was carried out in BALB/c nude mice. On the one hand, the tracking of lung cancer A549 cells was investigated by subcutaneous injection of 1×10^7 E1- and E2-labeled A549 cells to the right and left flanks of mice, respectively (Figure 5A). The injected cells were first tracked with *in vivo* FL, in which paramagnetic nanoemulsion E2-treated A549 cells showed weaker FL intensity than that of E1-treated cells due to the FL-quenching Fe^{3+} in nanoemulsion E2 (Figure 5B). Then, the A549 cells were tracked with ^{19}F MRI using ^{19}F density-dependent and T_1-dependent MRI sequences (Figure 5C). Notably, the cells injected into the left flank gave a 1.9-fold higher ^{19}F MRI SI than that of the right flank using a ^{19}F density-dependent sequence, while the ratio of SI was further improved to 3.3-fold using a T_1-dependent sequence (Figure 5D), showing the high efficacy of Fe^{3+} in improving ^{19}F MRI sensitivity. On the other hand, macrophage cells were labeled *in vivo* and tracked in a carrageenan-induced inflammation model. After tail vein injection of 100 μl nanoemulsions E1 and E2 at a ^{19}F concentration of 72 mM into the mice with right paw inflammation, the time-dependent FLI and ^{19}F MRI were recorded, respectively. The time-dependent FL images showed that the nanoemulsion-labeled macrophages accumulated mainly in the liver, lung, and kidney at 2 h post-injection and selectively accumulated in the right paw at 4 h post-injection, while neglectable FL was observed in the left paw (Figure 5E). The time-dependent FL intensity in the right paw region indicated that E2-labeled macrophages were eliminated

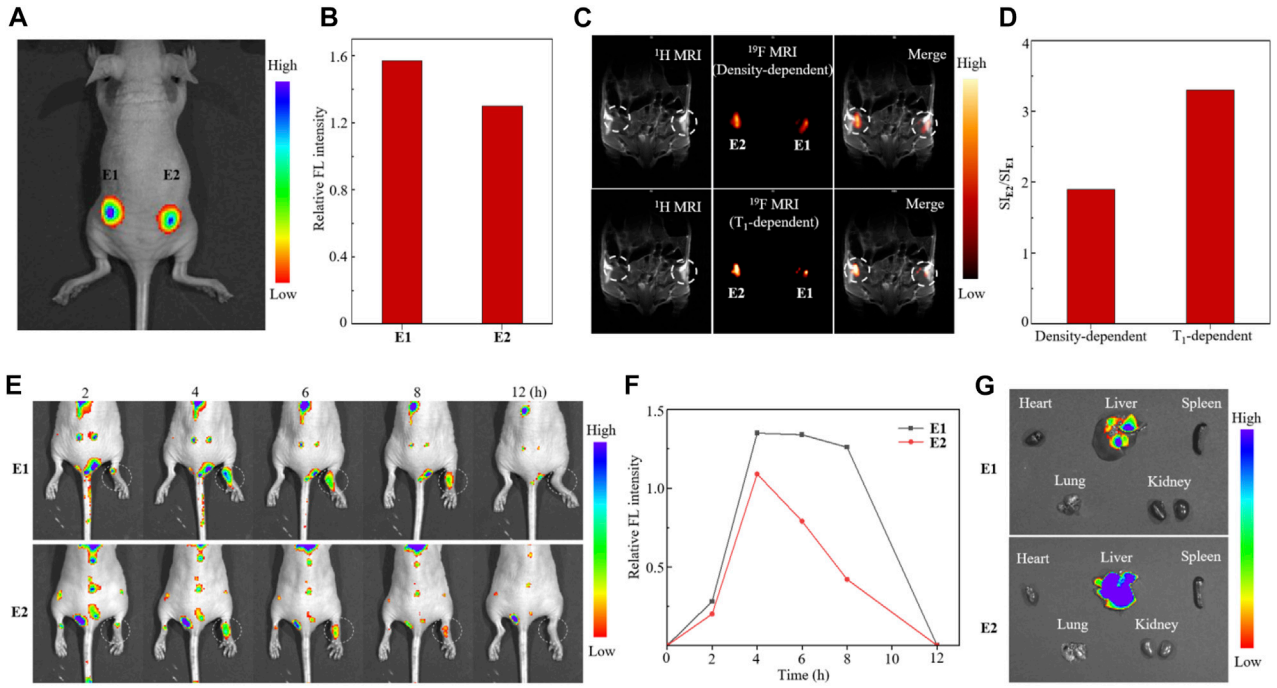

FIGURE 5
Fluorescence image **(A)**, quantitative analysis of relative FL intensity **(B)**, ^{19}F MRI [**(C)**, upper: ^{19}F density-dependent images, lower: ^{19}F T_1-dependent images], and quantitative analysis ^{19}F SI **(D)** of nude mice injected with nanoemulsion E1- and E2-labeled A549 cells. Time-dependent FL images **(E)**, quantitative analysis of FL intensity in the right paw region **(F)**, and FL images of internal organs [**(G)**, collected 4 h post-injection] of mice with carrageenan-induced paw inflammation after tail vein injection of nanoemulsions E1 and E2.

much faster than E1-labeled macrophages in this inflammation model (Figure 5F). The FL images of internal organs collected at 4 h post-injection illustrated the nanoemulsion mainly accumulated in the liver, while the accumulations in the heart, spleen, lung, and kidneys were not detected at this time (Figure 5G). Unfortunately, many attempts to track the nanoemulsion-labeled macrophages with ^{19}F MRI could not provide clear images of the inflamed paw, probably due to the low dose of E1 and E2.

Conclusion

In summary, we have developed partially fluorinated paramagnetic nanoemulsions from readily available chemicals for ^{19}F MRI-FLI dual-modal cell tracking. To address the challenge of ^{19}F MRI sensitivity in cell tracking, we have used many valuable strategies, including the efficient synthesis of fluorinated molecules with multiple symmetrical fluorine atoms and a strong ^{19}F signal, unifying the ^{19}F signals from all components in the nanoemulsions and shortening T_1 through the intermolecular interactions and the PRE effect of paramagnetic iron (III). Indeed, the partially fluorinated paramagnetic nanoemulsions exhibit high ^{19}F MRI sensitivity, which was detected at a low fluorine concentration of 2.5 mM with a short data collection time of 389 s. Further improvement in ^{19}F MRI sensitivity, for example, using HFCs 5 and 6 as ^{19}F signal molecules, is still needed to achieve more sensitive *in vivo* ^{19}F MRI cell tracking as indicated in the inflammation mice model. Meanwhile, efforts have been made to improve partially fluorinated nanoemulsions' physicochemical and biological properties. Through screening surfactants and adding soybean oil, highly monodispersed and stable nanoemulsions were obtained. The significant intra-molecular interactions of perfluoro-*tert*-butyl benzyl ethers have been shown to facilitate the successful encapsulation of functional molecules, including fluorinated chelators and aza-BODIPY, into stable nanoemulsions, which enables their dual-modal imaging and high biocompatibility toward a series of cells. Because of their peculiar physicochemical properties, the application of perfluorocarbon nanoemulsions in ^{19}F MRI cell tracking has been hampered by issues of sensitivity, biocompatibility, and multimodal compatibility. The strategy developed here, lowering the fluorine content while maintaining sensitivity and optimizing physicochemical properties, may address some of these issues and push ^{19}F MRI cell tracking into further clinical application.

Data availability statement

The original contributions presented in the study are included in the article/Supplementary Material; further inquiries can be directed to the corresponding authors.

Ethics statement

The animal study was reviewed and approved by the Animal Welfare and Research Ethics Committee at the Innovation Academy for Precision Measurement Science and Technology, Chinese Academy of Sciences.

Author contributions

TT, QZ, SL, HD, CT, and KC carried out experimental work, analyzed data, and drafted the figures and the manuscript; YL, MJ, and LZ carried out the NMR/MRI work and analyzed the data. XZ provided expert help and advice on molecular design and MRI work. SC, ZZ, and ZJ conceived, designed, and supervised the study and drafted the manuscript. All authors read, edited, and approved the final manuscript.

Funding

This work has received funding from the National Natural Science Foundation of China (22077098, 21921004, and 91859206), the Knowledge Innovation Program of Wuhan-Basic Research (2022020801010137), the National Key R&D Program of China (2018YFA0704000), the Laboratory of Tea and Health of Hengyang (202150083704), and the Undergraduate Research Learning and Innovative Experiment Project (S20221743071, S20221743277, and X202110555464).

Acknowledgments

We are thankful for the help and assistance from Tingjuan Wu, Anfeng Li, Jing Zhang, Meiju Sui, and Baolong Wang.

Conflict of interest

The authors declare that the research was conducted in the absence of any commercial or financial relationships that could be construed as a potential conflict of interest.

Publisher's note

All claims expressed in this article are solely those of the authors and do not necessarily represent those of their affiliated organizations, or those of the publisher, the editors, and the reviewers. Any product that may be evaluated in this article, or claim that may be made by its manufacturer, is not guaranteed or endorsed by the publisher.

Supplementary material

The Supplementary Material for this article can be found online at: https://www.frontiersin.org/articles/10.3389/fbioe.2022.1049750/full#supplementary-material

References

Ahrens, E. T., Flores, R., Xu, H., and Morel, P. A. (2005). *In vivo* imaging platform for tracking immunotherapeutic cells. *Nat. Biotechnol.* 23 (8), 983–987. doi:10.1038/nbt1121

Ahrens, E. T., and Zhong, J. (2013). *In vivo* MRI cell tracking using perfluorocarbon probes and fluorine-19 detection. *NMR Biomed.* 26 (7), 860–871. doi:10.1002/nbm.2948

Battistelli, G., Cantelli, A., Guidetti, G., Manzi, J., and Montalti, M. (2016). Ultra-bright and stimuli-responsive fluorescent nanoparticles for bioimaging. *WIREs Nanomed. Nanobiotechnol.* 8 (1), 139–150. doi:10.1002/wnan.1351

Bouvain, P., Flocke, V., Krämer, W., Schubert, R., Schrader, J., Flögel, U., et al. (2019). Dissociation of ^{19}F and fluorescence signal upon cellular uptake of dual-contrast perfluorocarbon nanoemulsions. *Magn. Reson. Mat. Phy.* 32 (1), 133–145. doi:10.1007/s10334-018-0723-7

Bulte, J. W., Arbab, A. S., Douglas, T., and Frank, J. A. (2004). Preparation of magnetically labeled cells for cell tracking by magnetic resonance imaging. *Methods Enzymol.* 386, 275–299. doi:10.1016/S0076-6879(04)86013-0

Bulte, J. W., and Daldrup-Link, H. E. (2018). Clinical tracking of cell transfer and cell transplantation: Trials and tribulations. *Radiology* 289 (3), 604–615. doi:10.1148/radiol.2018180449

Bulte, J. W. (2009). *In vivo* MRI cell tracking: Clinical studies. *Am. J. Roentgenol.* 193 (2), 314–325. doi:10.2214/AJR.09.3107

Chen, K., Wu, T., Jiang, M., Li, A., Peng, X., Chen, S., et al. (2022). Partially fluorinated nanoemulsions for ^{19}F MRI-fluorescence dual imaging cell tracking. *Colloids Surfaces B Biointerfaces* 215, 112493. doi:10.1016/j.colsurfb.2022.112493

Chudakov, D. M., Belousov, V. V., Zaraisky, A. G., Novoselov, V. V., Staroverov, D. B., Zorov, D. B., et al. (2003). Kindling fluorescent proteins for precise *in vivo* photolabeling. *Nat. Biotechnol.* 21 (2), 191–194. doi:10.1038/nbt778

Cromer Berman, S. M., Walczak, P., and Bulte, J. W. (2011). Tracking stem cells using magnetic nanoparticles. *WIREs. Nanomed. Nanobiotechnol.* 3 (4), 343–355. doi:10.1002/wnan.140

Deán-Ben, X. L., Weidenfeld, I., Degtyaruk, O., Ntziachristos, V., Stiel, A. C., and Razansky, D. (2020). Deep tissue volumetric optoacoustic tracking of individual circulating tumor cells in an intracardially perfused mouse model. *Neoplasia* 22 (9), 441–446. doi:10.1016/j.neo.2020.06.008

Doose, S., Neuweiler, H., and Sauer, M. (2009). Fluorescence quenching by photoinduced electron transfer: A reporter for conformational dynamics of macromolecules. *Chemphyschem* 10 (9-10), 1389–1398. doi:10.1002/cphc.200900238

Dutta, R., Liba, O., SoRelle, E. D., Winetraub, Y., Ramani, V. C., Jeffrey, S. S., et al. (2019). Real-time detection of circulating tumor cells in living animals using functionalized large gold nanorods. *Nano Lett.* 19 (4), 2334–2342. doi:10.1021/acs.nanolett.8b05005

El-Khouly, M. E., Ito, O., Smith, P. M., and Souza, F. D. (2004). Intermolecular and supramolecular photoinduced electron transfer processes of fullerene–porphyrin/phthalocyanine systems. *J. Photochem. Photobiol. C Photochem. Rev.* 5 (1), 79–104. doi:10.1016/j.jphotochemrev.2004.01.003

Ferreira, L., Karp, J. M., Nobre, L., and Langer, R. (2008). New opportunities: The use of nanotechnologies to manipulate and track stem cells. *Cell Stem Cell* 3 (2), 136–146. doi:10.1016/j.stem.2008.07.020

Fukuzumi, S., Honda, T., and Kojima, T. (2012). Structures and photoinduced electron transfer of protonated complexes of porphyrins and metallophthalocyanines. *Coord. Chem. Rev.* 256 (21-22), 2488–2502. doi:10.1016/j.ccr.2012.01.011

Gaudet, J. M., Hamilton, A. M., Chen, Y., Fox, M. S., and Foster, P. J. (2017). Application of dual ^{19}F and iron cellular MRI agents to track the infiltration of immune cells to the site of a rejected stem cell transplant. *Magn. Reson. Med.* 78 (2), 713–720. doi:10.1002/mrm.26400

Ghosh, R. P., Franklin, J. M., Draper, W. E., Shi, Q., Beltran, B., Spakowitz, A. J., et al. (2019). A fluorogenic array for temporally unlimited single-molecule tracking. *Nat. Chem. Biol.* 15 (4), 401–409. doi:10.1038/s41589-019-0241-6

Grimster, N. P., Connelly, S., Baranczak, A., Dong, J., Krasnova, L. B., Sharpless, K. B., et al. (2013). Aromatic sulfonyl fluorides covalently kinetically stabilize transthyretin to prevent amyloidogenesis while affording a fluorescent conjugate. *J. Am. Chem. Soc.* 135 (15), 5656–5668. doi:10.1021/ja311729d

Hong, H., Yang, Y., Zhang, Y., and Cai, W. (2011). Noninvasive cell tracking in cancer and cancer therapy. *Curr. Top. Med. Chem.* 10 (12), 1237–1248. doi:10.2174/156802610791384234

Janjic, J. M., Srinivas, M., Kadayakkara, D. K., and Ahrens, E. T. (2008). Self-delivering nanoemulsions for dual fluorine-19 MRI and fluorescence detection. *J. Am. Chem. Soc.* 130 (9), 2832–2841. doi:10.1021/ja077388j

Jokic, T., Borisov, S. M., Saf, R., Nielsen, D. A., Kühl, M., and Klimant, I. (2012). Highly photostable near-infrared fluorescent pH indicators and sensors based on BF2-chelated tetraarylazadipyrromethene dyes. *Anal. Chem.* 84 (15), 6723–6730. doi:10.1021/ac3011796

Kimura, A., Narazaki, M., Kanazawa, Y., and Fujiwara, H. (2004). ^{19}F Magnetic resonance imaging of perfluorooctanoic acid encapsulated in liposome for biodistribution measurement. *Magn. Reson. Imaging* 22 (6), 855–860. doi:10.1016/j.mri.2004.01.060

Kircher, M. F., Gambhir, S. S., and Grimm, J. (2011). Noninvasive cell-tracking methods. *Nat. Rev. Clin. Oncol.* 8 (11), 677–688. doi:10.1038/nrclinonc.2011.141

Lee, S. H., Park, S. A., Zou, Y., Seo, S. U., Jun, C. D., Lee, W. J., et al. (2018). Real-time monitoring of cancer cells in live mouse bone marrow. *Front. Immunol.* 9, 1681. doi:10.3389/fimmu.2018.01681

Li, L., Jiang, W., Luo, K., Song, H., Wu, Y., Gu, Z., et al. (2013). Superparamagnetic iron oxide nanoparticles as MRI contrast agents for noninvasive stem cell labeling and tracking. *Theranostics* 3 (8), 595–615. doi:10.7150/thno.5366

Maška, M., Daněk, O., Garasa, S., Rouzaut, A., Muñoz-Barrutia, A., and Ortiz-de-Solorzano, C. (2013). Segmentation and shape tracking of whole fluorescent cells based on the chan-vese model. *IEEE Trans. Med. Imaging* 32 (6), 995–1006. doi:10.1109/tmi.2013.2243463

Meyer, K. L., Carvlin, M. J., Mukherji, B., Sloviter, H. A., and Joseph, P. M. (1992). Fluorinated blood substitute retention in the rat measured by fluorine-19 magnetic resonance imaging. *Invest. Radiol.* 27 (8), 620–627. doi:10.1097/00004424-199208000-00012

Nedosekin, D. A., Juratli, M. A., Sarimollaoglu, M., Moore, C. L., Rusch, N. J., Smeltzer, M. S., et al. (2013). Photoacoustic and photothermal detection of circulating tumor cells, bacteria and nanoparticles in cerebrospinal fluid *in vivo* and *ex vivo*. *J. Biophot.* 6 (6-7), 523–533. doi:10.1002/jbio.201200242

Patel, S. K., Williams, J., and Janjic, J. M. (2013). Cell labeling for ^{19}F MRI: New and improved approach to perfluorocarbon nanoemulsion design. *Biosens. (Basel)* 3 (3), 341–359. doi:10.3390/bios3030341

Peng, Q., Li, Y., Bo, S., Yuan, Y., Yang, Z., Chen, S., et al. (2018). Paramagnetic nanoemulsions with unified signals for sensitive ^{19}F MRI cell tracking. *Chem. Commun.* 54 (47), 6000–6003. doi:10.1039/C8CC02938E

Stoll, G., Basse-Lüsebrink, T., Weise, G., and Jakob, P. (2012). Visualization of inflammation using ^{19}F-magnetic resonance imaging and perfluorocarbons. *WIREs. Nanomed. Nanobiotechnol.* 4 (4), 438–447. doi:10.1002/wnan.1168

Sun, N., Lee, A., and Wu, J. C. (2009). Long term noninvasive imaging of embryonic stem cells using reporter genes. *Nat. Protoc.* 4 (8), 1192–1201. doi:10.1038/nprot.2009.100

Tian, C., Yang, C., and Spencer, S. L. (2020). EllipTrack: A global-local cell-tracking pipeline for 2D fluorescence time-lapse microscopy. *Cell Rep.* 32 (5), 107984. doi:10.1016/j.celrep.2020.107984

Wang, Y., Xu, C., and Ow, H. (2013). Commercial nanoparticles for stem cell labeling and tracking. *Theranostics* 3 (8), 544–560. doi:10.7150/thno.5634

Wu, T., Li, A., Chen, K., Peng, X., Zhang, J., Jiang, M., et al. (2021). Perfluoro-tert-butanol: A cornerstone for high performance fluorine-19 magnetic resonance imaging. *Chem. Commun.* 57 (63), 7743–7757. doi:10.1039/d1cc02133h

Wu, T., Chen, K., Jiang, M., Li, A., Peng, X., Chen, S., et al. (2022). Hydrofluorocarbon nanoparticles for ^{19}F MRI-fluorescence dual imaging and chemo-photodynamic therapy. *Org. Biomol. Chem.* 20 (6), 1299–1305. doi:10.1039/d1ob02392f

Würthner, F., Kaiser, T. E., and Saha-Möller, C. R. (2011). J-Aggregates: From serendipitous discovery to supramolecular engineering of functional dye materials. *Angew. Chem. Int. Ed.* 50 (15), 3376–3410. doi:10.1002/anie.201002307

Xia, T., Jiang, H., Li, C., Tian, M., and Zhang, H. (2012). Molecular imaging in tracking tumor stem-like cells. *J. Biomed. Biotechnol.* 2012, 1–13. doi:10.1155/2012/420364

Zhao, X., Ng, W. Y., Lau, K. C., Collis, A. E., and Horváth, I. T. (2012). Generation of (nonafluoro-tert-butoxy)methyl ponytails for enhanced fluorous partition of aromatics and heterocycles. *Phys. Chem. Chem. Phys.* 14 (11), 3909–3914. doi:10.1039/c2cp23113a

frontiers | Frontiers in Bioengineering and Biotechnology

TYPE Original Research
PUBLISHED 24 November 2022
DOI 10.3389/fbioe.2022.1072205

OPEN ACCESS

EDITED BY
Lin Yu,
Fudan University, China

REVIEWED BY
Di Zhu,
Capital Medical University, China
Yun-Long Wu,
Xiamen University, China

*CORRESPONDENCE
Yuqi Zhu,
zhyqi001@163.com
Xu Cui,
cuixuprossor@163.com
Xing Wang,
wangxing@iccas.ac.cn

†These authors have contributed equally to this work

SPECIALTY SECTION
This article was submitted to Biomaterials, a section of the journal Frontiers in Bioengineering and Biotechnology

RECEIVED 17 October 2022
ACCEPTED 07 November 2022
PUBLISHED 24 November 2022

CITATION
Xu X, Chang S, Zhang X, Hou T, Yao H, Zhang S, Zhu Y, Cui X and Wang X (2022), Fabrication of a controlled-release delivery system for relieving sciatica nerve pain using an ultrasound-responsive microcapsule.
Front. Bioeng. Biotechnol. 10:1072205.
doi: 10.3389/fbioe.2022.1072205

Fabrication of a controlled-release delivery system for relieving sciatica nerve pain using an ultrasound-responsive microcapsule

Xiong Xu[1,2,3†], Shuai Chang[4†], Xiaoyi Zhang[3†], Taotao Hou[2], Hui Yao[5], Shusheng Zhang[6], Yuqi Zhu[5]*, Xu Cui[1]* and Xing Wang[3]*

[1]Department of Orthopaedics, The 8th Medical Center of PLA General Hospital, Beijing, China, [2]Department of Graduate, Hebei North University, Zhangjiakou, China, [3]Beijing National Laboratory for Molecular Sciences, Institute of Chemistry, Chinese Academy of Sciences, Beijing, China, [4]Orthopedics Department, Peking University Third Hospital, Beijing, China, [5]Department of Orthopedics, Eye Hospital, China Academy of Chinese Medical Sciences, Beijing, China, [6]ShenYang Tiantai Remote Medical Tech Development Co., Ltd., Shenyang, China

Lidocaine, a potent local anesthetic, is clinically used in nerve block and pain management. However, due to its short half-life, repeated administration is required. For this reason, here we designed and prepared a lidocaine-encapsulated polylactic acid-glycolic acid (Lidocaine@PLGA) microcapsule with ultrasound responsiveness to relieve the sciatica nerve pain. With a premixed membrane emulsification strategy, the fabricated lidocaine-embedded microcapsules possessed uniform particle size, good stability, injectability, and long-term sustained release both *in vitro* and *in vivo*. More importantly, Lidocaine@PLGA microcapsules had the function of ultrasonic responsive release, which made the drug release controllable with the effect of on-off administration. Our research showed that using ultrasound as a trigger switch could promote the rapid release of lidocaine from the microcapsules, achieving the dual effects of long-term sustained release and short-term ultrasound-triggered rapid release, which can enable the application of ultrasound-responsive Lidocaine@PLGA microcapsules to nerve root block and postoperative pain relief.

KEYWORDS

microcapsule, lidocaine, ultrasound responsive, sciatica relief, on-demand administration

Introduction

Lidocaine was first synthesized in the 1940s and was initially used as a local anesthetic and antiarrhythmic treatment (Hermanns et al., 2019). In the 1950s, as research on the molecular mechanism of lidocaine deepened, it was found that lidocaine can not only block sodium ion channels (Gawali et al., 2015) but also has critical effects on hyperpolarization-activated cyclic nucleotide-gated (HCN) channels. A certain inhibitory effect, which changes the conduction of action potentials, had analgesic properties (Zhou et al., 2015; De Cassai et al., 2021; Foo et al., 2021; Lee and Schraag, 2022) and played an important role in pain management (Dunn and Durieux, 2017; Soto et al., 2018). However, due to its poor water solubility and short half-life, the drug effects only last for 2 h, and thus it often requires the repeated administration to obtain satisfactory results to satisfy clinical application (Liu and Lv, 2014). In general, encapsulation of drugs into polymeric carriers has attracted emerging interests in recent years. Scientific teams have designed and developed sustained-release materials including microcapsules, nanoparticles, hydrogels, liposomes, and other sustained-release materials as drug carriers (Ma, 2014; Svirskis et al., 2016; Nagasaki et al., 2017; Butreddy et al., 2021; Escareño et al., 2021; Li et al., 2021; Zeng et al., 2021), and the embedded drugs in the sustained-release materials can provide long-term slow release under mild conditions (Sharma et al., 2018). However, due to differences in degree of pain and the pain tolerance, individualized treatment and on-demand administration are required in practical clinical applications, as the long-term sustained-release function alone also does not meet clinical needs (Suraphan et al., 2020).

Ultrasound-responsive polymeric materials had attracted significant attention for several decades. Compared to other traditional stimulate respondence, such as UV stimulus, thermal stimulus, and pH stimulus, the ultrasound-responsive materials were more applicable because of their efficient drug delivery and targeted treatment *via* non-invasive means. Commonly used ultrasound-responsive biomaterials mainly included micro/nano bubbles/droplets, polymeric micelles, prodrugs, hydrogels, and nanogels (Marin et al., 2001; Rapoport et al., 2011; Huebsch et al., 2014; Hernandez et al., 2017; Shende et al., 2018; Tang et al., 2018; Shende and Jain, 2019; Wei et al., 2020). Various drugs or bioactive molecules can therefore be delivered using these ultrasound-responsive delivery vehicles for a variety of disease therapies (Doukas and Kollias, 2004; Chung et al., 2008; Aryal et al., 2014; Yin et al., 2014; Yamaguchi et al., 2019; Wang et al., 2022).

In this work, we successfully prepared ultrasonic-responsive Lidocaine@PLGA microcapsule formulations by encapsulating insoluble lidocaine drugs inside the microcapsules through premix membrane emulsion (PME) combined with the water in oil in water (W/O/W) double emulsion method (Figure 1). Rational design made the Lidocaine@PLGA microcapsules uniform in particle size, well dispersible, and injectable. In addition, as a non-invasive external mechanical energy, ultrasound can controllably adjust the drug release of drug-loaded microcapsules to achieve on-demand drug delivery (Kost et al., 1989; Sirsi and Borden, 2014; Wallace and Wrenn, 2015; Gao et al., 2018; Chandan et al., 2020; Ben Daya et al., 2021; Yuan et al., 2021; Fan et al., 2022). The polymer PLGA is an important macromolecular organic compound with good biodegradability and biocompatibility, which is widely used in the field of biomedicine. Thanks to their unique encapsulation and globularity, some drugs, proteins, and vaccines can be encapsulated for long-term sustained slow release(Cappellano et al., 2019; Ospina-Villa et al., 2019; Rocha et al., 2022). *In vitro* and *in vivo* experiments confirmed that microcapsules with ultrasound responsiveness can switch drug delivery to become continuously released for more than 10 days, achieving dual effects of long-term sustained release and short-term ultrasound-triggered rapid release, achieving a novel on-demand drug delivery and thereby meeting a range of clinical requirements. The combination of polymer PLGA and ultrasound is a new discovery in medical materials, and it meets the clinical needs of long-term sustained release and short-term rapid release under ultrasonic intervention, which is helpful for deeper exploration and wide application in the field of biomedicine.

Materials and methods

Materials

PLGA (weight: 10,500; lactide/glycolide ratio, 75/25) was purchased from Yuanbohuike Institute of Biotechnology (Beijing, China). Lidocaine was purchased from Sarn Chemical Technology Co., Ltd. (Shanghai, China). Polyvinyl alcohol (PVA) was purchased from Shanghai Aladdin Biochemical Co., Ltd. (Shanghai, China). Dichloromethane was purchased from Concord Technology Co., Ltd. (Tianjin, China). The specification of the dialysis membrane purchased from Solarbio Technology Co., Ltd. (Beijing, China). Rapid membrane emulsification equipment (FMEM-500M) and Shirasu Porous Glass (SPG) membrane were purchased from National Engineering Research Center for Biotechnology. The SPG membranes were annulus cylinders with pore sizes of 7.0 μm. A hand-held ultrasound (Model TT-CC-X convex array) apparatus was purchased from Shenyang Tiantai Telemedicine Technology Development Co., Ltd. (Shenyang, China). A cell-crushing apparatus was purchased from Shanghai Xinzhi Biotechnology Research Institute (Shanghai China). An ultrasonic water bath apparatus was purchased from Kunshan Ultrasonic Instruments Co., Ltd. (Kunshan China). A high-speed centrifuge was purchased from Anhui Jiawen Instrument Equipment Co., Ltd. (Anhui China).

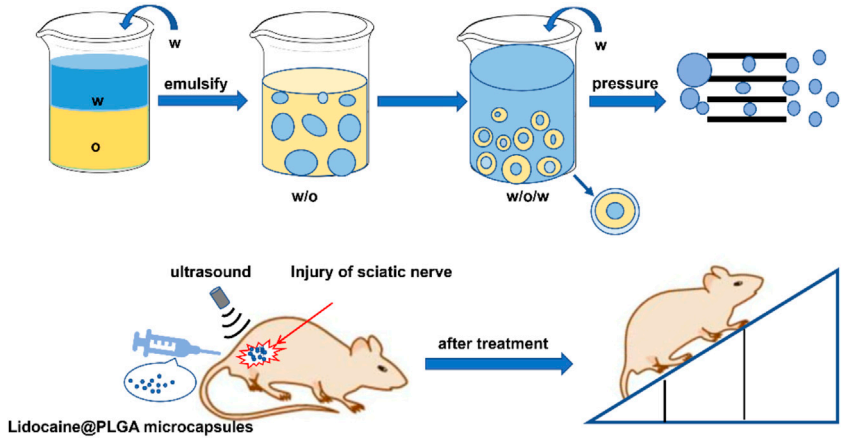

FIGURE 1
Schematic diagram of the preparation of Lidocaine@PLGA microcapsules *via* the PME method and their application in the rat sciatic nerve injury model.

Measurements

The morphology of the microcapsule was observed with scanning electron microscopy (SEM; JSM-6700F, JEOL, Japan) at an accelerating voltage of 5 kV. An aqueous solution of drug-loaded microcapsule particles was adhered to a metal circular table using conductive glue and vacuum-coated with a thin layer of platinum using a sputter coater (EM SCD 500, Leica, GER). Fourier transform infrared (FT-IR) spectra were recorded using the potassium bromide pellet method and an infrared spectrometer (Tensor 27, Bruker, GER). The microcapsule size was measured with dynamic light scattering (DLS, Nano-ZS90, Malvern, U.K.).

Preparation of Lidocaine@PLGA microcapsules

Lidocaine@PLGA microcapsules were prepared using a water-in-oil-in-water (W/O/W) membrane emulsification method. First measure 3 ml of deionized water as the inner water phase. An appropriate amount of 1% PVA aqueous solution was prepared as the outer water phase, and 400 mg of PLGA and 400 mg of lidocaine were dissolved in 8 ml of dichloromethane as the oil phase. The inner water phase was added to the oil phase, and emulsified by ultrasonic (power 200 W) with an ultrasonic cell disruptor to obtain a water-in-oil primary emulsion. The primary emulsion was then poured into 200 g of the outer aqueous phase to form a water-in-oil-in-water pre-reconstituted emulsion. The pre-recombination emulsion was quickly poured into the membrane emulsification device, and the re-emulsion emulsion was pressed through a membrane tube with a pore size of 7.0 μm with a nitrogen pressure of 0.07 MPa, repeated three times until a re-emulsion emulsion with uniform particle size was obtained. After stirring overnight at room temperature to allow the solution to completely evaporate, the solidified microspheres were collected by centrifugation, washed three times with distilled water, and freeze-dried in a liquid nitrogen freeze dryer for 24 h to obtain the targeted Lidocaine@PLGA microcapsules.

Determination of drug loading

A certain weight of Lidocaine@PLGA microcapsules was added into an appropriate amount of dichloromethane to dissolve. Then hydrochloric acid solution was extracted three times, mixed, and diluted into a bottle, and the absorbance was measured at 262.5 nm by UV spectrophotometry. The amount of lidocaine in the solution was calculated as follows.

$$\text{Drug loading}\ (\%) = \frac{\text{lidocaine amount}\ (\text{mg})}{\text{Lidocaine@PLGA microcapsules}\,(\text{mg})} * 100\% \quad (1)$$

In vitro drug release

The suspension of physiological saline and drug-loaded microcapsules was put into a dialysis tube (molecular weight cut-off: 3500), and the lidocaine release behavior of Lidocaine@PLGA microcapsules in the dialysis tube was monitored at 40 r/min in a constant temperature shaker at 37°C. To verify the ultrasound-responsive behavior of drug-loaded microcapsules, we used and compared three

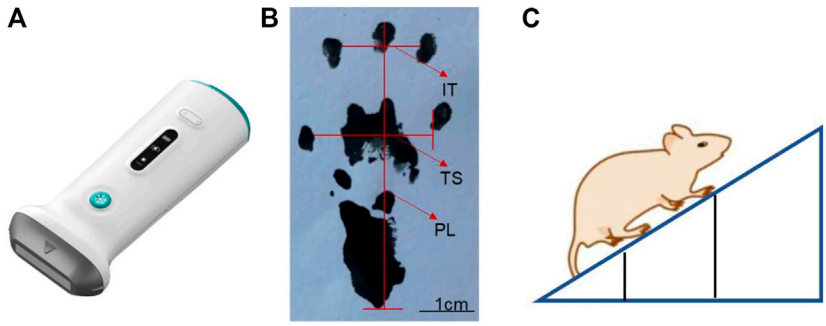

FIGURE 2
Schematic diagram of **(A)** handheld ultrasound instrument, **(B)** sciatic nerve index detection, and **(C)** oblique plate experiment.

instruments: a handheld ultrasound(Figure 2A), a water bath ultrasound, and a cell disruptor. The suspension of normal saline and drug-loaded microcapsules was put into a dialysis tube (molecular weight cut-off: 3500) and exposed to ultrasound instruments for the predetermined duration time. The control group was placed in a thermostatic shaker for 40 r/min without any intervention. At various time intervals, 5 ml solution outside the dialysis membrane was withdrawn and replaced with a freshly mixed solution. The absorbance was brought into the standard curve equation by UV spectrophotometry to calculate the cumulative release percentage, as follows.

$$\text{Cumulative release percentage } (\%) = \frac{V_0 * C_n + V * \sum_{i=1}^{n-1} C}{M * D} * 100\% \quad (2)$$

V_0: Volume of release medium, mL; C_n: Concentration of lidocaine hydrochloride at the *n*th sampling point, mg/mL; V: volume per sample, mL; M: The total mass of the microspheres in the delivery medium, mg; D: Drug loading of microspheres in release medium.

In vitro cytotoxicity assay

L929 cells were seeded in 96-well plates (30,000 cells per well) and cultured at 37°C in a 5% CO_2 for 24 h. Then, the prepared lidocaine microcapsules and blank microcapsules in different aqueous solutions were added to the orifice plate at 10-, 50-, 100-, 150-, and 200-fold dilution concentrations, and the unmedicated group was used as a negative control. After 24 h incubation, cell viability was calculated using cell Counting Kit-8 (CCK-8, Dojindo, Kumamoto, Japan) according to the manufacturer's instructions. Absorbance was read at a wavelength of 450 nm using a microplate reader (Varioskan Flash; Thermo Fisher Scientific, Waltham, MA, United States).

Establishment of animal models

In all, 12 healthy male SD rats aged 6–8 weeks with a body weight between 250 and 300 g were randomly divided into sham surgery group, lidocaine microcapsules group, and lidocaine microcapsules ultrasound group, with 4 in each group. To each, 0.1 ml/100 g of 3% pentobarbital intraperitoneal anesthesia was given; after the anesthesia is satisfactory, the skin was prepared on the back of the left lower extremity. After disinfection, an incision is performed of the skin and the subcutaneous fascia, and hemostatic forceps were used to separate the biceps femoral muscle and the hemimetic muscle until the coarse sciatic nerve was visible; blunt separation and ligation were performed with 4-0 suture at the front 2 mm of the trigeminal branch, in a ligation range is 5 mm and a ligation spacing is 1 mm, with the degree of ligation tightness subject to the twitching of the calf muscles. Physiological saline irrigation and hemostasis of the wound were performed after the operation was completed. The muscles, skin, and surgery area were disinfected in turn with alcohol. Rats in the sham surgery group were only free from the sciatic nerve and were not ligated. The experimental procedure ensured that all rat muscles were sutured with one stitch two skin sutures, and the entire surgical process was completed by the same operator.

Determination of sciatic nerve function index

Ink was dripped on the soles of the feet on both sides of the SD rats, and they were placed in the starting position on the paper runway. The two sides of the runway were covered with cardboard pieces to prompt the rats to run to the end of the runway. The bottom of the runway was covered with white

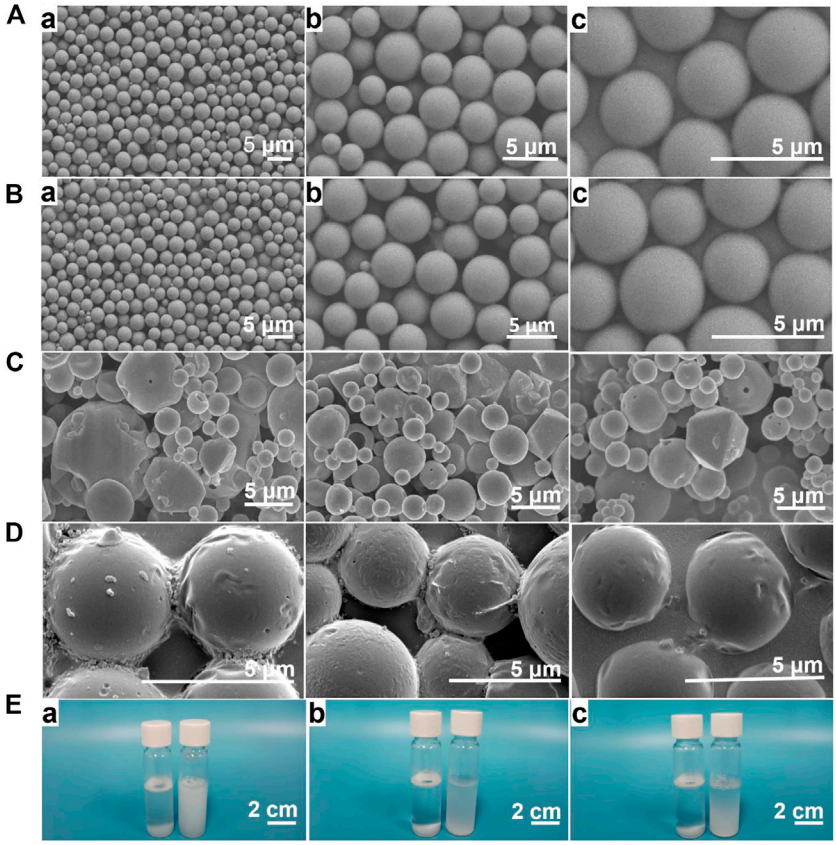

FIGURE 3
(A) PLGA microcapsule prepared with premixed membrane emulsification method. Lidocaine@PLGA microcapsule prepared with **(B)** and without **(C)** premixed membrane emulsification method by electron microscope at (a) 1000x, (b) 3000x, or (c) 5000x. **(D)** The morphology change of Lidocaine@PLGA microcapsule after ultrasound process. **(E)** Optical photographs of 3 mg/ml of Lidocaine@PLGA microcapsule with (right) and without (left) premixed membrane emulsification method in water after standing for (a) 0 h, (b) 6 h, and (c) 12 h.

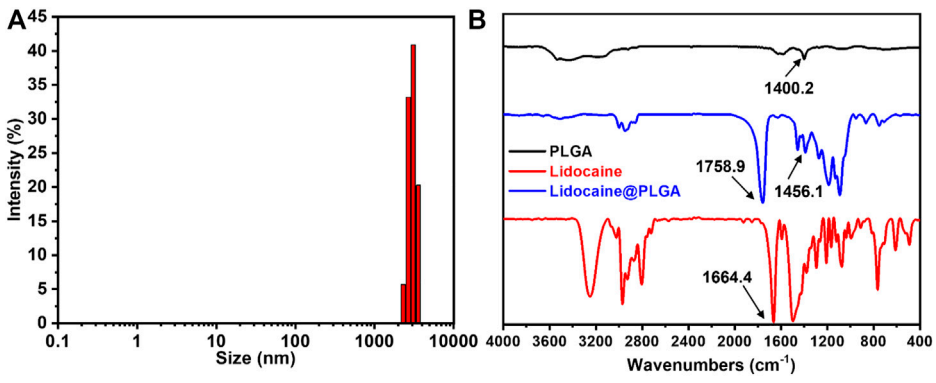

FIGURE 4
(A) DLS profile of the Lidocaine@PLGA microcapsule. **(B)** IR spectra of the drug, PLGA polymer, and the Lidocaine@PLGA microcapsule.

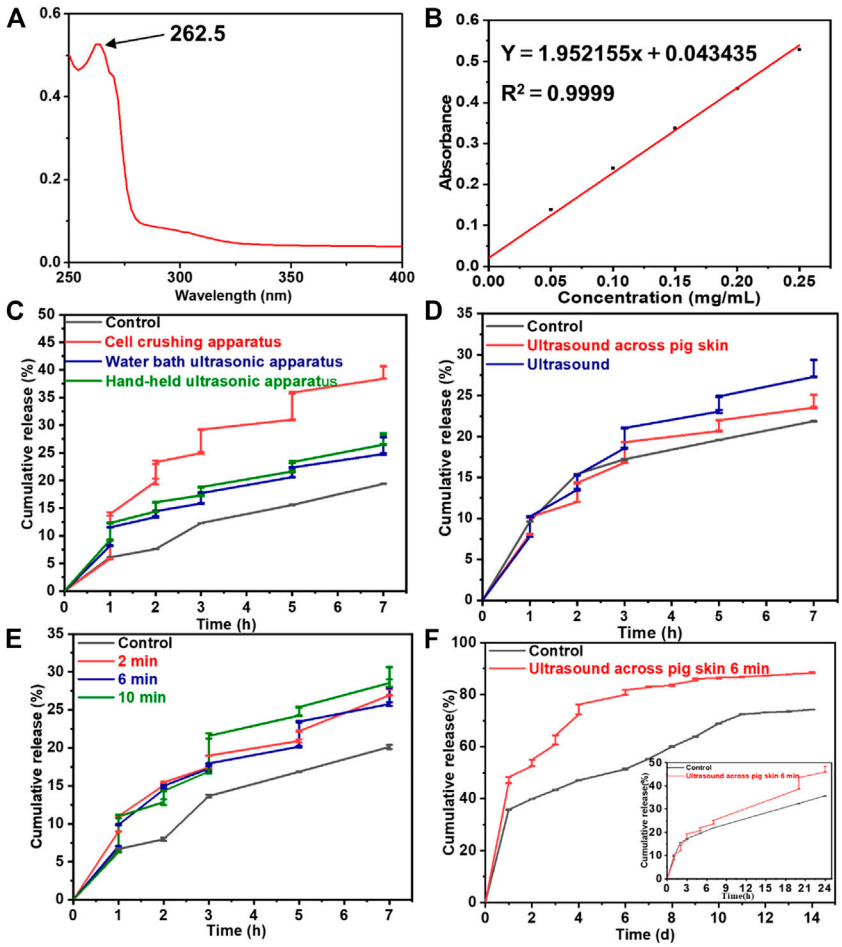

FIGURE 5
(A) The UV-scanning spectrum and **(B)** the standard curve of lidocaine. The drug release behaviors from Lidocaine@PLGA microcapsules with various **(C)** ultrasonic equipment, **(D)** ultrasound across pig skin, **(E)** ultrasonic duration time, and **(F)** cumulative release with each specific ultrasonic duration time of 6 min.

pieces of paper for easy recording of the rat footprints. The length of the runway was optimal for collection of the footprints of the 10 pairs of rats, and the width of the runway was just sufficient to accommodate the rats. The distances of the parts of the rat's footprint were measured at different time points (Figure 2B), and the sciatic nerve function index of rats was evaluated as follows.

$$SFI = 109.5(ETS - NTS)/NTS - 38.3(EPL - NPL)/NPL + 13.3(EIT - NIT)/NIT - 8.8 \quad (3)$$

SFI = 0 indicates normal sciatic nerve function,

SFI = -100 represents complete sciatic nerve injury. Here, experimental foot (E), normal foot (N), print length (PL), toe spread (TS), and intermediate toe spread (IT) are defined.

Inclined plate experiment

The rats were placed on the rectangular cube floor in turn, and after the rat adapted to the surrounding environment, they were close to the rectangular cube head side, and the body axis of the rat was kept perpendicular to the rectangular cube head side. This side was mounted with a lifter, so that it could be slowly raised, and the angle between the three-dimensional box bottom plate and the horizontal surface gradually increased. When the rat was had difficulty remaining attached to the three-dimensional box bottom plate for 5 s and began to slide down, the angle between the three-dimensional box floor and the horizontal surface was recorded (Figure 2C).

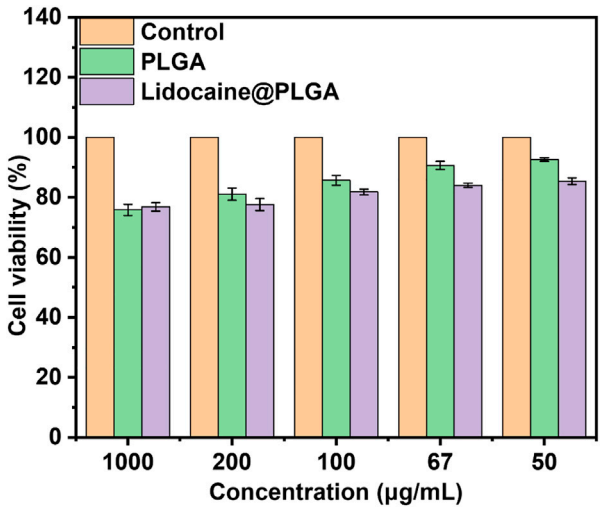

FIGURE 6
In vitro cytotoxicity of PLGA microcapsules with or without lidocaine laden.

Results and discussion

Preparation and characterization of Lidocaine@PLGA microcapsule

Scanning electron microscopy (SEM) showed that PLGA microcapsules and Lidocaine@PLGA microcapsules were spherical, with a regular shape and smooth surface (Figures 3A,3B), with no significant difference. By contrast, the prepared Lidocaine@PLGA microcapsules without premixed membrane emulsification method exhibited heterogeneous, unsystematic, and even disorderly morphologies and rough surface (Figure 3C). Then, we further observed the effect of the ultrasound on the microcapsules after a hiatus of 2 weeks and found that the surface was gradually changed from the smooth to the rough along the occurrence of some fold structures in Figure 3D, which indicated ultrasound-responsive drug release behavior from the Lidocaine@PLGA microcapsule. The obtained microcapsules with uniform particle size of ca. 3 μm were uniformly dispersed, and good suspension stability was seen under different magnifications. Relative to the traditional solvent evaporation method, the Lidocaine@PLGA microcapsule prepared by the membrane emulsification method can be evenly distributed in solutions even after standing for 12 h, which is beneficial for clinical application (Figure 3E).

The diameter of the Lidocaine@PLGA microcapsule was further measured using the DLS result, which exhibited a similar size to that seen in Figure 4A. The infrared spectrum results suggest the appearance of certain typical characteristic peaks of PLGA polymer and lidocaine. More importantly, some characteristic shift peaks were seen from 1400.2 cm^{-1} to 1456.1 cm^{-1} and from 1664.4 cm^{-1} to 1758.9 cm^{-1} (Figure 4B), which indicated a physical interaction between the two substances and lidocaine within the lidocaine microcapsules, powerfully revealing that the lidocaine was successfully encapsulated into the microcapsules, rather than being the result of a simple physical mixing.

The drug loading ratio of the Lidocaine@PLGA microcapsule was calculated as 15.5%. We investigated the ultrasound-responsive drug release of Lidocaine@PLGA microcapsules with a handheld ultrasound, a water bath ultrasound, and a cell rupture device, and we compared them with a blank control group. The UV-scanning spectrum and standard curve of Lidocaine are displayed in Figures 5A,5B, exhibiting the absorbance was at 262.5 nm by UV spectrophotometry. As shown in Figure 5C, Lidocaine@PLGA microcapsules were performed for continuous ultrasound of 6 min at 1, 2, 3, 5, and 7 h, respectively. After 7 h, the cumulative drug release rates of the blank control group, the handheld ultrasound group, the water bath ultrasound group, and the cell crushing apparatus group were calculated to 19.4%,

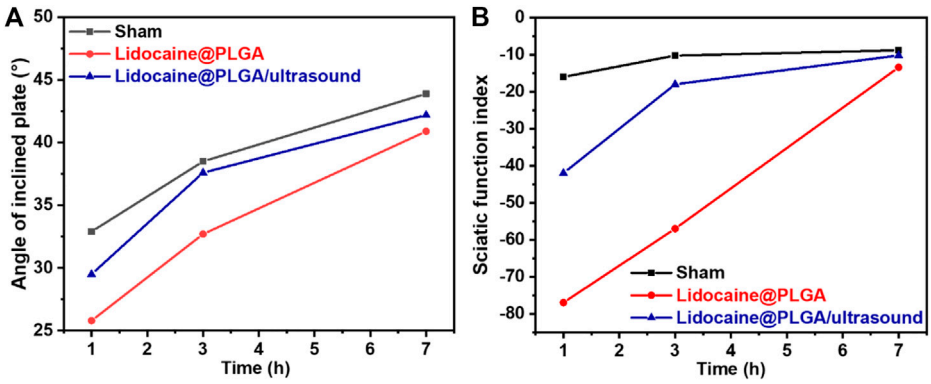

FIGURE 7
SD rats were tested for **(A)** sciatic nerve function index and **(B)** inclined plate experimental parameters after treatment at different times.

28.4%, 27.8%, and 40.7%, respectively. Moreover, the step-like release curve appears during the ultrasound stimulation process, indicating that the Lidocaine@PLGA microcapsules had good ultrasonic stimulation response according to these three ultrasound instruments. However, considering the facile manipulation, simple daily application, and ultrasound-responsive effects, we selected the feasible handheld ultrasound form Shenyang Tiantai Telemedicine Technology Development Co., Ltd. for the following ultrasound-responsive experiments, indicating that this kind of novel handheld ultrasonic instrument could have a broader application prospect in the clinic.

To verify whether the Lidocaine@PLGA microcapsules were responsive to handheld ultrasound when applied *in vivo* with skin barrier, we simulated a skin barrier by covering the surface of the handheld ultrasonic probe with a fresh pig skin. The results in Figure 5D showed that after the cumulative release of drugs in the pigskin ultrasound group after 7 h, the direct ultrasound group and the blank control group showed values of 25.1%, 29.3%, and 21.9%, respectively, which confirmed the simulated skin barrier conditions Lidocaine@PLGA microcapsules could be responsive to handheld ultrasound. To further increase the duration time of ultrasound on the drug release of Lidocaine@PLGA microcapsules, we covered the surface of the ultrasound probe with a layer of fresh pig skin and performed continuous ultrasound at the corresponding time points for 2 min, 6 min, and 10 min, respectively. The results in Figure 5E showed that the longer the period that the ultrasound time could cause the more obvious the stimulation response of the Lidocaine@PLGA microcapsules. Because long ultrasound times can damage the surrounding tissues and it was difficult to ensure a sufficiently long ultrasound time for a single treatment during clinical application, we selected 6 min as the optimal ultrasound duration time. Finally, we studied the long-term effects of handheld ultrasonography on Lidocaine@PLGA microcapsules under simulated skin barrier conditions, and the results showed that the ultrasound group and the control group had a burst release period in the first 20 h, with a cumulative release rate of 43.6% and 32.3%, respectively. Then these two curves gradually entered a slow-release period with gentle cumulative release behaviors. Figure 5F showed that cumulative release curve of ultrasound group at day 9 tended to flat with a high cumulative release rate of 86.2%, while the control group lasted until 11 days with a cumulative release rate of 72.4%. These *in vitro* experiments verified that Lidocaine@PLGA microcapsules with intermittent handheld ultrasound of 6 min under simulated skin conditions were still efficient for performing the ultrasound-responsive drug release, which could meet the dual needs of clinical long-term sustained release and/or temporary "on-off" control release.

Cell viability and proliferation

Cytotoxicity was tested for the viability of different concentrations of Lidocaine@PLGA microcapsules co-incubated with L-929 cells for 24 h. Compared with the control group, the cell viability of the blank microcapsule group and the Lidocaine@PLGA microcapsules group reached 90.6% and 84.1% at the concentration of 67 μg/ml, respectively; at the concentration of 50 μg/ml, the cell viability of the blank microcapsule group and Lidocaine@PLGA microcapsules was 92.6% and 85.4% respectively, indicating that the drug-loaded microspheres had good biocompatibility, safety, and non-toxicity in solution. As the concentration increased, the cell viability of the blank microcapsule group and that of the Lidocaine@PLGA microcapsule group were gradually decreased to 81.1% and 77.7%, respectively, at a concentration of 200 μg/ml. However, further increase of the concentration into 1000 μg/ml, the cell viability could still maintain the 75.8% and 76.9%, respectively, as shown in Figure 6. The drug-loaded microcapsule group had similar biocompatibility to the blank microcapsule group, which not only suggested that the drug had good stability in the microcapsule but also demonstrated that a drug-loaded microcapsule with good biocompatibility can be expected for the treatment of sciatica, even in areas that require higher drug concentrations.

Therapeutic effect of animal models

Each rat in the Lidocaine@PLGA group and Lidocaine@PLGA/ultrasound group was percutaneously injected into the sciatic nerve with 0.2 ml aqueous solution (equivalent to 1% lidocaine 6 mg), and the sciatic nerve function index measurement and oblique plate experiment were measured after injection for 1, 3, and 7 h, wherein Lidocaine@PLGA/ultrasound group was exposed to a 6 min of ultrasound intervention before each measurement. As shown in Figure 7, the sham group underwent measurements of sciatic nerve index and inclined plate experiments at the same time point. The results showed that at 1 or 3 h after the injection of Lidocaine@PLGA microcapsule, the sciatic nerve function index and inclined plate angle of rats after ultrasound intervention were significantly better than those of rats without ultrasound intervention, and the sciatic nerve function index and oblique plate angle of rats in the non-ultrasound intervention group were close to those in the ultrasound intervention group at 7 h. This may be because the earlier ultrasound had made a lot of lidocaine release from the microcapsules, and thus, the released drug concentration was not enough in the sciatic nerve in the late stage compared to that of the sustainable slow release of Lidocaine@PLGA microcapsule. In this case, the total drug concentration remained roughly the same after 7 h between these two groups. In other words, in the ultrasound intervention group, some of the remaining microcapsules underwent ultrasound intervention at 1 and 3 h, and the drug in the microcapsules within the 7 h may have been lower than that of the non-ultrasound intervention group. Likewise, the amount of drug release was lower than that of the non-ultrasound intervention group, producing the ultrasound intervention group and the rat-inclined plate experiment and sciatic nerve index results of the non-

ultrasound intervention group. The sciatic nerve index of Lidocaine@PLGA/ultrasound group rats rose from −42 to −10.17 at 1 h and from 29.5 to 42.2 in the inclined plate experiment within 7 h after administration. In the Lidocaine@PLGA group, the sciatic nerve index increased from −77 to −13.4 within 7 h and the slanted plate experiment rose from 25.8 to 40.9. As for the sham group, the sciatic nerve index increased from −16 to −8.8 and the angle of the inclined plate increased from 32.9 to 43.9. It was noted that the rats in the sham group also showed sciatic nerve damage, which may be because in the early stage of the experiment, the rats did not adapt to the test environment and could not walk according to the usual gait, and some rats even appeared to jump and walk, thus resulting in incomplete footprints and errors in data collection.

Conclusion

We developed an ultrasound-responsive Lidocaine@PLGA microcapsule by using a premixed membrane emulsification method. After optimization of ultrasound instrument and duration time, the Lidocaine@PLGA microcapsule can achieve a stimulus response even under simulated skin conditions. In addition, the *in vivo* results also showed that the Lidocaine@PLGA microcapsules could perform rapid ultrasound-responsive drug release and relieve the sciatica nerve pain under the rat model of sciatica. Importantly, the ultrasound-responsive drug release not only provided more chances for the rapidly increasing local drug concentration under ultrasonic conditions but also ensured long-term sustained release without outside intervention, demonstrating a true on-demand administration of drugs, which made up for the short-term control of the release rate of the sustained-release microcapsules in clinical applications. Using ultrasound as the trigger switch of the Lidocaine@PLGA microcapsule, the drug release of microcapsule can be feasibly adjusted, and the individualized diagnosis and treatment plan can be adopted according to the specific situation in clinical application.

Data availability statement

The raw data supporting the conclusion of this article will be made available by the authors, without undue reservation.

Ethics statement

The animal study was reviewed and approved by animal ethics committee of the 8th Medical Center of Chinese PLA General Hospital.

Author contributions

YZ, XC, and XW initiated the project. XX, SC, XZ, and SZ searched the data base, wrote, and finalized the manuscript. TH, SZ, HY, and XW made important suggestions and helped revising the paper. All authors reviewed and commented on the entire manuscript.

Funding

This work was supported by the National Natural Science Foundation of China (51973226 and 8197090038), the Youth Innovation Promotion Association CAS (2019031), and the Military Medical Science and Technology Youth Training Program (20QNPY118).

Conflict of interest

SZ was employed by the company ShenYang Tiantai Remote Medical Tech Development Co., Ltd.

The remaining authors declare that the research was conducted in the absence of any commercial or financial relationships that could be construed as a potential conflict of interest.

Publisher's note

All claims expressed in this article are solely those of the authors and do not necessarily represent those of their affiliated organizations, or those of the publisher, the editors, and the reviewers. Any product that may be evaluated in this article, or claim that may be made by its manufacturer, is not guaranteed or endorsed by the publisher.

References

Aryal, M., Arvanitis, C. D., Alexander, P. M., and McDannold, N. (2014). Ultrasoundmediated blood-brain barrier disruption for targeted drug delivery in the central nervous system. *Adv. Drug Deliv. Rev.* 72, 94–109. doi:10.1016/j.addr.2014.01.008

Ben Daya, S. M., Paul, V., Awad, N. S., Al Sawaftah, N. M., Al Sayah, M. H., and Husseini, G. A. (2021). Targeting breast cancer using hyaluronic acid-conjugated liposomes triggered with ultrasound. *J. Biomed. Nanotechnol.* 17 (1), 90–99. doi:10.1166/jbn.2021.3012

Butreddy, A., Gaddam, R. P., Kommineni, N., Dudhipala, N., and Voshavar, C. (2021). PLGA/PLA-Based long-acting injectable depot microspheres in clinical use: Production and characterization overview for protein/peptide delivery. *Int. J. Mol. Sci.* 22 (16), 8884. doi:10.3390/ijms22168884

Cappellano, G., Comi, C., Chiocchetti, A., and Dianzani, U. (2019). Exploiting PLGA-based biocompatible nanoparticles for next-generation tolerogenic vaccines against autoimmune disease. *Int. J. Mol. Sci.* 20 (1), 204. doi:10.3390/ijms20010204

Chandan, R. S., Mehta, S., and Banerjee, R. (2020). Ultrasound-responsive carriers for therapeutic applications. *ACS Biomater. Sci. Eng.* 6 (9), 4731–4747. doi:10.1021/acsbiomaterials.9b01979

Chung, T. W., Wang, S. S., and Tsai, W. J. (2008). Accelerating thrombolysis with chitosan-coated plasminogen activators encapsulated in poly-(lactide-co-glycolide) (PLGA) nanoparticles. *Biomaterials* 29 (2), 228–237. doi:10.1016/j.biomaterials.2007.09.027

De Cassai, A., Bonanno, C., Padrini, R., Geraldini, F., Boscolo, A., Navalesi, P., et al. (2021). Pharmacokinetics of lidocaine after bilateral ESP block. *Reg. Anesth. Pain Med.* 46 (1), 86–89. doi:10.1136/rapm-2020-101718

Doukas, A. G., and Kollias, N. (2004). Transdermal drug delivery with a pressure wave. *Adv. Drug Deliv. Rev.* 56 (5), 559–579. doi:10.1016/j.addr.2003.10.031

Dunn, L. K., and Durieux, M. E. (2017). Perioperative use of intravenous lidocaine. *Anesthesiology* 126 (4), 729–737. doi:10.1097/aln.0000000000001527

Escareño, N., Hassan, N., Kogan, M. J., Juarez, J., Topete, A., and Daneri-Navarro, A. (2021). Microfluidics-assisted conjugation of chitosan-coated polymeric nanoparticles with antibodies: Significance in drug release, uptake, and cytotoxicity in breast cancer cells. *J. Colloid Interface Sci.* 591, 440–450. doi:10.1016/j.jcis.2021.02.031

Fan, C. H., Ho, Y. J., Lin, C. W., Wu, N., Chiang, P. H., and Yeh, C. K. (2022). State-of-the-art of ultrasound-triggered drug delivery from ultrasound-responsive drug carriers. *Expert Opin. Drug Deliv.* 19 (8), 997–1009. doi:10.1080/17425247.2022.2110585

Foo, I., Macfarlane, A. J. R., Srivastava, D., Bhaskar, A., Barker, H., Knaggs, R., et al. (2021). The use of intravenous lidocaine for postoperative pain and recovery: International consensus statement on efficacy and safety. *Anaesthesia* 76 (2), 238–250. doi:10.1111/anae.15270

Gao, X., Nan, Y., Yuan, Y., Gong, X., Sun, Y., Zhou, H., et al. (2018). Gas-filled ultrasound microbubbles enhance the immunoactivity of the HSP70-MAGEA1 fusion protein against MAGEA1-expressing tumours. *Mol. Med. Rep.* 18 (1), 315–321. doi:10.3892/mmr.2018.9003

Gawali, V. S., Lukacs, P., Cervenka, R., Koenig, X., Rubi, L., Hilber, K., et al. (2015). Mechanism of modification, by lidocaine, of fast and slow recovery from inactivation of voltage-gated Na^+ channels. *Mol. Pharmacol.* 88 (5), 866–879. doi:10.1124/mol.115.099580

Hermanns, H., Hollmann, M. W., Stevens, M. F., Lirk, P., Brandenburger, T., Piegeler, T., et al. (2019). Molecular mechanisms of action of systemic lidocaine in acute and chronic pain: A narrative review. *Br. J. Anaesth.* 123 (3), 335–349. doi:10.1016/j.bja.2019.06.014

Hernandez, C., Gulati, S., Fioravanti, G., Stewart, P. L., and Exner, A. A. (2017). Cryo-EM visualization of lipid and polymer-stabilized perfluorocarbon gas nanobubbles - a step towards nanobubble mediated drug delivery. *Sci. Rep.* 7, 13517. doi:10.1038/s41598-017-13741-1

Huebsch, N., Kearney, C. J., Zhao, X., Kim, J., Cezar, C. A., Suo, Z., et al. (2014). Ultrasound-triggered disruption and self-healing of reversibly cross-linked hydrogels for drug delivery and enhanced chemotherapy. *Proc. Natl. Acad. Sci. U. S. A.* 111 (27), 9762–9767. doi:10.1073/pnas.1405469111

Kost, J. K., Leong, K., and Langer, R. (1989). Ultrasound-enhanced polymer degradation and release of incorporated substances. *Proc. Natl. Acad. Sci. U. S. A.* 86 (20), 7663–7666. doi:10.1073/pnas.86.20.7663

Lee, I. W., and Schraag, S. (2022). The use of intravenous lidocaine in perioperative medicine: Anaesthetic, analgesic and immune-modulatory aspects. *J. Clin. Med.* 11 (12), 3543. doi:10.3390/jcm11123543

Li, Y., Zhao, E., Li, L., Bai, L., and Zhang, W. (2021). Facile design of lidocaine-loaded polymeric hydrogel to persuade effects of local anesthesia drug delivery system: Complete *in vitro* and *in vivo* toxicity analyses. *Drug Deliv. (Lond).* 28 (1), 1080–1092. doi:10.1080/10717544.2021.1931558

Liu, J., and Lv, X. (2014). The pharmacokinetics and pharmacodynamics of lidocaine- loaded biodegradable poly(lactic-co-glycolic acid) microspheres. *Int. J. Mol. Sci.* 15 (10), 17469–17477. doi:10.3390/ijms151017469

Ma, G. (2014). Microencapsulation of protein drugs for drug delivery: Strategy, preparation, and applications. *J. Control. Release* 193, 324–340. doi:10.1016/j.jconrel.2014.09.003

Marin, A., Muniruzzaman, M., and Rapoport, N. (2001). Acoustic activation of drug delivery from polymeric micelles: Effect of pulsed ultrasound. *J. Control. Release* 71 (3), 239–249. doi:10.1016/s0168-3659(01)00216-4

Nagasaki, Y., Mizukoshi, Y., Gao, Z., Feliciano, C. P., Chang, K., Sekiyama, H., et al. (2017). Development of a local anesthetic lidocaine-loaded redox-active injectable gel for postoperative pain management. *Acta Biomater.* 57, 127–135. doi:10.1016/j.actbio.2017.04.031

Ospina-Villa, J. D., Gomez-Hoyos, C., Zuluaga-Gallego, R., and Triana-Chavez, O. (2019). Encapsulation of proteins from Leishmania panamensis into PLGA particles by a single emulsion-solvent evaporation method. *J. Microbiol. Methods* 162, 1–7. doi:10.1016/j.mimet.2019.05.004

Rapoport, N., Nam, K. H., Gupta, R., Gao, Z., Mohan, P., Payne, A., et al. (2011). Ultrasound-mediated tumor imaging and nanotherapy using drug loaded, block copolymer stabilized perfluorocarbon nanoemulsions. *J. Control. Release* 153 (1), 4–15. doi:10.1016/j.jconrel.2011.01.022

Rocha, C. V., Goncalves, V., da Silva, M. C., Banobre-Lopez, M., and Gallo, J. (2022). PLGA-based composites for various biomedical applications. *Int. J. Mol. Sci.* 23 (4), 2034. doi:10.3390/ijms23042034

Sharma, M., Chandramouli, K., Curley, L., Pontre, B., Reilly, K., Munro, J., et al. (2018). *In vitro* and *ex vivo* characterisation of an *in situ* gelling formulation for sustained lidocaine release with potential use following knee arthroplasty. *Drug Deliv. Transl. Res.* 8 (3), 820–829. doi:10.1007/s13346-018-0492-x

Shende, P., and Jain, S. (2019). Polymeric nanodroplets: An emerging trend in gaseous delivery system. *J. Drug Target.* 27 (10), 1035–1045. doi:10.1080/1061186x.2019.1588281

Shende, P. K., Desai, D., and Gaud, R. S. (2018). Role of solid-gas interface of nanobubbles for therapeutic applications. *Crit. Rev. Ther. Drug Carr. Syst.* 35 (5), 469–494. doi:10.1615/critrevtherdrugcarriersyst.2018020229

Sirsi, S. R., and Borden, M. A. (2014). State-of-the-art materials for ultrasound-triggered drug delivery. *Adv. Drug Deliv. Rev.* 72, 3–14. doi:10.1016/j.addr.2013.12.010

Soto, G., Naranjo Gonzalez, M., and Calero, F. (2018). Intravenous lidocaine infusion. *Rev. Espanola Anestesiol. Reanim.* 65 (5), 269–274. doi:10.1016/j.redare.2018.01.015

Suraphan, N., Fan, L., Liu, B., and Wu, D. (2020). Co-delivery of chlorantraniliprole and avermectin with a polylactide microcapsule formulation. *RSC Adv.* 10 (43), 25418–25425. doi:10.1039/d0ra03825c

Svirskis, D., Chandramouli, K., Bhusal, P., Wu, Z., Alphonso, J., Chow, J., et al. (2016). Injectable thermosensitive gelling delivery system for the sustained release of lidocaine. *Ther. Deliv.* 7 (6), 359–368. doi:10.4155/tde-2016-0014

Tang, W., Yang, Z., Wang, S., Wang, Z., Song, J., Yu, G., et al. (2018). Organic semiconducting photoacoustic nanodroplets for laseractivatable ultrasound imaging and combinational cancer therapy. *ACS Nano* 12 (3), 2610–2622. doi:10.1021/acsnano.7b08628

Wallace, N., and Wrenn, S. (2015). Ultrasound triggered drug delivery with liposomal nested microbubbles. *Ultrasonics* 63, 31–38. doi:10.1016/j.ultras.2015.06.006

Wang, H. F., Xu, S., Fan, D., Geng, X., Zhi, G., Wu, D., et al. (2022). Multifunctional microcapsules: A theranostic agent for US/MR/PAT multi-modality imaging and synergistic chemo-photothermal osteosarcoma therapy. *Bioact. Mat.* 7, 453–465. doi:10.1016/j.bioactmat.2021.05.004

Wei, P., Sun, M., Yang, B., Xiao, J., and Du, J. (2020). Ultrasound-responsive polymersomes capable of endosomal escape for efficient cancer therapy. *J. Control. Release* 322, 81–94. doi:10.1016/j.jconrel.2020.03.013

Yamaguchi, S., Higashi, K., Azuma, T., and Okamoto, A. (2019). Supramolecular polymeric hydrogels for ultrasound-guided protein release. *Biotechnol. J.* 14 (5), 1800530. doi:10.1002/biot.201800530

Yin, T., Wang, P., Li, J., Wang, Y., Zheng, B., Zheng, R., et al. (2014). Tumorpenetrating codelivery of siRNA and paclitaxel with ultrasoundresponsive nanobubbles hetero-assembled from polymeric micelles and liposomes. *Biomaterials* 35 (22), 5932–5943. doi:10.1016/j.biomaterials.2014.03.072

Yuan, F. Z., Wang, H. F., Guan, J., Fu, J. N., Yang, M., Zhang, J. Y., et al. (2021). Fabrication of injectable chitosan-chondroitin sulfate hydrogel embedding kartogenin-loaded microspheres as an ultrasound-triggered drug delivery system for cartilage tissue engineering. *Pharmaceutics* 13 (9), 1487. doi:10.3390/pharmaceutics13091487

Zeng, W., Hui, H., Liu, Z., Chang, Z., Wang, M., He, B., et al. (2021). TPP ionically cross-linked chitosan/PLGA microspheres for the delivery of NGF for peripheral nerve system repair. *Carbohydr. Polym.* 258, 117684. doi:10.1016/j.carbpol.2021.117684

Zhou, C., Ke, B., Zhao, Y., Liang, P., Liao, D., Li, T., et al. (2015). Hyperpolarization-activated cyclic nucleotide-gated channels may contribute to regional anesthetic effects of lidocaine. *Anesthesiology* 122 (3), 606–618. doi:10.1097/aln.0000000000000557

frontiers | Frontiers in Bioengineering and Biotechnology

TYPE Mini Review
PUBLISHED 06 January 2023
DOI 10.3389/fbioe.2022.1126774

OPEN ACCESS

EDITED BY
Hongzhong Chen,
Sun Yat-sen University, China

REVIEWED BY
Dongdong Wang,
University of Science and Technology of China, China
Fu JiaJun,
Nanjing University of Science and Technology, China

*CORRESPONDENCE
Seyed Morteza Naghib,
Naghib@iust.ac.ir
Wei Zhang,
wei.zhang@dlut.edu.cn

SPECIALTY SECTION
This article was submitted to Biomaterials, a section of the journal Frontiers in Bioengineering and Biotechnology

RECEIVED 18 December 2022
ACCEPTED 22 December 2022
PUBLISHED 06 January 2023

CITATION
Garshasbi H, Salehi S, Naghib SM, Ghorbanzadeh S and Zhang W (2023), Stimuli-responsive injectable chitosan-based hydrogels for controlled drug delivery systems.
Front. Bioeng. Biotechnol. 10:1126774.
doi: 10.3389/fbioe.2022.1126774

Stimuli-responsive injectable chitosan-based hydrogels for controlled drug delivery systems

Hamidreza Garshasbi[1], Saba Salehi[1], Seyed Morteza Naghib[1]*, Sadegh Ghorbanzadeh[2] and Wei Zhang[2]*

[1]Nanotechnology Department, School of Advanced Technologies, Iran University of Science and Technology and Biomaterials and Tissue Engineering Department, Breast Cancer Research Center, Motamed Cancer Institute, Iran University of Science and Technology (IUST), The Academic Center for Education, Culture and Research (ACECR), Tehran, Iran, [2]State Key Laboratory of Structure Analysis for Industrial Equipment, Department of Engineering Mechanics, Dalian University of Technology, Dalian, China

In the last decade, injectable hydrogels have attracted a lot of attention due to their excellent functional properties in the field of drug delivery for precise, non-invasive and focused tissue locations. Therefore, designing drug delivery systems (DDS) responsive to hydrogel stimuli to release a drug to an external stimulus with various advantages, can be very challenging. Due to their biocompatibility, mucosal adhesion, and hemostatic activity, chitosan (Chitosan)-based hydrogels offer a lot of potential for tissue engineering and drug delivery. It can be difficult to manage the structure of these stimuli-responsive CS hydrogels or they may require additional crosslinking agents, such as hydrogels with dual pH and thermo-responsiveness. Therefore, it is crucial to create these hydrogels for medicinal applications.

KEYWORDS

injectable, hydrogels, chitosan, stimuli-responsive, pH

1 Introduction

Potential delivery methods for controlled release of bioactive substances include injectable polymer hydrogels. Numerous stimuli, including pH, temperature, light, enzymes, and magnetic fields, can cause these polymers' sol-to-gel transitions in aqueous solutions to change. At room temperature, the low-viscous polymer solution may be conveniently combined with therapeutic agents, such as chemotherapeutics, protein medicines, or cells. Through the use of a syringe or catheter, therapeutic agent-containing solutions may be easily injected into the desired locations (Thambi et al., 2016).

Researchers have focused on developing the optimum drug delivery system (DDS) that can adapt to various physiological needs, such as liposomes, microspheres, nanoparticles, polymeric micelles, and hydrogels. The most prevalent form of responsive nano-system for cancer medication delivery is one that responds to pH variations, owing to the fact that tumors have extracellular pH values that are lower than those of healthy tissues and the circulation (pH = 7.4) (Andrade et al., 2021). More crucially, injectable hydrogels with mucoadhesive qualities may be tailored to a particular region because they attach to a specific spot in the mucosa. This prevents medication diffusion, which may significantly increase treatment efficacy and lessen adverse effects (Liang et al., 2019).

Chitosan (CS) is a polysaccharide identified as suitable for drug/gene delivery depots (Andrade et al., 2021). Due to its advantageous characteristics, including non-toxicity and biodegradability, it has been widely formed into various hydrogels for the administration of ophthalmic drugs. It is the second most prevalent natural polysaccharide after cellulose. (Lin et al., 2019). CS is generally prepared by partial deacetylation of chitin, which is found in the

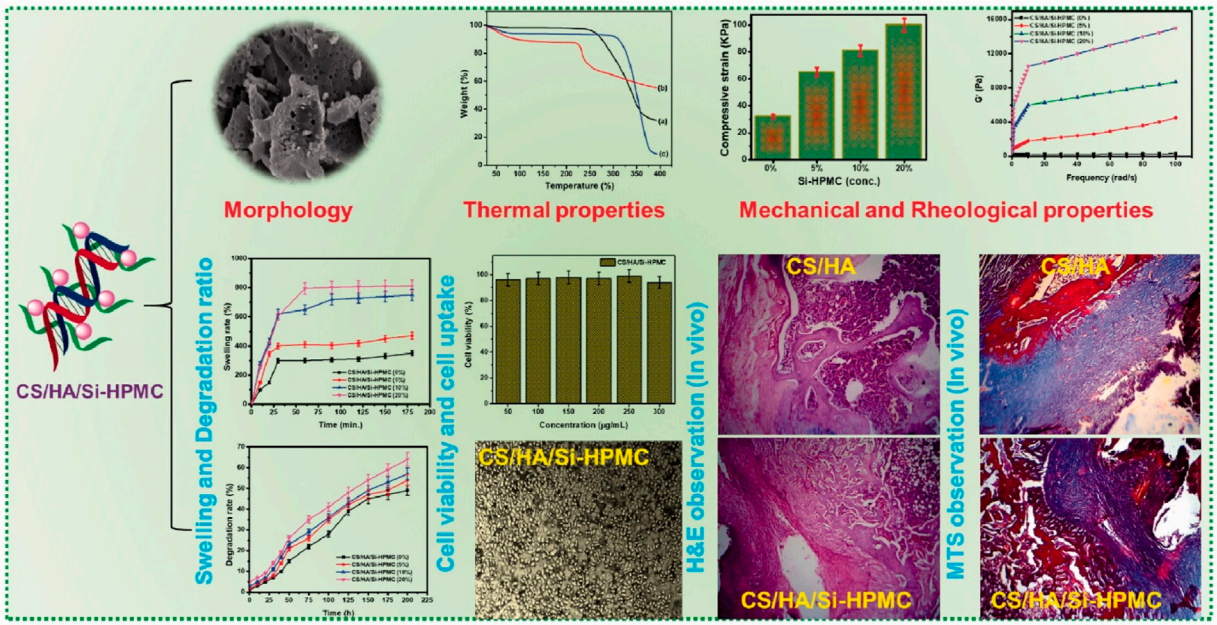

FIGURE 1
Schematic representation of the synthesis process of Si-HPMC incorporated CS/HA injectable hydrogel. The regeneration rate of the CS/HA/Si-HPMC (3%) was almost 79.5% at 21 days for long retention periods, demonstrating relatively good *in vivo* bone regeneration (Hu et al., 2021) (Open access).

exoskeletons of arthropods, such as crabs, shrimps, and lobsters. It has been researched in mucoadhesive delivery because its cationic character shows mucoadhesive qualities. CS hydrogels are formed by connecting hydrophilic polymer chains. Injectable CS hydrogels have lately been used to transport medications as well as produce bone, cartilage, and nerve tissue (Thambi et al., 2016).

2 Cartilage healing

An injectable carboxymethyl chitosan-oxidized chondroitin sulfate hydrogel (CMC-OCS) hydrogel containing microspheres (MPs) was made using the Schiff base crosslinking procedure. The kartogenin (KGN) loaded poly (lactide-co-glycolic acid) MPs (MPs/KGN) were made using the PME method. *In vitro*, the obtained CMC-OCS/MPs/KGN showed slower weight loss and a shorter gelation time than control hydrogels. The hydrogel/MPs' compressive elastic modulus was greatly enhanced, which is good for cartilage healing. While waiting, the PLGA MPs/KGN might release KGN in regulated bursts in response to ultrasound. *In vitro* rabbit bone marrow mesenchymal stem cells (rBMMSCs) sown in the scaffolds demonstrated noticeably enhanced vitality throughout a 7–10-day culture (Yuan et al., 2021).

A novel injectable hydrogel composite made of water-soluble CS/HA and silanized hydroxypropyl methylcellulose (Si-HPMC) was created for cartilage tissue creation (Figure 1). Si-HPMC was uniformly distributed all across CS/HA hydrogel system and had good impact on the mechanical properties by stabilizing the hydrogel network, and lowering weight loss at the expense of quickening the gelation process and enhancing the swelling ratio. The addition of SiHPMC (3.0%) in the CS/HA hydrogel had an effect on the surface characteristics and pore size of the composite scaffolds. The physicochemical characteristics of the hydrogel network, including its shape, surface properties, swelling rate, degradation behavior, and mechanical, rheological, and compressive capabilities, may be controlled by varying the weight ratio and concentration of the CS/HA hydrogel and Si-HPMC. Additionally, L929 cells were active and successfully multiplied on the CS/HA/Si-HPMC hydrogel throughout the *in vitro* cell culture period. One of the vital components of cartilage, HA, may be the result of this biocompatibility. In fact, when seeded in the composite CS/HA/SiHPMC hydrogels, the *in vitro* chondrocyte survival up to 21 days of culture is much higher. These results demonstrate that the CS/HA/Si-HPMC hydrogels, especially the one containing 3% (w/v) Si-HPMC, exhibited the best overall properties for use in bone regeneration. When coupled with chondrocytes in subcutaneous or nude mice, CS/HA/Si-HPMC hydrogels have been shown to be useful for cartilage tissue engineering. As a result, the injectable CS/HA hydrogel loaded with Si-HPMC is a promising tissue engineering approach with a lot of clinical cartilage tissue healing potential (Hu et al., 2021).

3 Injectable hydrogels for dental pulp stem cells

According to Samiei et al., the hydrogels that incorporate more gelatin have a somewhat looser network than the others. The hydrogel with less gelatin has a slightly higher value of G′, which denotes more elasticity as a result of more CS amine groups being crosslinked through a covalent connection with genipin. Since there were very few dead cells in any of the hydrogels, this demonstrated the remarkable biocompatibility of the made hydrogels for human dental pulp stem cells (hDPSCs). After 21 days, hDPSCs cultivated on produced hydrogels showed a considerable increase in calcium deposition, as shown by the quantitative findings of alizarin red staining. Furthermore, the greatest Alkaline phosphatase (ALP) activity was shown by hDPSCs cultivated on hydrogel that included more gelatin. After 21 days, the hydrogel with more gelatin expressed late osteogenic

genes such OCN and BMP-2 6 and 4 times, respectively, more than the control group. The Poly (N-isopropylacrylamide) (PNIPAAm-g-CS) copolymer/gelatin hybrid hydrogel that was created had excellent properties and produced the osteogenic differentiation required for dental tissue engineering (Samiei et al., 2022).

4 Drug delivery system

Focusing on the positive benefits of Fmoc-FF self-assembly and its electrostatic interaction with glycol chitosan (GCS), a straightforward method for producing injectable self-healing hydrogels for Doxorubicin (DOX) administration has been reported. The final product, a hydrogel-based technology, showed a novel Ph-responsive DOX release, with the drug release mechanism being improved in moderately acidic environments. This finding may pave the way for controlled drug release in a typical, moderately acidic tumor microenvironment. The new hydrogel was undoubtedly a successful method for the controlled release of DOX, given the slow rate of release of DOX under physiologically normal settings. Notably, the DOX-loaded hydrogel was efficiently cytotoxic to the human tumor cell line A549 in a test tube (Shim et al., 2021).

Physical mixing of CS with Pluronic-F127 (PF) produced the hydrogels. Tripolyphosphate (TPP) was further utilized as a crosslinking agent. In comparison to pluronic gel alone, the gel duration was lengthened by the addition of CS. The morphology of the hydrogels generated was altered by the addition of TPP to the substance. To test whether hydrogels were harmful to human chondrocytes, MTS and Live/Dead® assays were conducted. Dexamethasone (DMT) was released *in vitro* from the CS-PF and CS-PF-TPP gels over a longer period of time than the PF hydrogel. Studies conducted *in vivo* revealed that hydrogels kept the fluorescent component in the joint longer than when it was given in Phosphate-buffered saline (PBS) alone. These findings imply that the DMT-loaded CS-PF and CS-PF-TPP hydrogels may provide an effective drug delivery system for the osteoarthritis treatment (García-Couce et al., 2022).

According to the contact angle measurement, the chemically altered chitosan exhibits a less hydrophilic character than pure chitosan, which results in poor swelling in an aqueous environment. The hydrogel is made from graft copolymer, and because of the hydrogel's porous network-like structure, the drug molecules are shielded from their hostile environment. In comparison to pure chitosan, the graft copolymer has the ability to deliver the medicine in a sustained way, according to an *in vitro* drug release study. Graft copolymer is discovered to have a significantly higher rate of cellular absorption than pure medication, making it a more effective delivery method. The possibility of using the graft copolymers as an injectable hydrogel has been suggested by an *in vivo* gelation investigation in a rat model (Mahanta and Maiti, 2019).

5 Bone tissue engineering

To overcome the limitations of CS/β-Glycerophosphate (GP) hydrogel, a thermosensitive, injectable halloysite nanotubes (mHNTs)/CS/GP NC hydrogel was developed. The objective was to develop an injectable nanocomposite (NC) CS hydrogel containing modified mHNTs. This research enhances the mechanical robustness of the resultant scaffold mHNTs as well as the proliferation of human adipose tissue-derived stem cells (hASCs) within it. Overall, the results for bone differentiation showed that IC/mHNTs improved the mechanical strength of CS hydrogel and enhanced the difference of encapsulated hASCs into bone tissue because of their stiffness, tubular structure, and ability to dynamically deliver IC as an osteogenic inducer agent (Kazemi-Aghdam et al., 2021).

For tissue engineering applications, the optimal chitosan/oxidized-modified quince seed gum/curcumin-loaded (CS/OX-QSG) hydrogel (ratio of 25:75) with varied curcumin-loaded in halloysite nanotubes (CUR-HNT) levels was effectively synthesized. The hydrogel with the highest OX-QSG concentration (CS/OX-QSG 25:75) exhibited a spongy structure with bigger and smaller holes as well as a high crosslinking density. Because of their good mechanical and anti-bacterial capabilities, the results demonstrated that CS/OX-QSG hydrogels with a 25:75 ratio and 30% CUR-HNTs may provide a viable scaffold for tissue engineering applications (Yavari Maroufi and Ghorbani, 2021).

Using the enzymatic crosslinking process of horseradish peroxidase, Jung et al. created *in situ* forming CS/poly (ethylene glycol) (PEG) hydrogels with better mechanical characteristics. By altering the quantity (0%–100%), molecular weight (4, 10 and 20 kDa), and of the PEG derivatives, the impact of PEG on the physico-chemical characteristics of hybrid hydrogels was extensively clarified. The resultant hydrogels, which are equivalent to commercially available fibrin glue, showed outstanding hemostatic activity and are extremely biocompatible *in vivo* (Jung et al., 2021).

Kaur et al. have created injectable hydrogels that are mechanically strong and have enhanced osteogenic properties. The sol-gel transition occurs at 37 C, which is the physiological temperature, and all of the hydrogels have been found to be thermos-responsive. Due to the hydrogel components' positively and negatively charged groups, which attract Ca2+ and PO43 to form hydroxyapatite (Hap) on the surface, all of the hydrogels were demonstrated to be bioactive after only 1 day of incubation in simulated body fluid (SBF). Incorporating carboxylated single wall carbon nanotubes (COOH-SWCNTs) with CS and collagen (Coll) by the application of -GP increased cross-linking, created the greatest possible thermos-responsive and injectability characteristics, and significantly enhanced mechanical properties. Additionally, the hydrogels with COOH-SWCNTs incorporated significantly increase cell proliferation and support osteogenic differentiation as compared to pure CS/Coll (Kaur et al., 2021).

Taymouri et al. successfully developed a chitosan/Silk fibroin (CS2/SF0.5) thermosensitive hydrogel containing dipyridamole loaded polycaprolactone nanoparticles (DIP-PCLNPs) as a novel and non-invasive local drug delivery approach for bone tissue engineering. DIPPCL NPs were produced using the solvent-emulsification evaporation method, and the formulation factors were optimized using an irregular factorial design. The optimal conditions for producing DIP-PCL NPs were 7 mg DIP, 1.5% PVA, a W/O volume ratio of 4, and a 4-min sonication period. This perfect formulation was put into the CS2/SF0.5 thermosensitive hydrogel. Since the results demonstrated that the amount of the inserted SF altered the network structure of the CS hydrogel, the gel scaffolds containing 0.5% SF had a shorter gelation time and stronger compressive strength when compared to other composite hydrogels. In an *in vitro* cell culture examination, the DIP-PCL NPs- CS2/SF0.5 hydrogel shown the greatest capacity to encourage the proliferation and activity of MG-63 cells, as demonstrated by a significant increase in cell viability, ALP activity, and calcium deposition (Taymouri et al., 2021).

In order to increase cardiac tissue's functioning, cardiac tissue engineering supports, replaces, or repairs it. Application of the

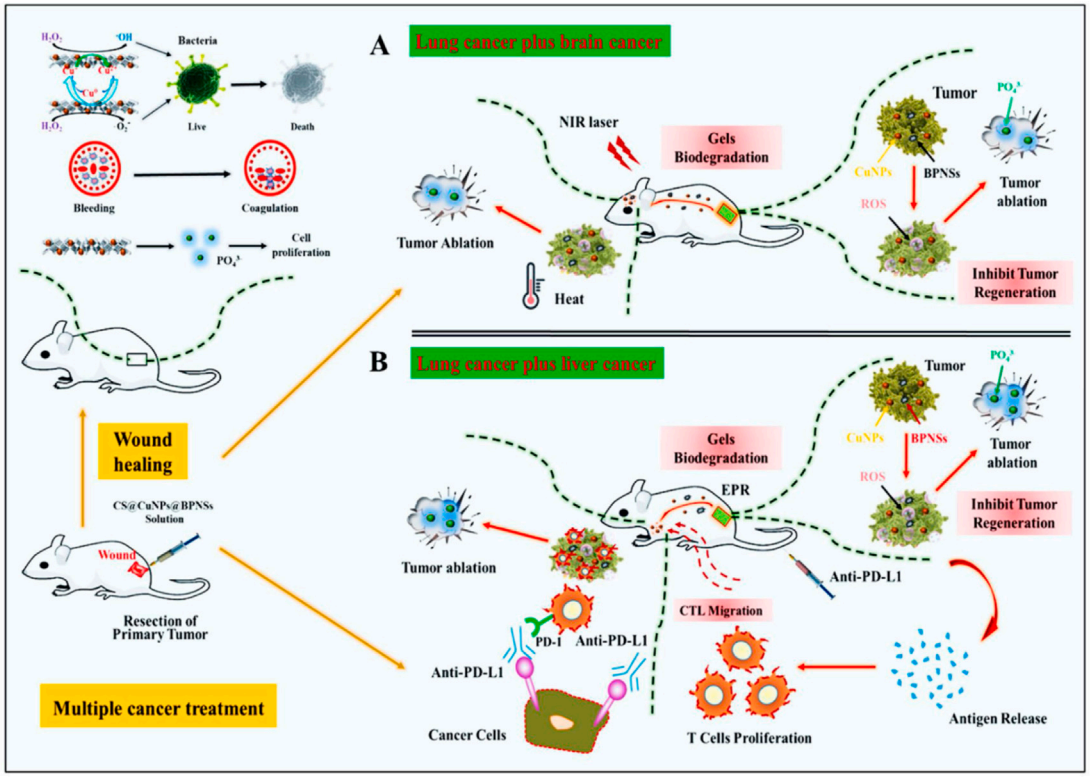

FIGURE 2
Illustration of the therapeutic mechanism of the hydrogel in inhibition of multiple cancer growth **(A)** Lung cancer with brain cancer **(B)** Lung cancer with liver cancer (Wang et al., 2021).

polysaccharides—of which chitosan is a key component—addresses the main problem with the vitality of the implanted cells. Chitosan aids in the provision of mechanical support, prevents the spread of pro-inflammatory chemicals, and encloses bioactive elements beneficial for the regeneration of heart tissue. Chitosan's positive charge and hydrophilicity, among other properties, enable the development of a soft tissue milieu, particularly when combined with biomolecules. Scaffolds made of chitosan support stem cell proliferation and differentiation by providing mechanical strength (Patel et al., 2021).

6 Anti-cancer

Injectable polysaccharide hydrogels that are biocompatible and self-healing have been produced by the first-ever chemical crosslinking of multialdehyde guar gum (MAGG) with numerous aldehyde groups and N, O-carboxymethyl chitosan (N, O-CMCS) *via* pH-sensitive, biodegradable, and dynamic Schiff base connections. These hydrogels were ideal for injectable drug administration because of their exceptional viscoelastic, thixotropic, and self-healing properties. After Dox loading for 5 days, these hydrogels demonstrated a pH-responsive release, with a higher release at tumoral pH than at physiological pH. MTT and hemolytic assays demonstrated the non-toxicity of these hydrogels. The Dox-loaded hydrogel significantly reduced MCF-7 cell viability, with 72% of the cells dying (Pandit et al., 2021).

To generate DOX@CSSH/HNTs-SH Gel, thiol group-modified halloysite nanotubes (HNTs) were first loaded with DOX before being added to the gel precursor. This gel loaded and gradually released water-soluble DOX to lessen the cytotoxicity of thiolated chitosan (CSSH) Gel while also enhancing its mechanical characteristics. The results showed that the HNTs-SH could be evenly distributed throughout the gel matrix to boost the gel's compressive strength and that the gel was pH sensitive to release DOX quickly in the tumor's acidic microenvironment, where MCF-7 cells could take it up and effectively inhibit MCF-7 cell growth. According to *in vivo* tumor resection and recurrence inhibition experiments, the gel may stop lung metastasis, lessen tumor recurrence, improve survival rates, and mend surgically injured tissues. The *in-situ* injectable DOX@CSSH/HNTs-SH Gel may be developed as a novel drug delivery system to inhibit tumor recurrence and heal surgical wound tissues after tumor removal (Li et al., 2021).

Wang et al. created a CS/CuNPs/black phosphate nanosheets (BPNSs) solution that is sustained-release, tumor microenvironment (TME) sensitive, and has superior photothermal and redox potential in the acidic TME (Figure 2). Under body temperature, this solution transforms into a biodegradable, spongy hydrogel. After surgery, the hydrogel condition within the body would significantly aid hemostasis and trap any remaining cancer cells in the blood. CuNPs would then take over the tumoricidal role by producing a sequence of redox reactions that would result in the formation of ROS, which could then kill any remaining cancer cells and stop the recurrence of an orthotopic tumor in order to simultaneously accomplish local antisepsis. The release of additional antigens, which significantly stimulates the systemic immune response, follows the cell death caused by the first chemo-dynamic treatment (CDT) action on the first primary tumor site throughout the therapeutic phase. The use of a PD-L1 enhances this response by protecting cytotoxic T lymphocyte (CTL) function. As a

TABLE 1 An overview for clinical trials of chitosan and derivatives.

ClinicalTrials.gov identifier	Conditions/Diseases	Status	References
NCT01278784	Dry Eye Syndromes	Phase 1, September 2011	https://clinicaltrials.gov/ct2/show/NCT01278784
NCT02323451	Osteoarthritis, Knee	Phase 4, April 2017	https://clinicaltrials.gov/ct2/show/NCT02323451
NCT02668055	Wounds	Phase 1, December 2015	https://clinicaltrials.gov/ct2/show/NCT02668055
NCT00454831	Hypercholesterolemia	Phase 2, September 2007	https://clinicaltrials.gov/ct2/show/NCT00454831
NCT0300765	Gynecologic Disease	Phase 3, August 2017	https://clinicaltrials.gov/ct2/show/NCT03007654
NCT01597817	Atopic Dermatitis	Phase 2, December,2012	https://clinicaltrials.gov/ct2/show/NCT01597817
NCT00521937	Diabetes Foot Ulcer	Phase 3, December,2010	https://clinicaltrials.gov/ct2/show/NCT00521937
NCT03202446	Breast Cancer Stage IIIA, IIIB and IV	Phase 3, January 2018	https://clinicaltrials.gov/ct2/show/NCT03202446
NCT03188289	Wisdom Teeth	Phase 4, September 2014	https://clinicaltrials.gov/ct2/show/NCT03188289
	Oral Surgery		

result, the activated CTLs and CDT impact of CuNPs might give synergistic treatment to the ectopic primary HCC tumor. The presence of BPNSs allowed biodegradable hydrogel fragments to pass the blood tumor barrier during NIR laser irradiation, resulting in the killing of brain cancer cells due to the CDT effect (Wang et al., 2021).

In order to create pH-degradable hydrogels, Gao et al. crosslinked carboxymethyl chitosan (CMCS) with an acid-labile ortho ester compound (OEDe). CMCS was subsequently cross-linked with a mixed cross-linker comprising OEDe and ethylene glycol diglycidyl ether (EGDE) at three different molar ratios in order to further adjust the pH-sensitivity and mechanical qualities. Then, hydrogels were wrapped around DOX-loaded gelatin nanoparticles with an average diameter of 50 nm to create a hybrid system that could be inserted into a tumor location in any shape for local chemotherapy. Intravenous injections of free DOX and DOX-loaded nanoparticles were tested for their ability to prevent tumor growth in mice harboring murine hepatoma tumors. The outcomes demonstrated that the cross-linked CMCS hydrogels could greatly extend the DOX release period as well as improve medication absorption into the tumor site. The hybrid hydrogels with the most pronounced anticancer activity were those with released DOX-loaded nanoparticles because they could further enhance the retention and permeation of DOX in tumor site. Therefore, the local therapy of solid tumors with pH-degradable hydrogels has significant potential (Gao et al., 2019).

Here in Table 1, we summarize clinical trials of chitosan.

7 Discussion

Injectable hydrogels use their carrier capability and processing flexibility as an *in-situ* gelling regime. Although a sol-gel transition under moderate circumstances and well-controlled kinetics is required to provide a medical injection, the administration would also have minimal invasion and enable for filling irregularly shaped gaps. However, there are still a few fundamental issues to be concerned about to fully utilize injectable hydrogels in the biomedical area, aside from focusing on developing novel characteristics and sophisticated functionalities. First, while designating "new" materials for prospective clinical trials, it is important to consider the greater risk involved. The second topic is how a hydrogel's properties could be impacted by the production process. Injectable gels must go through a sol-gel transition close to or at the desired insertion location, unlike *in situ* forming gels and 3D printing. As a result, the gelation shouldn't be too slow if the pregel isn't excessively viscous. Controlling the dosing of a hydrogel formulation could be challenging. Finding a solution with the right viscosity for injection, the necessary gelation kinetics, and the reliable mechanical characteristics of the harvested gel might not always be possible. The mechanical characteristics of the injected hydrogels are often poorer than those of the *in situ* generated ones, specifically for hydrogels with higher modulus or strength. Even though some clever approaches, such as the recently developed conjoined-network strategy, have been established for making high-performance hydrogels, a multistep synthesis procedure may reject the attempt to harvest such hydrogels by injection processing. However, given our focus on clinical users, we may anticipate more advancements in the creation of injectable hydrogels with improved and possibly "smart" features.

Author contributions

HG and SS contributed in literature review. SN convinced the idea, supervised the student and edited the paper. SG and WZ supported the fund and enriched and revised the paper.

Acknowledgments

This work was supported by the National Key R&D Project of China (2018YFA0704103,2018YFA0704104) and Fundamental Research Funds for the Central Universities (DUT22YG123, DUT21TD105).

Conflict of interest

The authors declare that the research was conducted in the absence of any commercial or financial relationships that could be construed as a potential conflict of interest.

Publisher's note

References

Andrade, F., Roca-Melendres, M. M., Durán-Lara, E. F., Rafael, D., and Schwartz, S. (2021). Stimuli-responsive hydrogels for cancer treatment: The role of pH, light, ionic strength and magnetic field. *Cancers (Basel)* 13, 1164–1217. doi:10.3390/cancers13051164

Gao, J., Xu, Y., Zheng, Y., Wang, X., Li, S., Yan, G., et al. (2019). pH-sensitive carboxymethyl chitosan hydrogels via acid-labile ortho ester linkage as an implantable drug delivery system. *Carbohydr. Polym.* 225, 115237. doi:10.1016/j.carbpol.2019.115237

García-Couce, J., Tomás, M., Fuentes, G., Que, I., Almirall, A., and Cruz, L. J. (2022). Chitosan/pluronic F127 thermosensitive hydrogel as an injectable dexamethasone delivery carrier. *Gels* 8, 44. doi:10.3390/gels8010044

Hu, M., Yang, J., and Xu, J. (2021). Structural and biological investigation of chitosan/hyaluronic acid with silanized-hydroxypropyl methylcellulose as an injectable reinforced interpenetrating network hydrogel for cartilage tissue engineering. *Drug Deliv.* 28, 607–619. doi:10.1080/10717544.2021.1895906

Jung, H. Y., Le Thi, P., HwangBo, K. H., Bae, J. W., and Park, K. D. (2021). Tunable and high tissue adhesive properties of injectable chitosan based hydrogels through polymer architecture modulation. *Carbohydr. Polym.* 261, 117810. doi:10.1016/j.carbpol.2021.117810

Kaur, K., Paiva, S. S., Caffrey, D., Cavanagh, B. L., and Murphy, C. M. (2021). Injectable chitosan/collagen hydrogels nano-engineered with functionalized single wall carbon nanotubes for minimally invasive applications in bone. *Mat. Sci. Eng. C* 128, 112340. doi:10.1016/j.msec.2021.112340

Kazemi-Aghdam, F., Jahed, V., Dehghan-Niri, M., Ganji, F., and Vasheghani-Farahani, E. (2021). Injectable chitosan hydrogel embedding modified halloysite nanotubes for bone tissue engineering. *Carbohydr. Polym.* 269, 118311. doi:10.1016/j.carbpol.2021.118311

Li, R., Zhang, Y., Lin, Z., Lei, Q., Liu, Y., Li, X., et al. (2021). Injectable halloysite-g-chitosan hydrogels as drug carriers to inhibit breast cancer recurrence. *Compos. Part B Eng.* 221, 109031. doi:10.1016/j.compositesb.2021.109031

Liang, Y., Zhao, X., Ma, P. X., Guo, B., Du, Y., and Han, X. (2019). pH-responsive injectable hydrogels with mucosal adhesiveness based on chitosan-grafted-dihydrocaffeic acid and oxidized pullulan for localized drug delivery. *J. Colloid Interface Sci.* 536, 224–234. doi:10.1016/j.jcis.2018.10.056

Lin, D., Lei, L., Shi, S., and Li, X. (2019). Stimulus-responsive hydrogel for ophthalmic drug delivery. *Macromol. Biosci.* 19, 1900001–1900012. doi:10.1002/mabi.201900001

Mahanta, A. K., and Maiti, P. (2019). Injectable hydrogel through hydrophobic grafting on chitosan for controlled drug delivery. *ACS Appl. Bio Mat.* 2, 5415–5426. doi:10.1021/acsabm.9b00733

Pandit, A. H., Nisar, S., Imtiyaz, K., Nadeem, M., Mazumdar, N., Rizvi, M. M. A., et al. (2021). Injectable, self-healing, and BiocompatibleN, O-carboxymethyl chitosan/multialdehyde guar gum hydrogels for sustained anticancer drug delivery. *Biomacromolecules* 22, 3731–3745. doi:10.1021/acs.biomac.1c00537

Patel, B., Manne, R., Patel, D. B., Gorityala, S., Palaniappan, A., and Kurakula, M. (2021). Chitosan as functional biomaterial for designing delivery systems in cardiac therapies. *Gels* 7, 253–321. doi:10.3390/gels7040253

Samiei, M., Abdollahinia, E. D., Amiryaghoubi, N., Fathi, M., Barar, J., and Omidi, Y. (2022). Injectable thermosensitive chitosan/gelatin hydrogel for dental pulp stem cells proliferation and differentiation. *BioImpacts*. doi:10.34172/bi.2022.23904

Shim, J., Kang, J., and Yun, S. I. (2021). Chitosan–dipeptide hydrogels as potential anticancer drug delivery systems. *Int. J. Biol. Macromol.* 187, 399–408. doi:10.1016/j.ijbiomac.2021.07.134

Taymouri, S., Amirkhani, S., and Mirian, M. (2021). Fabrication and characterization of injectable thermosensitive hydrogel containing dipyridamole loaded polycaprolactone nanoparticles for bone tissue engineering. *J. Drug Deliv. Sci. Technol.* 64, 102659. doi:10.1016/j.jddst.2021.102659

Thambi, T., Phan, V. H. G., and Lee, D. S. (2016). Stimuli-sensitive injectable hydrogels based on polysaccharides and their biomedical applications. *Macromol. Rapid Commun.* 37, 1881–1896. doi:10.1002/marc.201600371

Wang, W., Zhang, Q., Zhang, M., Lv, X., Li, Z., Mohammadniaei, M., et al. (2021). A novel biodegradable injectable chitosan hydrogel for overcoming postoperative trauma and combating multiple tumors. *Carbohydr. Polym.* 265, 118065. doi:10.1016/j.carbpol.2021.118065

Yavari Maroufi, L., and Ghorbani, M. (2021). Injectable chitosan-quince seed gum hydrogels encapsulated with curcumin loaded-halloysite nanotubes designed for tissue engineering application. *Int. J. Biol. Macromol.* 177, 485–494. doi:10.1016/j.ijbiomac.2021.02.113

Yuan, F. Z., Wang, H. F., Guan, J., Fu, J. N., Yang, M., Zhang, J. Y., et al. (2021). Fabrication of injectable chitosan-chondroitin sulfate hydrogel embedding kartogenin-loaded microspheres as an ultrasound-triggered drug delivery system for cartilage tissue engineering. *Pharmaceutics* 13, 1487–1515. doi:10.3390/pharmaceutics13091487

frontiers | Frontiers in Bioengineering and Biotechnology

TYPE Mini Review
PUBLISHED 09 February 2023
DOI 10.3389/fbioe.2023.1129768

OPEN ACCESS

EDITED BY
Xiaowei Zeng,
Sun Yat-Sen University, China

REVIEWED BY
Xiaojun Xiao,
Shenzhen University, China
Chuangnian Zhang,
Chinese Academy of Medical Sciences and Peking Union Medical College, China

*CORRESPONDENCE
Seyed Morteza Naghib,
Naghib@iust.ac.ir
Wei Zhang,
wei.zhang@dlut.edu.cn

SPECIALTY SECTION
This article was submitted to Biomaterials, a section of the journal Frontiers in Bioengineering and Biotechnology

RECEIVED 22 December 2022
ACCEPTED 19 January 2023
PUBLISHED 09 February 2023

CITATION
Khakpour E, Salehi S, Naghib SM, Ghorbanzadeh S and Zhang W (2023), Graphene-based nanomaterials for stimuli-sensitive controlled delivery of therapeutic molecules.
Front. Bioeng. Biotechnol. 11:1129768.
doi: 10.3389/fbioe.2023.1129768

Graphene-based nanomaterials for stimuli-sensitive controlled delivery of therapeutic molecules

Elnaz Khakpour[1], Saba Salehi[1], Seyed Morteza Naghib[1]*, Sadegh Ghorbanzadeh[2] and Wei Zhang[2]*

[1]Nanotechnology Department, School of Advanced Technologies, Iran University of Science and Technology and Biomaterials and Tissue Engineering Department, Breast Cancer Research Center, Motamed Cancer Institute, IUST, ACECR, Tehran, Iran, [2]State Key Laboratory of Structure Analysis for Industrial Equipment, Department of Engineering Mechanics, Dalian University of Technology, Dalian, China

Stimuli-responsive drug delivery has attracted tremendous attention in the past decades. It provides a spatial- and temporal-controlled release in response to different triggers, thus enabling highly efficient drug delivery and minimizing drug side effects. Graphene-based nanomaterials have been broadly explored, and they show great potential in smart drug delivery due to their stimuli-responsive behavior and high loading capacity for an extended range of drug molecules. These characteristics are a result of high surface area, mechanical stability and chemical stability, and excellent optical, electrical, and thermal properties. Their great and infinite functionalization potential also allows them to be integrated into several types of polymers, macromolecules, or other nanoparticles, leading to the fabrication of novel nanocarriers with enhanced biocompatibility and trigger-sensitive properties. Thus, numerous studies have been dedicated to graphene modification and functionalization. In the current review, we introduce graphene derivatives and different graphene-based nanomaterials utilized in drug delivery and discuss the most important advances in their functionalization and modification. Also, their potential and progress in an intelligent drug release in response to different types of stimuli either endogenous (pH, redox conditions, and reactive oxygen species (ROS)) or exogenous (temperature, near-infrared (NIR) radiation, and electric field) will be debated.

KEYWORDS

graphene, nanomaterials, stimuli-sensitive, smart drug delivery, endogenous, exogenous

Introduction

Conventional drug delivery methods usually lead to unwanted side effects due to high drug concentrations inserted into the body. Advances in pharmaceutics and material science have led to the invention of controllable drug delivery systems that can minimize toxicity and decrease therapeutic costs. They can load and selectively release a controlled dosage of drug molecules in a specific targeted site, improving the efficiency of therapeutic agents (Bawa et al., 2009; Mura et al., 2013; Chen et al., 2016). However, they only provide a constant release rate and are not adaptable to physiological body conditions (Kost and Langer, 2012). More recently, stimuli-responsive drug delivery systems, being capable of recognizing and reacting to their microenvironment, have provided on-demand drug delivery (Mura et al., 2013). In stimuli-responsive drug delivery systems, a trigger is employed to selectively separate drug molecules from their carrier, thus mimicking the *in vivo* pulsatile release of several types of physiological chemicals, such as hormones, like estrogen and insulin (Murdan, 2003; Raza et al., 2019). The trigger can either be an internal biological inducing factor, resulting from a specific pathological

change that is known as an endogenous stimulus, or a physical external factor inserted from outside of the body that is called an exogenous stimulus (Raza et al., 2019). An endogenous stimulus can be pH, redox conditions, or reactive oxygen species (ROS) (Figure 1). Exogenous stimuli include NIR radiation, temperature, and an electric field (Xie et al., 2022).

Nanotechnology plays a crucial role in such smart drug delivery by enabling the synthesis of ideal drug carriers (Chamundeeswari et al., 2019). The exceptional physicochemical properties of nanocarriers allow them to carry high loadings of drugs and deliver them to the targeted tissue with high efficiency (Hossen et al., 2019). Stimuli-responsive nanocarriers are nanomaterial-based compounds than can be designed specifically to release their therapeutic loading upon a particular biochemical, chemical, or physical stimulus (Kamaly et al., 2016). An ideal nanosystem must inherently contain specific targeting functional groups, trigger an explicit biological response, and be detectable. Carbon nanostructures such as graphene and carbon nanotubes (CNTs), due to having rich functionalization potential, can coordinate the fabrication of interesting nanovectors for the targeted delivery of drugs. Graphene with a biocompatible coating and small size appears to not be obviously toxic to animals in a reasonable dose range, as revealed by a number of different studies (Mendes et al., 2013).

Graphene-based nanomaterials for drug delivery

Graphene is a two-dimensional (2D) carbon allotrope with a hexagonal honeycomb crystal structure (Yu et al., 2020; Patil et al., 2021). Each carbon atom in a graphene monolayer builds a strong sigma (σ) bond with three adjacent carbon atoms. This covalent bond has a short length of ~1.42 Å that gives graphene an exceptionally strong structure. On the other hand, the presence of free π electrons provides an interlayer binding through weak van der Waals interactions that lead to graphene's flexibility. Free π electrons can also act as reactive sites that enable graphene to undergo unique surface reactions (Goenka et al., 2014; Yang et al., 2018). Emerging trends show that graphene-based nanomaterials develop unique properties and can be employed for biomedical applications, particularly in drug delivery and tissue engineering (Goenka et al., 2014). Graphene has been recognized as an efficient carrier for an extended range of drug molecules due to its mechanical and chemical stability, the high surface area of its planar structure, great loading potential, and excellent optical, electrical, and thermal properties. Additionally, it has the ability to react to several stimuli such as electric and magnetic fields, pH, temperature, and sound which makes it an ideal candidate for stimuli-responsive drug delivery (Sun et al., 2008; Liu et al., 2011; Bai and Husseini, 2019; Patil et al., 2021). Graphene usage in drug delivery applications was, for the first time, reported by the Dai research group in 2008. They utilized graphene as an effective drug carrier for cancer therapy, which opened the path for its extensive research later on, as a promising material in drug delivery (Song et al., 2020). However, there are still some challenges associated with graphene's drug loading and release. For example, graphene shows cytotoxicity in biological solutions due to its aggregation. On the other hand, as a strong yet flexible carbon backbone, graphene shows fundamentally unlimited potential for its modification or functionalization (Zhu et al., 2010). Biological modification promotes graphene by enhancing its solubility, selectivity, stability, and biocompatibility (Wang et al., 2011). This will be explained in detail in the modification sector.

Graphene oxide (GO)

Graphene oxide (GO) is a graphene derivative with a 2D atomic layer, composed of sp2 carbon and sp3 carbon together with oxygen functionalities such as epoxide, hydroxyl, and carboxylic groups. The hexagonal carbon structures and these functional groups lead to versatile surface chemistry and make it possible to form covalent and non-covalent bonds. Rich surface chemistry makes GO more popular than pristine graphene in biomedical applications such as drug delivery. Furthermore, in comparison with graphene, which is insoluble in biological solutions and tends to agglomerate, GO has excellent water solubility (Yang et al., 2015; Kim et al., 2016). Free π electrons in unmodified areas of GO provide hydrophobic regions which are suitable for loading hydrophobic drugs through van der Waals forces (Ghawanmeh et al., 2019). For example, when added to hydrogels, GO's physical crosslinking enhances the loading capacity of hydrophobic drugs and also improves the stimuli-responsive properties (Chen et al., 2018; Olate-Moya and Palza, 2022).

Graphene quantum dots (GQDs)

GQDs, as a new generation of carbon-based nanomaterials, have recently displayed great potential in nanomedicine and drug delivery. GQDs have typical dimensions of up to a few nanometers and circular or elliptical shapes (Henna and Pramod, 2020). The active groups present on the GQD surface, similar to graphene and GO, enable them to be conjugated to other molecules, hence making them ideal nanocarriers to simultaneously track and treat the diseased cells. Research studies show that GQD can efficiently prompt the nuclear accumulation of drugs, such as cisplatin and doxorubicin (DOX) (Yang et al., 2015). Additionally, their small size and good biocompatibility serve as favorable properties required for being drug delivery carriers (Zheng et al., 2015). GQDs have also demonstrated therapeutic effects in several diseases like Parkinson's disease, Alzheimer's disease, and diabetes in addition to being antibacterial. They also provide drug delivery across the blood–brain barrier (Henna and Pramod, 2020).

Graphene derivative modification for drug delivery

Numerous studies have been dedicated to graphene modification and functionalization. Graphene and its derivatives can be modified by both covalent functionalization and non-covalent functionalization. GO and rGO, due to having oxygen groups and highly active defects, are more popular than pristine graphene for their modification goals (Zhang et al., 2017). Novel nanohybrids have been developed by conjugating graphene derivatives to different types of materials such as biomacromolecules, polymers, and other nanoparticles to produce unique graphene-based nanocarriers for biocompatible and more effective drug delivery (Wang et al., 2017).

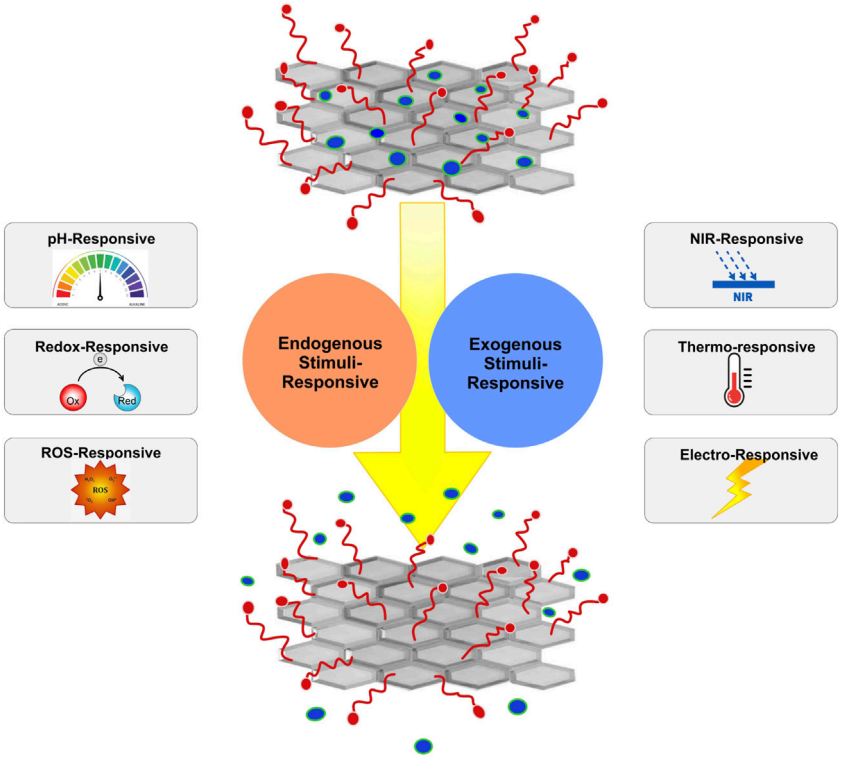

FIGURE 1
Schematic representation of stimuli-sensitive nanomaterials for the controlled delivery of therapeutic molecules.

Modification with polymers

The functionalization of graphene derivatives by suitable polymers enhances graphene's biocompatibility, solubility, stability, and *in vivo* circulation times. Polyethylene glycol (PEG) is the most extensively researched biocompatible polymer for graphene modification. Its uptake by the reticuloendothelial system is low, and its functionalization on graphene sheets leads to high aqueous solubility and physiological stability, as well as reduced toxicity (Charmi et al., 2019; Sattari et al., 2021). For instance, Charmi et al. (2019) PEGylated GO using the EDC/NHS catalyst *via* esterification bonding, and the fabricated nanohybrid provided a 4.5% loading of curcumin, which is an anticancer drug. The nanocarrier's ability to pursue pH-responsive delivery was also indicated both *in vitro* and *in vivo*. The phagocytic activity was delayed in blood circulation due to the surface charges, so biocompatibility was confirmed (Charmi et al., 2019). Hyaluronic acid (HA), which is a linear hydrophilic macromolecular polymer, also has been used to modify graphene nanocarriers by several researchers. In a study, HA was conjugated to graphene *via* H-bonding formation between the epoxy groups in GO and the amine groups of HA. The resulting HA–GO nanohybrid was used for targeted and pH-responsive delivery of DOX in certain cancer cells, and it was demonstrated that HA decoration, similar to PEG, improved the solubility and physiological stability of GO, as well as its loading capacity for DOX. Moreover, HA functions as an active targeting moiety to recognize the transmembrane glycoprotein CD44 receptor, which is overexpressed on surfaces of various tumor cells (Song et al., 2014). Furthermore, several research studies have been dedicated to the integration of hydrogels onto graphene in order to enhance drug loading and release. Hydrogels, which are a biocompatible 3D framework of hydrophilic polymers, have been widely used in controlled drug release as they swell in water, and their gel structure changes under different environmental conditions. They can also preserve drugs from the enzymes and acidic environment in the stomach (Tao et al., 2012; Sun et al., 2019). Although hydrogels are suitable carriers for water-soluble drugs such as peptides and proteins, they cannot load efficient amounts of hydrophilic compounds. By adding graphene to such materials, efficient loading capacity for hydrophobic drugs can be provided (Leganés et al., 2020). Polyethylenimine (PEI), chitosan, dendrimers, and hyper-branched polymers are other common polymers used as graphene modifiers for targeted drug delivery (Sattari et al., 2021).

Modification with biomacromolecules

Biomacromolecules, such as proteins, DNA, and peptides, have attracted so much attention in drug delivery because of their rich functions, biocompatibility, and stability in the body environment. It has been indicated that the conjugation of such macromolecules to graphene derivatives can result in efficient nanocarriers for controlled drug delivery (Wang et al., 2017). For example, Mo et al. (2015) conjugated graphene with an adenosine-50 triphosphate (ATP) aptamer and two single-stranded DNA molecules, which were ATP-responsive. The graphene-DNA crosslinked hybrid inhibited the ATP-responsive release of DOX from GO nanosheets to cancer cells effectively. The high loading capacity of DOX and the site-specific

10.3389/fbioe.2023.1129768

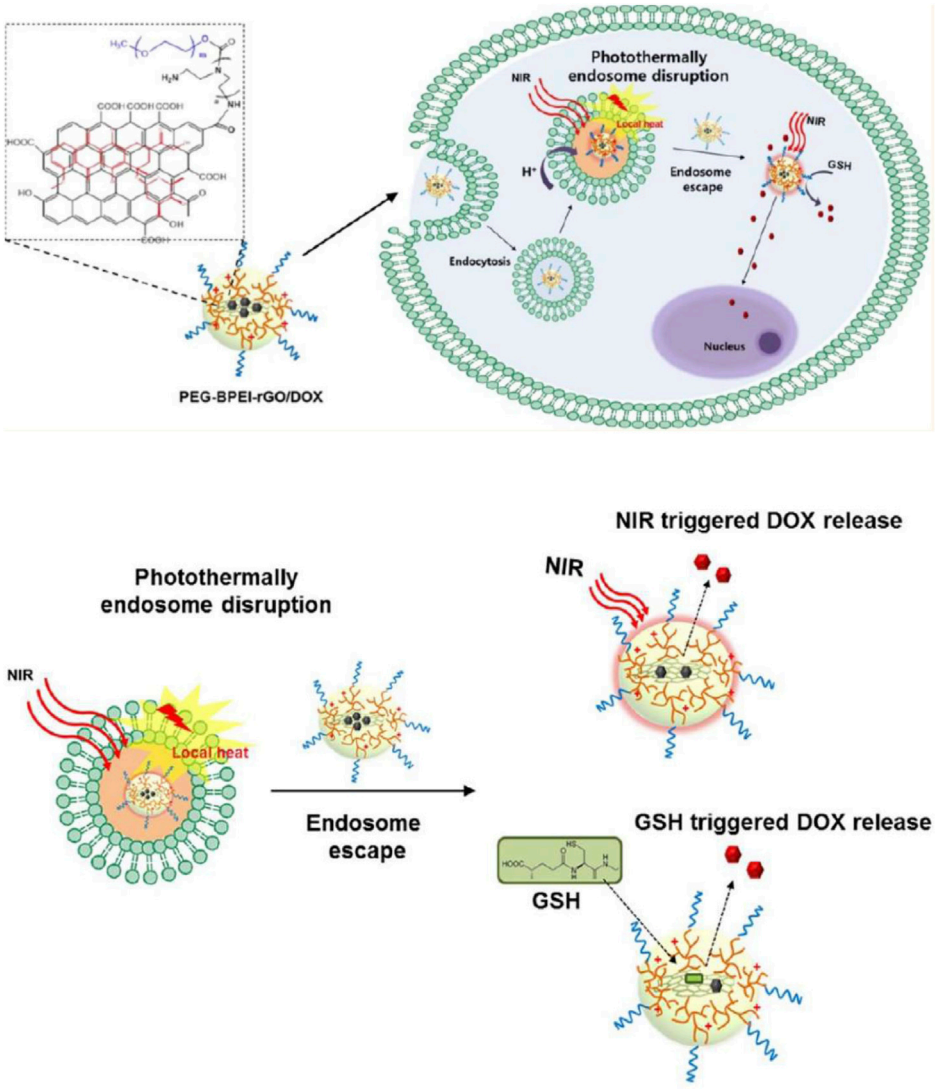

FIGURE 2
Schematic representation of the mechanism of cytosolic drug release by near-infrared (NIR) radiation and glutathione (GSH) after photothermally induced endosome disruption, reprinted with permission from Kim et al. (2013), copyright 2013, American Chemical Society.

drug release were achieved (Mo et al., 2015). Sima et al. (2020) also functionalized GO nanocolloids by non-covalent conjugation of bovine serum albumin (BSA) protein onto the GO surface to minimize graphene cytotoxicity and as a carrier for anticancer drugs (Sima et al., 2020). Recently, Muzi functionalized GO with hen egg lysozyme (HEL) through a simple non-covalent conjugation method and used the nanocarrier for the selective targeting of B lymphocytes in autoimmune diseases. It was suggested that the same process could be used for other proteins or peptides capable of targeting certain new B cells (Muzi et al., 2021).

Modification with nanoparticles

In numerous studies, a variety of inorganic nanoparticles have been incorporated into the derivative surface of graphene, providing superior drug delivery. Moreover, the optical and magnetic characteristics of nanoparticles can be used to enable external stimuli-responsive drug delivery and bioimaging. The functional groups and abundant structural defects of GO and rGO offer the benefit of conjugation to nanoparticles, including silica, Au, Ag, Ni, Pt, and Fe_3O_4 (Liu et al., 2013).

Mesoporous silica nanoparticles (MSNs), owing to their tunable porosity, large specific surface area, high loading capacity, good biocompatibility, and simple conjugation to target ligands for specific cellular recognition, can develop efficient drug delivery systems. Being functionalized onto graphene, its dispensability and cellular uptake would improve, and an enhanced controlled drug release would be obtained (Manzano and Vallet-Regí, 2020). For example, Tran et al. developed a GO-MSN system for the delivery of cisplatin, a chemophotothermal agent, through NIR/pH-responsive release and fluorescent imaging (Tran et al., 2018). Gold nanoparticles have also been known as promising nanoparticles for drug delivery goals, owing to their exceptional biological and physicochemical

features, attachment capability to biomolecules *via* the Au–S bond, photothermal effect, monodispersity, low toxicity, and simple fabrication process. Zhang et al. (2018) utilized the NIR-responsive characteristics of both rGO and gold nanorods (AuNRs) to fabricate a NIR stimuli drug delivery system. The boosted photothermal effect between rGO and AuNPs led to superior photothermal conversion efficiency (about 39%); thus, a more rapid drug release was provided. Moreover, the loading capacity and thermal stability considerably improved (Zhang et al., 2018). Mo et al. (2015) incorporated AuNPs onto GO for effective delivery of DOX to HeLa cells for chemotherapy. AuNPs enabled intracellular Raman imaging as well (Ma et al., 2013). More recently, AuNPs were decorated on PEGylated GO by Samadian et al. for pH-sensitive DOX release. GNPs improved the thermal stability of the nanocarrier, and excellent anticancer performance was achieved mostly due to their high drug-loading capability (Samadian et al., 2020). Ag nanoparticles (AgNPs) incorporated in GO can also enhance the drug loading and release behavior. Rahmani et al. (2022) fabricated polyvinyl alcohol (PVA)-GO-Ag nanofibers loaded with curcumin by electrospinning. It was used for wound healing and was indicated to have a significant inhibitory effect on bacterial growth. Drug loading and encapsulation efficiency rose to 56% and 86%, respectively, owing to the presence of AgNPs. Curcumin release increased in the acidic microenvironment, and also, the growth and proliferation of cells cultured on nanofibers accelerated (Rahmani et al., 2022).

Graphene-based nanocarriers for stimuli-responsive drug delivery

Endogenous stimuli-responsive drug delivery

pH-sensitive drug delivery

Different tissues and cellular parts of the body have distinct pH levels that can operate as a stimulus in pH-sensitive drug delivery systems (Zhu and Chen, 2015). In certain abnormal physiological conditions such as cancer, inflammation, and infection, substantial variations of pH have been recognized at the diseased sites. For example, in tumor tissue, glycolysis occurs at high rates, and lactic acid accumulates due to the rapid proliferation of tumor cells and nutrient deficiency. This leads to a notable pH decrease in the tumor microenvironment (5.5–6.8) in comparison with blood and normal tissues (≈7.4), which can act as an endogenous stimulus for acid-sensitive drug delivery systems. In acidic environments, hydrophobic drug molecules like doxorubicin undergo protonation, and hence, the π–π stacking and hydrophobic interactions with the graphene surface weaken, which leads to a pH-responsive release of the drug (Zhu and Chen, 2015; Kamaly et al., 2016; Yang et al., 2016). In 2008, Yang et al. (2016) loaded doxorubicin, an anticancer drug, onto GO for the first time. GO and DOX were mixed in an aqueous solution under mild sonication, and as a result, a high loading of DOX on GO and a strongly pH-dependent drug release was achieved. The high drug loading was attributed to hydrophobic interactions and *π–π* stacking between GO and the quinone part of DOX. Furthermore, hydrogen bonding formed between the -NH_2 and -OH groups on DOX, and -COOH and -OH groups on GO sheets. It was shown that this strong bonding in neutral conditions is responsible for DOX release in acidic and basic environments (Yang et al., 2008). Kavitha et al. (2013) also loaded GO with pH-sensitive poly(2-(diethylamino) ethyl methacrylate) (PDEA) *via* covalent bonding and fabricated a nanocarrier for camptothecin (CPT), a water-insoluble drug, which was attached to GO-PDEA through by π–π stacking and hydrophobic interactions. The nanocarrier released the drug in the lower pH of the tumor environment (pH = 5.5), while no release happened in neutral and basic conditions (Kavitha et al., 2013). In a more recent study, Boddu et al. (2022) developed highly tunable pH-responsive rGO-embedded chitosan beads for the co-delivery of curcumin and 5-fluorouracil and an effective function against MCF7 cells; so, it resulted in the intrinsic anticancer capability (Boddu et al., 2022).

Redox-responsive drug delivery

Disulfide bonds (–S-S–) can play a key role in drug delivery devices since they are highly sensitive to redox conditions. They rapidly break inside cells, where the environment is a reducing one due to the high concentration of glutathione (GSH), while the oxidizing extracellular environment provides them long-term stability (Bauhuber et al., 2009). More importantly, GSH concentration in cancer cells is at least four times more than that of normal cells, which causes a bigger intracellular and extracellular redox gradient, leading to efficient drug release in tumor cells (Wang et al., 2016). Research studies have shown that redox-sensitive surface modification of GO with the help of disulfide bonds would enable controllable drug release in a reducing environment (Yang et al., 2016). For example, Kim et al. (2018) conjugated graphene oxide nanoparticles (GONPs) with methoxy poly(ethylene glycol) (MePEG) to fabricate a redox-responsive drug delivery system. They used it to release chlorin e6 (Ce6), a therapeutic compound for cholangiocarcinoma (CCA) cell treatment. GONPs were found to cause a faster release in the presence of glutathione, representing their redox-responsive properties. They also led to a considerably higher amount of drug uptake and ROS yield in the cells, in comparison with Ce6 itself. Moreover, GONPs well accumulated in tumor tissue, while Ce6 itself is mostly gathered in the liver (Kim et al., 2018). It was also demonstrated that the biodegradability of GO could be adjusted by its redox-sensitive surface coating. The Li research group found out that when GO was coated with macromolecules like PEG to fabricate a biocompatible device, it could not be considerably degraded during enzyme-induced oxidization. Hence, they utilized cleavable disulfide bonds for conjugating PEG to GO. The obtained GO-SS-PEG was shown to become considerably degradable. Thus, it was discovered that the redox-responsive surface coating of GO would result in both intelligent drug delivery and tunable biodegradation behaviors (Li et al., 2014).

ROS-responsive drug delivery

Reactive oxygen species such as singlet oxygen ($^1O_2$) superoxide (O_2^-), hydroxyl radical (·OH), hydrogen peroxide (H_2O_2), and hypochlorite ion (OCl^-) are oxygen ions and free radicals with high reactivity. ROS is produced at low levels in a healthy body and is responsible for adjusting cell signaling and proliferation. However, elevated ROS levels inflict harm on proteins, lipids, and DNA (Trachootham et al., 2009; Saravanakumar et al., 2017). Aging and many pathological conditions such as cancer, inflammation, and atherosclerosis are associated with ROS over-production in the body (Yang et al., 2016). Typical injection of oxidation-responsive nanoparticles and hydrogels often results in rapid degradation or low bioavailability in ROS conditions and would not work efficiently. Wu et al. (2022) could fabricate a ROS-responsive nanofiber

membrane using rGO as a nanocarrier and PEGDA-EDT as a ROS-sensitive motif for fucoxanthin (Fx) delivery. In an H_2O_2 environment, the nanofiber membrane showed a sustained and long-term Fx release behavior and low toxicity (Wu et al., 2022).

Exogenous stimuli-responsive drug delivery

NIR-responsive drug delivery

Near-infrared (NIR) radiation has been verified to be a capable method for photothermal cancer treatment. Having a wavelength between 650 and 900 nm, NIR radiation has minimal body absorbance, while it could easily penetrate tissue for micrometers to centimeters, allowing photothermal drug release (Timko et al., 2010). Carbon-based nanomaterials are popular agents in NIR-responsive drug delivery systems due to high optical absorbance in the NIR range (Song et al., 2016). Light-responsive drug delivery is generally achieved through either photothermal or photochemical reactions. In photothermally induced drug delivery, nanocarriers go under light-heat transformation when they are exposed to an optical trigger and the obtained increasing local temperature would lead to drug release. By contrast, photochemically triggered drug delivery is achieved by photo-induced cleavage or reactions, or photo-dimerization or isomerization due to the presence of groups or bonds sensitive to light (Xiao et al., 2012). Graphene oxide has been reported to have great photothermal properties. In 2013, Kim et al. developed a photothermal-responsive cytosolic nanocarrier by functionalizing reduced graphene oxide to PEG-BPEIrGO for DOX delivery into cancer cells. First, endosome disruption occurred by photothermal induction, and then, the drug was released by NIR irradiation. Additionally, the presence of GSH induced more rapid DOX release by deteriorating the π–π stacking and non-covalent hydrophobic interactions of GO. The reported nanotemplate had a greater loading capacity for DOX and also higher water stability than PEG-BPEI-GO which contained unreduced GO due to hydrophobic interactions and π–π stacking. After cellular uptake and before lysosomal degradation, the nanocarrier successfully escaped from the endosome by photothermally induced endosomal disruption of rGO and the proton sponge effect of BPEI. Subsequently, the efficient GSH-mediated release of DOX into the cytosol was observed (Figure 2) (Kim et al., 2013).

Wang et al. (2021) reported the synthesis of chitosan hydrogel films loaded with reduced graphene oxide (CS/rGO) as NIR light-responsive nanocarriers for local delivery of teriparatide, a drug for osteoporosis treatment. The biomimetic pulsatile release was achieved through photothermal conversion for osteoporotic bone regeneration in rats. The results showed that by increasing hydrogel's rGO content, the teriparatide loading capacity rose, and when rGO content reached 0.7%, 85% drug loading was obtained. Also, by dedicating more time to NIR irradiation, more drug amounts were released. Furthermore, more blood vessels were noticed among the regenerated bone and the defect's center. The fabricated system provided a new approach to repairing osteoporotic bone defects by keeping more amounts of the drug in the defective area without any systemic side effects. It has also been reported that GO can photochemically respond to NIR radiation (Wang et al., 2021). For example, He et al. fabricated a photochemically induced NIR-responsive nanocarrier (MnCO-GO) by captivating Mn-carbonyl CORMs in a small GO nanosheet. The nanomedicine was demonstrated to be highly controllable and NIR-responsive/sensitive to CO release from trapped CORMs. When it was subjected to NIR radiation, GO absorbed the light and converted the photons to active electrons. The electrons in the GO sheet were transferred to Mn-carbonyl molecules, and contesting 3d orbitals of Mn with carbonyls resulted in CO separation from Mn (He et al., 2015).

Thermo-responsive drug delivery

Thermo-responsive hydrogels are relatively the most researched responsive hydrogel systems because they show exclusive properties in controlled drug delivery systems. Among them, poly (N-isopropylacrylamide) (PNIPAAm)-based hydrogels have been widely used in thermo-responsive drug delivery since they exhibit a reversible phase transition temperature of about 32°C that is close to the body temperature. Yet, they face challenges including low biocompatibility, low mechanical strength, and slow response that limit their feasibility. To prompt their response, nanohydrogels have been developed. It is also essential to avoid using chemical crosslinkers in synthesizing hydrogels since it results in their toxicity. Functionalizing GO with many biocompatible polymers such as chitosan, polyethylene glycol, and PNIPAAm has benefited gene and tumor drug delivery. Sattari et al. fabricated thermo-responsive GO-based hydrogels through *in situ* polymerization of NIPAAm in a GO/modified matrix as a non-toxic hydrogel crosslinker. They showed that by increasing the GO content in a hydrogel composite, the hydrogel's phase transition temperature, thermal stability, and internal network crosslinking increased (Sattari et al., 2017).

Havanur and JagadeeshBabu (2018) synthesized a novel intelligent DOX carrier using the poly (N,N-diethyl acrylamide) (PDEA) hydrogel, which is a temperature-responsive macroporous polymer. They loaded it with graphene quantum dots to increase its lower critical solution temperature (LCST). It was demonstrated that by loading more GQD content, the hydrogel's porous structure got more interconnected by having a higher number of smaller pores. It happened due to water molecule crystallization in its swollen state. As a result, the hydrogel's equilibrium swelling ratio (ESR) increased considerably and led to more rapid water transport, and subsequently caused improved temperature sensitivity. The addition of GODs also decreased DOX cytotoxicity by enhancing the hydrogel's loading capacity from 70% to 99% (Havanur and JagadeeshBabu, 2018).

A thermo-responsive hydrogel scaffold was also developed by Mauri et al., in 2020, that incorporated pristine few-layer graphene without distortions associated with the oxidation processes. Diclofenac, a non-steroidal drug for the treatment of musculoskeletal and systemic inflammations, was physically adsorbed on the carrier matrix by providing π–π interactions between its twisted phenyl rings and graphene. Additionally, the defects or vacancies of pristine graphene provided van der Waals interaction and hydrophobic interaction, as well as hydrogen bonds upon the energy and polarizability of the bonds and interactions. By increasing the temperature from 25°C (room conditions) to 44°C (hyperthermia treatment conditions) over time, tunable drug release was identified, while a temperature-independent release kinetic was observed in the lattice without few-layer graphene. Thus, it was suggested that graphene's π-conjugated structure would modify the electrostatic interactions with the diclofenac molecule and promote the thermal response (Mauri et al., 2021).

Electro-responsive drug delivery

Electric field, as an exogenous stimulation for intelligent drug delivery, has attracted so much attention. This is mostly because of its simplicity, portability, and low cost so that it can be easily utilized for

personalized applications by inducing a low voltage. Using molecules that orient their dipoles under electric fields is necessary for electro-responsive devices. Nevertheless, responsiveness is more commonly obtained by molecules that undergo an electrically induced redox reaction (Zhao et al., 2016). Electro-responsive nanomaterials are generally synthesized by utilizing polyelectrolytes, which have the ability to shrink or swell when subjected to electrical fields. However, most of the polymers, which have been commonly used in drug release systems, lack essential electrical conductivity. It has become possible to overcome this limitation by integrating conducting nanomaterials into polymeric scaffolds. When graphene or its derivatives are incorporated into polymers and hydrogels, unique chemical structures and attractive physiochemical properties of graphene lead to the synthesis of composites that are highly biodegradable and biocompatible in a cellular environment and have great cellular uptake and highly responsive behavior (Cirillo et al., 2016). In 2013, Liu et al. fabricated rGO-based hydrogels for the delivery of lidocaine hydrochloride through the stimulation of an external electric field. Although it was demonstrated that the addition of GO led to a highly controllable and responsive release in the presence of an electrical trigger, large voltages were needed to modulate drug release and this might damage biological tissues (Liu et al., 2012). Servant et al., in 2014, developed an electro-responsive macroporous hydrogel matrix loaded with pristine graphene sheets for *in vivo* pulsatile drug release. The reported hybrid scaffold solved the two major challenges that the prior electro-responsive drug delivery devices had dealt with. First, the resistive heating and the following temperature rise caused by the electric field stimuli were eliminated. Due to the presence of pristine graphene at low concentrations, drug release became possible through short stimulations and at low voltages. Second, the drug release reproducibility was provided between the ON–OFF electrical stimulation upon using low electrical voltages (Servant et al., 2014). By depositing GO into a conductive polymer network, Weaver et al. also achieved an electro-responsive drug delivery device with dosage flexibility, favorable electrical properties, and a high level of temporal control for the delivery of dexamethasone, an anti-inflammatory molecule. They could tune the drug loading content and release profile by lowering the thickness and size of GO nanosheets (Weaver et al., 2014). More recently, Sahoo et al. (2022) developed a novel electro-responsive graphene oxide (GO) nanoparticle system and examined it for *in vitro* simultaneous delivery of aspirin and doxorubicin in MDA-MB 231 breast cancer cells. Dual drug delivery is more effective than utilizing a single drug delivery and leads to lower drug resistance and fewer side effects. The on-demand drug delivery in the presence of external low voltage was remotely controlled by a mobile phone (Du et al., 2020).

Conclusion

Graphene has been identified to have selective and exceptional drug loading and release characteristics, owing to its high surface area, mechanical and chemical stability, and excellent optical, electrical, and thermal properties. Moreover, it can react to several stimuli such as electric field, pH, and temperature. In this review, graphene-based nanocarriers for smart drug delivery were introduced. Graphene oxide, due to containing oxygen functionalities such as epoxide, hydroxyl, and carboxylic groups, has a more versatile surface chemistry than pristine graphene which makes it soluble in biological solutions and enables its conjugation to several molecules and drugs. Graphene quantum dots also prompt the nuclear accumulation of drugs, and having a reduced size makes them an advantageous carrier for more efficient drug delivery. Additionally, the surface modification of graphene derivatives with appropriate molecules such as polymers, biomacromolecules, and nanoparticles, which can be conjugated by either covalent and/or non-covalent interactions, has been summarized. The addition of these molecules to graphene derivatives reduces their toxicity and enhances biocompatibility, solubility, and stability, thus providing unique graphene-based nanocarriers for biocompatible and more effective drug delivery. Furthermore, response to both internal and external stimuli such as pH gradients, reducing agents, ROS, electric field, temperature, and NIR radiation, which have been researched numerously, was debated.

Author contributions

EK, SS, and SMN conceived the idea, collected the papers, and wrote the manuscript. SG and WZ supported, edited, and revised the work.

Acknowledgments

This work was supported by the National Key R&D Project of China (2018YFA0704103, 2018YFA0704104) and Fundamental Research Funds for the Central Universities (DUT22YG123, DUT21TD105).

Conflict of interest

The authors declare that the research was conducted in the absence of any commercial or financial relationships that could be construed as a potential conflict of interest.

Publisher's note

References

Bai, R. G., and Husseini, G. A. (2019). "Graphene-based drug delivery systems," in *Biomimetic nanoengineered Materials for advanced drug delivery* (Amsterdam, Netherlands: Elsevier), 149–168.

Bauhuber, S., Hozsa, C., Breunig, M., and Göpferich, A. (2009). Delivery of nucleic acids via disulfide-based carrier systems. *Adv. Mater.* 21, 3286–3306. doi:10.1002/adma.200802453

Bawa, P., Pillay, V., Choonara, Y. E., and Du Toit, L. C. (2009). Stimuli-responsive polymers and their applications in drug delivery. *Biomed. Mater.* 4, 022001. doi:10.1088/1748-6041/4/2/022001

Boddu, A., Obireddy, S. R., Zhang, D., Rao, K. K., and Lai, W.-F. (2022). ROS-generating, pH-responsive and highly tunable reduced graphene oxide-embedded microbeads showing intrinsic anticancer properties and multi-drug co-delivery capacity for combination cancer therapy. *Drug Deliv.* 29, 2481–2490. doi:10.1080/10717544.2022.2100512

Chamundeeswari, M., Jeslin, J., and Verma, M. L. (2019). Nanocarriers for drug delivery applications. *Environ. Chem. Lett.* 17, 849–865. doi:10.1007/s10311-018-00841-1

Charmi, J., Nosrati, H., Amjad, J. M., Mohammadkhani, R., and Danafar, H. (2019). Polyethylene glycol (PEG) decorated graphene oxide nanosheets for controlled release curcumin delivery. *Heliyon* 5, e01466. doi:10.1016/j.heliyon.2019.e01466

Chen, H., Liu, D., and Guo, Z. (2016). Endogenous stimuli-responsive nanocarriers for drug delivery. *Chem. Lett.* 45, 242–249. doi:10.1246/cl.151176

Chen, Y., Cheng, W., Teng, L., Jin, M., Lu, B., Ren, L., et al. (2018). Graphene oxide hybrid supramolecular hydrogels with self-healable, bioadhesive and stimuli-responsive properties and drug delivery application. *Macromol. Mater. Eng.* 303, 1700660. doi:10.1002/mame.201700660

Cirillo, G., Gianfranco Spizzirri, U., Curcio, M., Hampel, S., Vittorio, O., Restuccia, D., et al. (2016). Carbon nanohybrids as electro-responsive drug delivery systems. *Mini Rev. Med. Chem.* 16, 658–667. doi:10.2174/1389557515666150709104444

Du, P., Yan, J., Long, S., Xiong, H., Wen, N., Cai, S., et al. (2020). Tumor microenvironment and NIR laser dual-responsive release of berberine 9-O-pyrazole alkyl derivative loaded in graphene oxide nanosheets for chemo-photothermal synergetic cancer therapy. *J. Mater. Chem. B* 8, 4046–4055. doi:10.1039/d0tb00489h

Ghawanmeh, A. A., Ali, G. A., Algarni, H., Sarkar, S. M., and Chong, K. F. (2019). Graphene oxide-based hydrogels as a nanocarrier for anticancer drug delivery. *Nano Res.* 12, 973–990. doi:10.1007/s12274-019-2300-4

Goenka, S., Sant, V., and Sant, S. (2014). Graphene-based nanomaterials for drug delivery and tissue engineering. *J. Control. Release* 173, 75–88. doi:10.1016/j.jconrel.2013.10.017

Havanur, S., and Jagadeeshbabu, P. (2018). Role of graphene quantum dots synthesized through pyrolysis in the release behavior of temperature responsive poly (N, N-diethyl acrylamide) hydrogel loaded with doxorubicin. *Int. J. Polym. Analysis Charact.* 23, 606–620. doi:10.1080/1023666x.2018.1484207

He, Q., Kiesewetter, D. O., Qu, Y., Fu, X., Fan, J., Huang, P., et al. (2015). NIR-responsive on-demand release of CO from metal carbonyl-caged graphene oxide nanomedicine. *Adv. Mater. Deerf. Beach, Fla.)* 27, 6741–6746. doi:10.1002/adma.201502762

Henna, T., and Pramod, K. (2020). Graphene quantum dots redefine nanobiomedicine. *Mater. Sci. Eng. C* 110, 110651. doi:10.1016/j.msec.2020.110651

Hossen, S., Hossain, M. K., Basher, M., Mia, M., Rahman, M., and Uddin, M. J. (2019). Smart nanocarrier-based drug delivery systems for cancer therapy and toxicity studies: A review. *J. Adv. Res.* 15, 1–18. doi:10.1016/j.jare.2018.06.005

Kamaly, N., Yameen, B., Wu, J., and Farokhzad, O. C. (2016). Degradable controlled-release polymers and polymeric nanoparticles: Mechanisms of controlling drug release. *Chem. Rev.* 116, 2602–2663. doi:10.1021/acs.chemrev.5b00346

Kavitha, T., Abdi, S. I. H., and Park, S.-Y. (2013). pH-sensitive nanocargo based on smart polymer functionalized graphene oxide for site-specific drug delivery. *Phys. Chem. Chem. Phys.* 15, 5176–5185. doi:10.1039/c3cp00008g

Kim, D. J., Kim, J., Lee, H. L., Lee, S., Choi, J. S., Kim, S. J., et al. (2018). Redox-Responsive Nanocomposites Composed of Graphene Oxide and Chlorin e6 for Photodynamic Treatment of Cholangiocarcinoma. *Bull. Korean Chem. Soc.* 39, 1073–1082. doi:10.1002/bkcs.11552

Kim, H., Chung, K., Lee, S., Kim, D. H., and Lee, H. (2016). Near-infrared light-responsive nanomaterials for cancer theranostics. *Wiley Interdiscip. Rev. Nanomedicine Nanobiotechnology* 8, 23–45. doi:10.1002/wnan.1347

Kim, H., Lee, D., Kim, J., Kim, T.-I., and Kim, W. J. (2013). Photothermally triggered cytosolic drug delivery via endosome disruption using a functionalized reduced graphene oxide. *ACS Nano* 7, 6735–6746. doi:10.1021/nn403096s

Kost, J., and Langer, R. (2012). Responsive polymeric delivery systems. *Adv. drug Deliv. Rev.* 64, 327–341. doi:10.1016/j.addr.2012.09.014

Leganés, J., Sánchez-Migallón, A., Merino, S., and Vázquez, E. (2020). Stimuli-responsive graphene-based hydrogel driven by disruption of triazine hydrophobic interactions. *Nanoscale* 12, 7072–7081. doi:10.1039/c9nr10588c

Li, Y., Feng, L., Shi, X., Wang, X., Yang, Y., Yang, K., et al. (2014). Surface coating-dependent cytotoxicity and degradation of graphene derivatives: Towards the design of non-toxic, degradable nano-graphene. *Small* 10, 1544–1554. doi:10.1002/smll.201303234

Liu, H.-W., Hu, S.-H., Chen, Y.-W., and Chen, S.-Y. (2012). Characterization and drug release behavior of highly responsive chip-like electrically modulated reduced graphene oxide–poly (vinyl alcohol) membranes. *J. Mater. Chem.* 22, 17311–17320. doi:10.1039/c2jm32772d

Liu, J., Cui, L., and Losic, D. (2013). Graphene and graphene oxide as new nanocarriers for drug delivery applications. *Acta biomater.* 9, 9243–9257. doi:10.1016/j.actbio.2013.08.016

Liu, Z., Robinson, J. T., Tabakman, S. M., Yang, K., and Dai, H. (2011). Carbon materials for drug delivery & cancer therapy. *Mater. today* 14, 316–323. doi:10.1016/s1369-7021(11)70161-4

Ma, X., Qu, Q., Zhao, Y., Luo, Z., Zhao, Y., Ng, K. W., et al. (2013). Graphene oxide wrapped gold nanoparticles for intracellular Raman imaging and drug delivery. *J. Mater. Chem. B* 1, 6495–6500. doi:10.1039/c3tb21385d

Manzano, M., and Vallet-Regí, M. (2020). Mesoporous silica nanoparticles for drug delivery. *Adv. Funct. Mater.* 30, 1902634. doi:10.1002/adfm.201902634

Mauri, E., Salvati, A., Cataldo, A., Mozetic, P., Basoli, F., Abbruzzese, F., et al. (2021). Graphene-laden hydrogels: A strategy for thermally triggered drug delivery. *Mater. Sci. Eng. C* 118, 111353. doi:10.1016/j.msec.2020.111353

Mendes, R. G., Bachmatiuk, A., Büchner, B., Cuniberti, G., and Rümmeli, M. H. (2013). Carbon nanostructures as multi-functional drug delivery platforms. *J. Mater. Chem. B* 1, 401–428. doi:10.1039/c2tb00085g

Mo, R., Jiang, T., Sun, W., and Gu, Z. (2015). ATP-responsive DNA-graphene hybrid nanoaggregates for anticancer drug delivery. *Biomaterials* 50, 67–74. doi:10.1016/j.biomaterials.2015.01.053

Mura, S., Nicolas, J., and Couvreur, P. (2013). Stimuli-responsive nanocarriers for drug delivery. *Nat. Mater.* 12, 991–1003. doi:10.1038/nmat3776

Murdan, S. (2003). Electro-responsive drug delivery from hydrogels. *J. Control. release* 92, 1–17. doi:10.1016/s0168-3659(03)00303-1

Muzi, L., Seifert, C., Soltani, R., Ménard-Moyon, C., Dumortier, H., and Bianco, A. (2021). Targeting B lymphocytes using protein-functionalized graphene oxide. *Adv. NanoBiomed Res.* 1, 2100060. doi:10.1002/anbr.202100060

Olate-Moya, F., and Palza, H. (2022). Effect of graphene oxide on the pH-responsive drug release from supramolecular hydrogels. *J. Appl. Polym. Sci.* 139, 51420. doi:10.1002/app.51420

Patil, T. V., Patel, D. K., Dutta, S. D., Ganguly, K., and Lim, K.-T. (2021). Graphene oxide-based stimuli-responsive platforms for biomedical applications. *Molecules* 26, 2797. doi:10.3390/molecules26092797

Rahmani, E., Pourmadadi, M., Zandi, N., Rahdar, A., and Baino, F. (2022). pH-responsive PVA-based nanofibers containing GO modified with Ag nanoparticles: Physico-chemical characterization, wound dressing, and drug delivery. *Micromachines* 13, 1847. doi:10.3390/mi13111847

Raza, A., Rasheed, T., Nabeel, F., Hayat, U., Bilal, M., and Iqbal, H. M. (2019). Endogenous and exogenous stimuli-responsive drug delivery systems for programmed site-specific release. *Molecules* 24, 1117. doi:10.3390/molecules24061117

Sahoo, D., Mitra, T., Chakraborty, K., and Sarkar, P. (2022). Remotely controlled electro-responsive on-demand nanotherapy based on amine-modified graphene oxide for synergistic dual drug delivery. *Mater. Today Chem.* 25, 100987

Samadian, H., Mohammad-Rezaei, R., Jahanban-Esfahlan, R., Massoumi, B., Abbasian, M., Jafarizad, A., et al. (2020). A de novo theranostic nanomedicine composed of PEGylated graphene oxide and gold nanoparticles for cancer therapy. *J. Mater. Res.* 35, 430–441. doi:10.1557/jmr.2020.3

Saravanakumar, G., Kim, J., and Kim, W. J. (2017). Reactive-oxygen-species-responsive drug delivery systems: Promises and challenges. *Adv. Sci.* 4, 1600124. doi:10.1002/advs.201600124

Sattari, M., Fathi, M., Daei, M., Erfan-Niya, H., Barar, J., and Entezami, A. A. (2017). Thermoresponsive graphene oxide–starch micro/nanohydrogel composite as biocompatible drug delivery system. *BioImpacts BI* 7, 167–175. doi:10.15171/bi.2017.20

Sattari, S., Adeli, M., Beyranvand, S., and Nemati, M. (2021). Functionalized graphene platforms for anticancer drug delivery. *Int. J. Nanomedicine* 16, 5955–5980. doi:10.2147/ijn.s249712

Servant, A., Leon, V., Jasim, D., Methven, L., Limousin, P., Fernandez-Pacheco, E. V., et al. (2014). Graphene-based electroresponsive scaffolds as polymeric implants for on-demand drug delivery. *Adv. Healthc. Mater.* 3, 1334–1343. doi:10.1002/adhm.201400016

Sima, L. E., Chiritoiu, G., Negut, I., Grumezescu, V., Orobeti, S., Munteanu, C. V., et al. (2020). Functionalized graphene oxide thin films for anti-tumor drug delivery to melanoma cells. *Front. Chem.* 8, 184. doi:10.3389/fchem.2020.00184

Song, E., Han, W., Li, C., Cheng, D., Li, L., Liu, L., et al. (2014). Hyaluronic acid-decorated graphene oxide nanohybrids as nanocarriers for targeted and pH-responsive anticancer drug delivery. *ACS Appl. Mater. interfaces* 6, 11882–11890. doi:10.1021/am502423r

Song, J., Qu, J., Swihart, M. T., and Prasad, P. N. (2016). Near-IR responsive nanostructures for nanobiophotonics: Emerging impacts on nanomedicine. *Nanomedicine Nanotechnol. Biol. Med.* 12, 771–788. doi:10.1016/j.nano.2015.11.009

Song, S., Shen, H., Wang, Y., Chu, X., Xie, J., Zhou, N., et al. (2020). Biomedical application of graphene: From drug delivery, tumor therapy, to theranostics. *Colloids Surfaces B Biointerfaces* 185, 110596. doi:10.1016/j.colsurfb.2019.110596

Sun, X., Liu, Z., Welsher, K., Robinson, J. T., Goodwin, A., Zaric, S., et al. (2008). Nano-graphene oxide for cellular imaging and drug delivery. *Nano Res.* 1, 203–212. doi:10.1007/s12274-008-8021-8

Sun, Z., Song, C., Wang, C., Hu, Y., and Wu, J. (2019). Hydrogel-based controlled drug delivery for cancer treatment: A review. *Mol. Pharm.* 17, 373–391. doi:10.1021/acs.molpharmaceut.9b01020

Tao, C.-A., Wang, J., Qin, S., Lv, Y., Long, Y., Zhu, H., et al. (2012). Fabrication of pH-sensitive graphene oxide–drug supramolecular hydrogels as controlled release systems. *J. Mater. Chem.* 22, 24856–24861. doi:10.1039/c2jm34461k

Timko, B. P., Dvir, T., and Kohane, D. S. (2010). Remotely triggerable drug delivery systems. *Adv. Mater.* 22, 4925–4943. doi:10.1002/adma.201002072

Trachootham, D., Alexandre, J., and Huang, P. (2009). Targeting cancer cells by ROS-mediated mechanisms: A radical therapeutic approach? *Nat. Rev. Drug Discov.* 8, 579–591. doi:10.1038/nrd2803

Tran, A.-V., Shim, K., Thi, T.-T. V., Kook, J.-K., An, S. S. A., and Lee, S.-W. (2018). Targeted and controlled drug delivery by multifunctional mesoporous silica nanoparticles with internal fluorescent conjugates and external polydopamine and graphene oxide layers. *Acta biomater.* 74, 397–413. doi:10.1016/j.actbio.2018.05.022

Wang, K., Liu, N., Zhang, P., Guo, Y., Zhang, Y., Zhao, Z., et al. (2016). Synthetic methods of disulfide bonds applied in drug delivery systems. *Curr. Org. Chem.* 20, 1477–1489. doi:10.2174/1385272820666151207194002

Wang, X., Guo, W., Li, L., Yu, F., Li, J., Liu, L., et al. (2021). Photothermally triggered biomimetic drug delivery of Teriparatide via reduced graphene oxide loaded chitosan hydrogel for osteoporotic bone regeneration. *Chem. Eng. J.* 413, 127413. doi:10.1016/j.cej.2020.127413

Wang, Y., Li, Z., Wang, J., Li, J., and Lin, Y. (2011). Graphene and graphene oxide: Biofunctionalization and applications in biotechnology. *Trends Biotechnol.* 29, 205–212. doi:10.1016/j.tibtech.2011.01.008

Wang, Z., Colombi Ciacchi, L., and Wei, G. (2017). Recent advances in the synthesis of graphene-based nanomaterials for controlled drug delivery. *Appl. Sci.* 7, 1175. doi:10.3390/app7111175

Weaver, C. L., Larosa, J. M., Luo, X., and Cui, X. T. (2014). Electrically controlled drug delivery from graphene oxide nanocomposite films. *ACS Nano* 8, 1834–1843. doi:10.1021/nn406223e

Wu, J., Qin, Z., Jiang, X., Fang, D., Lu, Z., Zheng, L., et al. (2022). ROS-responsive PPGF nanofiber membrane as a drug delivery system for long-term drug release in attenuation of osteoarthritis. *npj Regen. Med.* 7, 66. doi:10.1038/s41536-022-00254-3

Xiao, Z., Ji, C., Shi, J., Pridgen, E. M., Frieder, J., Wu, J., et al. (2012). DNA self-assembly of targeted near-infrared-responsive gold nanoparticles for cancer thermo-chemotherapy. *Angew. Chem.* 124, 12023–12027. doi:10.1002/ange.201204018

Xie, F., Wang, M., Chen, Q., Chi, T., Zhu, S., Wei, P., et al. (2022). Endogenous stimuli-responsive nanoparticles for cancer therapy: From bench to bedside. *Pharmacol. Res.* 186, 106522. doi:10.1016/j.phrs.2022.106522

Yang, G., Li, L., Lee, W. B., and Ng, M. C. (2018). Structure of graphene and its disorders: A review. *Sci. Technol. Adv. Mater.* 19, 613–648. doi:10.1080/14686996.2018.1494493

Yang, K., Feng, L., and Liu, Z. (2016). Stimuli responsive drug delivery systems based on nano-graphene for cancer therapy. *Adv. drug Deliv. Rev.* 105, 228–241. doi:10.1016/j.addr.2016.05.015

Yang, K., Feng, L., and Liu, Z. (2015). The advancing uses of nano-graphene in drug delivery. *Expert Opin. drug Deliv.* 12, 601–612. doi:10.1517/17425247.2015.978760

Yang, X., Zhang, X., Liu, Z., Ma, Y., Huang, Y., and Chen, Y. (2008). High-efficiency loading and controlled release of doxorubicin hydrochloride on graphene oxide. *J. Phys. Chem. C* 112, 17554–17558. doi:10.1021/jp806751k

Yu, W., Sisi, L., Haiyan, Y., and Jie, L. (2020). Progress in the functional modification of graphene/graphene oxide: A review. *RSC Adv.* 10, 15328–15345. doi:10.1039/d0ra01068e

Zhang, Q., Wu, Z., Li, N., Pu, Y., Wang, B., Zhang, T., et al. (2017). Advanced review of graphene-based nanomaterials in drug delivery systems: Synthesis, modification, toxicity and application. *Mater. Sci. Eng. C* 77, 1363–1375. doi:10.1016/j.msec.2017.03.196

Zhang, Z., Shi, J., Song, Z., Zhu, X., Zhu, Y., and Cao, S. (2018). A synergistically enhanced photothermal transition effect from mesoporous silica nanoparticles with gold nanorods wrapped in reduced graphene oxide. *J. Mater. Sci.* 53, 1810–1823. doi:10.1007/s10853-017-1628-y

Zhao, Y., Tavares, A. C., and Gauthier, M. A. (2016). Nano-engineered electro-responsive drug delivery systems. *J. Mater. Chem. B* 4, 3019–3030. doi:10.1039/c6tb00049e

Zheng, X. T., Ananthanarayanan, A., Luo, K. Q., and Chen, P. (2015). Glowing graphene quantum dots and carbon dots: Properties, syntheses, and biological applications. *small* 11, 1620–1636. doi:10.1002/smll.201402648

Zhu, Y. J., and Chen, F. (2015). pH-responsive drug-delivery systems. *Chemistry–An Asian J.* 10, 284–305. doi:10.1002/asia.201402715

Zhu, Y., Murali, S., Cai, W., Li, X., Suk, J. W., Potts, J. R., et al. (2010). Graphene and graphene oxide: Synthesis, properties, and applications. *Adv. Mater.* 22, 3906–3924. doi:10.1002/adma.201001068

frontiers | Frontiers in Bioengineering and Biotechnology

TYPE Review
PUBLISHED 20 February 2023
DOI 10.3389/fbioe.2023.1111977

OPEN ACCESS

EDITED BY
Guoqing Pan,
Jiangsu University, China

REVIEWED BY
Chaoliang He,
Changchun Institute of Applied Chemistry (CAS), China
Qun Treen Huo,
University of Central Florida, United States

*CORRESPONDENCE
Binghai Chen,
chenbhny@163.com

SPECIALTY SECTION
This article was submitted to Biomaterials, a section of the journal Frontiers in Bioengineering and Biotechnology

RECEIVED 30 November 2022
ACCEPTED 07 February 2023
PUBLISHED 20 February 2023

CITATION
Qian Z, Zhang Y, Yuan J, Gong S and Chen B (2023), Current applications of nanomaterials in urinary system tumors. *Front. Bioeng. Biotechnol.* 11:1111977. doi: 10.3389/fbioe.2023.1111977

Current applications of nanomaterials in urinary system tumors

Zhounan Qian, Yang Zhang, Jie Yuan, Sun Gong and Binghai Chen*

Department of Urology, Affiliated Hospital of Jiangsu University, Zhenjiang, China

The development of nanotechnology and nanomaterials has provided insights into the treatment of urinary system tumors. Nanoparticles can be used as sensitizers or carriers to transport drugs. Some nanoparticles have intrinsic therapeutic effects on tumor cells. Poor patient prognosis and highly drug-resistant malignant urinary tumors are worrisome to clinicians. The application of nanomaterials and the associated technology against urinary system tumors offers the possibility of improving treatment. At present, many achievements have been made in the application of nanomaterials against urinary system tumors. This review summarizes the latest research on nanomaterials in the diagnosis and treatment of urinary system tumors and provides novel ideas for future research on nanotechnologies in this field.

KEYWORDS

mesoporous silica nanoparticles (MSN), gold nanoparticles (Au NPs), carbon nanotubes, magnetic nanoparticles (MNP), urinary tumors, quantum dots, liposome

1 Introduction

The development of nanotechnology has brought new breakthroughs in the diagnosis and treatment of cancer (Wakaskar, 2018; Chaturvedi et al., 2019; Khan et al., 2020). Nanoparticles are usually loaded with therapeutic drugs, proteins, photothermal agents, imaging agents or immune molecules (Liu et al., 2018). Nanoparticles are modified on demand, and those with recognizable ligands are easily taken up by target cells after receptor–ligand interactions (Song et al., 2017). Nanoparticles are powerful drug carriers and can increase drug uptake by tumors by prolonging drug circulation and reducing the risk of adverse toxic effects on nearby healthy tissue (Ahmed et al., 2012).

Urinary system tumors are common malignant tumors in humans with gradually increasing incidence (Siegel et al., 2019). The treatment of urinary system tumors is diverse. For example, chemotherapy and radiotherapy are the main treatment strategies for advanced renal cancer. However, drug resistance is very common (Penticuff and Kyprianou, 2015). Nanotechnology can be used to enhance the therapeutic effects of cancer drugs (Jaishree and Gupta, 2012). Although targeted therapy and immunotherapy are widely used, resistance to these modalities is inevitable, and the development of nanomaterials provides an alternative direction. Moreover, traditional treatment methods, such as surgery, radiotherapy and endocrine therapy, are facing great challenges. The development of nanomaterials provides novel ideas for the treatment of urinary tract tumors. Thus, this review summarizes the applications of several nanomaterials commonly used to treat urinary tract tumors.

10.3389/fbioe.2023.1111977

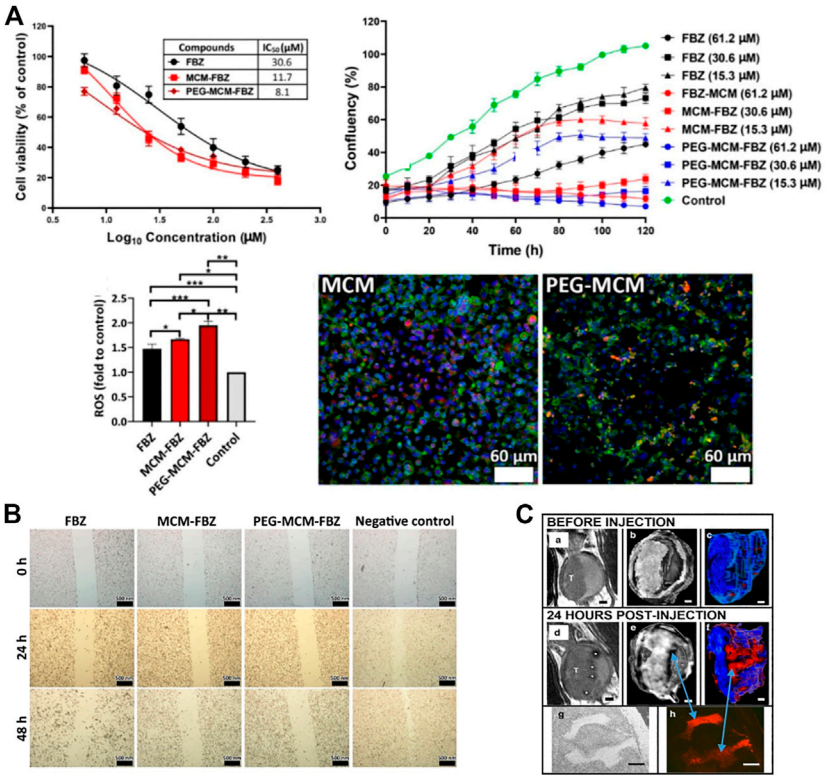

FIGURE 1
Synthesis and applications of mesoporous silica nanoparticles (MSNs). **(A)** The cytotoxicity of FBZ increased when it was bound the nanomaterial. Moreover, the inhibition of prostate cancer (PCa) cell proliferation was significantly increased. The intracellular ROS contents were also increased, thus inhibiting the proliferation of tumor cells. Fluorescence experiments showed that the FBZ complexes, especially the PEG-MCM-FBZ complex, increased the uptake of FBZ. **(B)** The complex effectively inhibits the migration of PCa cells. **(C)** Bladder tumor cells absorbed PEG-Gd_2O_3-TRITC-MSN particles with higher affinity than normal bladder epithelial cells and can be used for MRI T2 scanning.

2 Mesoporous silica nanoparticles (MSNs)

MSNs have well-defined mesoporous structures with diameters ranging from 2 to 10 nm, large pore volumes of 0.6–1 cm^3/g and high surface areas of 700–1,000 m^2/g (Iturrioz-Rodriguez et al., 2019). MSNs have certain characteristics, such as a uniform structure, large surface area, and modifiable pore size, and work as a suitable repository for loading therapeutic/diagnostic agents. MSNs protect their cargo from premature release and subsequent undesirable degradation in the stomach and intestine until they reach the target location (He and Shi, 2014; Nawaz et al., 2018). MSNs in the size range of 50–300 nm can promote endocytosis in living animal and plant cells without producing any significant cytotoxicity. In drug delivery and cancer treatment, the particle size of nanocarriers must be less than 100 nm to circulate in blood vessels for a long time and serve as a passive drug delivery carriers based on enhanced permeability and retention (EPR) effects. On the other hand, the pore sizes of MSNs can be adjusted from 2 to 6 nm, which allows the loading of different drug molecules. Therefore, MSNs have high drug loading and packaging efficiency (Porrang et al., 2022).

2.1 Application of MSNs in PCa

MSNs can be used in the treatment of PCa. Many researchers have used MSNs as carriers to load therapeutic drugs, and MSNs can deliver these drugs to tumor cells. For example, the study of Zanib Chaudhary et al. investigated resveratrol (RES), a polyphenol with antitumor properties. However, its poor pharmacokinetics and stability and low solubility limit its clinical application. Loading RES onto MSNs can significantly improve the efficacy of RES in PCa (Chaudhary et al., 2019). Fenbendazole (FBZ) is a potential anticancer drug whose application is limited by its low water solubility. The water solubility of FBZ can be increased when serialized on β-lactoglobulin-modified MSNs, which can increase the cytotoxicity of FBZ and inhibit the migration of PCa cells (Koohi et al., 2022). (Figures 1A,B) It is also possible to serialize FBZ on pegylated MSN (MCM-41) to improve its cytotoxicity and increase its delivery to PCa cells (Esfahani et al., 2021).

Studies have found that functionalized MSNs themselves can also inhibit tumors. *Walterinnesia aegyptia* venom (WEV) serialized on MSNs is more effective than WEV alone. Researchers have also demonstrated that snake venom silica nanoparticles could alter the cell cycle in PCa cells and accelerate cell apoptosis. A study showed that the continuous delivery of nanoparticles carrying WEV is an

effective treatment for PCa (Badr et al., 2013). pH-sensitive delivery systems can provide on-demand and selective drug release at acidic tumor sites. Polyacrylic acid (PAA)-functionalized MSNs (PAA-MSNs) can be used as an effective pH response template with great potential for effective controlled release in cancer therapy. PAA-MSNs also showed strong cellular uptake and a longer circulation time *in vivo*, and good results were obtained when they were linked to bicalutamide for the treatment of PCa (Saroj and Rajput, 2019). Researchers also linked etoposide (ETS) to PAA-MSNs, which greatly increased the cytotoxicity of ETS (Saroj and Rajput, 2018). Moreover, when calcium peroxide (CaO_2) was loaded into PAA-MSNs, free CaO_2 without antitumor effects can release reactive oxygen species (ROS) in response to the acidic microenvironment. This induces mitochondria-mediated apoptosis through significant oxidative stress, minimizes damage to normal tissues, and exerts excellent antitumor effects. This system represents a new way to treat PCa (Wu et al., 2020).

MSNs can also be used to diagnose PCa. Researchers developed an electrochemical immunosensor based on MSNs (Wang et al., 2013). Other researchers designed MSNs containing pH indicator molecules for PCa detection, which can improve the sensitivity of detecting prostate-specific antigen (PSA) (Shao et al., 2018). PSA-targeted manganese-oxide MSNs were found to be useful for detecting PCa, as they can accumulate in PCa cells but not in non-cancerous cells. PCa can be visualized using PSA-targeted fluorescence and Magnetic Resonance (MR) dual-function nanoparticles. They can be used as an MR contrast agent (Du et al., 2020). It is generally harder to detect low molecular weight biomarkers *in vivo* by traditional spectrometric methods, as they often exist in low concentrations and are covered by many other proteins. In fact, studies have shown that less than 25% of PCa cases with increased PSA levels were diagnosed appropriately.

In addition, a second biopsy can diagnose PCa in approximately 30% of patients with a previously benign biopsy result. Researchers have designed diagnostic systems for PCa. These use mercaptan MSN (MSN-SH) to detect low molecular weight proteins and distinguish between patients with benign prostatic hyperplasia and those with PCa with elevated PSA levels (Vidaurre-Agut et al., 2019).

2.2 Application of MSNs in bladder cancer

Researchers have linked targeted doxorubicin (DOX) to MSNs and the peptide conjugate CSNRDARRC (DOX-loaded MSNs@PDA-PEP) to form a complex. Further study suggested that the complex significantly improved cell uptake efficiency compared with DOX alone (Wei et al., 2017). Researchers invented a compound based on MSNs and found that 70% of bladder cancer cells were labeled by nanoparticles. The tumor contrast was enhanced by the nanoparticles, which could be used for tumor staging, treatment monitoring and drug delivery (Sweeney et al., 2016). At present, there are many studies on microRNAs, indicating that these RNAs have antitumor effects. Researchers have reported combinations of microRNA and MSNs as delivery agents. The uptake of these multifunctional nanoparticles by bladder cancer cells overexpressing EGFR was enhanced *via* receptor-mediated cellular internalization (Haddick et al., 2020). Moreover, modified MSNs were constructed and used as delivery carriers to deliver both miRNA-34a and si-PD-L1 to bladder cancer cells. Notably, the nanoparticles were biocompatible, which protects the compound from degradation. Therefore, this system could be used as a treatment for bladder cancers (Shahidi et al., 2022).

2.3 Application of MSNs in renal cancer

Lonidamine (LND), a heat-sensitive inhibitor of mitochondrial metabolism, was used in combination with photothermal-polydopamine (PDA) in the treatment of renal cell carcinoma (RCC). LND and PDA were loaded into MSNs with a star shape. The results indicated that the complex had excellent tumor targeting ability. LND and PDA combined with laser treatment enhanced the antiproliferation and anticancer abilities with good biocompatibility (Chen et al., 2021).

3 Gold nanoparticles (AuNPs)

Gold nanoparticles (AuNPs) have attracted great attention in biomedicine (Pissuwan et al., 2011; Dykman and Khlebtsov, 2012). AuNPs have large surfaces and different properties and are of great potential in diagnosis, delivery, photothermal and radiation therapy, enzyme fixation, and cell imaging (Zhang et al., 2010; Li et al., 2011; Nimesh et al., 2011; Pissuwan et al., 2011). AuNPs come in very diverse shapes, although spherical nanoparticles are thought to be the main type. Depending on the production method, AuNPs can be made in different forms: triangles, hexagons, octahedrons, cells, nanospheres, pores, stars, and nanorods (Ovais et al., 2017). The different form determines what the AuNP carries (Boisselier and Astruc, 2009). AuNPs can interact with biological fluids, and the nanoparticles acquire a biological component known as a protein corona (PC) (Maiorano et al., 2010; Corbo et al., 2016; Rampado et al., 2020). Thus, AuNPs can be widely used in the medical field.

3.1 Application of AuNPs in PCa

AuNPs can be used to detect PCa. Researchers designed a sensitive electrochemical immunosensor for the determination of PSA. AuNP/aminothiol-functionalized graphene-oxide composites were constructed and modified before they were used as an immunosensor platform to elevate the amount of PSA antibody 1 (Ab1) for PSA determination (Medetalibeyoglu et al., 2020). Studies have detected PCA3, a potential urinary biomarker, in urine using AuNPs (Htoo et al., 2019). Based on supramolecular hydrogel-AuNP spheres, an imaging biosensor with high sensitivity and specificity was developed for the determination of exosomes derived from PCa cells (Chen et al., 2020). The gold nanoprobes consisted of a specific peptide, and the AuNPs were used for the determination of PSA (Li et al., 2019a). Studies evaluated AuNPs *in vitro* and *in vivo* and found that these nanoparticles showed good potential features for cancer cell uptake and biodistribution and could also be used to detect PCa by fluorescence imaging (Pretze et al., 2018). (Figure 2A)

10.3389/fbioe.2023.1111977

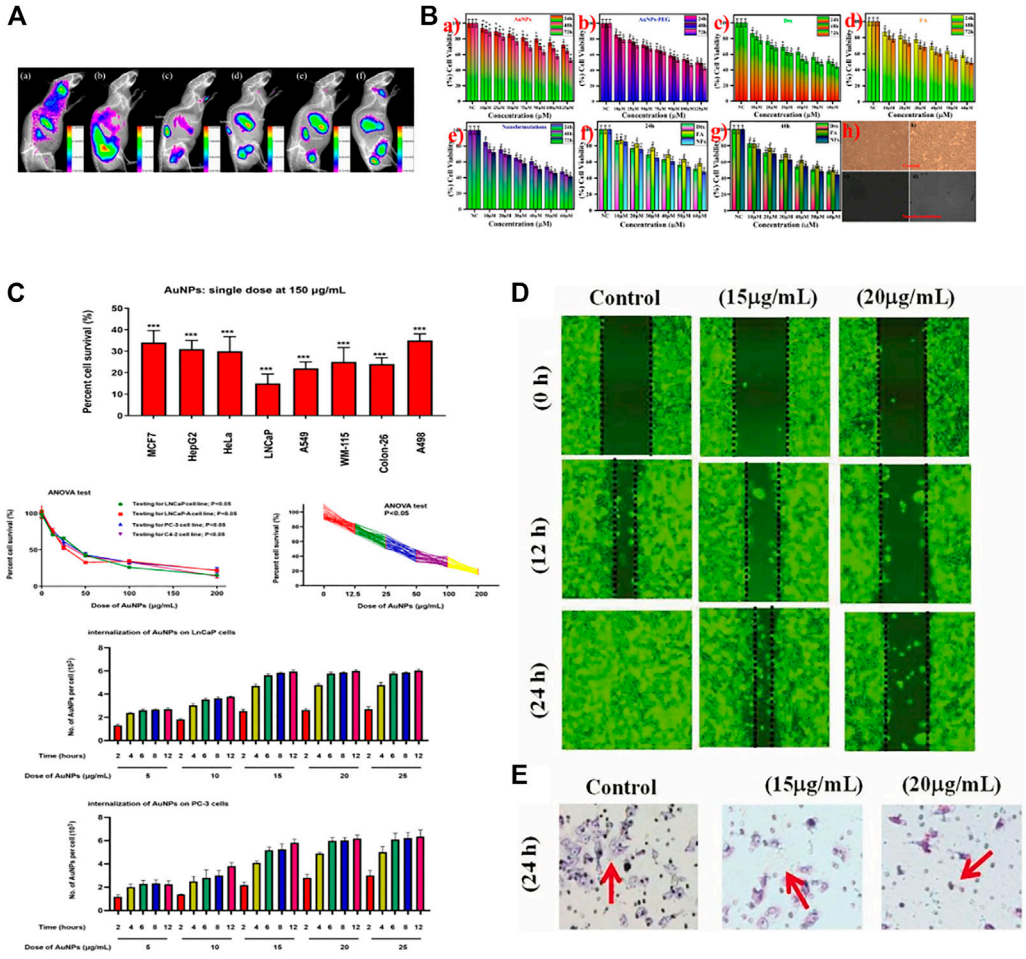

FIGURE 2
Applications of gold nanoparticles (AuNPs) in cancer. **(A)** PCA cells were treated with ultrafine AuNPs containing the gastrin-releasing peptide receptor. After 72 h, up to 6% of the AuNPs remained in the body, which could be used to detect PCa. **(B)** Docetaxel-coated AuNPs showed toxicity to PCa cells *in vitro*. **(C)** AuNPs were found to be toxic to eight types of tumor cells, most notably to PCa cells, showing toxic effects to all PCa cells tested. **(D)** AuNPs synthesized from abies fir plant extracts inhibited bladder cancer T24 cell migration in a concentration-dependent manner. **(E)** AuNPs mediated T24 cell death.

The application of AuNPs in the treatment of PCa is also very extensive. AuNPs can be used as carriers to deliver antitumor drugs to PCa cells. Researchers synthesized novel AuNPs conjugated with abiraterone (AuNPs-AB), which have shown good prospects for the treatment of PCa (Stolarczyk et al., 2020). Docetaxel (Dtx) was encapsulated by AuNPs for delivery to PCa cells (Thambiraj et al., 2021). A synthetic Gen-AuNP conjugate (Gen@AuNPs) selectively inhibited the proliferation of PCa cells. The authors also demonstrated the stability and bioactivity of the AuNPs along with their low toxicity to normal cells (Vodnik et al., 2021). Phosphatidylserine (PS) is an essential lipid that mediates macrophage exocytosis and is dysregulated in tumors. Biomimetic phosphatidylserine-coated AuNPs (PS-AuNPs) were synthesized, and their potential in PCa was investigated *in vitro*. After evaluating histone-associated DNA fragments as a marker of apoptosis, the researchers found that DNA fragmentation was significantly increased after PS-AuNP treatment compared with control treatment. Therefore, PS-AuNPs were indicated as a potential PCa treatment (Radaic et al., 2021).

AuNPs themselves can also be therapeutic for PCa. AuNPs have been shown to exert powerful cytotoxic effects, with synthetic AuNPs showing the most significant efficacy against PCa, whether or not the tumor cells were androgen-dependent. Further studies on the molecular mechanism showed that AuNPs can trigger the secretion of anticancer factors and myeloid cell-polarizing factors from tumor cells through MMP9 inhibition, thereby achieving antitumor effects (Hao et al., 2021). (Figure 2C) The same AuNPs decay at a high energy level and their radiation can be delivered to the tumor site without destroying the normal tissues or organs. Using AuNPs is a promising way to treat PCa (Al-Yasiri et al., 2019). AuNPs have also been widely used to treat PCa due to their unique optical properties. A silicon dioxide-coated AuNP cluster was proposed to address the therapeutic limitations of individual AuNPs and utilize their photothermal effects to treat typical PCa PC-3 cells. AuNP clusters have shown excellent therapeutic effects in photothermal tests under near-infrared radiation (Kim et al., 2020).

The combination of AuNPs and Gd(III) provides better cancer inhibition after radiotherapy. Precise tumor targeting by PSMA-1-modified AuNPs can achieve precise radiotherapy, reduce the irradiation dose, and minimize side effects (Luo et al., 2020). AuNPs are also effective radiosensitizers, and RALA (a short amphiphilic peptide)/AuNPs were synthesized, providing functional evidence of RALA-AuNP nuclear accumulation. RALA-AuNP produced meaningful radiosensitization using low microgram AuNP treatment concentrations (Bennie et al., 2021).

3.2 Application of AuNPs in RCC

Few studies of AuNPs in RCC have been reported. Researchers have found that 200 nm AuNPs have an antitumor effect in 786-O RCC cells by promoting cell apoptosis and inhibiting proliferation (Zhao et al., 2020). C. wenyujin is the main component of turmeric and has antioxidant, antiproliferative and antitumor properties. Researchers used C. wenyujin to synthesize AuNPs and found that the produced CW-AuNPs could activate the proapoptotic proteins caspase-3, caspase-9, Bid and Bad in renal cancer A498 cells *in vitro*. CW-AuNPs can reduce the level of Bcl-2 and thereby induce apoptosis of A498 cells (Liu et al., 2019). Other studies have found that AuNP treatment reduces the viability of cancer cells, suggesting a potential alternative to nephrectomy (Nikzad et al., 2017).

3.3 Application of AuNPs in bladder cancer

Hyaluronidase (HAase) is a bladder cancer biomarker found in urine. HAase can prevent the redshift observed when cationic gold nanoparticles (CTAB) aggregate with other substances. Therefore, this color change can be used for the diagnosis of bladder cancer (Nossier et al., 2014). Other researchers considered urine hepatocellular carcinoma upregulated RNA (HURP) as a biomarker of bladder cancer and developed a AuNP assay to directly detect unamplified HURP RNA for bladder cancer diagnosis (Eissa et al., 2014).

AuNPs can also be used in the treatment of bladder cancer. Researchers found that by combining fir extract with AuNPs, apoptosis of tumor cells could be promoted to play an anticancer role (Wu et al., 2019). (Figures 2D,E) Because AuNPs are effective enhancers of radiotherapy, some researchers improved the control of locally advanced bladder cancer. They used AuNPs to locate bladder tumors and found that the AuNPs were distributed throughout the bladder wall. However, most AuNPs are related to extracellular keratins, and their localization in the tumor stroma contributes to their specific radiotherapy enhancement for muscle-invasive bladder cancer (Smilowitz et al., 2017). AuNPs themselves also have therapeutic effects. Researchers have studied the cancer suppression effects of AuNPs in 5637 bladder cancer cells exposed to different concentrations of AuNPs for 24 h. The results showed that the AuNPs could reduce the survival of 5637 cells in a dose-dependent manner. In addition, ROS production was significantly increased in cells treated with 25 and 50 μg/mL AuNPs. These AuNPs could promote the apoptosis of tumor cells by inducing Bax overexpression and downregulating Bcl-2 (Daei et al., 2022).

4 Quantum dots (QDs)

Quantum dots (QDs) are nanomaterials with diameters of 2–10 nm (Sukhanova et al., 2018). QDs have unique physical and chemical properties, including high stability. Moreover, most QDs are considered non-toxic, so they are widely used in various fields of medicine (Rajendiran et al., 2019). QDs are potential smart drug delivery tools that can be used in cancer therapy, and their photostability, tunable emission, and wide excitation range make them more effective fluorescent markers than organic dyes in biological applications (Breus et al., 2015; Manshian et al., 2017; Hossen et al., 2019). (Figure 3A)

4.1 Application of QDs in PCa

Researchers synthesized highly stable AgInSe/ZnS QDs that can selectively target PCa and be taken up in large amounts. Therefore, AgInSe/ZnS QDs can be used as imaging probes to guide diagnosis and treatment (Ncapayi et al., 2021). (Figures 3B–D) Researchers used yeast cells and *Saccharomyces cerevisiae* to synthesize cadmium telluride (CdTe) QDs in modified Czapek medium through biological methods. *In vitro* experiments showed that the CdTe QDs induced a significant increase in ROS levels in PC-3 cells. Moreover, CdTe also arrested PC-3 cell growth in the G2/M phase of the cell cycle. Thus, CdTe QDs induced cell death and nuclear apoptosis in a dose-dependent manner (Jigyasu et al., 2020). Nanocomplexes containing QDs and β-cyclodextrin have been synthesized. This nanoconjugate has folate-targeting properties and has been used to deliver the anticancer Compound C-2028 to PCa cells. The QDs enter the cell through multiple endocytic pathways with various efficiencies to deliver the drug to cancer cells (Pilch et al., 2022). Researchers designed and synthesized a nanoparticle probe PSMA receptor-targeted QD (PSMA-QD655) by combining functionalized amino-PEG QDs with DUPA-targeted polypeptide constructs through heterobifunctional joints. PSMA-QD655 is a near-infrared imaging agent that can be used for navigation during surgery (Asha et al., 2021). Through the electrostatic adsorption of a large number of QDs on superparamagnetic Fe_3O_4, researchers prepared red and green magnetic QD nanobeads (MQBs) with excellent magnetic and high luminescence properties. MQBs can be used as multifunctional probes for the simultaneous determination of free and total PSA (Rong et al., 2019).

4.2 Application of QDs in bladder cancer

QDs have also been widely used in bladder cancer. Researchers prepared QD fluorescent probes conjured with prostate stem cell antigen (PSCA) monoclonal antibody (QD-PSCA). The probe specifically identifies PSCA expressed in bladder cancer cells. The stable fluorescence of the probe can be used as a specific marker (Yuan et al., 2018). A nanocarrier system was constructed with Mn: ZnS QDs. This delivery system can improve drug delivery efficacy in bladder cancer (Manan et al., 2021). The molecular detection of malignant nuclear matrix protein 22 (NMP22) in the urine has been introduced into clinical practice to identify bladder tumors.

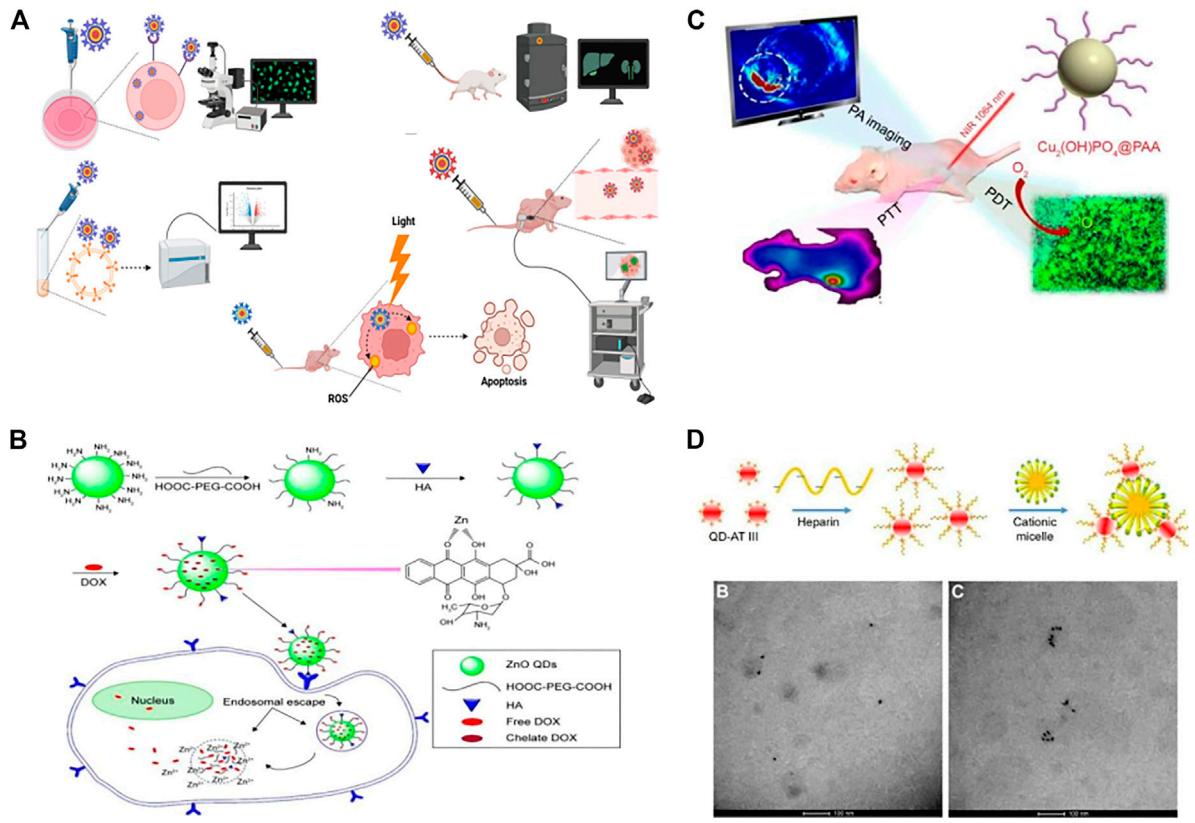

FIGURE 3
Biomedical applications of quantum dots (QDs). **(A)** QDs were used for intracellular imaging, *in vivo* imaging, fluorescence-activated cell sorting, photodynamic therapy, and traceable drug delivery. **(B)** QDs were used for drug delivery, such as the hyaluronic acid-ZnO QD-polyethylene glycol (HA-ZnO-PEG) material. This drug delivery system can release DOX (doxorubicin) in acidic cells. **(C)** QDs can be used for imaging and enable a combination of photodynamic therapy and photothermal therapy as well as photoacoustic imaging. **(D)** QDs have been used in sensors. TEM images of QDs-AT III-heparin without CTAB can be easily distinguished from TEM images of QD aggregates with CTAB after quantum dot synthesis and polymerization.

Researchers have also designed two-color QDs that can detect NMP22 with high sensitivity (Othman et al., 2020).

4.3 Application of QDs in RCC

Black phosphorus QDs (BP-QDs) can enhance the apoptosis of RCC cells after ionizing radiation (IR), indicating that BP-QDs have potential application value in the RCC radiosensitization therapy (Lang et al., 2022). Researchers have measured the expression of the proteins Tiam1 and Rac1 in RCC using immunohistochemistry (IHC) and QD labeling methods. It was found that the expression levels of Tiam1 and Rac1 are related to the differentiation, staging and lymphatic metastasis of RCC, suggesting that they are critical in RCC invasion and metastasis (Shan et al., 2017).

5 Carbon nanotubes (CNTs)

Carbon nanotubes (CNTs) are sheets of graphene 1 nm in diameter and a few microns in length. Single-walled CNTs (SWCNTs) and multiwalled CNTs (MWCNTs) (Elhissi et al., 2012) are the two common types of CNTs. Functionalized CNTs have the ability to cross the cell membrane, which allows functionalized CNTs to target specific tumor cells through endocytosis (Lacerda et al., 2012). (Figure 4A) Modified CNTs can be used to evaluate treatment, cell survival and apoptosis (Rastogi et al., 2014).

5.1 Application of CNTs in PCa

A nanoparticle delivery system including MWCNTs conjugated with the polypeptide H3R6 has been discovered for PCa immunotherapy in which the immunotherapeutic agents can be efficiently delivered to the prostate and lymph nodes (Xia et al., 2018). A novel nanoultrasound contrast agent based on MWCNTs was reported. Compared with traditional contrast materials, this contrast agent provides better visibility and accuracy and can target PCa cells more effectively (Gu et al., 2018). (Figures 4B,C) Researchers designed an optical sensor based on the fluorescence characteristics of SWCNTs. These sensors are expected to be used to distinguish between invasive PCa and inert prostate cells and reduce excessive treatment options for this disease (Williams et al., 2018). (Figures 4D,E)

10.3389/fbioe.2023.1111977

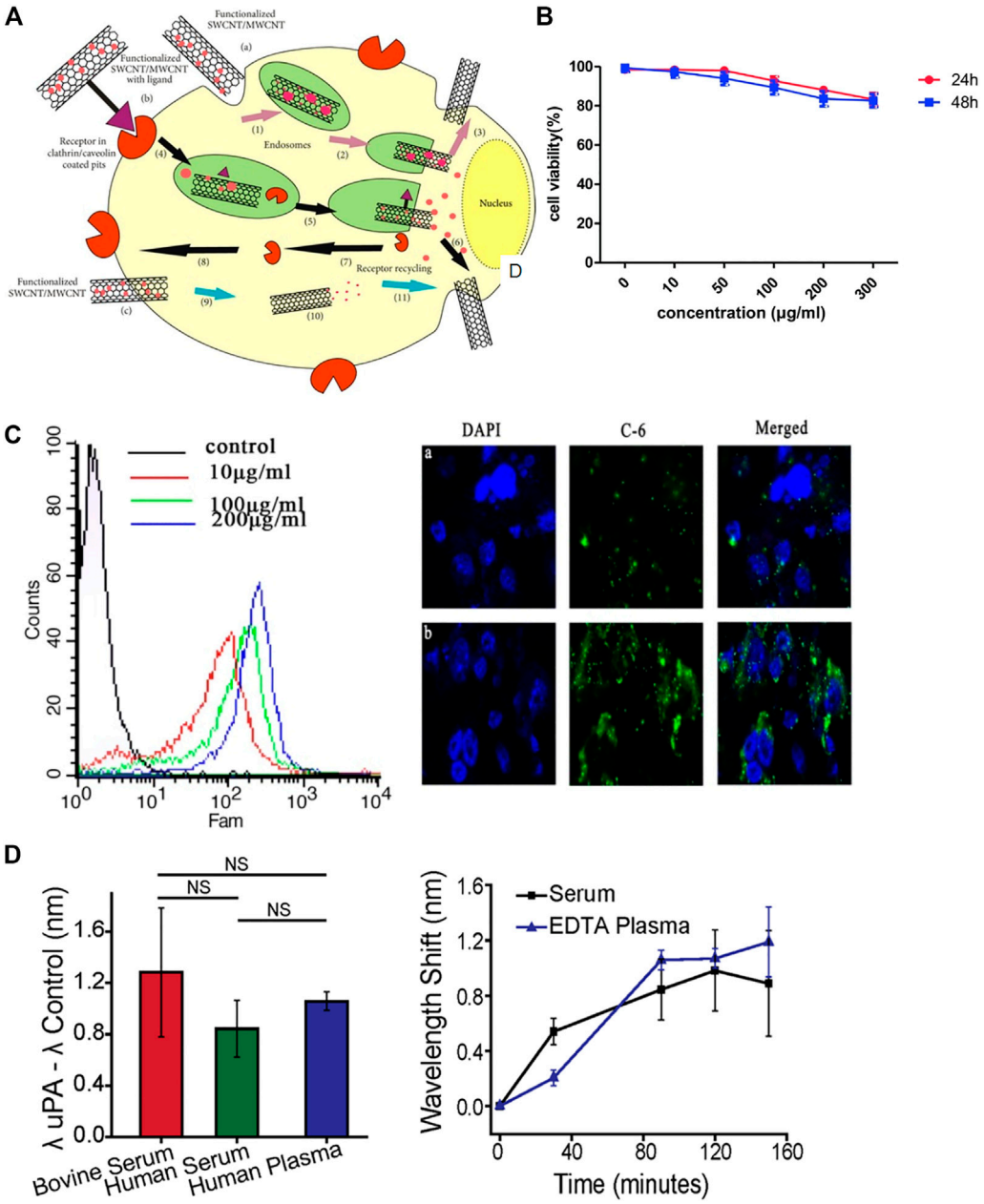

FIGURE 4
Biological applications of carbon nanotubes (CNTs). **(A)** CNTs penetrate into cells through various ways, including non-receptor-mediated endocytosis, receptor-mediated endocytosis and endocytosis-independent methods. **(B)** Flow cytometry and immunofluorescence assays indicated the uptake of CNT-PEG. **(C)** Cytotoxicity of CNT-PEG uPA at different concentrations. **(D)** Sensor detection of uPA in human blood products.

5.2 Application of CNTs in bladder cancer

Bladder tumor-specific SWCNTs are delivered to the bladder at a low dose. Then, the nanotubes are heated with 360° NIR light for 30 s. NIR light can heat the tumor while protecting the healthy bladder wall (Virani et al., 2018). Epirubicin (EPI) was loaded on magnetic MWCNTs (MMWCNTs-EPI) for intravesical infusion. The MMWCNT-EPI system has high efficiency in enhancing cytotoxicity and inhibiting proliferation *in vitro* and *in vivo*, showing potential clinical application value (Suo et al., 2019).

6 Liposomes

Liposomes are spherical structures with sizes ranging from 25 nm to 2.5 μm (Akbarzadeh et al., 2013) Liposomes can be structured as monolayer (ULV) or multilayer (MLV). ULVs are suitable for the encapsulation of hydrophilic drugs or antigens. MLVs feature multiple lipid bilayers, which act as barriers to resist enzymes, certain pH conditions, and free radicals *in vivo*. Thus, liposomes prevent drug degradation until its release at target cells, organs, or systems. Due to their high biocompatibility, degradability,

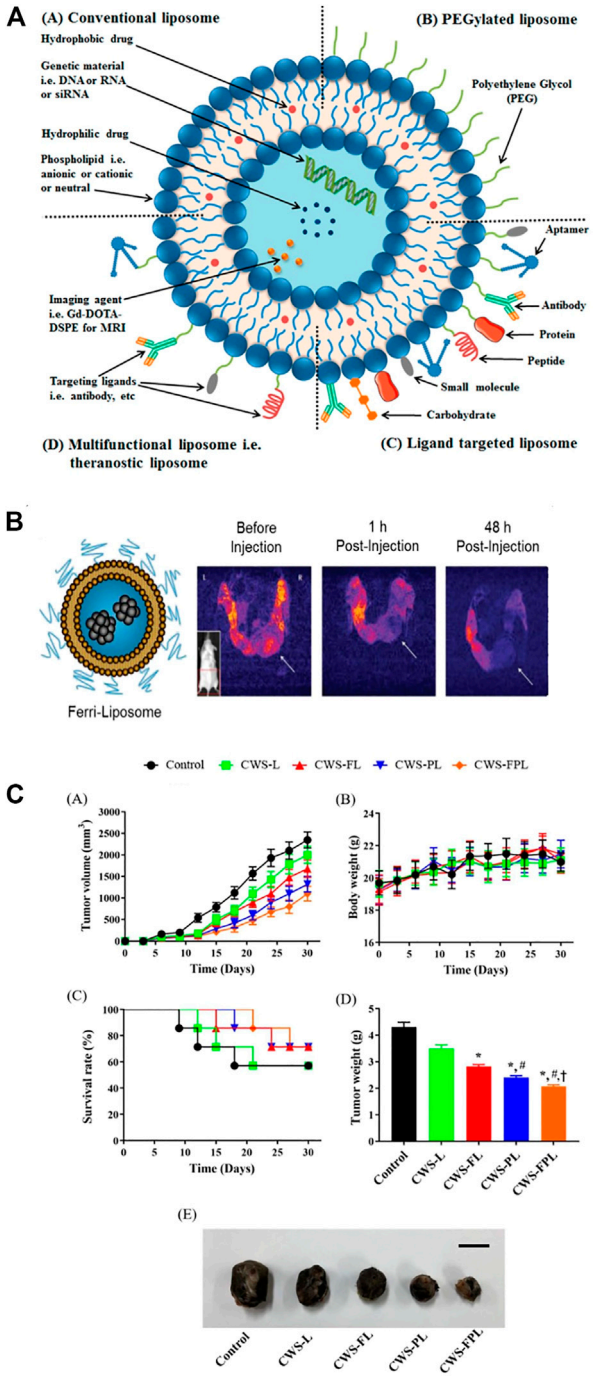

FIGURE 5
Liposomes have been used for cancer diagnosis and therapy. **(A)** A specific targeting ligand was incorporated to modify the surface of PEGylated liposomes. **(B)** T2-weighted MR images of a transgenic mouse before and after injection of Ferri-liposomes. **(C)** An *in vivo* study indicated that various liposomal formulations inhibited tumor growth.

low toxicity, and ability to encapsulate hydrophilic and hydrophobic compounds, liposomes represent the most successful drug delivery system because of their high biocompatibility, degradability and low toxicity (Felice et al., 2014; Bozzuto and Molinari, 2015). (Figures 5A,B)

6.1 Application of liposomes in PCa

The considerable side effects of the anthracycline doxorubicin (DOX) are major drawbacks. Simvastatin (Sim) can be used in combination with DOX. Researchers combined DOX and Sim on herceptin-conjugated liposomes. Studies have shown that liposomes can target PCa cells and exert an antitumor effect (Li et al., 2019b). Antisense oligonucleotides (ASOs) have a significant advantage due to their ability to provide virtually unlimited targeting of any gene. However, ASOs have the disadvantage of poor delivery *in vivo*. Researchers used the penetrating peptide iRGD to functionalize liposomes as anti-androgen receptor (AR) vectors. IRGD/liposomes significantly elevated the concentration of AR/ASO in target tissues and therefore inhibited tumor growth (Guan et al., 2021).

Liposomes increase the solubility the complexes, enhance the cytotoxicity of PCa drugs, and significantly reduce the growth rate of PCa cells, resulting in high radiotherapy efficacy in patients with locally advanced PCa (Silva et al., 2021). PSMA is a marker used for the diagnosis of advanced PCa and is recognized for targeted drug delivery. A liposome composed of a PSMA ligand and polyethylene glycol was synthesized. Liposomes with small PSMA binding motifs can be used to specifically identify PSMA + PCa cells (Yari et al., 2019).

6.2 Application of liposomes in bladder cancer

The BCG cell wall skeleton (BCG/CWS) was encapsulated in liposomes. Specific ligands were then conjugated on the surface of the liposomes to facilitate targeting and cell penetration. The modified liposomes significantly elevated the endocytosis of BCG/CWS by bladder cancer cells and strengthened the antitumor effect. Thus, BCG/CWS-modified liposomes could be a potential, highly efficacious therapeutic candidate in bladder cancer. (Figures 5C,D). The accumulation and distribution of DOX within liposomes in the bladder are significantly higher than those of intravenously administered DOX (Mikhail et al., 2017). Researchers developed a cationic liposome that combines three subclasses of mycolic acid (MA). This liposome can be effectively absorbed by MB49 bladder cancer cells and then induce antitumor immunity *in vivo* (Yoshino et al., 2019).

6.3 Application of liposomes in RCC

A liposome specifically targeting tumors was synthesized with phospholipids and cholesterol and showed excellent tumor-specific uptake as well as tumor inhibition (Pal et al., 2019).

7 Magnetic nanoparticles (MNPs)

Magnetic nanoparticles are an important class of nanoparticles that are usually made of pure metals (Fe, Co., and Ni) or mixtures of metals and polymers. The utilization of MNPs has increased in hyperthermic cancer treatment, controlled drug release, magnetic resonance imaging, and

10.3389/fbioe.2023.1111977

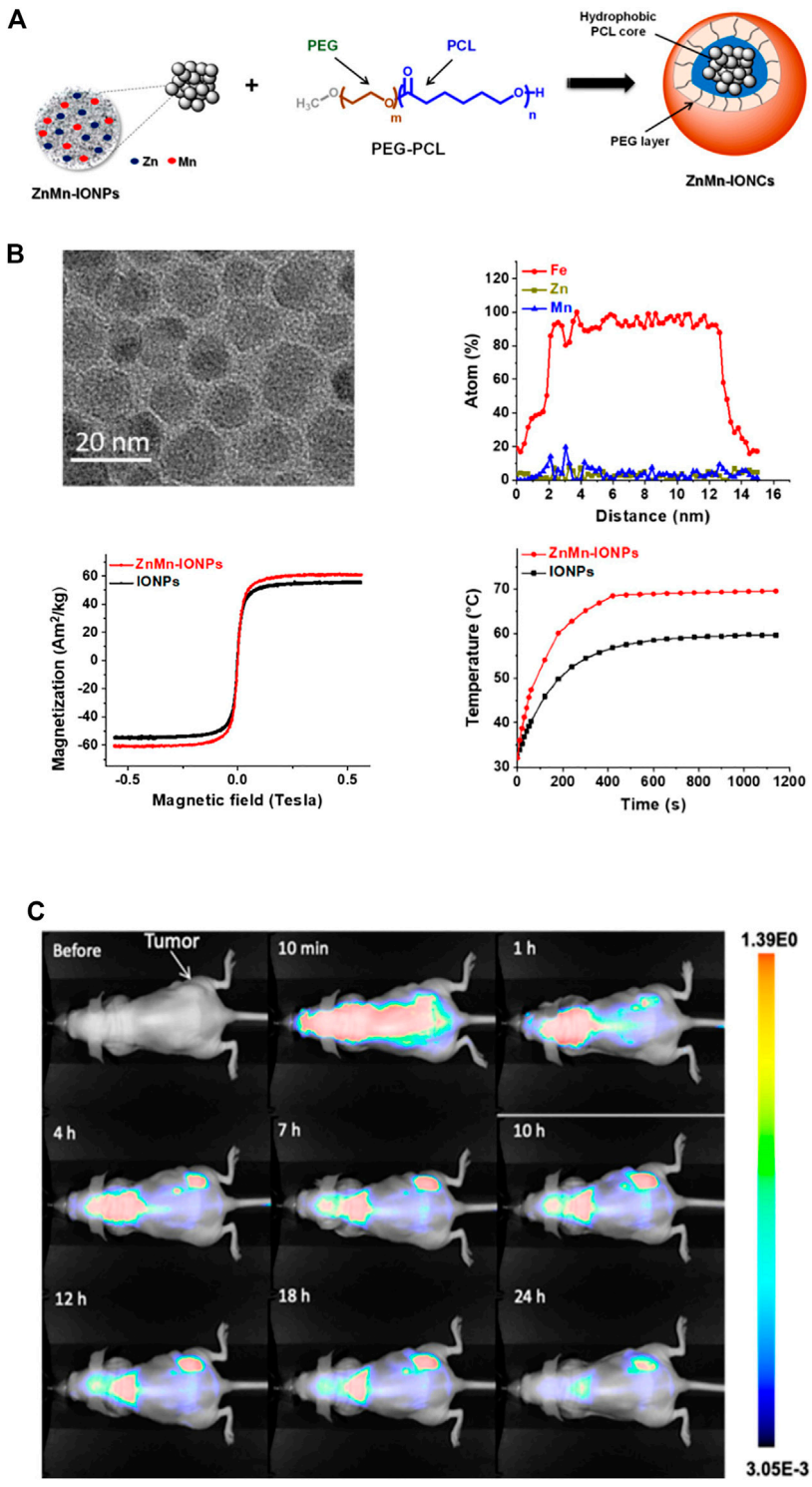

FIGURE 6
Biological applications of magnetic nanoparticles (MNPs). **(A)** Iron oxide nanoparticles with Zn and Mn were encapsulated into a nanocarrier. **(B)** Enhanced heating efficiency was achieved upon exposure to an alternating magnetic field. **(C)** *In vivo* evaluation of the nanoparticles suggested that ZnMn-IONCs started to accumulate in tumors. The fluorescence intensity in the tumors was higher than that the liver, kidneys, spleen and lungs.

biosensing. A key advantage of MNPs is their ability to be magnetically manipulated by external magnetic fields (Farzin et al., 2020). MNPs can alter drug pharmacokinetics to reduce cytotoxicity and increase the drug release rate. In addition to the possibility of localizing MNPs to cancer cells by the application of magnetic fields, MNPs can be modified with high-affinity ligands. Additionally, MNPs can be applied to improve the MRI image contrast in the target tissue. MNPs can be localized to tissue sites

TABLE 1 Nanoparticle summary.

Nano particle	Key characteristic(s)	Advantages	Disadvantage(s)	Applications
MSNs	Mesoporous structures	High biocompatibility, adjustable particle size multifunctional surface, high loading capacity	Cytotoxicity, genotoxicity	Drug and gene delivery, MSN-assisted bioimaging, tissue regeneration, MSN-based carriers, MSN-based biosensors
AuNPs	Au	Large surface area, superior conductivity high biocompatibility, easy entry into the host	Cytotoxicity, organ toxicity neurotoxicity	Drug delivery, photothermal therapy, radiation therapy, immunotherapy, enzyme fixation, cell imaging
QDs	Quantum dot	High photochemical stability, fluorescence quantum yield and biocompatibility	Contain heavy metals, organ toxicity, environmental pollution, immunotoxicity	Biomolecule targeting, luminescence imaging, drug delivery
CNTs	Grapheme sheets	Small volume, high specific surface area, good cell penetration, can be combined with more biological macromolecules and drugs	Organ toxicity, genotoxicity	Biosensor, drug and gene delivery, vaccine delivery, tissue engineering, regenerative medicine, biomedical imaging, biosensors, biomolecular detection
Liposomes	Spherical structures	High biocompatibility, non-toxicnonimmunogenic, easy surface modification	Poor stability, low drug loading easy leakage	Drug delivery, increase drug stability, non-invasive imaging, drug targeting, gene therapy, tissue engineering
MNPs	Pure metals or their mixtures	High biocompatibility, magnetothermal effect, superparamagnetism	Cytotoxicity	Hyperthermia cancer treatment, controlled drug release, magnetic resonance imaging, biosensing, tumor imaging, radiotherapy

to increase proton relaxation and improve visibility (Sun et al., 2008).

7.1 Application of MNPs in PCa

Magnetic hyperthermia (MHT) is a promising treatment for solid tumors. MHT generates heat in the presence of an alternating magnetic field (AMF). Researchers found new magnetic nanoparticles with enhanced heating efficiency that generate ideal intratumoral temperatures when exposed to an AMF. *In vivo* experiments confirmed that the nanoclusters significantly accumulate in tumor sites within hours and elevate the temperature to more than 42°C after exposure to an AMF. Finally, MHT application showed great inhibition of PCa cell growth with no side effects (Albarqi et al., 2020) (Figure 6). Galbanic acid, a natural sesquiterpenoid coumarin compound, causes significant toxicity to LNCaP PCa cells. Galbanic acid was loaded onto Fe_3O_4-coated MNPs and showed significant toxicity to all PCa cells (Mohtashami et al., 2019) Researchers also developed multifunctional MSNs that bind photosensitizers. These MSNs demonstrated significant anticancer effects by inducing apoptosis in PCa cells (Choi et al., 2018).

8 Discussion

The development of nanotechnology and nanomaterials for the diagnosis and treatment of urinary system tumors has brought great achievements and opportunities (Table 1). Many of these studies are still in the experimental stage, and many of these concepts have not reached clinical application. There have been a few reports on nanotechnology and nanomaterials in bladder cancer and kidney cancer; however, we are far from fully understanding these technologies. We believe that through the efforts of researchers and clinicians, more diagnosis and treatment methods will be invented for patients with urinary tract tumors.

Despite the therapeutic benefits, problems of nanotechnology and nanomaterials in terms of biological safety as well as metabolism *in vivo* should be given sufficient attention. Nanomaterials vary in their distribution, which depends on their shape, size, porosity, surface functionalization, etc. (He et al., 2011). For instance, MSNs are mainly present in the liver and spleen (Fu et al., 2013). AuNPs are primarily concentrated in the liver, spleen and bone marrow (Blanco et al., 2015). CNTs are different from other nanomaterials. They enter the cells in two ways, through endocytosis and passive diffusion, while QDs are mainly distributed and accumulate in the reticuloendothelial system and kidney. These differences in distribution result in various metabolic fates, applications and toxicities. As far as metabolism is concerned, first, the clearance of nanomaterials, including MSNs and AuNPs, depends on clearance by the kidney and biliary tract. Second, nanomaterial metabolism depends on their size. Small AuNPs (less than 10 nm) are easier to metabolize than large AuNPs (Zhou et al., 2011). QDs with larger particle sizes remain unchanged *in vivo* for a longer time and are more difficult to remove. In addition, nanomaterials can combine with specific proteins and be found in systemic circulation. Thus, these nanomaterials can be absorbed by phagocytic cells in the liver and spleen, such as liver Kupffer cells and splenic B Cells. Finally, the nanomaterials can be excreted from the body after phagocytosis by the macrophages in the alveoli (Huang et al., 2011). In addition to their dosage, the particle size of nanomaterials has a great impact on their toxicity (Greish et al., 2012; Shao et al., 2017). Moreover, the nanoparticle surface properties are the most important factor that affects toxicity. Nanoparticles with positive charges are more likely to induce an

immune response and cytotoxicity than neutral or negatively charged nanoparticles (Pisani et al., 2017; Li et al., 2019c). The cytotoxicity of nanoparticles is also considered to be shape-dependent (Lopez-Chaves et al., 2018) and depends on the biomolecules present on their surface (Xie et al., 2017).

Many problems with nanoparticles remain to be solved before these new developments can be applied in clinical settings. First, how can we improve the targeting efficiency of nanoparticles? Higher efficiency indicates that lower doses can be used with less toxicity. Second, we need to try to reduce particle loss in the targeting process, which is another way to increase efficiency and reduce toxicity. Third, and one of the most important issues, is how to reduce the side effects caused by nanoparticles, which usually lead to impairment of the kidney and liver. Fourth, we should also pay increasing attention to simplifying the manufacturing of nanoparticles so that their cost could be lower for wide use in the clinic. Finally, the waste from the production of these nanoparticles may pollute the environment, and we should thus optimize the production process to reduce this threat.

Furthermore, more clinical studies need to be conducted based on the issues mentioned above. For example, it is still unknown whether patient characteristics (e.g., age, sex, tumor type, tumor location, previous treatment) will alter the effects of some nanoparticles. In addition, it is also unknown whether nanoparticles can induce acute exacerbation of other diseases, such as asthma and diabetes. Third, nanoparticle application requires a complete set of platforms, which report the intake, distribution and metabolism of the drug in the body. Finally, most of the current research is focused on the design, production and targeting of nanoparticles to treat tumors. We believe that patients could benefit more from novel clinical research, including nanoparticle localization, which is also crucial in tumor therapy, for continuous anticancer effects.

At present, we are only beginning to study nanoparticles, most of which have not been put into clinical application. More clinical studies will have to be done to assure safety and effectiveness. Although many studies have shown the advantages of nanoparticles in the diagnosis and treatment of tumors, their potential biosafety and toxicity should also be given more attention. More critical questions should also be answered, including whether the age, weight, basic disease status, etc. of patients influence the effects of nanoparticles. Therefore, there is a long way to go before these nanoparticles can be widely accepted and used. Moreover, we could focus on modifying nanoparticles, which augments their application and minimizes cell and organ toxicity. Finally, nanoparticles have mainly focused on PCa in terms of urinary tumors, and research in bladder cancer and kidney cancer is still insufficient. Further studies in these patients are also important and worthy of investigation. Thus, more efforts should be made to investigate the applications of nanoparticles, which we believe that we could lead to increasingly applicable and creative treatments for urinary tumors.

Author contributions

ZQ and YZ drafted the manuscript. JY and SG contributed to the figures. BC provided specific academic guidance and improvement for the important intellectual content of the manuscript.

Funding

This work was supported by the grants No. 81402100 from National Natural Science Foundation of China, No.BK20211123 from Natural Science Foundation of Jiangsu Province and No. SH2021033 from Social Development Foundation of Zhenjiang.

Conflict of interest

The authors declare that the research was conducted in the absence of any commercial or financial relationships that could be construed as a potential conflict of interest.

The handling editor GP declared a shared parent affiliation with the authors at the time of review.

Publisher's note

References

Ahmed, N., Fessi, H., and Elaissari, A. (2012). Theranostic applications of nanoparticles in cancer. *Drug Discov. Today* 17 (17-18), 928–934. doi:10.1016/j.drudis.2012.03.010

Akbarzadeh, A., Rezaei-Sadabady, R., Davaran, S., Joo, S. W., Zarghami, N., Hanifehpour, Y., et al. (2013). Liposome: Classification, preparation, and applications. *Nanoscale Res. Lett.* 8 (1), 102. doi:10.1186/1556-276x-8-102

Al-Yasiri, A. Y., White, N. E., Katti, K. V., and Loyalka, S. K. (2019). Estimation of tumor and local tissue dose in gold nanoparticles radiotherapy for prostate cancer. *Rep. Pract. Oncol. Radiother.* 24 (3), 288–293. doi:10.1016/j.rpor.2019.02.006

Albarqi, H. A., Demessie, A. A., Sabei, F. Y., Moses, A. S., Hansen, M. N., Dhagat, P., et al. (2020). Systemically delivered magnetic hyperthermia for prostate cancer treatment. *Pharmaceutics* 12 (11), 1020. doi:10.3390/pharmaceutics12111020

Asha, K. M., Yadav, K., Roach, P., and Chelvam, V. (2021). A targeted near-infrared nanoprobe for deep-tissue penetration and imaging of prostate cancer. *Biomater. Sci.* 9 (6), 2295–2312. doi:10.1039/d0bm01970d

Badr, G., Al-Sadoon, M. K., Rabah, D. M., and Sayed, D. (2013). Snake (Walterinnesia aegyptia) venom-loaded silica nanoparticles induce apoptosis and growth arrest in human prostate cancer cells. *Apoptosis* 18 (3), 300–314. doi:10.1007/s10495-012-0787-1

Bennie, L. A., Feng, J., Emmerson, C., Hyland, W. B., Matchett, K. B., McCarthy, H. O., et al. (2021). Formulating RALA/Au nanocomplexes to enhance nanoparticle internalisation efficiency, sensitising prostate tumour models to radiation treatment. *J. Nanobiotechnology* 19 (1), 279. doi:10.1186/s12951-021-01019-8

Blanco, E., Shen, H., and Ferrari, M. (2015). Principles of nanoparticle design for overcoming biological barriers to drug delivery. *Nat. Biotechnol.* 33 (9), 941–951. doi:10.1038/nbt.3330

Boisselier, E., and Astruc, D. (2009). Gold nanoparticles in nanomedicine: Preparations, imaging, diagnostics, therapies and toxicity. *Chem. Soc. Rev.* 38 (6), 1759–1782. doi:10.1039/b806051g

Bozzuto, G., and Molinari, A. (2015). Liposomes as nanomedical devices. *Int. J. Nanomedicine* 10, 975–999. doi:10.2147/IJN.S68861

Breus, V. V., Pietuch, A., Tarantola, M., Basche, T., and Janshoff, A. (2015). The effect of surface charge on nonspecific uptake and cytotoxicity of CdSe/ZnS core/shell quantum dots. *Beilstein J. Nanotechnol.* 6, 281–292. doi:10.3762/bjnano.6.26

Chaturvedi, V. K., Singh, A., Singh, V. K., and Singh, M. P. (2019). Cancer nanotechnology: A new revolution for cancer diagnosis and therapy. *Curr. Drug Metab.* 20 (6), 416–429. doi:10.2174/1389200219666180918111528

Chaudhary, Z., Subramaniam, S., Khan, G. M., Abeer, M. M., Qu, Z., Janjua, T., et al. (2019). Encapsulation and controlled release of resveratrol within functionalized mesoporous silica nanoparticles for prostate cancer therapy. *Front. Bioeng. Biotechnol.* 7, 225. doi:10.3389/fbioe.2019.00225

Chen, J., Ren, F., Cao, W., Wu, Z., Ju, G., Xiao, C., et al. (2021). Photothermal therapy enhance the anti-mitochondrial metabolism effect of lonidamine to renal cell carcinoma in homologous-targeted nanosystem. *Nanomedicine* 34, 102370. doi:10.1016/j.nano.2021.102370

Chen, W., Li, J., Wei, X., Fan, Y., Qian, H., Li, S., et al. (2020). Surface plasmon resonance biosensor using hydrogel-AuNP supramolecular spheres for determination of prostate cancer-derived exosomes. *Mikrochim. Acta* 187 (11), 590. doi:10.1007/s00604-020-04573-4

Choi, K. H., Nam, K. C., Cho, G., Jung, J. S., and Park, B. (2018). Enhanced Photodynamic Anticancer Activities of Multifunctional Magnetic Nanoparticles (Fe3O4) Conjugated with Chlorin e6 and Folic Acid in Prostate and Breast Cancer Cells. *Nanomater. (Basel)* 8 (9), 722. doi:10.3390/nano8090722

Corbo, C., Molinaro, R., Parodi, A., Toledano Furman, N. E., Salvatore, F., and Tasciotti, E. (2016). The impact of nanoparticle protein corona on cytotoxicity, immunotoxicity and target drug delivery. *Nanomedicine (Lond)* 11 (1), 81–100. doi:10.2217/nnm.15.188

Daei, S., Ziamajidi, N., Abbasalipourkabir, R., Khanaki, K., and Bahreini, F. (2022). Anticancer effects of gold nanoparticles by inducing apoptosis in bladder cancer 5637 cells. *Biol. Trace Elem. Res.* 200 (6), 2673–2683. doi:10.1007/s12011-021-02895-9

Du, D., Fu, H. J., Ren, W. W., Li, X. L., and Guo, L. H. (2020). PSA targeted dual-modality manganese oxide–mesoporous silica nanoparticles for prostate cancer imaging. *Biomed. Pharmacother.* 121, 109614. doi:10.1016/j.biopha.2019.109614

Dykman, L., and Khlebtsov, N. (2012). Gold nanoparticles in biomedical applications: Recent advances and perspectives. *Chem. Soc. Rev.* 41 (6), 2256–2282. doi:10.1039/c1cs15166e

Eissa, S., Shawky, S. M., Matboli, M., Mohamed, S., and Azzazy, H. M. (2014). Direct detection of unamplified hepatoma upregulated protein RNA in urine using gold nanoparticles for bladder cancer diagnosis. *Clin. Biochem.* 47 (1-2), 104–110. doi:10.1016/j.clinbiochem.2013.10.022

Elhissi, A. M., Ahmed, W., Hassan, I. U., Dhanak, V. R., and D'Emanuele, A. (2012). Carbon nanotubes in cancer therapy and drug delivery. *J. Drug Deliv.* 2012, 837327. doi:10.1155/2012/837327

Esfahani, M., Alavi, S. E., Cabot, P. J., Islam, N., and Izake, E. L. (2021). PEGylated mesoporous silica nanoparticles (MCM-41): A promising carrier for the targeted delivery of fenbendazole into prostrate cancer cells. *Pharmaceutics* 13 (10), 1605. doi:10.3390/pharmaceutics13101605

Farzin, A., Etesami, S. A., Quint, J., Memic, A., and Tamayol, A. (2020). Magnetic nanoparticles in cancer therapy and diagnosis. *Adv. Healthc. Mater* 9 (9), e1901058. doi:10.1002/adhm.201901058

Felice, B., Prabhakaran, M. P., Rodriguez, A. P., and Ramakrishna, S. (2014). Drug delivery vehicles on a nano-engineering perspective. *Mater Sci. Eng. C Mater Biol. Appl.* 41, 178–195. doi:10.1016/j.msec.2014.04.049

Fu, C., Liu, T., Li, L., Liu, H., Chen, D., and Tang, F. (2013). The absorption, distribution, excretion and toxicity of mesoporous silica nanoparticles in mice following different exposure routes. *Biomaterials* 34 (10), 2565–2575. doi:10.1016/j.biomaterials.2012.12.043

Greish, K., Thiagarajan, G., Herd, H., Price, R., Bauer, H., Hubbard, D., et al. (2012). Size and surface charge significantly influence the toxicity of silica and dendritic nanoparticles. *Nanotoxicology* 6 (7), 713–723. doi:10.3109/17435390.2011.604442

Gu, F., Hu, C., Xia, Q., Gong, C., Gao, S., and Chen, Z. (2018). Aptamer-conjugated multi-walled carbon nanotubes as a new targeted ultrasound contrast agent for the diagnosis of prostate cancer. *J. Nanopart Res.* 20 (11), 303. doi:10.1007/s11051-018-4407-z

Guan, J., Guo, H., Tang, T., Wang, Y., Wei, Y., Seth, P., et al. (2021). iRGD-liposomes enhance tumor delivery and therapeutic efficacy of antisense oligonucleotide drugs against primary prostate cancer and bone metastasis. *Adv. Funct. Mater* 31 (24), 2100478. doi:10.1002/adfm.202100478

Haddick, L., Zhang, W., Reinhard, S., Moller, K., Engelke, H., Wagner, E., et al. (2020). Particle-size-dependent delivery of antitumoral miRNA using targeted mesoporous silica nanoparticles. *Pharmaceutics* 12 (6), 505. doi:10.3390/pharmaceutics12060505

Hao, Y., Hu, J., Wang, H., and Wang, C. (2021). Gold nanoparticles regulate the antitumor secretome and have potent cytotoxic effects against prostate cancer cells. *J. Appl. Toxicol.* 41 (8), 1286–1303. doi:10.1002/jat.4117

He, Q., and Shi, J. (2014). MSN anti-cancer nanomedicines: Chemotherapy enhancement, overcoming of drug resistance, and metastasis inhibition. *Adv. Mater* 26 (3), 391–411. doi:10.1002/adma.201303123

He, Q., Zhang, Z., Gao, F., Li, Y., and Shi, J. (2011). *In vivo* biodistribution and urinary excretion of mesoporous silica nanoparticles: Effects of particle size and PEGylation. *Small* 7 (2), 271–280. doi:10.1002/smll.201001459

Hossen, S., Hossain, M. K., Basher, M. K., Mia, M., Rahman, M., and Uddin, M. J. (2019). Smart nanocarrier-based drug delivery systems for cancer therapy and toxicity studies: A review. *J. Adv. Res.* 15, 1–18. doi:10.1016/j.jare.2018.06.005

Htoo, K., Yamkamon, V., Yainoy, S., Suksrichavalit, T., Viseshsindh, W., and Eiamphungporn, W. (2019). Colorimetric detection of PCA3 in urine for prostate cancer diagnosis using thiol-labeled PCR primer and unmodified gold nanoparticles. *Clin. Chim. Acta* 488, 40–49. doi:10.1016/j.cca.2018.10.036

Huang, X., Li, L., Liu, T., Hao, N., Liu, H., Chen, D., et al. (2011). The shape effect of mesoporous silica nanoparticles on biodistribution, clearance, and biocompatibility *in vivo*. *ACS Nano* 5 (7), 5390–5399. doi:10.1021/nn200365a

Iturrioz-Rodriguez, N., Correa-Duarte, M. A., and Fanarraga, M. L. (2019). <p> Controlled drug delivery systems for cancer based on mesoporous silica nanoparticles</p>. *Int. J. Nanomedicine* 14, 3389–3401. doi:10.2147/ijn.s198848

Jaishree, V., and Gupta, P. D. (2012). Nanotechnology: A revolution in cancer diagnosis. *Indian J. Clin. Biochem.* 27 (3), 214–220. doi:10.1007/s12291-012-0221-z

Jigyasu, A. K., Siddiqui, S., Jafri, A., Arshad, M., Lohani, M., and Khan, I. A. (2020). Biological synthesis of CdTe quantum dots and their anti-proliferative assessment against prostate cancer cell line. *J. Nanosci. Nanotechnol.* 20 (6), 3398–3403. doi:10.1166/jnn.2020.17316

Khan, A., Dias, F., Neekhra, S., Singh, B., and Srivastava, R. (2020). Designing and immunomodulating multiresponsive nanomaterial for cancer theranostics. *Front. Chem.* 8, 631351. doi:10.3389/fchem.2020.631351

Kim, J., Chun, S. H., Amornkitbamrung, L., Song, C., Yuk, J. S., Ahn, S. Y., et al. (2020). Gold nanoparticle clusters for the investigation of therapeutic efficiency against prostate cancer under near-infrared irradiation. *Nano Converg.* 7 (1), 5. doi:10.1186/s40580-019-0216-z

Koohi, M. E. M., Alavi, S. E., Cabot, P. J., Islam, N., Izake, E. L., et al. (2022). Beta-lactoglobulin-modified mesoporous silica nanoparticles: A promising carrier for the targeted delivery of fenbendazole into prostate cancer cells[J]. *Pharmaceutics* 14 (4).

Lacerda, L., Russier, J., Pastorin, G., Herrero, M. A., Venturelli, E., Dumortier, H., et al. (2012). Translocation mechanisms of chemically functionalised carbon nanotubes across plasma membranes. *Biomaterials* 33 (11), 3334–3343. doi:10.1016/j.biomaterials.2012.01.024

Lang, Y., Tian, X., Dong, H. Y., Zhang, X. X., Yu, L., Li, M., et al. (2022). Black phosphorus quantum dots enhance the radiosensitivity of human renal cell carcinoma cells through inhibition of DNA-PKcs kinase. *Cells* 11 (10), 1651. doi:10.3390/cells11101651

Li, H., Wu, X., Yang, B., Li, J., Xu, L., Liu, H., et al. (2019). Evaluation of biomimetically synthesized mesoporous silica nanoparticles as drug carriers: Structure, wettability, degradation, biocompatibility and brain distribution. *Mater Sci. Eng. C Mater Biol. Appl.* 94, 453–464. doi:10.1016/j.msec.2018.09.053

Li, N., Xie, X., Hu, Y., He, H., Fu, X., Fang, T., et al. (2019). Herceptin-conjugated liposomes co-loaded with doxorubicin and simvastatin in targeted prostate cancer therapy. *Am. J. Transl. Res.* 11 (3), 1255–1269.

Li, X., Zhou, H., Yang, L., Du, G., Pai-Panandiker, A. S., Huang, X., et al. (2011). Enhancement of cell recognition *in vitro* by dual-ligand cancer targeting gold nanoparticles. *Biomaterials* 32 (10), 2540–2545. doi:10.1016/j.biomaterials.2010.12.031

Li, Z., Wang, S., Fan, X., Cao, B., and Zhou, C. (2019). A novel gold nanoprobe for a simple electrochemiluminescence determination of a prostate-specific antigen based on a peptide cleavage reaction. *Anal. Sci.* 35 (2), 195–199. doi:10.2116/analsci.18p377

Liu, R., Pei, Q., Shou, T., Zhang, W., Hu, J., and Li, W. (2019). <p>Apoptotic effect of green synthesized gold nanoparticles from Curcuma wenyujin extract against human renal cell carcinoma A498 cells</p>. *Int. J. Nanomedicine* 14, 4091–4103. doi:10.2147/ijn.s203222

Liu, Y., Wang, X., Hussain, M., Lv, M., Dong, X., Wang, T., et al. (2018). Theranostics applications of nanoparticles in cancer immunotherapy. *Med. Sci. (Basel)* 6 (4), 100. doi:10.3390/medsci6040100

Lopez-Chaves, C., Soto-Alvaredo, J., Montes-Bayon, M., Bettmer, J., Llopis, J., and Sanchez-Gonzalez, C. (2018). Gold nanoparticles: Distribution, bioaccumulation and toxicity. *in vitro* and *in vivo* studies. *Nanomedicine* 14 (1), 1–12. doi:10.1016/j.nano.2017.08.011

Luo, D., Johnson, A., Wang, X., Li, H., Erokwu, B. O., Springer, S., et al. (2020). Targeted radiosensitizers for MR-guided radiation therapy of prostate cancer. *Nano Lett.* 20 (10), 7159–7167. doi:10.1021/acs.nanolett.0c02487

Maiorano, G., Sabella, S., Sorce, B., Brunetti, V., Malvindi, M. A., Cingolani, R., et al. (2010). Effects of cell culture media on the dynamic formation of Protein–Nanoparticle complexes and influence on the cellular response. *ACS Nano* 4 (12), 7481–7491. doi:10.1021/nn101557e

Manan, F., Yusof, N. A., Abdullah, J., Mohammad, F., Nurdin, A., Yazan, L. S., et al. (2021). Drug release profiles of mitomycin C encapsulated quantum dots-chitosan nanocarrier system for the possible treatment of non-muscle invasive bladder cancer. *J. Pharm.* 13 (9), 1379. doi:10.3390/pharmaceutics13091379

Manshian, B. B., Martens, T. F., Kantner, K., Braeckmans, K., De Smedt, S. C., Demeester, J., et al. (2017). The role of intracellular trafficking of CdSe/ZnS QDs on their consequent toxicity profile. *J. Nanobiotechnology* 15 (1), 45. doi:10.1186/s12951-017-0279-0

Medetalibeyoglu, H., Kotan, G., Atar, N., and Yola, M. L. (2020). A novel and ultrasensitive sandwich-type electrochemical immunosensor based on delaminated MXene@AuNPs as signal amplification for prostate specific antigen (PSA) detection and immunosensor validation. *Talanta* 220, 121403. doi:10.1016/j.talanta.2020.121403

Mikhail, A. S., Negussie, A. H., Pritchard, W. F., Haemmerich, D., Woods, D., Bakhutashvili, I., et al. (2017). Lyso-thermosensitive liposomal doxorubicin for treatment of bladder cancer. *Int. J. Hyperth.* 33 (7), 733–740. doi:10.1080/02656736.2017.1315459

Mohtashami, L., Ghows, N., Tayarani-Najaran, Z., and Iranshahi, M. (2019). Galbanic acid-coated Fe3O4 magnetic nanoparticles with enhanced cytotoxicity to prostate cancer cells. *Planta Med.* 85 (2), 169–178. doi:10.1055/a-0721-1886

Nawaz, Q., Rehman, M., Burkovski, A., Schmidt, J., Beltran, A. M., Shahid, A., et al. (2018). Synthesis and characterization of manganese containing mesoporous bioactive glass nanoparticles for biomedical applications. *J. Mater Sci. Mater Med.* 29 (5), 64. doi:10.1007/s10856-018-6070-4

Ncapayi, V., Ninan, N., Lebepe, T. C., Parani, S., Girija, A. R., Bright, R., et al. (2021). Diagnosis of prostate cancer and prostatitis using near infra-red fluorescent AgInSe/ZnS quantum dots. *Int. J. Mol. Sci.* 22 (22), 12514. doi:10.3390/ijms222212514

Nikzad, S., Mahmoudi, G., Amini, P., Baradaran-Ghahfarokhi, M., Vahdat-Moaddab, A., Sharafi, S. M., et al. (2017). Effects of radiofrequency radiation in the presence of gold nanoparticles for the treatment of renal cell carcinoma. *J. Ren. Inj. Prev.* 6 (2), 103–108. doi:10.15171/jrip.2017.20

Nimesh, S., Gupta, N., and Chandra, R. (2011). Cationic polymer based nanocarriers for delivery of therapeutic nucleic acids. *J. Biomed. Nanotechnol.* 7 (4), 504–520. doi:10.1166/jbn.2011.1313

Nossier, A. I., Eissa, S., Ismail, M. F., Hamdy, M. A., and Azzazy, H. M. E. S. (2014). Direct detection of hyaluronidase in urine using cationic gold nanoparticles: A potential diagnostic test for bladder cancer. *Biosens. Bioelectron.* 54, 7–14. doi:10.1016/j.bios.2013.10.024

Othman, H. O., Salehnia, F., Fakhri, N., Hassan, R., Hosseini, M., Faizullah, A., et al. (2020). A highly sensitive fluorescent immunosensor for sensitive detection of nuclear matrix protein 22 as biomarker for early stage diagnosis of bladder cancer. *RSC Adv.* 10 (48), 28865–28871. doi:10.1039/d0ra06191c

Ovais, M., Raza, A., Naz, S., Islam, N. U., Khalil, A. T., Ali, S., et al. (2017). Current state and prospects of the phytosynthesized colloidal gold nanoparticles and their applications in cancer theranostics. *Appl. Microbiol. Biotechnol.* 101 (9), 3551–3565. doi:10.1007/s00253-017-8250-4

Pal, K., Madamsetty, V. S., Dutta, S. K., and Mukhopadhyay, D. (2019). <p>Co-delivery of everolimus and vinorelbine via a tumor-targeted liposomal formulation inhibits tumor growth and metastasis in RCC</p>. *Int. J. Nanomedicine* 14, 5109–5123. doi:10.2147/ijn.s204221

Penticuff, J. C., and Kyprianou, N. (2015). Therapeutic challenges in renal cell carcinoma. *Am. J. Clin. Exp. Urol.* 3 (2), 77–90.

Pilch, J., Kowalik, P., Kowalczyk, A., Bujak, P., Kasprzak, A., Paluszkiewicz, E., et al. (2022). Foliate-targeting quantum dots-β-cyclodextrin nanocarrier for efficient delivery of unsymmetrical bisacridines to lung and prostate cancer cells. *Int. J. Mol. Sci.* 23 (3), 1261. doi:10.3390/ijms23031261

Pisani, C., Rascol, E., Dorandeu, C., Charnay, C., Guari, Y., Chopineau, J., et al. (2017). Biocompatibility assessment of functionalized magnetic mesoporous silica nanoparticles in human HepaRG cells. *Nanotoxicology* 11 (7), 871–890. doi:10.1080/17435390.2017.1378749

Pissuwan, D., Niidome, T., and Cortie, M. B. (2011). The forthcoming applications of gold nanoparticles in drug and gene delivery systems. *J. Control Release* 149 (1), 65–71. doi:10.1016/j.jconrel.2009.12.006

Porrang, S., Davaran, S., Rahemi, N., Allahyari, S., and Mostafavi, E. (2022). How advancing are mesoporous silica nanoparticles? A comprehensive review of the literature[J]. *Int. J. Nanomedicine* 17, 1803–1827. doi:10.2147/ijn.s353349

Pretze, M., Hien, A., Radle, M., Schirrmacher, R., Wangler, C., and Wangler, B. (2018). Gastrin-releasing peptide receptor- and prostate-specific membrane antigen-specific ultrasmall gold nanoparticles for characterization and diagnosis of prostate carcinoma via fluorescence imaging. *Bioconjug Chem.* 29 (5), 1525–1533. doi:10.1021/acs.bioconjchem.8b00067

Radaic, A., Joo, N. E., Jeong, S. H., Yoo, S. I., Kotov, N., and Kapila, Y. L. (2021). Phosphatidylserine-gold nanoparticles (PS-AuNP) induce prostate and breast cancer cell apoptosis. *J. Pharm.* 13 (7), 1094. doi:10.3390/pharmaceutics13071094

Rajendiran, K., Zhao, Z., Pei, D. S., and Fu, A. (2019). Antimicrobial activity and mechanism of functionalized quantum dots. *J. Polym. (Basel)* 11 (10), 1670. doi:10.3390/polym11101670

Rampado, R., Crotti, S., Caliceti, P., Pucciarelli, S., and Agostini, M. (2020). Recent advances in understanding the protein corona of nanoparticles and in the formulation of "stealthy" nanomaterials. *Front. Bioeng. Biotechnol.* 8, 166. doi:10.3389/fbioe.2020.00166

Rastogi, V., Yadav, P., Bhattacharya, S. S., Mishra, A. K., Verma, N., Verma, A., et al. (2014). Carbon nanotubes: An emerging drug carrier for targeting cancer cells. *J. Drug Deliv.* 2014, 670815. doi:10.1155/2014/670815

Rong, Z., Bai, Z., Li, J., Tang, H., Shen, T., Wang, Q., et al. (2019). Dual-color magnetic-quantum dot nanobeads as versatile fluorescent probes in test strip for simultaneous point-of-care detection of free and complexed prostate-specific antigen. *Biosens. Bioelectron.* 145, 111719. doi:10.1016/j.bios.2019.111719

Saroj, S., and Rajput, S. J. (2019). Facile development, characterization, and evaluation of novel bicalutamide loaded pH-sensitive mesoporous silica nanoparticles for enhanced prostate cancer therapy. *Drug Dev. Ind. Pharm.* 45 (4), 532–547. doi:10.1080/03639045.2018.1562463

Saroj, S., and Rajput, S. J. (2018). Tailor-made pH-sensitive polyacrylic acid functionalized mesoporous silica nanoparticles for efficient and controlled delivery of anti-cancer drug Etoposide. *Drug Dev. Ind. Pharm.* 44 (7), 1198–1211. doi:10.1080/03639045.2018.1438467

Shahidi, M., Abazari, O., Dayati, P., Bakhshi, A., Zavarreza, J., Modarresi, M. H., et al. (2022). Multicomponent siRNA/miRNA-loaded modified mesoporous silica nanoparticles targeted bladder cancer for a highly effective combination therapy. *Front. Bioeng. Biotechnol.* 10, 949704. doi:10.3389/fbioe.2022.949704

Shan, G., Tang, T., Qian, H., and Xia, Y. (2017). Expression of Tiam1 and Rac1 proteins in renal cell carcinoma and its clinical-pathological features. *Int. J. Clin. Exp. Pathol.* 10 (11), 11114–11121.

Shao, D., Lu, M. M., Zhao, Y. W., Zhang, F., Tan, Y. f., Zheng, X., et al. (2017). The shape effect of magnetic mesoporous silica nanoparticles on endocytosis, biocompatibility and biodistribution. *Acta Biomater.* 49, 531–540. doi:10.1016/j.actbio.2016.11.007

Shao, F., Zhang, L., Jiao, L., Wang, X., Miao, L., Li, H., et al. (2018). Enzyme-free immunosorbent assay of prostate specific antigen amplified by releasing pH indicator molecules entrapped in mesoporous silica nanoparticles. *Anal. Chem.* 90 (14), 8673–8679. doi:10.1021/acs.analchem.8b02019

Siegel, R. L., Miller, K. D., and Jemal, A. (2019). Cancer statistics, 2019. *CA Cancer J. Clin.* 69 (1), 7–34. doi:10.3322/caac.21551

Silva, V. L., Ruiz, A., Ali, A., Pereira, S., Seitsonen, J., Ruokolainen, J., et al. (2021). Hypoxia-targeted cupric-tirapazamine liposomes potentiate radiotherapy in prostate cancer spheroids. *Int. J. Pharm.* 607, 121018. doi:10.1016/j.ijpharm.2021.121018

Smilowitz, H. M., Tarmu, L. J., Sanders, M. M., Taylor III, J., Choudhary, D., Xue, C., et al. (2017). Biodistribution of gold nanoparticles in BBN-induced muscle-invasive bladder cancer in mice. *Int. J. Nanomedicine* 12, 7937–7946. doi:10.2147/ijn.s140977

Song, W., Musetti, S. N., and Huang, L. (2017). Nanomaterials for cancer immunotherapy. *Biomaterials* 148, 16–30. doi:10.1016/j.biomaterials.2017.09.017

Stolarczyk, E. U., Les, A., Laszcz, M., Kubiszewski, M., Strzempek, W., Menaszek, E., et al. (2020). The ligand exchange of citrates to thioabiraterone on gold nanoparticles for prostate cancer therapy. *Int. J. Pharm.* 583, 119319. doi:10.1016/j.ijpharm.2020.119319

Sukhanova, A., Bozrova, S., Sokolov, P., Berestovoy, M., Karaulov, A., and Nabiev, I. (2018). Dependence of nanoparticle toxicity on their physical and chemical properties. *Nanoscale Res. Lett.* 13 (1), 44. doi:10.1186/s11671-018-2457-x

Sun, C., Lee, J., and Zhang, M. (2008). Magnetic nanoparticles in MR imaging and drug delivery. *Adv. Drug Deliv. Rev.* 60 (11), 1252–1265. doi:10.1016/j.addr.2008.03.018

Suo, N., Wang, M., Jin, Y., Ding, J., Gao, X., Sun, X., et al. (2019). <p>Magnetic multiwalled carbon nanotubes with controlled release of epirubicin: An intravesical instillation system for bladder cancer</p>. *Int. J. Nanomedicine* 14, 1241–1254. doi:10.2147/ijn.s189688

Sweeney, S. K., Luo, Y., O'Donnell, M. A., and Assouline, J. (2016). Nanotechnology and cancer: Improving real-time monitoring and staging of bladder cancer with multimodal mesoporous silica nanoparticles. *Cancer Nanotechnol.* 7, 3. doi:10.1186/s12645-016-0015-8

Thambiraj, S., Vijayalakshmi, R., and Ravi, S. D. (2021). An effective strategy for development of docetaxel encapsulated gold nanoformulations for treatment of prostate cancer. *Sci. Rep.* 11 (1), 2808. doi:10.1038/s41598-020-80529-1

Vidaurre-Agut, C., Rivero-Buceta, E., Romani-Cubells, E., Clemments, A. M., Vera-Donoso, C. D., Landry, C. C., et al. (2019). Protein corona over mesoporous silica nanoparticles: Influence of the pore diameter on competitive adsorption and application to prostate cancer diagnostics. *ACS Omega* 4 (5), 8852–8861. doi:10.1021/acsomega.9b00460

Virani, N. A., Davis, C., McKernan, P., Hauser, P., Hurst, R. E., Slaton, J., et al. (2018). Phosphatidylserine targeted single-walled carbon nanotubes for photothermal ablation of bladder cancer. *Nanotechnology* 29 (3), 035101. doi:10.1088/1361-6528/aa9c0c

Vodnik, V. V., Mojic, M., Stamenovic, U., Otonicar, M., Ajdzanovic, V., Maksimovic-Ivanic, D., et al. (2021). Development of genistein-loaded gold nanoparticles and their antitumor potential against prostate cancer cell lines. *Mater Sci. Eng. C Mater Biol. Appl.* 124, 112078. doi:10.1016/j.msec.2021.112078

Wakaskar, R. R. (2018). Promising effects of nanomedicine in cancer drug delivery. *J. Drug Target* 26 (4), 319–324. doi:10.1080/1061186x.2017.1377207

Wang, H., Zhang, Y., Yu, H., Wu, D., Ma, H., Li, H., et al. (2013). Label-free electrochemical immunosensor for prostate-specific antigen based on silver hybridized mesoporous silica nanoparticles. *Anal. Biochem.* 434 (1), 123–127. doi:10.1016/j.ab.2012.11.012

Wei, Y., Gao, L., Wang, L., Shi, L., Wei, E., Zhou, B., et al. (2017). Polydopamine and peptide decorated doxorubicin-loaded mesoporous silica nanoparticles as a targeted drug delivery system for bladder cancer therapy. *Drug Deliv.* 24 (1), 681–691. doi:10.1080/10717544.2017.1309475

Williams, R. M., Lee, C., and Heller, D. A. (2018). A fluorescent carbon nanotube sensor detects the metastatic prostate cancer biomarker uPA. *ACS Sens.* 3 (9), 1838–1845. doi:10.1021/acssensors.8b00631

Wu, D., Zhu, Z. Q., Tang, H. X., Shi, Z. E., Kang, J., Liu, Q., et al. (2020). Efficacy-shaping nanomedicine by loading calcium peroxide into tumor microenvironment-responsive nanoparticles for the antitumor therapy of prostate cancer. *Theranostics* 10 (21), 9808–9829. doi:10.7150/thno.43631

Wu, T., Duan, X., Hu, C., Wu, C., Chen, X., Huang, J., et al. (2019). Synthesis and characterization of gold nanoparticles from *Abies spectabilis* extract and its anticancer activity on bladder cancer T24 cells. *Artif. Cells Nanomed Biotechnol.* 47 (1), 512–523. doi:10.1080/21691401.2018.1560305

Xia, Q., Gong, C., Gu, F., Wang, Z., Hu, C., Zhang, L., et al. (2018). Functionalized multi-walled carbon nanotubes for targeting delivery of immunostimulatory CpG oligonucleotides against prostate cancer. *J. Biomed. Nanotechnol.* 14 (9), 1613–1626. doi:10.1166/jbn.2018.2605

Xie, X., Liao, J., Shao, X., Li, Q., and Lin, Y. (2017). The effect of shape on cellular uptake of gold nanoparticles in the forms of stars, rods, and triangles. *Sci. Rep.* 7 (1), 3827. doi:10.1038/s41598-017-04229-z

Yari, H., Nkepang, G., and Awasthi, V. (2019). Surface modification of liposomes by a lipopolymer targeting prostate specific membrane antigen for theranostic delivery in prostate cancer. *Mater. (Basel)* 12 (5), 756. doi:10.3390/ma12050756

Yoshino, T., Miyazaki, J., Kojima, T., Kandori, S., Shiga, M., Kawahara, T., et al. (2019). Cationized liposomal keto-mycolic acids isolated from Mycobacterium bovis bacillus Calmette-Guérin induce antitumor immunity in a syngeneic murine bladder cancer model. *PLoS One* 14 (1), e0209196. doi:10.1371/journal.pone.0209196

Yuan, R., Rao, T., Cheng, F., Yu, W. M., Ruan, Y., Zhang, X. B., et al. (2018). Quantum dot-based fluorescent probes for targeted imaging of the EJ human bladder urothelial cancer cell line. *Exp. Ther. Med.* 16 (6), 4779–4783. doi:10.3892/etm.2018.6805

Zhang, X. D., Wu, H. Y., Wu, D., Wang, Y. Y., Chang, J. H., Zhai, Z. B., et al. (2010). Toxicologic effects of gold nanoparticles *in vivo* by different administration routes. *Int. J. Nanomedicine* 5, 771–781. doi:10.2147/IJN.S8428

Zhao, P., Chen, X., Wang, Q., Zou, H., Xie, Y., Liu, H., et al. (2020). Differential toxicity mechanism of gold nanoparticles in HK-2 renal proximal tubular cells and 786-0 carcinoma cells. *Nanomedicine (Lond)* 15 (11), 1079–1096. doi:10.2217/nnm-2019-0417

Zhou, C., Long, M., Qin, Y., Sun, X., and Zheng, J. (2011). Luminescent gold nanoparticles with efficient renal clearance. *Angew. Chem. Int. Ed. Engl.* 50 (14), 3168–3172. doi:10.1002/anie.201007321

frontiers | Frontiers in Bioengineering and Biotechnology

TYPE Original Research
PUBLISHED 04 May 2023
DOI 10.3389/fbioe.2023.1182080

OPEN ACCESS

EDITED BY
Xiaowei Zeng,
Sun Yat-sen University, China

REVIEWED BY
Jun Yue,
Sun Yat-sen University, China
Sumit Ghosh,
The Research Institute at Nationwide Children's Hospital, United States
Yanmin Bao,
Shenzhen Children's Hospital, China

*CORRESPONDENCE
Qinmiao Huang,
hqmwwb@163.com
Shau-Ku Huang,
skhuang1@gmail.com
Xiaojun Xiao,
xiaojun1985918@szu.edu.cn

†These authors have contributed equally to this work and share first authorship

RECEIVED 08 March 2023
ACCEPTED 20 April 2023
PUBLISHED 04 May 2023

CITATION
Wang J, Xian M, Cao H, Wu L, Zhou L, Ma Y, Fan L, Lin L, Li G, Huang Q, Huang S-K and Xiao X (2023), Prophylactic and therapeutic potential of magnolol-loaded PLGA-PEG nanoparticles in a chronic murine model of allergic asthma.
Front. Bioeng. Biotechnol. 11:1182080.
doi: 10.3389/fbioe.2023.1182080

Prophylactic and therapeutic potential of magnolol-loaded PLGA-PEG nanoparticles in a chronic murine model of allergic asthma

Junyi Wang[1,2†], Mo Xian[3†], Hui Cao[1,4†], Lei Wu[5,6,7], Libo Zhou[8], Yihe Ma[1,4], Long Fan[5,6,7], Lin Lin[5,6,7], Guoping Li[2], Qinmiao Huang[4]*, Shau-Ku Huang[1,4]* and Xiaojun Xiao[1,4]*

[1]Shenzhen Key Laboratory of Allergy and Immunology, Guangdong Provincial Standardization Allergen Engineering Research Center, State Key Laboratory of Respiratory Disease Shenzhen University Division, Institute of Allergy and Immunology, Shenzhen University School of Medicine, Shenzhen, China, [2]Laboratory of Allergy and Precision Medicine, Department of Pulmonary and Critical Care Medicine, Chengdu Institute of Respiratory Health, The Third People's Hospital of Chengdu, Affiliated Hospital of Southwest Jiaotong University, Chengdu, China, [3]Department of Allergy and Clinical Immunology, State Key Laboratory of Respiratory Disease, The First Affiliated Hospital of Guangzhou Medical University, Guangzhou, China, [4]Department of Pulmonary and Critical Care Medicine, Third Affiliated Hospital of Shenzhen University, Shenzhen, China, [5]State Key Laboratory of Dampness Syndrome of Chinese Medicine, The Second Affiliated Hospital of Guangzhou University of Chinese Medicine, Guangzhou, China, [6]Guangdong Provincial Hospital of Chinese Medicine, Guangdong Provincial Academy of Chinese Medical Sciences, Guangzhou, China, [7]Guangdong-Hong Kong-Macau Joint Lab on Chinese Medicine and Immune Disease Research, Guangzhou, China, [8]Department of Urology, The First Affiliated Hospital of Nanchang University, Nanchang, China

Magnolol is a chemically defined and active polyphenol extracted from magnolia plants possessing anti-allergic activity, but its low solubility and rapid metabolism dramatically hinder its clinical application. To improve the therapeutic effects, magnolol-encapsulated polymeric poly (DL-lactide-co-glycolide)–poly (ethylene glycol) (PLGA-PEG) nanoparticles were constructed and characterized. The prophylactic and therapeutic efficacy in a chronic murine model of OVA-induced asthma and the mechanisms were investigated. The results showed that administration of magnolol-loaded PLGA-PEG nanoparticles significantly reduced airway hyperresponsiveness, lung tissue eosinophil infiltration, and levels of IL-4, IL-13, TGF-β_1, IL-17A, and allergen-specific IgE and IgG_1 in OVA-exposed mice compared to their empty nanoparticles-treated mouse counterparts. Magnolol-loaded PLGA-PEG nanoparticles also significantly prevented mouse chronic allergic airway mucus overproduction and collagen deposition. Moreover, magnolol-encapsulated PLGA-PEG nanoparticles showed better therapeutic effects on suppressing allergen-induced airway hyperactivity, airway eosinophilic inflammation, airway collagen deposition, and airway mucus hypersecretion, as compared with magnolol-encapsulated poly (lactic-co-glycolic acid) (PLGA) nanoparticles or magnolol alone. These data demonstrate the protective effect of magnolol-loaded PLGA-PEG nanoparticles against the development of allergic phenotypes, implicating its potential usefulness for the asthma treatment.

KEYWORDS

asthma, murine model, magnolol, nanoparticles, anti-allergic drugs

Introduction

Asthma is a common chronic inflammatory disease affecting an estimated 262 million people in different countries (Asher et al., 2020). Airway hyperresponsiveness (AHR), type 2 inflammation, airway remodeling, and mucus hypersecretion are hallmarks of asthmatic processes (Holgate et al., 2015). These pathological changes cause asthma symptoms, which can be any combination of coughing, wheezing, shortness of breath, and chest tightness. To date, glucocorticoids still represent the mainstay of asthma control, but these drugs come with side effects, including suppression of the host defense and metabolic impairments, particularly with systematic use (Okwuofu et al., 2022).

Magnolol (5,5′-diallyl-2,2′-dihydroxybiphenyl) is an active polyphenol extracted from *Magnolia officinalis*, which is a traditional Chinese medicine with a long history of application to prevent cardiovascular and cerebrovascular diseases, treat depression and anxiety, and relieve asthma and cough (Yang et al., 2023). Pharmaceutically, magnolol has anti-oxidant, anti-inflammatory, anti-microbial, anti-tumor, cardiovascular, and neural protective properties (Mainardi et al., 2009). Recently, magnolol has been found to have anti-allergic effects on allergic rhinitis via the inhibition of ORAI1 (calcium release-activated calcium channel protein 1) and ANO1 (a calcium-activated anion channel 1) channels (Phan et al., 2022). Moreover, magnolol exerts anti-asthmatic effects via its ability to modulate Th1/Th2/Th17 cytokines in ovalbumin-sensitized asthmatic mice (Huang et al., 2019). Its isomer, honokiol, has also been shown to alleviate the inflammatory processes contributing to asthma (Munroe et al., 2010). However, the low water solubility and bioavailability and the rapid metabolism of magnolol dramatically limit its clinical application (Tang et al., 2018). Thus, a critical question regarding magnolol usage is how bioavailability and stability can be improved.

Biodegradable polymeric nanoparticles have various advantages, such as high biocompatibility and biosafety, in potentiating the efficacy of drugs (Shao et al., 2022). Although poly (lactic-co-glycolic acid) (PLGA), a synthetic polymeric material certified by the FDA, is widely used to prevent clinical drugs from degradation, it suffers from an array of shortcomings, including low encapsulation efficiency of polar drugs and high capture rate by the reticuloendothelial system due to its hydrophobicity (Younis et al., 2022). Poly (ethylene glycol) (PEG) has the two affinity characteristics of dissolving in water and organic solvents, meaning it shows a potential to promote the hydrophilicity, drug encapsulation efficiency, and blood circulation time of PLGA (Padin-Gonzalez et al., 2022). Previously, we found that the *Ambrosia artemisiifolia* allergen Amb a 1-loaded poly (DL-lactide-co-glycolide)-poly (ethylene glycol) (PLGA-PEG) nanoparticles have an immunotherapeutic effect on allergic conjunctivitis in mice (Cao et al., 2022). In this study, we hypothesized that magnolol-loaded PLGA-PEG nanoparticles could be effective in attenuating asthma phenotypes in a chronic murine model.

Materials and methods

Animals

Female BALB/c mice (specific pathogen-free grade, body weight 16–22 g, 6–8 weeks old) were purchased from the Animal Center of Guangdong Province and maintained under specific pathogen-free conditions in the Animal Experimental Center of Shenzhen University. All experiments were approved by the Animal Ethic Committee at Shenzhen University. The experiments were carried out following the Institutional Guidelines for the Care and Use of Laboratory Animals.

Preparation of magnolol-loaded nanoparticles

The nanoparticles were prepared by the emulsification–solvent evaporation method (Paswan and Saini, 2017). Briefly, 1 mg magnolol (MCE, United States) and 4 mg PLGA-PEG/PLGA (Merck, Germany) were dissolved in a 2 mL mixture of dichloromethane and ethanol (4:1, v/v) and injected into 4 mL 1.5% aqueous PVA solution. The mixture was homogenized with a probe-ultrasound machine (VCX750, Sonics, United States) for 5 min in an ice bath and stirred uncovered for 12 h at room temperature to volatilize the organic solvent completely. Then, the nanoparticle suspension was filtered by a 0.22 μm microporous membrane.

Characterization of magnolol-loaded nanoparticles

The zeta potential of the nanoparticles was measured by the Zetasizer Ultra instrument (Malvern, United Kingdom). After the nanoparticles were diluted with ultrapure water, the size distribution of the nanoparticles was also measured by this instrument. After the nanoparticles were fixed on the stub with double-sided adhesive tape, they were coated with a platinum layer by an automatic fine platinum coater (JFC-1300, JEOL) for 1 min, and then their morphology was observed by a field-emission scanning electron microscope (FESEM). For the measurement of encapsulation efficiency, the prepared nanoparticle suspension was added into an ultrafiltration tube with a molecular weight cut-off of 3 kD, centrifuged at 4,000 rpm for 30 min to separate the magnolol that was not coated by nanoparticles, and the concentration of magnolol was measured by HPLC. The following formula was used to calculate the encapsulation efficiency (EE): EE (%) = [(mtotal-mfree)/mtotal] × 100%. Mtotal is the concentration of magnolol in total suspension, and Mfree is the concentration of magnolol in the ultrafiltrate.

Sensitization, challenge, and administration protocols

As shown schematically in Figure 2A, the mice were immunized intraperitoneally with 10 μg OVA (Sigma-Aldrich, United States) adsorbed to 1 mg of alum (Thermo Scientific, United States) on days 0 and 14 (Royce et al., 2013; Wang et al., 2017a). At day 21, the mice were challenged with intranasal instillation of 20 μg OVA in a 20 μL PBS. The OVA challenge was performed three times per week for 6 weeks. Twenty mg/kg of magnolol (Herbpurify, China) and magnolol-

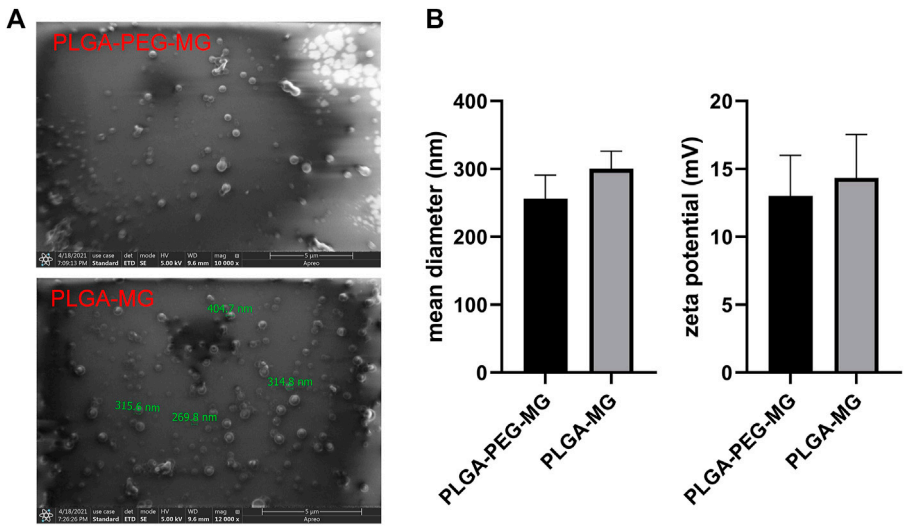

FIGURE 1
Characterization of magnolol-loaded PLGA-PEG nanoparticles. **(A)** Field emission scanning electron microscopic image. **(B)** Mean diameter and zeta potential of the two nanoparticle preparations (n = 3). PLGA-MG: magnolol-loaded PLGA nanoparticle; PLGA-PEG-MG: magnolol-loaded PLGA-PEG nanoparticle.

loaded nanoparticles were administered intraperitoneally 24 h before the first OVA challenge and 2 h before each of the remaining OVA challenges (Tian et al., 2018; Huang et al., 2019). PBS was used as an experimental control.

AHR assay

AHR was measured with the Buxco whole-body plethysmography (WBP) system (Buxco Research Company, United States) in response to inhaled methacholine. After 24 h of the last OVA challenge, the mice were monitored for about 10 min in the chamber until their breathing became stable. After a baseline recording for 5 min, the responses were assessed for 5 min after the inhaling of different concentrations of atomized methacholine solutions (0, 6.25, 12.5, 25, 50, and 100 mg/mL). In order to allow the respiratory intensity to get back to the baseline, an interval of 5 min was given between each test. AHR was expressed as enhanced pause (Penh), as described in detail previously (Wang et al., 2017b).

Bronchoalveolar lavage fluid (BALF) collection

The mice were subjected to tracheotomy and intubation after euthanasia via carbon dioxide inhalation. A five-bouts lavage with 0.8 mL PBS was performed on each mouse three times. A total volume of about 2 mL BALF per mouse (recovery rate >80%) was collected and centrifuged at 4°C, 1500 rpm for 10 min. The supernatant was used for cytokine determination, and the precipitate was resuspended and stained for inflammatory cell differential counting via Liu's staining method, following the instructions of the manufacturer (Baso, China).

Lung histological staining

The lungs were immediately removed after sacrifice, fixed in 4% paraformaldehyde, and embedded in paraffin. Lung sections (4 μm) were stained with hematoxylin–eosin (H&E), periodic acid–Schiff (PAS), and Masson's trichrome methods. The degree of inflammatory infiltration on H&E staining sections was scored using previously described methods (Wang et al., 2017b). PAS staining was used to identify the mucus-producing goblet cells in the airway mucosa (Wang et al., 2017b). Masson's trichrome staining was used to detect peri-bronchial collagen deposition. A score ranging from 0 to 3 was applied to each observed bronchus, with an approximate total of 10 areas being scored (Li et al., 2013).

Quantitative reverse transcription PCR (qRT-PCR)

The total RNA was extracted from the lung tissues with TRIzol Reagent (Thermo Scientific, United States), as recommended by the manufacturer. A total of 1.5 μg of total RNA preparation was reverse transcribed using a cDNA synthesis kit (RevertAid First Strand cDNA Synthesis Kit, Thermo Scientific, United States). cDNA was 1/5 diluted, and 5 μL was used as a template in a 50 μL SYBR-Green PCR reaction system, according to the manufacturer's instruction (iQ™ SYBR® Green, Bio-Rad, United States). β-actin premier (sense, 5′-CATCCGTAAAGACCTCTATGCCAAC-3'; antisense, 5′-ATG GAGCCACCGATCCACA-3′), *Muc5ac* premier (sense, 5′-CTG TGACATTATCCCATAAGCCC-3'; antisense, 5′-ACCGATCCC GCCCAGTGACA-3′), and *Col1a1* premier (sense, 5′-TGTTCG TGGTTCTCAGGGTAG-3'; antisense, 5′-TTGTCGTAGCAG GGTTCTTTC-3′) were synthesized by Sangon Biotech (Shanghai, China). Specificity was controlled by the omission of the template or the reverse transcription. All the samples were run in

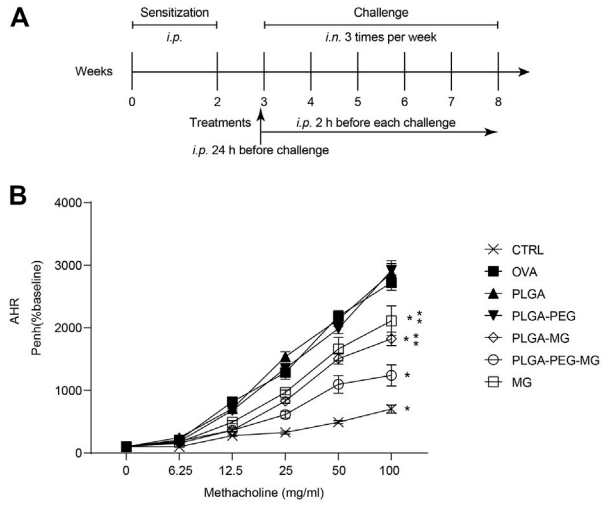

FIGURE 2
Magnolol-loaded PLGA-PEG nanoparticles migrate allergen-induced AHR. **(A)** Schematic representation of the mouse model. **(B)** The data are shown as means ± SD from four individual mice. CTRL: saline control group; OVA: OVA model group; PLGA: drug-free PLGA nanoparticle group; PLAG-PEG: drug-free PLGA-PEG nanoparticle group; PLGA-MG: magnolol-loaded PLGA nanoparticle group; PLGA-PEG-MG: magnolol-loaded PLGA-PEG nanoparticle group; MG: magnolol group. *$p < 0.05$ versus OVA group, **$p < 0.05$ versus magnolol-loaded PLGA-PEG nanoparticle group.

triplicate, and the qRT-PCR results were obtained using the $2^{-\triangle\triangle Ct}$ method and were normalized to β-actin.

Enzyme-linked immunosorbent assay (ELISA)

The levels of IL-4, IL-13, IL-17A, and TGF-β_1 in the BALF were determined by ELISA with commercial kits (eBioscience, United States), in accordance with instructions of the manufacturer. OVA-specific IgE (sIgE) and OVA-specific IgG_1 ($sIgG_1$) were measured by indirect ELISA (Tian et al., 2018). Briefly, the 96-well plates were coated with 100 ng OVA overnight at 4°C, blocked at room temperature for 1 h, and 100 μL murine serum (diluted 5 times) was added to each well for 2 h. Peroxidase-conjugated rat anti-mouse IgE and IgG_1 (1: 2000 dilution, Southern Biotech, United States) were added to each well for 1 h (37°C), and then 100 μL/well tetramethylbenzidine was added to develop. After being stopped by 2 M H_2SO_4 (50 μL/well), the results were measured by an absorbance microplate reader (BioTek, United States) at 450 nm.

Statistical methodology

The data were represented as means ± SD from at least three independent experiments. Statistical analyses were performed using a non-paired *t*-test for comparing two groups, and multiple comparisons were carried out with ANOVA, followed by Dunnett's test or the Bonferroni test for those with more than two groups. $p < 0.05$ was considered statistically significant. All data were analyzed by the SPSS 21.0 software.

Results

Characterization of magnolol-loaded PLGA-PEG nanoparticles

We prepared the magnolol-loaded nanoparticles with PLGA-PEG and PLGA as carriers (Figure 1A), and their average particle size and zeta potential are shown in Figure 1B. The average particle size and zeta potential of PLGA-PEG-magnolol were 230 nm and 12.5 mV, respectively. The average particle size and zeta potential of PLGA-magnolol were 290 nm and 14.5 mV, respectively. The encapsulation efficiency of PLGA-PEG to magnolol was 90.5% ± 5%, and PLGA to magnolol was 90.2% ± 4%.

Magnolol-loaded PLGA-PEG nanoparticles migrate allergen-induced AHR

AHR is a fundamental hallmark of asthma (Holgate et al., 2015). In order to investigate whether the magnolol-loaded nanoparticles improved lung function in asthmatic mice, we assessed AHR by methacholine exposure 24 h after the last OVA challenge (Figure 2B). The enhanced pause (Penh) scores of the OVA model (OVA) group and the two drug-free vehicle nanoparticle (PLGA and PLAG-PEG) groups were increased in a dose-dependent manner as compared to the saline control (CTRL) group. However, AHR was significantly inhibited in the magnolol-treated (MG) group and the two magnolol-loaded nanoparticles (PLGA-MG and PLGA-PEG-MG) groups. Moreover, among the three groups, the PLGA-PEG-MG group exhibited the lowest Penh levels. These data show that magnolol-loaded PLGA-PEG nanoparticles markedly inhibit OVA-induced AHR.

Magnolol-loaded PLGA-PEG nanoparticles alleviate OVA-induced lung inflammation

The lung tissues and bronchoalveolar lavage fluid (BALF) were collected 24 h after the last OVA exposure. To evaluate the inflammatory infiltration, the lung tissues were stained with H&E (Figure 3A) and scored in a blinded fashion (Figure 3B). The number of infiltrating inflammatory cells was also evaluated on the HE-stained sections (Figure 3C). Compared to the OVA group, the inflammatory cell infiltration in the lungs was reduced in PLGA-PEG-MG group, PLGA-MG group, and MG group. The PLGA-PEG-MG group had less inflammatory infiltration in the lungs compared to the PLGA-MG group and MG group. In the meantime, the counts of total cells, eosinophils, and lymphocytes in the BALF upon OVA exposure were also decreased significantly after the treatments of magnolol-loaded nanoparticles and magnolol alone (Figure 3D). Of these, the treatment of the magnolol-loaded PLGA-PEG nanoparticles exhibited the most pronounced reduction in inflammatory cell numbers. However, the mice treated with drug-free nanoparticles did not display the similar reduction of

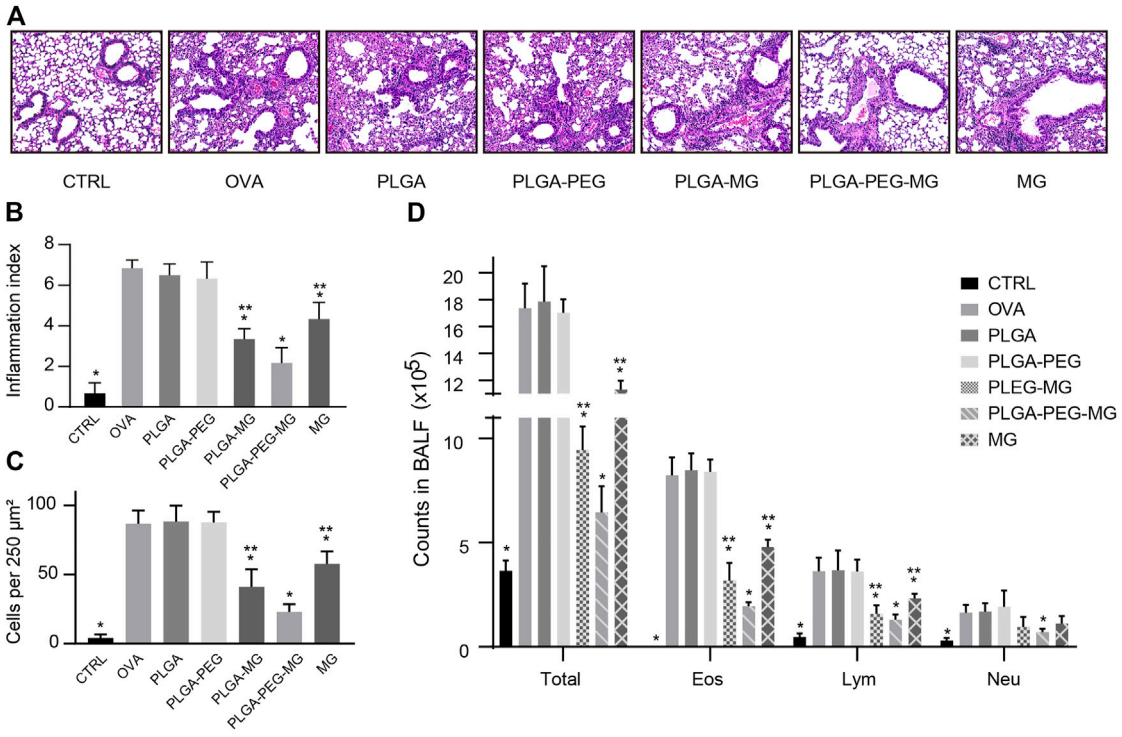

FIGURE 3
Magnolol-loaded PLGA-PEG nanoparticles alleviate OVA-induced lung inflammation. **(A)** Representative histological images of lungs by H&E staining (Magnification: ×200). **(B,C)** Inflammation scores **(B)** and numbers of inflammatory cells **(C)** estimated from lung tissues with H&E staining. **(D)** Counts of total cells, eosinophils, lymphocytes, and neutrophils in the BALF. The data are shown as means ± SD from six individual mice. CTRL: saline control group; OVA: OVA model group; PLGA: drug-free PLGA nanoparticle group; PLAG-PEG: drug-free PLGA-PEG nanoparticle group; PLGA-MG: magnolol-loaded PLGA nanoparticle group; PLGA-PEG-MG: magnolol-loaded PLGA-PEG nanoparticle group; MG: magnolol group. *p < 0.05 versus OVA group, **p < 0.05 versus magnolol-loaded PLGA-PEG nanoparticle group.

inflammatory cell infiltration both in the lungs and BALF. These findings indicate that magnolol-loaded PLGA-PEG nanoparticles attenuate OVA-induced lung inflammation.

Magnolol-loaded PLGA-PEG nanoparticles inhibit OVA-induced airway mucus hypersecretion

Excessive mucus in asthma obstructs airflow, leading to severe and potentially fatal outcomes (Holgate et al., 2015). A previous study suggested that chronic allergen exposure promotes goblet cell hyperplasia and mucin overproduction (Southam et al., 2008). We first observed the impact of the magnolol-loaded nanoparticles on aspects of goblet cell hyperplasia by PAS staining (Figures 4A, B). The PAS-positive cells were readily seen in the OVA group and the two drug-free nanoparticle groups, but they were much less apparent in the PLGA-PEG-MG group, PLGA-MG group, and MG group. Furthermore, the number of positively stained cells was significantly lower in the PLGA-PEG-MG group than those of the PLGA-MG group and MG group. We then determined the *Muc5ac* expression levels in the lungs via qRT-PCR (Figure 4C). Consistently, the expression of *Muc5ac* induced by OVA exposure was dramatically inhibited by treatments with magnolol-loaded nanoparticles and magnolol alone. In particular, the PLGA-PEG-MG group had the lowest expression of *Muc5ac*. Treatment with drug-free nanoparticles had no effect on the PAS-positive cell number and *Muc5ac* expression. These results suggest that magnolol-loaded PLGA-PEG nanoparticles reduce OVA-induced goblet cell hyperplasia and mucin hyperproduction.

Magnolol-loaded PLGA-PEG nanoparticles suppress OVA-induced peri-bronchial collagen deposition

Airway remodeling contributes to the progressive loss of lung function in asthma (Li et al., 2013). Collagen deposition is an acknowledged feature of airway remodeling during asthma (Ramis et al., 2022). Using Masson's trichrome staining (Figures 5A, B), we found that chronic OVA exposure increased the deposition of collagen around the airways, and these increases were attenuated in the PLGA-PEG-MG group, PLGA-MG group, and MG group. Furthermore, the PLGA-PEG-MG group had the greatest inhibition in the three treatments. Meanwhile, the expression of *Col1a1* was evaluated by qRT-PCR (Figure 5C). Consistently, the treatments of magnolol-loaded nanoparticles and magnolol alone suppressed the enhanced levels of *Col1a1* in OVA-exposed mice. Compared with the magnolol-loaded PLGA nanoparticles and magnolol-treated mice, the levels of *Col1a1*

10.3389/fbioe.2023.1182080

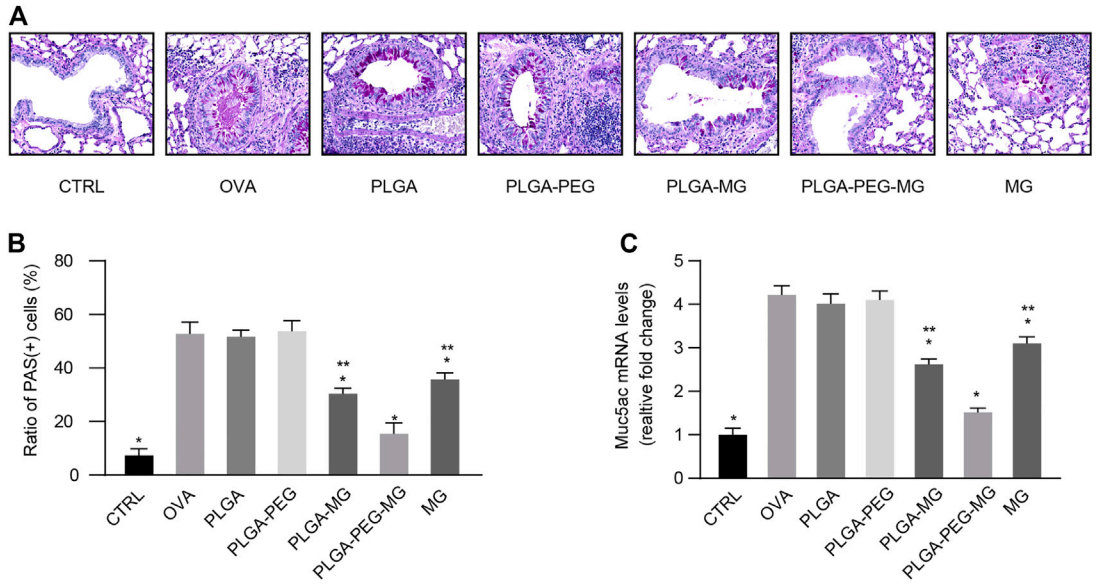

FIGURE 4
Magnolol-loaded PLGA-PEG nanoparticles inhibit OVA-induced airway mucus hypersecretion. **(A)** Representative histological images of lungs by PAS staining (Magnification: ×400). **(B)** Scoring for PAS-positive mucus-producing cells from lung tissues. **(C)** qRT-PCR determination of mRNA levels for *Muc5ac*. The data are shown as means ± SD from three individual mice. CTRL: saline control group; OVA: OVA model group; PLGA: drug-free PLGA nanoparticle group; PLAG-PEG: drug-free PLGA-PEG nanoparticle group; PLGA-MG: magnolol-loaded PLGA nanoparticle group; PLGA-PEG-MG: magnolol-loaded PLGA-PEG nanoparticle group; MG: magnolol group. *$p < 0.05$ versus OVA group, **$p < 0.05$ versus magnolol-loaded PLGA-PEG nanoparticle group.

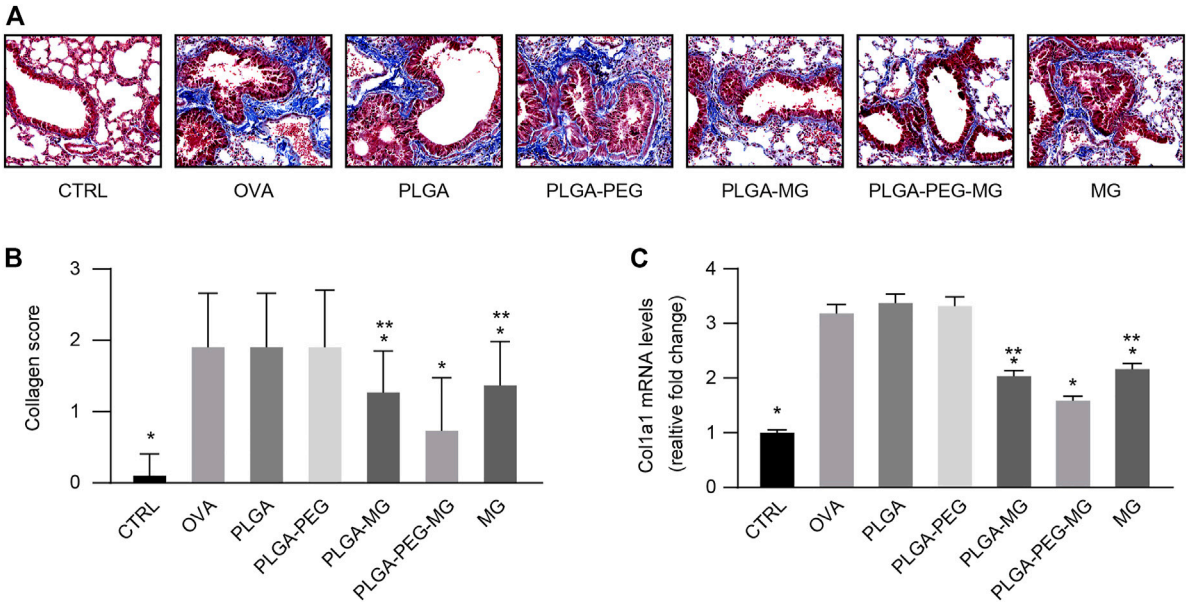

FIGURE 5
Magnolol-loaded PLGA-PEG nanoparticles suppress OVA-induced peri-bronchial collagen deposition. **(A)** Representative histological images of lungs by Masson's trichrome staining (Magnification: ×400). **(B)** Peri-bronchial collagen deposition scores estimated from lung tissues with Masson's trichrome staining. **(C)** qRT-PCR determination of mRNA levels for *Col1a1*. The data are shown as means ± SD from three individual mice. CTRL: saline control group; OVA: OVA model group; PLGA: drug-free PLGA nanoparticle group; PLAG-PEG: drug-free PLGA-PEG nanoparticle group; PLGA-MG: magnolol-loaded PLGA nanoparticle group; PLGA-PEG-MG: magnolol-loaded PLGA-PEG nanoparticle group; MG: magnolol group. *$p < 0.05$ versus OVA group, **$p < 0.05$ versus magnolol-loaded PLGA-PEG nanoparticle group.

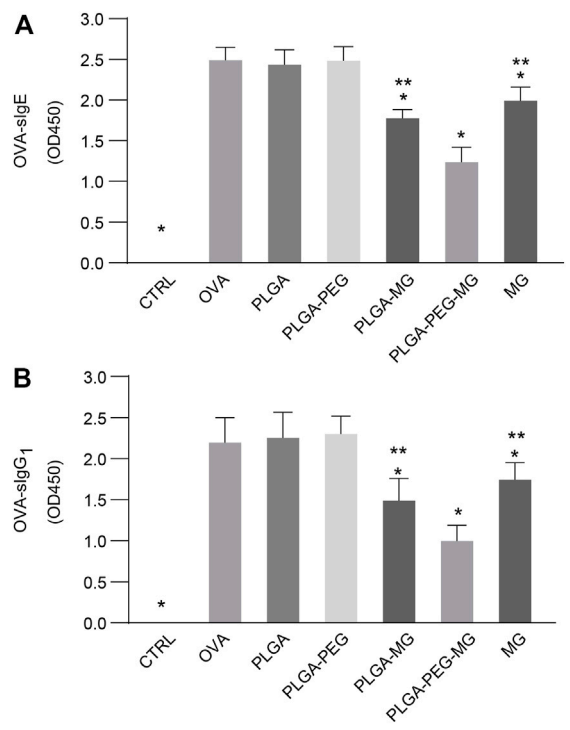

FIGURE 6
Magnolol-loaded PLGA-PEG nanoparticles reduce OVA-induced specific immunoglobulin levels in serum. **(A,B)** OVA-specific IgE **(A)** and OVA-specific IgG_1 **(B)** levels in serum by indirect ELISA. The data are shown as means ± SD from six individual mice. CTRL: saline control group; OVA: OVA model group; PLGA: drug-free PLGA nanoparticle group; PLAG-PEG: drug-free PLGA-PEG nanoparticle group; PLGA-MG: magnolol-loaded PLGA nanoparticle group; PLGA-PEG-MG: magnolol-loaded PLGA-PEG nanoparticle group; MG: magnolol group. *$p < 0.05$ versus OVA group, **$p < 0.05$ versus magnolol-loaded PLGA-PEG nanoparticle group.

mRNA were significantly decreased in the magnolol-loaded PLGA-PEG nanoparticles-treated mice. In addition, no significant inhibition of either collagen deposition or *Col1a1* expression was observed in drug-free nanoparticles-treated mice. These results demonstrate that PLGA-PEG nanoparticles containing magnolol suppress collagen deposition induced by chronic OVA exposure.

Magnolol-loaded PLGA-PEG nanoparticles reduce OVA-induced specific immunoglobulin levels in serum

Serum was collected 24 h after the last OVA challenge, and then OVA-specific IgE (sIgE) (Figure 6A) and OVA-specific IgG1 ($sIgG_1$) (Figure 6B) levels were determined via ELISA. OVA exposure with or without administration of empty nanoparticles led to a marked elevation in the levels of sIgE and $sIgG_1$ as compared with the control mice. These elevations were suppressed by the magnolol-loaded PLGA-PEG nanoparticles, magnolol-loaded PLGA nanoparticles, and magnolol. The suppression of the magnolol-loaded PLGA-PEG nanoparticles was greater than those of the magnolol-loaded PLGA nanoparticles and magnolol. These findings indicate that magnolol-loaded PLGA-PEG nanoparticles decrease OVA-induced sIgE and $sIgG_1$ secretion in serum.

Magnolol-loaded PLGA-PEG nanoparticles regulate OVA-induced cytokine production

The levels of cytokines in the BALF were measured with ELISA. We observed a robust reduction of IL-4 (Figure 7A), IL-13 (Figure 7B), TGF-β_1 (Figure 7C), and IL-17A (Figure 7D) levels in the magnolol-loaded nanoparticles and magnolol-treated animals compared to the OVA-exposed animals. Meanwhile, the concentrations of IL-4, IL-13, TGF-β_1, and IL-17A in the PLGA-PEG-MG mice were significantly lower compared to the PLGA-MG mice and MG mice. These results suggest that magnolol-loaded PLGA-PEG nanoparticles decrease IL-4, IL-13, TGF-β_1, and IL-17A expression during OVA-induced airway inflammation.

Discussion

Here, we successfully constructed magnolol-loaded PLGA-PEG nanoparticles through the w/o/w double emulsion–solvent evaporation method. The results showed that the mean hydrodynamic size of the magnolol-loaded PLGA-PEG nanoparticles was about 200.1–260.2 nm in diameter. This property is excellent for passive targeting to the sites of inflammation. Moreover, the size distribution of the magnolol-loaded nanoparticles was comparatively narrow, which is conducive for magnolol delivery.

Allergic airway inflammation is mainly orchestrated by type 2 cytokines such as IL-4 and IL-13, and it is marked by the massive infiltration of eosinophils (Holgate et al., 2015). Activation of the IL-4/IL-13 pathway promotes profound airway hyperresponsiveness (Manson et al., 2020). Inhibition of IL-4 and IL-13 significantly reduces IgE secretion in response to allergen challenge and further improves the infiltration of inflammatory cells in the airways (Castro et al., 2018). In an acute allergic mouse model, Huang et al. found that magnolol decreased cellular infiltration in the lungs, levels of IL-4 and IL-13 in the BALF, and sIgE levels in serum induced by an allergen (Huang et al., 2019). In this study, accompanied by high levels of IL-4, IL-13, and allergen-specific immunoglobulins, AHR and the number of eosinophils increased significantly in the lungs of chronic OVA-exposed mice. The treatments of magnolol-loaded PLGA-PEG nanoparticles, magnolol-loaded PLGA nanoparticles, and magnolol effectively mitigated these pathological changes. As expected, the magnolol-loaded PLGA-PEG nanoparticles successfully exhibited a more dramatic effect on the inhibition of AHR and type 2 cytokine-mediated airway inflammation, indicating a therapeutic potential of PLGA-PEG nanoparticles coated with anti-inflammatory drugs in allergic diseases.

Airway remodeling is a prominent clinical feature of severe asthma and may be responsible for the failure of standard anti-asthmatic therapy (Hirota and Martin, 2013). On the one hand, goblet cell hyperplasia and mucus hypersecretion are critical features of airway remodeling, leading to airway plugging and an increased risk of mortality (Boonpiyathad et al., 2019). Type 2 cytokines such as IL-13 promote hyperplasia of the goblet cell and hypersecretion of mucins including MUC5AC in asthmatics (Conde et al., 2021). Here, in addition to inhibition of type 2 cytokines, we also found that

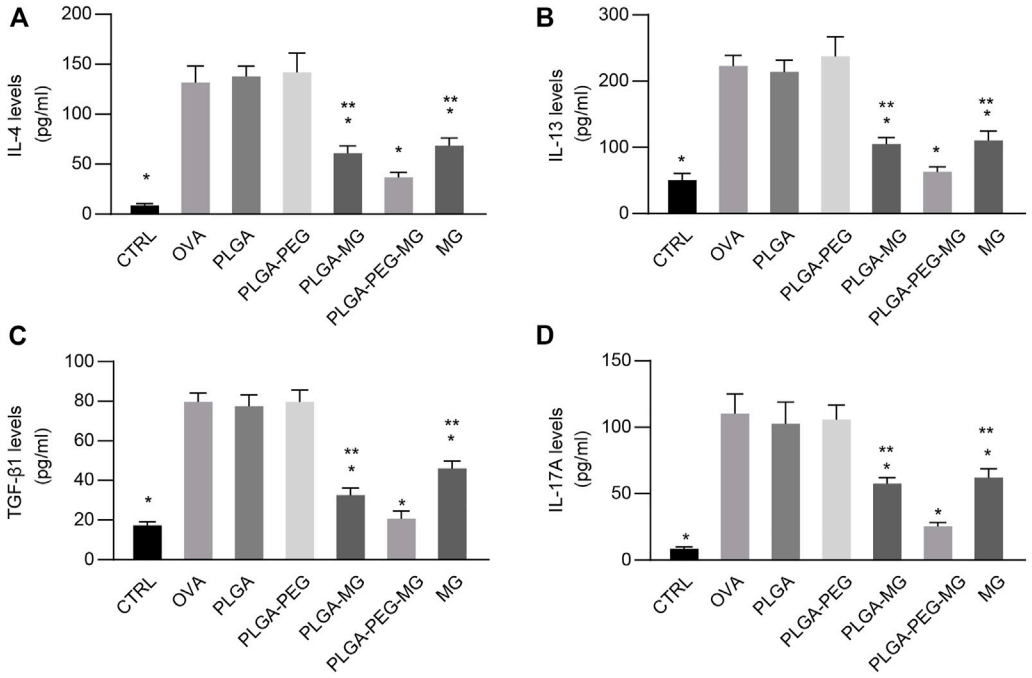

FIGURE 7
Magnolol-loaded PLGA-PEG nanoparticles regulate OVA-induced cytokine production. **(A–D)** IL-4 **(A)**, IL-13 **(B)**, TGF-β_1 **(C)**, and IL-17A **(D)** levels in the BALF by ELISA. The data are shown as means ± SD from six individual mice. CTRL: saline control group; OVA: OVA model group; PLGA: drug-free PLGA nanoparticle group; PLAG-PEG: drug-free PLGA-PEG nanoparticle group; PLGA-MG: magnolol-loaded PLGA nanoparticle group; PLGA-PEG-MG: magnolol-loaded PLGA-PEG nanoparticle group; MG: magnolol group. *$p < 0.05$ versus OVA group, **$p < 0.05$ versus magnolol-loaded PLGA-PEG nanoparticle group.

magnolol-loaded PLGA-PEG nanoparticles exhibited a greater improvement of goblet hyperplasia and MUC5AC overproduction than those of magnolol-loaded PLGA nanoparticles and magnolol. On the other hand, the chronic deposition of collagen fibers thickened the air–blood barrier, contributing to an irreversible decrement in lung function (Hirota and Martin, 2013). TGF-β_1 is a member of the family of growth factors of crucial importance in fibrogenesis, and it plays an integral role in airway remodeling (Ojiaku et al., 2017). In the present study, peri-bronchial collagen deposition induced by allergen exposure was apparently decreased by the administration of magnolol-loaded nanoparticles and magnolol. The effects of magnolol-loaded PLGA-PEG nanoparticles were found to be much better than those of magnolol-loaded PLGA nanoparticles and magnolol alone. It was further confirmed by the observation that magnolol-loaded PLGA-PEG nanoparticles effectively downregulated TGF-β_1 production in the lungs.

In addition, Th17 cells have emerged as an independent subset of $CD4^+$ T-help cells. Th17 cells synthesizing IL-17A have been shown to play a crucial role in the induction of inflammatory diseases (Saviano et al., 2022). Accumulating evidence suggests that activation of the IL-17-producing cells is associated with the development of severe forms of asthma (Xie et al., 2022). A previous study showed that magnolol exerts anti-inflammatory effects when reducing the serum levels of IL-17 and IL-6 in a rat colitis model (Zhang et al., 2018). Another study showed that magnolol reduced the Th17 cell population and effectively modulated the JAK-STAT and Notch-1 signaling (Huang et al., 2019). Consistently, it had been also shown in the present study that magnolol-loaded PLGA-PEG nanoparticles remarkably suppressed the IL-17A expression in lungs and had a more potent effect than magnolol-loaded PLGA nanoparticles and magnolol alone.

In conclusion, we constructed PLGA-PEG nanoparticles as a magnolol delivery system and developed an OVA-induced chronic asthma murine model to evaluate the anti-inflammatory effects of these drug-loaded nanoparticles. Our results proved that magnolol-loaded PLGA-PEG nanoparticles could effectively suppress allergen-induced airway hyperactivity, airway eosinophilic inflammation, airway collagen deposition, and airway mucus hypersecretion. Furthermore, magnolol-loaded PLGA-PEG nanoparticles have a better therapeutic effect on OVA-induced asthmatic phenotypes than magnolol-loaded PLGA nanoparticles and magnolol alone, which may be due to their greater hydrophilicity, stability, and passive targeting effects. It should be acknowledged, however, that our study is limited by the OVA-induced model, which does not mimic the natural route of exposure to allergens. Future studies with more relevant allergic models, such as fungi and dust mites, are needed to validate and expand upon our findings.

Data availability statement

The raw data supporting the conclusion of this article will be made available by the authors, without undue reservation.

Ethics statement

The animal study was reviewed and approved by Animal Ethic Committee at Shenzhen University.

Author contributions

Conceptualization: JW, HC, and GL; Methodology: JW and MX; Validation: LW and LZ; Resources: XX; Data curation: YM, LF, and LL; writing—original draft preparation: JW and HC; writing—review and editing: S-KH and XX; Supervision: QH; Project administration: QH, S-KH, and XX; Funding acquisition: QH, S-KH, and XX. All authors have read and agreed to the published version of the manuscript.

Funding

The National Natural Science Foundation (81929001, 82073950, 82060007, 82200079), Science and Technology Planning Project of Guangdong (2020B1212030006, 20221175, 2020A1313030065, 2022B1515120055), Natural Science Foundation of Sichuan (2022NSFSC1324), Sichuan Medical Association (Q21061), Science and Technology Program of Shenzhen (Nos. JCYJ20200109143435556, SGDX20201103095609027, JCYJ20210324134209026, JCYJ20180306171550045), the Science and Technology Program of Guangzhou (No. 202102010352), Health Commission of Chengdu (2022194), State Key Laboratory of Respiratory Disease (SKLRD-Z-202111, SKLRD-Z-202216, SKLRD-OP-202007), State Key Laboratory of Dampness Syndrome of Chinese Medicine (SZ2021ZZ42), Software Science Research Program of Shenzhen Luohu (LX20200408), and Double First-Class and High-Level University Discipline Collaborative Innovation Team Project of Guangzhou University of Chinese Medicine (2021XK27).

Conflict of interest

The authors declare that the research was conducted in the absence of any commercial or financial relationships that could be construed as a potential conflict of interest.

Publisher's note

All claims expressed in this article are solely those of the authors and do not necessarily represent those of their affiliated organizations, or those of the publisher, the editors and the reviewers. Any product that may be evaluated in this article, or claim that may be made by its manufacturer, is not guaranteed or endorsed by the publisher.

References

Asher, M. I., Garcia-Marcos, L., Pearce, N. E., and Strachan, D. P. (2020). Trends in worldwide asthma prevalence. *Eur. Respir. J.* 56 (6), 2002094. doi:10.1183/13993003.02094-2020

Boonpiyathad, T., Sozener, Z. C., Satitsuksanoa, P., and Akdis, C. A. (2019). Immunologic mechanisms in asthma. *Semin. Immunol.* 46, 101333. doi:10.1016/j.smim.2019.101333

Cao, H., Liu, L., Wang, J., Gong, M., Yuan, R., Lu, J., et al. (2022). Effects of rAmb a 1-loaded PLGA-PEG nanoparticles in a murine model of allergic conjunctivitis. *Molecules* 27 (3), 598. doi:10.3390/molecules27030598

Castro, M., Corren, J., Pavord, I. D., Maspero, J., Wenzel, S., Rabe, K. F., et al. (2018). Dupilumab efficacy and safety in moderate-to-severe uncontrolled asthma. *N. Engl. J. Med.* 378 (26), 2486–2496. doi:10.1056/NEJMoa1804092

Conde, E., Bertrand, R., Balbino, B., Bonnefoy, J., Stackowicz, J., Caillot, N., et al. (2021). Dual vaccination against IL-4 and IL-13 protects against chronic allergic asthma in mice. *Nat. Commun.* 12 (1), 2574. doi:10.1038/s41467-021-22834-5

Hirota, N., and Martin, J. G. (2013). Mechanisms of airway remodeling. *Chest* 144 (3), 1026–1032. doi:10.1378/chest.12-3073

Holgate, S. T., Wenzel, S., Postma, D. S., Weiss, S. T., Renz, H., and Sly, P. D. (2015). *Asthma*. Nat. Rev. Dis. Prim. 1, 15025. doi:10.1038/nrdp.2015.25

Huang, Q., Han, L., Lv, R., and Ling, L. (2019). Magnolol exerts anti-asthmatic effects by regulating Janus kinase-signal transduction and activation of transcription and Notch signaling pathways and modulating Th1/Th2/Th17 cytokines in ovalbumin-sensitized asthmatic mice. *Korean J. Physiol. Pharmacol.* 23 (4), 251–261. doi:10.4196/kjpp.2019.23.4.251

Li, G., Fox, J., 3rd, Liu, Z., Liu, J., Gao, G. F., Jin, Y., et al. (2013). Lyn mitigates mouse airway remodeling by downregulating the TGF-β3 isoform in house dust mite models. *J. Immunol.* 191 (11), 5359–5370. doi:10.4049/jimmunol.1301596

Mainardi, T., Kapoor, S., and Bielory, L. (2009). Complementary and alternative medicine: Herbs, phytochemicals and vitamins and their immunologic effects. *J. Allergy Clin. Immunol.* 123 (2), 283–294.e10. quiz 295-6. doi:10.1016/j.jaci.2008.12.023

Manson, M. L., Safholm, J., James, A., Johnsson, A. K., Bergman, P., Al-Ameri, M., et al. (2020). IL-13 and IL-4, but not IL-5 nor IL-17A, induce hyperresponsiveness in isolated human small airways. *J. Allergy Clin. Immunol.* 145 (3), 808–817 e2. doi:10.1016/j.jaci.2019.10.037

Munroe, M. E., Businga, T. R., Kline, J. N., and Bishop, G. A. (2010). Anti-inflammatory effects of the neurotransmitter agonist Honokiol in a mouse model of allergic asthma. *J. Immunol.* 185 (9), 5586–5597. doi:10.4049/jimmunol.1000630

Ojiaku, C. A., Yoo, E. J., and Panettieri, R. A., Jr. (2017). Transforming growth factor beta1 function in airway remodeling and hyperresponsiveness. The missing link? *Am. J. Respir. Cell Mol. Biol.* 56 (4), 432–442. doi:10.1165/rcmb.2016-0307TR

Okwuofu, E. O., Yong, A. C. H., Lim, J. C. W., and Stanslas, J. (2022). Molecular and immunomodulatory actions of new antiasthmatic agents: Exploring the diversity of biologics in Th2 endotype asthma. *Pharmacol. Res.* 181, 106280. doi:10.1016/j.phrs.2022.106280

Padin-Gonzalez, E., Lancaster, P., Bottini, M., Gasco, P., Tran, L., Fadeel, B., et al. (2022). Understanding the role and impact of poly (ethylene glycol) (PEG) on nanoparticle formulation: Implications for COVID-19 vaccines. *Front. Bioeng. Biotechnol.* 10, 882363. doi:10.3389/fbioe.2022.882363

Paswan, S. K., and Saini, T. R. (2017). Purification of drug loaded PLGA nanoparticles prepared by emulsification solvent evaporation using stirred cell ultrafiltration technique. *Pharm. Res.* 34, 2779–2786. doi:10.1007/s11095-017-2257-5

Phan, H. T. L., Nam, Y. R., Kim, H. J., Woo, J. H., NamKung, W., Nam, J. H., et al. (2022). *In-vitro* and *in-vivo* anti-allergic effects of magnolol on allergic rhinitis via inhibition of ORAI1 and ANO1 channels. *J. Ethnopharmacol.* 289, 115061. doi:10.1016/j.jep.2022.115061

Ramis, J., Middlewick, R., Pappalardo, F., Cairns, J. T., Stewart, I. D., John, A. E., et al. (2022). Lysyl oxidase like 2 is increased in asthma and contributes to asthmatic airway remodelling. *Eur. Respir. J.* 60 (1), 2004361. doi:10.1183/13993003.04361-2020

Royce, S. G., Lim, C., Muljadi, R. C., Samuel, C. S., Ververis, K., Karagiannis, T. C., et al. (2013). Trefoil factor-2 reverses airway remodeling changes in allergic airways disease. *Am. J. Respir. Cell Mol. Biol.* 48 (1), 135–144. doi:10.1165/rcmb.2011-0320OC

Saviano, A., Raucci, F., Casillo, G. M., Mansour, A. A., Piccolo, V., Montesano, C., et al. (2022). Anti-inflammatory and immunomodulatory activity of Mangifera indica L. reveals the modulation of COX-2/mPGES-1 axis and Th17/Treg ratio. *Pharmacol. Res.* 182, 106283. doi:10.1016/j.phrs.2022.106283

Shao, L., Shen, S., and Liu, H. (2022). Recent advances in PLGA micro/nanoparticle delivery systems as novel therapeutic approach for drug-resistant tuberculosis. *Front. Bioeng. Biotechnol.* 10, 941077. doi:10.3389/fbioe.2022.941077

Southam, D. S., Ellis, R., Wattie, J., Glass, W., and Inman, M. D. (2008). Goblet cell rebound and airway dysfunction with corticosteroid withdrawal in a mouse model of asthma. *Am. J. Respir. Crit. Care Med.* 178 (11), 1115–1122. doi:10.1164/rccm.200801-084OC

Tang, H., Zhang, Y., Li, D., Fu, S., Tang, M., Wan, L., et al. (2018). Discovery and synthesis of novel magnolol derivatives with potent anticancer activity in non-

small cell lung cancer. *Eur. J. Med. Chem.* 156, 190–205. doi:10.1016/j.ejmech.2018.06.048

Tian, Y., Feng, H., Han, L., Wu, L., Lv, H., Shen, B., et al. (2018). Magnolol alleviates inflammatory responses and lipid accumulation by AMP-activated protein kinase-dependent peroxisome proliferator-activated receptor alpha activation. *Front. Immunol.* 9, 147. doi:10.3389/fimmu.2018.00147

Wang, J., Liu, X., Wang, H., Li, Y., Lan, N., Yuan, X., et al. (2017). Allergen specific immunotherapy enhanced defense against bacteria via TGF-β1-induced CYP27B1 in asthma. *Oncotarget* 8 (40), 68681–68695. doi:10.18632/oncotarget.19826

Wang, X., Yang, X., Li, Y., Wang, X., Zhang, Y., Dai, X., et al. (2017). Lyn kinase represses mucus hypersecretion by regulating IL-13-induced endoplasmic reticulum stress in asthma. *EBioMedicine* 15, 137–149. doi:10.1016/j.ebiom.2016.12.010

Xie, Y., Abel, P. W., Casale, T. B., and Tu, Y. (2022). TH17 cells and corticosteroid insensitivity in severe asthma. *J. Allergy Clin. Immunol.* 149 (2), 467–479. doi:10.1016/j.jaci.2021.12.769

Yang, J., Wang, Z. X., Fang, L., Li, T. S., Liu, Z. H., Pan, Y., et al. (2023). Atractylodes lancea and Magnolia officinalis combination protects against high fructose-impaired insulin signaling in glomerular podocytes through upregulating Sirt1 to inhibit p53-driven miR-221. *J. Ethnopharmacol.* 300, 115688. doi:10.1016/j.jep.2022.115688

Younis, N. K., Roumieh, R., Bassil, E. P., Ghoubaira, J. A., Kobeissy, F., and Eid, A. H. (2022). Nanoparticles: Attractive tools to treat colorectal cancer. *Semin. Cancer Biol.* 86 (2), 1–13. doi:10.1016/j.semcancer.2022.08.006

Zhang, Y., Fu, L. T., and Tang, F. (2018). The protective effects of magnolol on acute trinitrobenzene sulfonic acidinduced colitis in rats. *Mol. Med. Rep.* 17 (3), 3455–3464. doi:10.3892/mmr.2017.8321

frontiers | Frontiers in Bioengineering and Biotechnology

TYPE Original Research
PUBLISHED 05 May 2023
DOI 10.3389/fbioe.2023.1174014

OPEN ACCESS

EDITED BY
Jianxun Ding,
Changchun Institute of Applied Chemistry (CAS), China

REVIEWED BY
Manzar Abbas,
Khalifa University, United Arab Emirates
Jinjun Shao,
Nanjing Tech University, China
Jingxin Mo,
University of New South Wales, Australia

*CORRESPONDENCE
Xiaowei Zeng,
zengxw23@mail.sysu.edu.cn
Qiuxu Wang,
wangqx@sj-hospital.org
Zhigang Liang,
liangzhigang@yeah.net

RECEIVED 25 February 2023
ACCEPTED 03 April 2023
PUBLISHED 05 May 2023

CITATION
Yin X, Li Z, Zhang Y, Zeng X, Wang Q and Liang Z (2023), Polydopamine surface-modified hyperbranched polymeric nanoparticles for synergistic chemo/photothermal therapy of oral cancer. *Front. Bioeng. Biotechnol.* 11:1174014. doi: 10.3389/fbioe.2023.1174014

Polydopamine surface-modified hyperbranched polymeric nanoparticles for synergistic chemo/photothermal therapy of oral cancer

Xingyong Yin[1,2], Zimu Li[3], Yi Zhang[3], Xiaowei Zeng[3]*, Qiuxu Wang[1]* and Zhigang Liang[1]*

[1]Department of Stomatology, Shenzhen Second People's Hospital, Shenzhen, China, [2]Guangzhou Medical University, Guangzhou, China, [3]School of Pharmaceutical Sciences (Shenzhen), Sun Yat-sen University, Shenzhen, China

A novel drug delivery system for the treatment of oral cancer was developed using a facile polydopamine (PDA)-based surface modification and a binding mechanism linking folic acid-targeting ligands. The system was able to achieve the following objectives: loading of chemotherapeutic agents, active targeting, pH responsiveness, and prolonged *in vivo* blood circulation. DOX-loaded polymeric nanoparticles (DOX/H20-PLA@PDA NPs) were functionalized with amino-poly (ethylene glycol)-folic acid (H_2N-PEG-FA) after coating them with PDA to form the targeting combination, DOX/H20-PLA@PDA-PEG-FA NPs. The novel NPs exhibited drug delivery characteristics similar to DOX/H20-PLA@ PDA NPs. Meanwhile, the incorporated H_2N-PEG-FA contributed to active targeting, as illustrated in cellular uptake assays and animal studies. *In vitro* cytotoxicity and *in vivo* anti-tumor studies have shown that the novel nanoplatforms exhibit extremely effective therapeutic effects. In conclusion, the multifunctional PDA-modified H20-PLA@PDA-PEG-FA NPs offer a promising chemotherapeutic strategy to improve the treatment of oral cancer.

KEYWORDS

cancer nanotechnology, polydopamine, surface modification, oral cancer, synergistic therapy

Introduction

Approximately 4% of cancers occur in the oral cavity or oropharynx (Nandini et al., 2020). According to statistics, there were about 355,000 cases of oral cancer worldwide in 2018. The number of oral cancer patients in 2020 increased by about 53,260 new cases worldwide from the previous year, and as of the same year, the number of deaths was about 10,750 more than in previous years (Mosaddad et al., 2021). Among oral malignancies, squamous cell carcinoma (SCC) is the most common pathologic classification in the clinical field, and the number of cases of tongue squamous cell carcinoma (TSCC) has been increasing year by year in recent decades (da Silva Souto et al., 2021). At present, the main treatment method for oral cancer is still radical surgery (Marcazzan et al., 2018). Some postoperative patients have to accept postoperative radiotherapy and chemotherapy due to an insufficient pathological evaluation margin and a highly malignant pathological classification (Huang and O'Sullivan, 2013). To remove cancer cells as thoroughly as

possible, radical surgery requires a uniform expansion of the resection of the surrounding normal tissue. Therefore, a large number of patients have postoperative maxillofacial deformities, which may lead to the loss of speech, chewing, taste, or other basic functions (Sun et al., 2020). Despite the development of modern medicine, we can repair excised soft tissues with vascularly anastomosed musculocutaneous flap grafts (Girhe et al., 2021), but the appearance and function after the repair are still unsatisfactory. The failure of radiotherapy to target cancer cells leads to non-specific cell death, and many patients experience complications such as mucositis, osteomyelitis, mouth ulcers, and rampant dental caries (Minhas et al., 2017). Chemotherapeutic drugs also have toxic effects on normal cells, and their mode of drug delivery makes them have non-specific tissue distribution in the body, which is easy to cause greater damage to the healthy tissues of the body and produces serious adverse reactions (Zhang et al., 2020).

Breast cancer, lung cancer, cervical cancer, ovarian cancer, prostate cancer, and pancreatic cancer have all been successfully treated in nanomedicine research, and several nanoplatforms have even received clinical approval (Shi et al., 2017; Duo et al., 2018; Zeng et al., 2018; Banstola et al., 2019; Zeng et al., 2019; Yang et al., 2022). Due to the high incidence and poor prognosis of oral squamous cell carcinoma (Li et al., 2020), at present, a variety of effective carrier systems based on nanotechnology have been widely studied as a treatment for oral squamous cell cancer (Gharat et al., 2016). However, there are still no approved nanoplatforms for the clinical treatment of oral cancer. Nanomedicine platforms can also achieve synergistic anticancer therapy, such as chemotherapy combined with photothermal therapy (Liu et al., 2018; Peng et al., 2018; Li et al., 2021; Li et al., 2022), photodynamic therapy (Tao et al., 2018; Mo et al., 2022), immunotherapy (Liang et al., 2020; Jia et al., 2022), photothermal therapy combined with immunotherapy (Zeng et al., 2022), and more. These are conducive to improving the cure rate of malignant tumors. Phototherapies, including photodynamic therapy (PDT) and photothermal therapy (PTT), are non-invasive techniques for cancer treatment. Broadly speaking, phototherapies involve two major steps: first, the delivery of a photosensitizer to tumors, and second, the irradiation of the tumor sites with specific light to activate the photosensitizer. However, most of the reported photosensitizers are highly hydrophobic and cannot be directly applied for treatment purposes (Abbas et al., 2017). Nanomedicine delivery vehicles are promising for loading the photosensitizers into nanoparticles, ensuring that the photosensitizers are stable in an aqueous solution, and also providing better accumulation in tumor tissues through the enhanced permeability and retention (EPR) effect (Zhou et al., 2015; Abbas et al., 2017; Abbas et al., 2018). The vast majority of oral cancers arise from mutations in the oral mucosa or epithelium (Scully and Bagan, 2009), and the lesion is located at the exposed oral site. In superficial local solid tumors, photothermal therapy has been shown to have strong killing effects (Zhang et al., 2019). Therefore, the use of photothermal therapy in the treatment of tumors at exposed oral sites is of great significance for the research. Early stages of oral cancer usually present with persistent oral ulcers, oral masses, or other obvious premalignant lesions (Brandizzi et al., 2008), which contributes to the early detection of lesions. Therefore, the strong killing of local tumor cells by photothermal therapy and targeted chemotherapy can achieve a radical cure for oral cancer in the early stage of the disease and reduce adverse reactions to the body.

The following benefits of polydopamine surface modification make it suitable for different nanoparticle drug carriers: to begin with, PDA membranes contain a dense, cross-linked fabric that increases the stability of nanoparticles (NPs) *in vivo* and prevents early drug release (Park et al., 2014; Zeng et al., 2018; Ci et al., 2019). Furthermore, the abundant quinone groups on the surface of PDA readily react with amino-containing and thiol-containing substances, enabling surface modifications such as binding to PEG and tumor-targeting ligands (Park et al., 2014; Tao et al., 2016; Zhu et al., 2016; Cheng et al., 2017a). Additionally, the PDA surface effectively adsorbs drugs, especially doxorubicin (DOX) (Chang et al., 2016; Cheng et al., 2017b; Liu et al., 2019). Finally, PDA has a high near-infrared photothermal energy conversion efficiency, which suggests that it is a promising and effective phototherapeutic agent (Cheng et al., 2017c; Peng et al., 2018; Zeng et al., 2018).

In addition to passive targeting through EPR effects or active targeting, NPs can increase drug efficacy by improving drug encapsulation and delivery, prolonging cycle half-life, and constantly targeting drug release (Luk and Zhang, 2014; Wei et al., 2016). NPs serve as customizable targeted drug delivery carriers to deliver chemotherapeutic drugs or therapeutic genes to tumor cells. Lower doses of toxic substances can be used because the drug is delivered directly to the target tissue (Poonia et al., 2017). NPs can improve drug stability and control their targeted delivery, thus maintaining constant and uniform concentrations at the lesion site and promoting drug extravasation into the tumor system, thereby reducing side effects. Nanoparticles loaded with photosensitizers can reach the most sensitive subcellular sites, with the ability to treat superficial oral cancers or premalignant lesions (Calixto et al., 2014).

This paper aims to investigate the use of DOX/H20-PLA@PDA-PEG-FA for synergistic chemotherapy and photothermal therapy of oral cancer, which may lead to the development of new oral cancer therapeutic approaches with relatively low side effects.

Methods

Characterization of NPs

Transmission electron microscopy image

The prepared NPs were resuspended in ethanol, treated with ultrasound to spread them uniformly, and added dropwise to the copper mesh coated with carbon film. After the samples were dried, the surface morphology of the NPs (DOX/H20-PLA NPs, DOX/H20-PLA@PDA-PEG-FA) was observed by transmission electron microscopy.

Fourier transform infrared spectroscopy (FT-IR) analysis

The Fourier transform infrared spectra of NPs (DOX/H20-PLA, DOX/H20-PLA@PDA, DOX/H20-PLA@PDA-PEG, DOX/H20-PLA@PDA-PEG-FA) were recorded to analyze the elemental composition of the nanoparticle surface and the chemical modification of the surface.

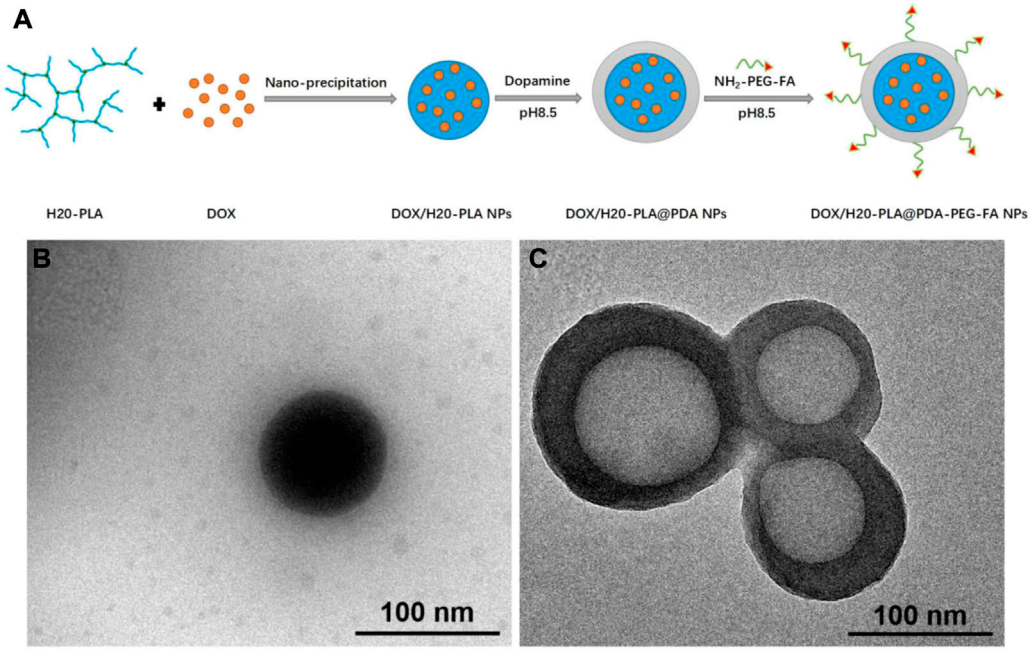

FIGURE 1
(A) Schematic illustration of the preparation procedure of the targeted DOX/H20-PLA@PDA-PEG-FA NPs, **(B)** TEM images of DOX/H20-PLA NPs, **(C)** DOX/H20-PLA@PDA-PEG-FA NPs.

Size distribution and zeta potential (size and zeta potential)

The prepared NPs were resuspended in DI water and treated with ultrasound to spread them uniformly. Dynamic light scattering (DLS) was performed to evaluate the NPs (DOX/H20-PLA, DOX/H20-PLA@PDA, DOX/H20-PLA@PDA-PEG, DOX/H20-PLA@PDA-PEG-FA) in terms of particle size distribution and zeta potential. All experiments were repeated three times independently, and the means were taken.

Drug loading content

The supernatant collected from each of the above steps was used to establish the drug loading of the NPs. The drug concentration was calculated by high-performance liquid chromatography (HPLC). For DOX, the mobile phases were phosphate buffer, methanol, and acetonitrile (30:20:50, v/v) at a flow rate of 1 mL/min with 20 μL per injection, and DOX was detected at 233 nm using an ultraviolet-visible (UV-Vis) detector. The *LC* (%) was calculated from the drug standard curve using the following equation.

$$\mathrm{LC}(\%) = \frac{\text{Weight of DOX in NPs}}{\text{Weight of NPs}} \times 100\% \quad (1)$$

Evaluation of the photothermal effect

To evaluate the photothermal properties of the modified nano-drug delivery systems, various NPs (200 μg/mL) and PBS, which were the blank controls, were irradiated under the 808 nm laser with a laser intensity of 1.0 W/cm^2 for 10 min. Then, the DOX/H20-PLA@PDA-PEG-FA NPs at concentrations of 50, 100, 200, and 500 μg/mL were irradiated under the 808 nm laser with a laser intensity of 1.0 W/cm^2 for 10 min. To determine the influence of different laser power densities on the photothermal effect, the DOX/H20-PLA@PDA-PEG-FA NPs (200 μg/mL) were irradiated for 10 min under a laser intensity of 0.5, 1.0, 1.5, and 2.0 W/cm^2, respectively. Finally, to investigate the stability of DOX/H20-PLA@PDA-PEG-FA NPs, they were irradiated for five cycles under a laser intensity of 1.0 W/cm^2, and each cycle was irradiated for 10 min and then cooled for 10 min. In all experiments, the temperature changes were recorded by a near-infrared imaging camera (Ti 450, Fluke, US), and the temperature curves were plotted.

Cell viability study

An MTT assay was used to ascertain the cytotoxicity of NPs on SCC-9 cells and TCA-8113 cells. After the SCC-9 cells and the TCA-8113 cells were seeded into a 96-well plate at a concentration of 1 × 10^6 cells/wells, respectively, they were cultured overnight. The drug-loaded NPs (DOX/H20-PLA@PDA-PEG and DOX/H20-PLA@PDA-PEG-FA) at DOX concentrations of 0, 0.1, 1, 5, and 10 μg/mL were added and cultured for another 24 h and 48 h. Then MTT solution (20 μL, 5 mg/mL) was added to each well, and the cells were cultured for an additional 4 h. The media containing MTT was aspired after 4 h. Then the DMSO was dropped into each well and the crystals were allowed to dissolve for 2 h in the dark at 37°C. The optical density value of each well was detected using a microplate reader at a wavelength of 490 nm. The control group (drug-free H20-PLA@PDA-PEG-FA NPs) represented zero absorbance. Cell viability was evaluated by MTT at each time point. In addition, the toxicity of the above-mentioned drug-loaded NPs to the target cells after

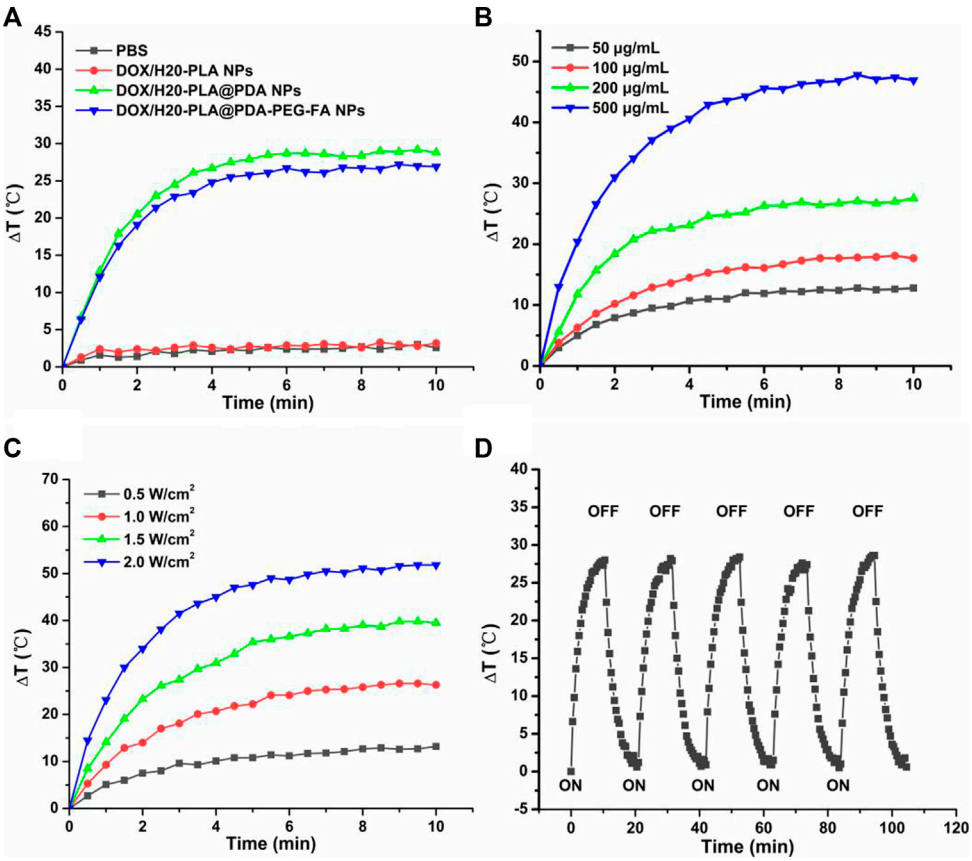

FIGURE 2
(A) Temperature variation curves of the aqueous dispersions of PBS, DOX/H20-PLA NPs, DOX/H20-PLA@PDA NPs, and DOX/H20-PLA@PDA-PEG-FA NPs (200 μg/mL) exposed to an 808 nm laser at a power density of 1.0 W/cm^2 for 10 min. **(B)** Temperature variation curves of DOX/H20-PLA@PDA-PEG-FA NPs with different concentrations. **(C)** Temperature variation curves of DOX/H20-PLA@PDA-PEG-FA NPs (200 μg/mL) under different power intensities. **(D)** Temperature variation curves of DOX/H20-PLA@PDA-PEG-FA NPs (200 μg/mL) with five cycles of consecutive laser irradiation.

laser irradiation was compared. Cell viability data compared to control subjects were examined by curve fitting.

Animals and tumor model

Female nude mice (BALB/c-nude, 4–5 weeks old) were purchased from the Guangdong Medical Laboratory Animal Center (China), and all *in vivo* experimental protocols were approved by the Institutional Animal Care and Use Committee of Sun Yat-sen University (Approval No. SYSU-IACUC-2022-000836). After 1–2 weeks of culture in a specific pathogen-free (SPF) grade laboratory chamber, each mouse (18–20 g) was injected with 100 μL suspended SCC-9 cells (2×10^6 cells) in PBS to establish the cell xenograft model. The tumor volume (V) was measured with a vernier caliper and then calculated by aliquot: $V = A \times B^2/2$, where A and B refer to the length and width of the tumor, respectively.

In Vivo anti-tumor efficacy

After the tumor volume was increased to 200 mm^3, the mice were randomly divided into 6 groups (n = 5). Intravenous saline was administered as a control. Every 4 days (0, 4, 8, 12, 16), each group of nude mice was injected separately with 100 μL saline, drug-free H20-PLA@PDA-PEG-FA, DOX, and drug-loaded NPs (DOX/H20-PLA@PDA-PEG, DOX/H20-PLA@PDA-PEG-FA) via the tail vein at a DOX density of 10 mg/kg. In addition, the photothermal group was irradiated after each injection of DOX/H20-PLA@PDA-PEG-FA NPs. The tumor volume was recorded every 1 day with a caliper, and its weight was measured once. Mice were sacrificed after 20 days of treatment, and their tumor tissues were isolated and weighed. Major organs (heart, lung, liver, spleen, and kidney) and tumors were then collected and fixed in 10% neutral formalin for histological analysis. After paraffin embedding, tissues, and samples were cut into approximately 4 μm sections and analyzed by light microscopy after staining with hematoxylin and eosin (H&E).

Results and discussion

Synthesis of polymeric NPs

The preparation of the dendritic copolymer H20-PLA by ring-opening polymerization is shown in Supplementary Figure S1. As

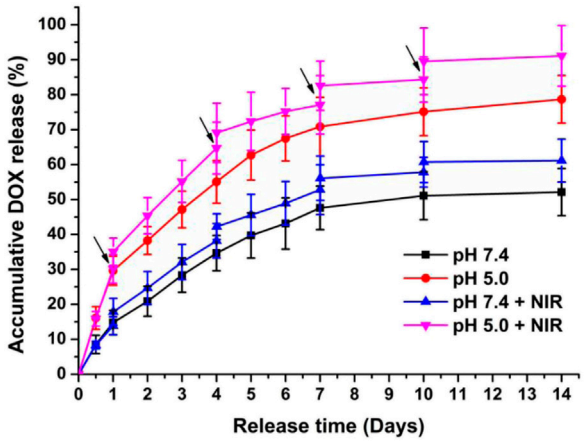

FIGURE 3
In vitro drug release profiles of DOX/H20-PLA@PDA-PEG-FA NPs at different pH with or without NIR laser irradiation (808 nm, 1.0W/cm^2). ↓: NIR irradiation for 10 min.

shown in Figure 1A, the preparation process of the target NPs mainly included the loading with the broad-spectrum anticancer drug doxorubicin (DOX), the surface modification of polydopamine, and the attachment of the targeting ligands. Under weakly alkaline conditions, dopamine monomers were oxidized to quinones and polymerized to form polydopamine to adhere to the surface of the nanoparticles, which was useful to achieve both targeting ligand attachment and anticancer drug adsorption with good photothermal efficiency (Scully and Bagan, 2009). H_2N-PEG-FA was used as the targeting ligand and attached to the polydopamine on the nanoparticle surface via the Michael addition reaction under alkaline conditions. The DOX/H20-PLA@PDA-PEG-FA NPs were obtained as a targeted nano-delivery system for combined chemotherapy and photothermal therapy.

Characterization of polymeric NPs

According to Figures 1B,C and Supplementary Figure S2, both DOX/H20-PLA NPs and DOX/H20-PLA@PDA-PEG-FA NPs were observed as smooth nanospheres under transmission electron microscopy. The DOX/H20-PLA@PDA-PEG-FA NPs had an apparent core-shell structure, demonstrating that the PDA layer was deposited on the surface of the NPs (Liu et al., 2019). As evidence, Supplementary Figure S3 showed that: 1) the FT-IR spectra of all NPs can be found with absorption peaks at 1760 cm^{-1}, representing the carbonyl group in H20-PLA; 2) the absorption peak at 1,510 cm^{-1} is attributed to the bending vibration of N-H; and 3) the broad absorption between 3,600 cm^{-1} and 3,300 cm^{-1} is due to the stretching vibration of the N-H/O-H group. The above results suggest that the surface of the NPs is modified with PDA in addition to PEG or PEG-FA.

Both the size and zeta potential of NPs are essential for their stabilization and EPR effects (Bertrand et al., 2014; Sykes et al., 2014). NPs in the 10–200 nm diameter range are most likely to be taken up by tumor tissue through the EPR effects (Sykes et al., 2014; Liu et al., 2019). Dynamic light scattering (DLS) was used to determine the size and size distribution of the nanoparticles. As illustrated in Supplementary Table S1 and Supplementary Figure S4, the average diameters of the drug-loaded NPs (DOX/H20-PLA NPs, DOX/H20-PLA@PDA NPs, DOX/H20-PLA@PDA-PEG NPs and DOX/H20-PLA@PDA-PEG-FA NPs) were approximately in the range of 100–160 nm, respectively. The low polydispersity index (PDI <0.2) indicates that they have a relatively uniform size distribution, which facilitates drug delivery *in vivo*. The zeta potentials of NPs were negative, which facilitated prolonged cycling before tumor tissue enrichment (Zhu et al., 2015; Linlin et al., 2016). After surface modification of DOX/H20-PLA NPs with polydopamine, the zeta potential was still negative. This is probably explained by the deprotonation of the phenolic hydroxyl group of polydopamine at neutral pH (Yu et al., 2010; Kim et al., 2014). The modified hydrophilic PEG segment reduced the absolute value of the zeta potential due to the surface charge shielding effect (Chen et al., 2017). According to the test results, the drug loading of the NPs was greater than 8.4%, indicating that the nanoparticles' surface modification did not significantly reduce the drug loading and the drug-loaded NPs had a good level of drug loading.

When NPs are temporarily stored after preparation, they appear to aggregate depending on the decrease in the absolute value of the zeta potential. Maintaining the stability of NPs is essential for therapeutic efficacy. Their average size and zeta potential were examined every 10 days after preparation to observe the stability of the drug-loaded NPs under storage conditions. As shown in Supplementary Figure S5, the size and zeta potential of the NPs did not change significantly during storage (90 days), and the data suggest that the NPs are quite stable.

Photothermal effect and drug release profiles of NPs

As shown in Figure 2A, the temperature of DOX/H20-PLA@PDA NPs and DOX/H20-PLA@PDA-PEG-FA NPs rapidly increased by more than 25°C within 10 min under irradiation at an intensity of 1.0 W/cm^2. In contrast, the temperature of PBS and DOX/H20-PLA NPs under the same conditions showed no significant change. The results indicate that the drug-loaded polymer nanoparticles (DOX/H20-PLA NPs) do not have photothermal properties by themselves but have photothermal conversion properties after their PDA surface modification. This is also consistent with many previous studies showing that PDA has obvious NIR absorption and better photothermal conversion efficiency. In addition, as shown in Figures 2B,C, both power intensity and nanoparticle concentration also affected the photothermal efficiency of NPs. For example, as the power intensity of the layer increased from 0.5 to 2.0 W/cm^2, the temperature of 200 μg/mL DOX/H2O-PLA@PDA-PEG-FA NPs increased rapidly, or as the nanoparticle concentration increased from 50 to 500 μg/mL, the temperature of DOX/H20-PLA@PDA-PEG-FA NPs at the laser intensity of 1.0 W/cm^2 also increased rapidly. Therefore, DOX/H20-PLA@PDA-PEG-FA NPs exhibited photothermal efficiency depending on laser power intensity and concentration. 200 μg/mL DOX/H20-PLA@PDA-PEG-FA NPs were irradiated for 5 on/off cycles at a laser intensity of 1.0 W/cm^2. In each cycle, irradiation was performed for 10 min followed by cooling for 10 min. Through cycling experiments (Figure 2D), we

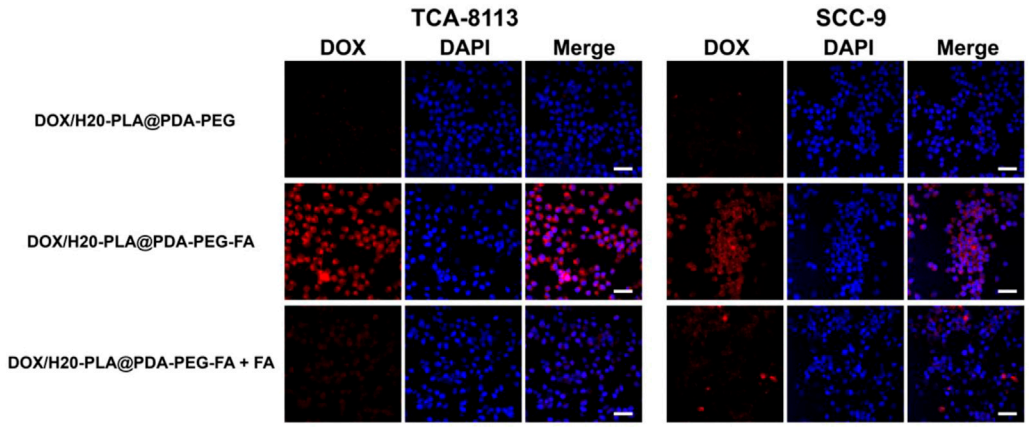

FIGURE 4
Confocal laser scanning microscopy (CLSM) images of TCA-8113/SCC-9 cells after incubation with NPs for 2 h. Blue: DAPI-stained nucleus. Scale bar = 20 μm.

found that the temperature change of DOX/H20-PLA@PDA-PEG-FA NPs is not significant, which indicates that DOX/H20-PLA@PDA-PEG-FA NPs have good photothermal stability. In conclusion, DOX/H20-PLA@PDA-PEG-FA NPs may become a promising potential photothermal cancer therapy.

The NPs will be exposed to different microenvironments whose pH values are quite different during *in vivo* delivery, such as pH~7.4 in the bloodstream and pH~5.0 in the lysosome. The drug release curves of DOX/H20-PLA@PDA-PEG-FA NPs in the medium of pH = 7.4/5.0 were shown in Figure 3. The results indicated that the DOX release curves of DOX/H20-PLA@PDA-PEG-FA NPs showed obvious pH responsiveness and the laser irradiation dependence. All of the above drug release curves displayed an explosive release of DOX in the primary stage and then entered a slow-release stage. After 14 days, the final drug release levels were approximately 75% and 50% at pH 5.0 and pH 7.4, respectively, which was probably attributable to the shedding of the PDA film from the acidic environment. This facilitated the release of DOX. Furthermore, the DOX/H20-PLA@PDA-PEG-FA NPs enhanced the drug release by about 10%–15% each time under laser irradiation, which may be attributed to the photothermal effect of PDA. It may reduce premature DOX release during cycling and increase specific release in the acidic tumor microenvironment due to this pH responsiveness and the laser radiation dependence of NPs. This also reduces the side effects of the drug as well as modulates the volume of drug release in the cells. Therefore, this drug delivery system may be desirable and promising.

Cellular uptake of fluorescent NPs

To investigate the uptake of NPs by tumor cells, these (TCA-8113 cells/SCC-9 cells) were labeled with DAPI and analyzed by confocal laser scanning microscopy (CLSM). Figure 4 shows that DOX/H20-PLA@PDA-PEG NPs were not well taken up by the two aforementioned tongue squamous carcinoma cells, as no red fluorescence was observed in the non-aptamer group. On the contrary, the red fluorescence around the blue fluorescence of the nucleus could be seen in the aptamer group, indicating that a large amount of DOX/H20-PLA@PDA-PEG-FA NPs entered the tumor cytoplasm, and no significant difference was observed in the two types of tongue squamous carcinoma cells. To verify whether the cellular uptake mechanism in the active targeting group was mediated by aptamers or not, both active targeting NPs and free aptamers were added to the cell cultures in the control group. According to Figure 4, the addition of aptamers significantly reduced the red fluorescence, suggesting that the uptake of active targeting NPs was associated with aptamer-mediated endocytosis.

Effect of NPs on cell viability

The cytotoxicity of the nanoparticles to SCC-9 cells and TCA-8113 cells *in vitro* was assessed using MTT assays and compared with the toxicity of the same nanoparticles to the target cells after laser irradiation. Drug-free H20-PLA@PDA-PEG-FA NPs were used to evaluate the toxicity of the drug vehicle to cells.

The cytotoxicity of the nano-drug carriers used in this experiment was evaluated by measuring the cell viability of SCC-9 and TCA-8113 cells after 24 h (Figure 5A; Figure 6A) and 48 h (Figure 5B; Figure 6B) of therapy with drug-free H20-PLA@PDA-PEG-FA NPs. According to the results, the cells treated with drug-free H20-PLA@PDA-PEG-FA NPs exhibited a survival rate close to 100% under all conditions, indicating that the vector material was essentially non-toxic to both cells.

The following results were obtained: 1) the toxicity of all drug-loaded NPs to TCA-8113 cells intensified with increasing drug concentration and also with increasing duration of action (Figure 6); 2) the toxicity of all drug-loaded NPs to SCC-9 cells intensified with increasing drug concentration, but the cytotoxicity decreased after the duration of action beyond 24 h (Figure 5); 3) under the same treatment time and the same drug concentration, the cytotoxicity of drug-loaded NPs with targeting ligands was significantly higher than that of NPs without targeting ligands (Figure 5; Figure 6), indicating that the active targeting mechanism

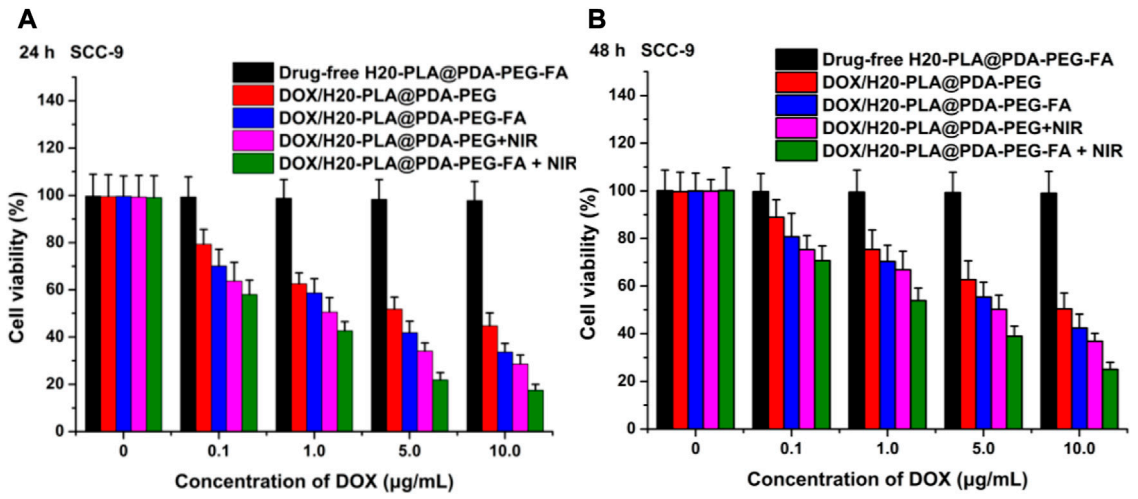

FIGURE 5
Viability of SCC-9 cells cultured with drug-loaded NPs (DOX/H20-PLA@PDA-PEG NPs, DOX/H20-PLA@PDA-PEG-FA NPs) with or without NIR laser irradiation (808 nm, 1.0W/cm^2) compared with drug-free NPs at the same dose for **(A)** 24 h and **(B)** 48 h (t-test, *p < .05, **p < .01, ***p < .001).

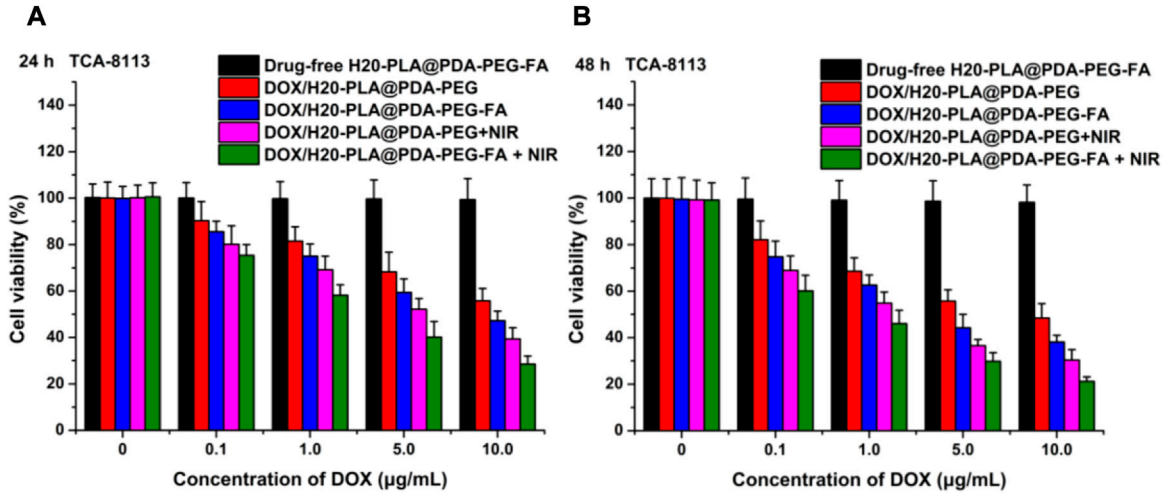

FIGURE 6
Viability of TCA-8113 cells cultured with drug-loaded NPs (DOX/H20-PLA@PDA-PEG NPs, DOX/H20-PLA@PDA-PEG-FA NPs) with or without NIR laser irradiation (808 nm, 1.0W/cm^2) compared with drug-free NPs at the same dose for **(A)** 24 h and **(B)** 48 h (t-test, *p < .05, **p < .01, ***p < .001).

mediated by folic acid was more helpful for drug-loaded NPs to kill tumor cells than the passive accumulation mechanism; 4) under the same treatment time and the same drug concentration, the cytotoxicity of different drug-loaded NPs significantly increased under NIR laser irradiation (Figure 5; Figure 6), which was consistent with the laser irradiation-dependent toxicity of the drug-loaded nanoparticles in the *in vitro* drug release experiment; 5) for TCA-8113 cells, the experimental group treated with DOX/H20-PLA@PDA-PEG-FA NPs at a DOX concentration of 10.0 μg/mL for 48 h and simultaneously treated with laser irradiation exhibited the lowest cell viability, i.e., the highest cytotoxicity, among all the experimental groups; 6) for SCC-9 cells, the group treated with DOX/H20-PLA@PDA-PEG-FA NPs at a concentration of 10.0 μg/mL for 24 h and simultaneously treated with laser irradiation exhibited the lowest cell survival rate, i.e., the highest cytotoxicity, among all the experimental groups. In conclusion, the active targeting mechanism combined with synergistic photothermal treatment improved the cytotoxicity of the tumor cells.

In Vivo anti-tumor efficacy

Based on the cytotoxicity assay, the *in vivo* anti-tumor effect of drug-loaded nanoparticles was further investigated to verify the *in*

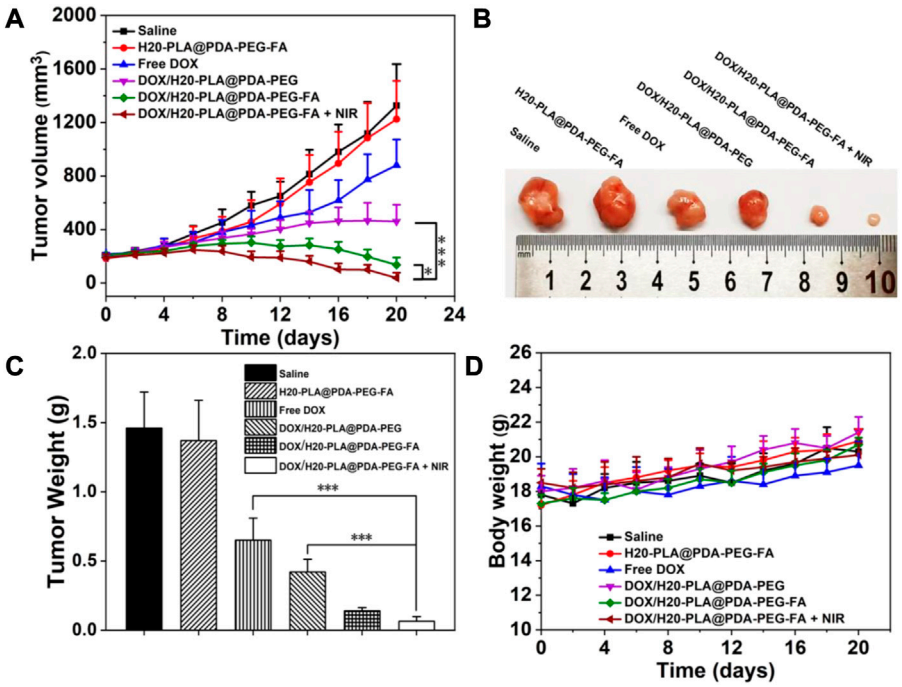

FIGURE 7
(A) Changes in tumor volumes treated with different NPs. **(B)** Morphology of representative tumors removed from the sacrificed mice treated with different NPs. **(C)** Tumor weights of each group treated with different NPs. **(D)** Changes in body weight of mice treated with different NPs. Data are expressed as mean ± SD (n = 5). $*p < 0.05$ and $***p < 0.001$.

vivo tumor suppressive effect. We used injected saline as a blank control and injected drug-free H20-PLA@PDA-PEG-FA NPs, DOX, drug-loaded NPs (DOX/H20-PLA@PDA-PEG NPs, DOX/H20-PLA@PDA-PEG-FA NPs), and DOX/H20-PLA@PDA-PEG-FA NPs + NIR (as photothermal treatment). Injections were given every 4 days during the 20-day treatment cycle, and the photothermal team was treated with laser irradiation after 24 h. Tumor volume measurements using vernier calipers and weighing of nude mice were performed every 1 day. The nude mice were sacrificed 20 days later, and the tumor tissue was isolated.

The results were as follows: 1) there was no significant difference in tumor volume and weight between the saline and drug-free NPs groups (Figures 7A–C), indicating that drug-free NPs were not lethal to the tumor tissue; 2) the tumor volume and weight in the naked drug group were larger than all experimental groups containing drug-loaded NPs (Figures 7A–C), which may be due to the hydrophilic PEG modification on the surface of NPs, which helped to reduce the reticuloendothelial tissue clearance, resulting in a greater effective drug accumulation at the tumor site in the drug-loaded NPs group than in the naked drug group; 3) the tumor volume in the DOX/H20-PLA@PDA-PEG-FA NPs group during the experimental cycle was basically smaller than that in the DOX/H20-PLA@PDA-PEG NPs group (Figure 7A), and finally, the DOX/H20-PLA@PDA-PEG -FA NPs experimental group also had a significantly lower tumor tissue weight than the DOX/H20-PLA@PDA-PEG NPs experimental group (Figure 7C), indicating that the targeting ligand folic acid binds to the folic acid receptor overexpressed on the surface of tumor cells and facilitates the uptake of drug-loaded nanoparticles by tumor cells; 4) the volume of tumors in the experimental group treated with DOX/H20-PLA@PDA-PEG-FA NPs + NIR gradually decreased during the treatment cycle (Figure 7A), indicating that the targeted nano-delivery system combined with photothermal treatment could significantly inhibit tumor growth; 5) the tumor volume of the experimental group treated with DOX/H20-PLA@PDA-PEG-FA NPs basically did not increase during the treatment cycle (Figure 7A), indicating its effect in inhibiting tumor growth; 6) in the same time period, the body weight of nude mice in each experimental group was basically not different from that of the saline group (Figure 7D), indicating that the drug-loaded NPs had no obvious toxic side effects on nude mice. In conclusion, the targeted nano-drug delivery system based on polydopamine in combination with photothermal therapy can inhibit tumor growth with essentially no toxic side effects and has good prospects for tumor treatment.

Histological analysis

The nude mice were sacrificed and their major organs (heart, lung, liver, spleen, and kidney) collected, and the effects of drug-loaded nanoparticles on the major organs were further investigated using a tissue section analysis assay. As shown in Figure 8, there was no significant damage to the major organs and tumor tissues in both the saline control group and the nude mice with drug-free nanoparticles, which means that the drug-free nanoparticles were not cytotoxic. For the drug-loaded nanoparticle group, there was no significant damage to the major organ sections, but the tumor tissue sections had a wide range of apoptosis and damage: large areas of cell

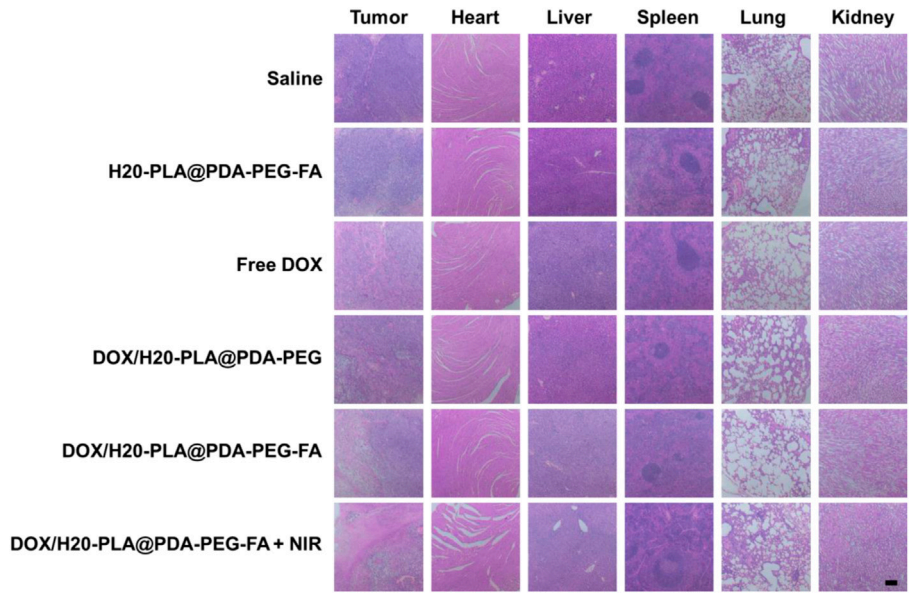

FIGURE 8
Representative H&E stained images of tumors and major organs (heart, liver, spleen, lung, and kidney) of each group treated with different NPs. Scale bar = 200 μm.

necrosis were observed in the tumor tissue sections treated with DOX/H20-PLA@PDA-PEG-FA + NIR, indicating that it caused more severe damage to the tumor and improved tumor suppression efficacy.

In conclusion, the tumor-inhibiting effect of drug-loaded nanoparticles *in vivo* and the results of cytotoxicity experiments are mutually consistent. The drug-loaded nanoparticles essentially inhibited tumor growth without causing damage to major organs. Therefore, DOX/H20-PLA@PDA-PEG-FA + NIR therapy may be a safe and effective novel tumor treatment modality.

Conclusion

The DOX/H20-PLA@PDA-PEG-FA NPs used in this experiment were prepared according to the following steps: DOX loading, surface modification with polydopamine, and targeting ligand attachment. The surface modification of the nanoparticles with a polydopamine molecular layer and targeting ligands promoted the passive accumulation and active targeting of the nanoparticles in the tumor tissue, respectively, which further improved the distribution of the nanoparticles *in vivo*. Due to the photothermal effect and the pH sensitivity of the PDA films, drug release was accelerated in the acidic tumor microenvironment under laser irradiation. *In vitro* results show that the NPs display non-cytotoxicity and high biocompatibility. In addition, the NPs showed outstanding chemotherapeutic-photothermal synergy under laser irradiation, probably due to their excellent photothermal conversion properties. In conclusion, the NPs exhibit the following characteristics: long-lasting cycling *in vivo* (PEG), active targeting (FA), pH responsiveness (PDA), and chemotherapeutic drug loading and release. This novel polydopamine-surface-modified nanoplatform offers a new direction in oral cancer therapy with significant potential for tumor therapy.

Data availability statement

The original contributions presented in the study are included in the article/Supplementary Material, further inquiries can be directed to the corresponding authors.

Ethics statement

The animal study was reviewed and approved by the Institutional Animal Care and Use Committee of Sun Yat-sen University.

Author contributions

XZ, QW, and ZL conceived the research project. XY, ZL, and YZ performed the experiments and drafted the manuscript. XY and ZL participated in data analysis and manuscript writing. The final draft of the article was approved by all authors.

Acknowledgments

The authors are grateful for the financial support from the Science, Technology and Innovation Commission of Shenzhen Municipality (JCYJ20210324102810028).

Conflict of interest

The authors declare that the research was conducted in the absence of any commercial or financial relationships that could be construed as a potential conflict of interest.

Publisher's note

All claims expressed in this article are solely those of the authors and do not necessarily represent those of their affiliated organizations, or those of the publisher, the editors and the reviewers. Any product that may be evaluated in this article, or claim that may be made by its manufacturer, is not guaranteed or endorsed by the publisher.

Supplementary material

The Supplementary Material for this article can be found online at: https://www.frontiersin.org/articles/10.3389/fbioe.2023.1174014/full#supplementary-material

References

Abbas, M., Xing, R., Zhang, N., Zou, Q., and Yan, X. (2018). Antitumor photodynamic therapy based on dipeptide fibrous hydrogels with incorporation of photosensitive drugs. *ACS Biomater. Sci. Eng.* 4 (6), 2046–2052. doi:10.1021/acsbiomaterials.7b00624

Abbas, M., Zou, Q., Li, S., and Yan, X. (2017). Self-assembled peptide- and protein-based nanomaterials for antitumor photodynamic and photothermal therapy. *Adv. Mater* 29 (12), 1605021. doi:10.1002/adma.201605021

Banstola, A., Pham, T. T., Jeong, J. H., and Yook, S. (2019). Polydopamine-tailored paclitaxel-loaded polymeric microspheres with adhered NIR-controllable gold nanoparticles for chemo-phototherapy of pancreatic cancer. *Drug Deliv.* 26 (1), 629–640. doi:10.1080/10717544.2019.1628118

Bertrand, N., Wu, J., Xu, X., Kamaly, N., and Farokhzad, O. C. (2014). Cancer nanotechnology: The impact of passive and active targeting in the era of modern cancer biology. *Adv. Drug Deliv. Rev.* 66, 2–25. doi:10.1016/j.addr.2013.11.009

Brandizzi, D., Gandolfo, M., Velazco, M. L., Cabrini, R. L., and Lanfranchi, H. E. (2008). Clinical features and evolution of oral cancer: A study of 274 cases in buenos aires, Argentina. *Med. Oral Patol. Oral Cir. Bucal* 13 (9), E544–E548.

Calixto, G., Fonseca-Santos, B., Chorilli, M., and Bernegossi, J. (2014). Nanotechnology-based drug delivery systems for treatment of oral cancer: A review. *Int. J. Nanomedicine* 9, 3719–3735. doi:10.2147/ijn.s61670

Chang, D., Gao, Y., Wang, L., Liu, G., Chen, Y., Wang, T., et al. (2016). Polydopamine-based surface modification of mesoporous silica nanoparticles as pH-sensitive drug delivery vehicles for cancer therapy. *J. Colloid Interface Sci.* 463, 279–287. doi:10.1016/j.jcis.2015.11.001

Chen, J., Wu, Q., Luo, L., Wang, Y., Zhong, Y., Dai, H., et al. (2017). Dual tumor-targeted poly(lactic-co-glycolic acid)–polyethylene glycol– folic acid nanoparticles: A novel biodegradable nanocarrier for secure and efficient antitumor drug delivery. *Int. J. Nanomedicine* 12, 5745–5760. doi:10.2147/ijn.s136488

Cheng, W., Liang, C., Xu, L., Liu, G., Gao, N., Tao, W., et al. (2017). TPGS-functionalized polydopamine-modified mesoporous silica as drug nanocarriers for enhanced lung cancer chemotherapy against multidrug resistance. *Small* 13 (29), 1700623. doi:10.1002/smll.201700623

Cheng, W., Nie, J., Gao, N., Liu, G., Tao, W., Xiao, X., et al. (2017). A multifunctional nanoplatform against multidrug resistant cancer: Merging the best of targeted chemo/gene/photothermal therapy. *Adv. Funct. Mater.* 27 (45), 1704135. doi:10.1002/adfm.201704135

Cheng, W., Nie, J., Xu, L., Liang, C., Peng, Y., Liu, G., et al. (2017). pH-sensitive delivery vehicle based on folic acid-conjugated polydopamine-modified mesoporous silica nanoparticles for targeted cancer therapy. *ACS Appl. Mater Interfaces* 9 (22), 18462–18473. doi:10.1021/acsami.7b02457

Ci, L. Q., Huang, Z. g., Lv, F. m., Wang, J., Feng, L. l., Sun, F., et al. (2019). Enhanced delivery of imatinib into vaginal mucosa via a new positively charged nanocrystal-loaded *in situ* hydrogel formulation for treatment of cervical cancer. *Pharmaceutics* 11 (1), 15. doi:10.3390/pharmaceutics11010015

da Silva Souto, A. C., Vieira Heimlich, F., Lima de Oliveira, L., Bergmann, A., Dias, F. L., Spíndola Antunes, H., et al. (2021). Epidemiology of tongue squamous cell carcinoma: A retrospective cohort study. *Oral Dis.* 29, 402–410. doi:10.1111/odi.13897

Duo, Y., Yang, M., Du, Z., Feng, C., Xing, C., Wu, Y., et al. (2018). CX-5461-loaded nucleolus-targeting nanoplatform for cancer therapy through induction of pro-death autophagy. *Acta Biomater.* 79, 317–330. doi:10.1016/j.actbio.2018.08.035

Gharat, S. A., Momin, M., and Bhavsar, C. (2016). Oral squamous cell carcinoma: Current treatment strategies and nanotechnology-based approaches for prevention and therapy. *Crit. Rev. Ther. Drug Carr. Syst.* 33 (4), 363–400. doi:10.1615/critrevtherdrugcarriersyst.2016016272

Girhe, V., Auti, A. A., Girhe, P., and Wagre, R. (2021). Nuts and bolts of pmmc flap in oral cancer and its clinical outcome in 168 indian patients: A retrospective analysis. *J. Oral Biol. Craniofac Res.* 11 (2), 361–364. doi:10.1016/j.jobcr.2021.02.003

Huang, S. H., and O'Sullivan, B. (2013). Oral cancer: Current role of radiotherapy and chemotherapy. *Med. Oral Patol. Oral Cir. Bucal* 18 (2), e233–e240. doi:10.4317/medoral.18772

Jia, C., Zhang, F., Lin, J., Feng, L., Wang, T., Feng, Y., et al. (2022). Black phosphorus-Au-thiosugar nanosheets mediated photothermal induced anti-tumor effect enhancement by promoting infiltration of NK cells in hepatocellular carcinoma. *J. Nanobiotechnology* 20 (1), 90. doi:10.1186/s12951-022-01286-z

Kim, K. Y., Yang, E., Lee, M. Y., Chae, K. J., Kim, C. M., and Kim, I. S. (2014). Polydopamine coating effects on ultrafiltration membrane to enhance power density and mitigate biofouling of ultrafiltration microbial fuel cells (UF-MFCs). *Water Res.* 54, 62–68. doi:10.1016/j.watres.2014.01.045

Li, Q., Dong, H., Yang, G., Song, Y., Mou, Y., and Ni, Y. (2020). Mouse tumor-bearing models as preclinical study platforms for oral squamous cell carcinoma. *Front. Oncol.* 10, 212. doi:10.3389/fonc.2020.00212

Li, Z., Yang, Y., Wei, H., Shan, X., Wang, X., Ou, M., et al. (2021). Charge-reversal biodegradable MSNs for tumor synergetic chemo/photothermal and visualized therapy. *J. Control Release* 338, 719–730. doi:10.1016/j.jconrel.2021.09.005

Li, Z., Yu, Y., Zeng, W., Ding, F., Zhang, D., Cheng, W., et al. (2022). Mussel-inspired ligand clicking and ion coordination on 2D black phosphorus for cancer multimodal imaging and therapy. *Small* 18 (26), e2201803. doi:10.1002/smll.202201803

Liang, J., Wang, H., Ding, W., Huang, J., Zhou, X., Wang, H., et al. (2020). Nanoparticle-enhanced chemo-immunotherapy to trigger robust antitumor immunity. *Sci. Adv.* 6 (35), eabc3646. doi:10.1126/sciadv.abc3646

Linlin, Z., Yang, L., Gan, L., Duo, X., Sheng, L., Xinyuan, Z., et al. (2016). Prolonging the plasma circulation of proteins by nano-encapsulation with phosphorylcholine-based polymer. *Nano Res.* 9, 2424–2432. doi:10.1007/s12274-016-1128-4

Liu, G., Gao, N., Zhou, Y., Nie, J., Cheng, W., Luo, M., et al. (2019). Polydopamine-based "Four-in-One" versatile nanoplatforms for targeted dual chemo and photothermal synergistic cancer therapy. *Pharmaceutics* 11 (10), 507. doi:10.3390/pharmaceutics11100507

Liu, S., Pan, J., Liu, J., Ma, Y., Qiu, F., and Mei, L. (2018). Dynamically PEGylated and borate-coordination-polymer-coated polydopamine nanoparticles for synergetic tumor-targeted, chemo-photothermal combination therapy. *Small* 14 (13), e1703968. doi:10.1002/smll.201703968

Luk, B. T., and Zhang, L. (2014). Current advances in polymer-based nanotheranostics for cancer treatment and diagnosis. *ACS Appl. Mater Interfaces* 6 (24), 21859–21873. doi:10.1021/am5036225

Marcazzan, S., Varoni, E. M., Blanco, E., Lodi, G., and Ferrari, M. (2018). Nanomedicine, an emerging therapeutic strategy for oral cancer therapy. *Oral Oncol.* 76, 1–7. doi:10.1016/j.oraloncology.2017.11.014

Minhas, S., Kashif, M., Altaf, W., Afzal, N., and Nagi, A. H. (2017). Concomitant-chemoradiotherapy-associated oral lesions in patients with oral squamous-cell carcinoma. *Cancer Biol. Med.* 14 (02), 176–182. doi:10.20892/j.issn.2095-3941.2016.0096

Mo, J., Chen, X., Li, M., Liu, W., Zhao, W., Lim, L. Y., et al. (2022). Upconversion nanoparticle-based cell membrane-coated cRGD peptide bioorthogonally labeled nanoplatform for glioblastoma treatment. *ACS Appl. Mater Interfaces*. doi:10.1021/acsami.2c11284

Mosaddad, S. A., Beigi, K., Doroodizadeh, T., Haghnegahdar, M., Golfeshan, F., Ranjbar, R., et al. (2021). Therapeutic applications of herbal/synthetic/bio-drug in oral cancer: An update. *Eur. J. Pharmacol.* 890, 173657. doi:10.1016/j.ejphar.2020.173657

Nandini, D. B., Rao, R., Hosmani, J., Khan, S., Patil, S., and Awan, K. H. (2020). Novel therapies in the management of oral cancer: An update. *Dis. Mon.* 66 (12), 101036. doi:10.1016/j.disamonth.2020.101036

Park, J., Brust, T. F., Lee, H. J., Lee, S. C., Watts, V. J., and Yeo, Y. (2014). Polydopamine-based simple and versatile surface modification of polymeric nano drug carriers. *ACS Nano* 8 (4), 3347–3356. doi:10.1021/nn405809c

Peng, Y., Nie, J., Cheng, W., Liu, G., Zhu, D., Zhang, L., et al. (2018). A multifunctional nanoplatform for cancer chemo-photothermal synergistic therapy and overcoming multidrug resistance. *Biomater. Sci.* 6 (5), 1084–1098. doi:10.1039/c7bm01206c

Poonia, M., Ramalingam, K., Goyal, S., and Sidhu, S. K. (2017). Nanotechnology in oral cancer: A comprehensive review. *J. Oral Maxillofac. Pathol.* 21 (3), 407–414. doi:10.4103/jomfp.JOMFP_29_17

Scully, C., and Bagan, J. (2009). Oral squamous cell carcinoma overview. *Oral Oncol.* 45 (4-5), 301–308. doi:10.1016/j.oraloncology.2009.01.004

Shi, J., Kantoff, P. W., Wooster, R., and Farokhzad, O. C. (2017). Cancer nanomedicine: Progress, challenges and opportunities. *Nat. Rev. Cancer* 17 (1), 20–37. doi:10.1038/nrc.2016.108

Sun, L., Xu, Y., Zhang, X., Gao, Y., Chen, J., Zhou, A., et al. (2020). Mesenchymal stem cells functionalized sonodynamic treatment for improving therapeutic efficacy and compliance of orthotopic oral cancer. *Adv. Mater* 32 (48), e2005295. doi:10.1002/adma.202005295

Sykes, E. A., Chen, J., Zheng, G., and Chan, W. C. (2014). Investigating the impact of nanoparticle size on active and passive tumor targeting efficiency. *ACS Nano* 8 (6), 5696–5706. doi:10.1021/nn500299p

Tao, W., Ji, X., Zhu, X., Li, L., Wang, J., Zhang, Y., et al. (2018). Two-dimensional antimonene-based photonic nanomedicine for cancer theranostics. *Adv. Mater* 30 (38), e1802061. doi:10.1002/adma.201802061

Tao, W., Zeng, X., Wu, J., Zhu, X., Yu, X., Zhang, X., et al. (2016). Polydopamine-based surface modification of novel nanoparticle-aptamer bioconjugates for *in vivo* breast cancer targeting and enhanced therapeutic effects. *Theranostics* 6 (4), 470–484. doi:10.7150/thno.14184

Wei, X., Luo, Q., Sun, L., Li, X., Zhu, H., Guan, P., et al. (2016). Enzyme- and pH-sensitive branched polymer-doxorubicin conjugate-based nanoscale drug delivery system for cancer therapy. *ACS Appl. Mater Interfaces* 8 (18), 11765–11778. doi:10.1021/acsami.6b02006

Yang, B., Liu, W., Li, M., and Mo, J. (2022). GSK-J1-loaded, hyaluronic acid-decorated metal-organic frameworks for the treatment of ovarian cancer. *Front. Pharmacol.* 13, 1023719. doi:10.3389/fphar.2022.1023719

Yu, B., Liu, J., Liu, S., and Zhou, F. (2010). Pdop layer exhibiting zwitterionicity: A simple electrochemical interface for governing ion permeability. *Chem. Commun. (Camb)* 46 (32), 5900–5902. doi:10.1039/c0cc00596g

Zeng, D., Wang, L., Tian, L., Zhao, S., Zhang, X., and Li, H. (2019). Synergistic photothermal/photodynamic suppression of prostatic carcinoma by targeted biodegradable MnO(2) nanosheets. *Drug Deliv.* 26 (1), 661–672. doi:10.1080/10717544.2019.1631409

Zeng, W. F., Li, Z., Chen, H., Zeng, X., and Mei, L. (2022). An optimal portfolio of photothermal combined immunotherapy. *Cell Rep. Phys. Sci.* 3 (6), 100898. doi:10.1016/j.xcrp.2022.100898

Zeng, X., Luo, M., Liu, G., Wang, X., Tao, W., Lin, Y., et al. (2018). Polydopamine-modified black phosphorous nanocapsule with enhanced stability and photothermal performance for tumor multimodal treatments. *Adv. Sci. (Weinh)* 5 (10), 1800510. doi:10.1002/advs.201800510

Zhang, H. J., Zeng, W., Pan, C., Feng, L., Ou, M., Zeng, X., et al. (2019). SnTe@MnO2-SP nanosheet-based intelligent nanoplatform for second near-infrared light-mediated cancer theranostics. *Adv. Funct. Mater.* 29 (37), 1903791. doi:10.1002/adfm.201903791

Zhang, M., Liang, J., Yang, Y., Liang, H., and Jia, H. (2020). Current trends of targeted drug delivery for oral cancer therapy. *Front. Bioeng. Biotechnol.* 8, 618931. doi:10.3389/fbioe.2020.618931

Zhou, C., Abbas, M., Zhang, M., Zou, Q., Shen, G., Chen, C., et al. (2015). One-step nanoengineering of hydrophobic photosensitive drugs for the photodynamic therapy. *J. Nanosci. Nanotechnol.* 15 (12), 10141–10148. doi:10.1166/jnn.2015.11695

Zhu, D., Tao, W., Zhang, H., Liu, G., Wang, T., Zhang, L., et al. (2016). Docetaxel (DTX)-loaded polydopamine-modified TPGS-PLA nanoparticles as a targeted drug delivery system for the treatment of liver cancer. *Acta Biomater.* 30, 144–154. doi:10.1016/j.actbio.2015.11.031

Zhu, X., Xu, Y., Solis, L. M., Tao, W., Wang, L., Behrens, C., et al. (2015). Long-circulating siRNA nanoparticles for validating Prohibitin1-targeted non-small cell lung cancer treatment. *Proc. Natl. Acad. Sci. U. S. A.* 112 (25), 7779–7784. doi:10.1073/pnas.1505629112

frontiers | Frontiers in Bioengineering and Biotechnology

TYPE Original Research
PUBLISHED 09 June 2023
DOI 10.3389/fbioe.2023.1197404

OPEN ACCESS

EDITED BY
Hongzhong Chen,
Sun Yat-sen University, China

REVIEWED BY
Lisi Xie,
Sun Yat-sen Memorial Hospital, China
Keni Yang,
Suzhou Institute of Nano-tech and Nano-bionics (CAS), China

*CORRESPONDENCE
An Gao,
tmu_gaoan@163.com
Chunyang Sun,
chysun412@163.com

RECEIVED 31 March 2023
ACCEPTED 22 May 2023
PUBLISHED 09 June 2023

CITATION
Zhang Z, Feng J, Zhang T, Gao A and Sun C (2023), Application of tumor pH/hypoxia-responsive nanoparticles for combined photodynamic therapy and hypoxia-activated chemotherapy. *Front. Bioeng. Biotechnol.* 11:1197404. doi: 10.3389/fbioe.2023.1197404

Application of tumor pH/hypoxia-responsive nanoparticles for combined photodynamic therapy and hypoxia-activated chemotherapy

Zhang Zhang[1], Jintang Feng[1], Tianzhu Zhang[1], An Gao[2]* and Chunyang Sun[1,3]*

[1]Department of Radiology and Tianjin Key Laboratory of Functional Imaging, Tianjin Medical University General Hospital, Tianjin, China, [2]Department of Radiology, Tianjin Medical University Cancer Institute and Hospital, Tianjin, China, [3]Multimodality Preclinical Molecular Imaging Center, Tianjin Medical University General Hospital, Tianjin, China

Introduction: Cancer selectivity, including targeted internalization and accelerated drug release in tumor cells, remains a major challenge for designing novel stimuli-responsive nanocarriers to promote therapeutic efficacy. The hypoxic microenvironment created by photodynamic therapy (PDT) is believed to play a critical role in chemoresistance.

Methods: We construct dual-responsive carriers ($^{DA}NP_{CT}$) that encapsulate the photosensitizer chlorin e6 (Ce6) and hypoxia-activated prodrug tirapazamine (TPZ) to enable efficient PDT and PDT-boosted hypoxia-activated chemotherapy.

Results and discussion: Due to TAT masking, $^{DA}NP_{CT}$ prolonged payload circulation in the bloodstream, and selective tumor cell uptake occurred via acidity-triggered TAT presentation. PDT was performed with a spatially controlled 660-nm laser to enable precise cell killing and exacerbate hypoxia. Hypoxia-responsive conversion of the hydrophobic NI moiety led to the disassembly of $^{DA}NP_{CT}$, facilitating TPZ release. TPZ was reduced to cytotoxic radicals under hypoxic conditions, contributing to the chemotherapeutic cascade. This work offers a sophisticated strategy for programmed chemo-PDT.

KEYWORDS

tumor pH, responsive nanocarriers, hypoxia-activated prodrug, TAT reactivation, combined therapy

Introduction

In recent years, a variety of nanocarriers has been designed to deliver therapeutic agents for combined chemo-photodynamic therapy (chemo-PDT) (Kim et al., 2017; Pei et al., 2019; Yu et al., 2023). The complementary cell-killing mechanisms of combined chemo-PDT eliminate the limitations of monotherapy and improve anticancer therapeutic efficacy (Conte et al., 2016; Cheng et al., 2020; Majerník et al., 2022). Despite the theoretical promise of chemo-PDT, outcomes are significantly limited by a lack of precise tumor targeting. Rather than relying on passive enrichment in tumors via enhanced permeability and retention (EPR), tethering cell-penetrating peptides (CPPs) to the nanocarriers promotes payload delivery to tumor cells (Guidotti et al., 2017; Zorko et al., 2022). However, the clearance by macrophages and non-specific distribution in healthy

tissue are major obstacles that limit the efficacy of CPPs (Deshpande et al., 2013; Futaki and Nakase, 2017). To overcome these limitations, CPP function must be precisely masked in the bloodstream and activated only within the targeted solid tumors (Dohmen and Wagner., 2011; Zhu et al., 2013). Many studies have focused on developing strategies for spatially controlled, tumor-specific CPP presentation (Huang et al., 2013; Li et al., 2014; Ruoslahti, 2017; Jing et al., 2018; Mohammed et al., 2019). Due to its homogeneity and stability, extracellular acidity (pH_e ~6.5–6.8) is a promising stimulus, and growing evidence has suggested the outstanding sensitivity of the dimethyl maleate (DA) moiety to pH_e (Du et al., 2011; Gao et al., 2017; Ma and Sun, 2020).

The photosensitization reaction generally produces many toxic reactive oxygen species (ROS) by consuming surrounding oxygen (Abrahamse and Hamblin, 2016; Han et al., 2022; Tang et al., 2022). As a result, cells that survive PDT exist in a hypoxic microenvironment, and hypoxia-induced chemoresistance has become a critical issue in these residual cells (Wang et al., 2017; Yang et al., 2021). Hypoxia-inducible factor-1α activity is upregulated, altering metabolism and drug efflux in hypoxic tumor cells (Majmundar et al., 2010; Cairns et al., 2011; Ma et al., 2022). Hypoxia also alters DNA methylation and autophagy, which are related to chemotherapy resistance (Jing et al., 2019; Kopecka et al., 2021). Pioneering studies have demonstrated that hypoxia-activated prodrugs (HAPs), which can be converted from non-toxic to toxic molecules under hypoxic conditions, offer a powerful strategy that can be combined with PDT for the selective killing of hypoxic cells after PDT (Feng et al., 2017; Sun et al., 2019; Zhu et al., 2019; Jiang et al., 2022). HAPs typically interact with nuclear DNA, so boosted intracellular drug release is also a highly desirable feature of nanocarriers (Li et al., 2021; Yang et al., 2022). Specific and effective cancer therapy requires the design of nanosystems with pH_e-sensitive TAT presentation and hypoxia-boosted cargo release to simultaneously achieve tumor homing and HAP liberation and activation inside the targeted tumor.

We developed a mixed polymeric micelle ($^{DA}NP_{CT}$) capable of TAT presentation at pH_e and hypoxia-responsive dissociation for controlled PDT and hypoxia-activated chemotherapy. TAT-modified poly (ethylene glycol)-polyphosphoesters (TAT-PEG-PHEP) and 2-nitroimidazole-grafted PEGylated polyphosphoesters PEG-*b*-P (AEP-*g*-NI) were self-assembled to encapsulate chlorin e6 (Ce6; photosensitizer) and tirapazamine (TPZ; HAPs). We hypothesized that $^{DA}NP_{CT}$ could achieve prolonged blood circulation due to temporary shielding of the TAT ligands via the DA moiety (Figure 1). After entering the tumor matrix, pH_e-induced DA deshielding activated the TAT to promote cellular penetration. PDT with a 660-nm laser triggered the production of cytotoxic ROS, thus leading to cell killing and O_2 consumption. Local hypoxia converted hydrophobic NI to hydrophilic 2-aminoimidazole to facilitate $^{DA}NP_{CT}$ dissociation and TPZ release and activation to produce toxic radical species for the selective killing of hypoxic cells that remain after PDT. Cascade-amplified therapeutic outcomes were studied *in vitro* and *in vivo*.

Materials and methods

Materials

Ce6, 2,2-dimethoxy-2-phenyl acetophenone (DMPA), and TPZ were obtained from Macklin. We synthesized (2-nitro-1H-imidazol-

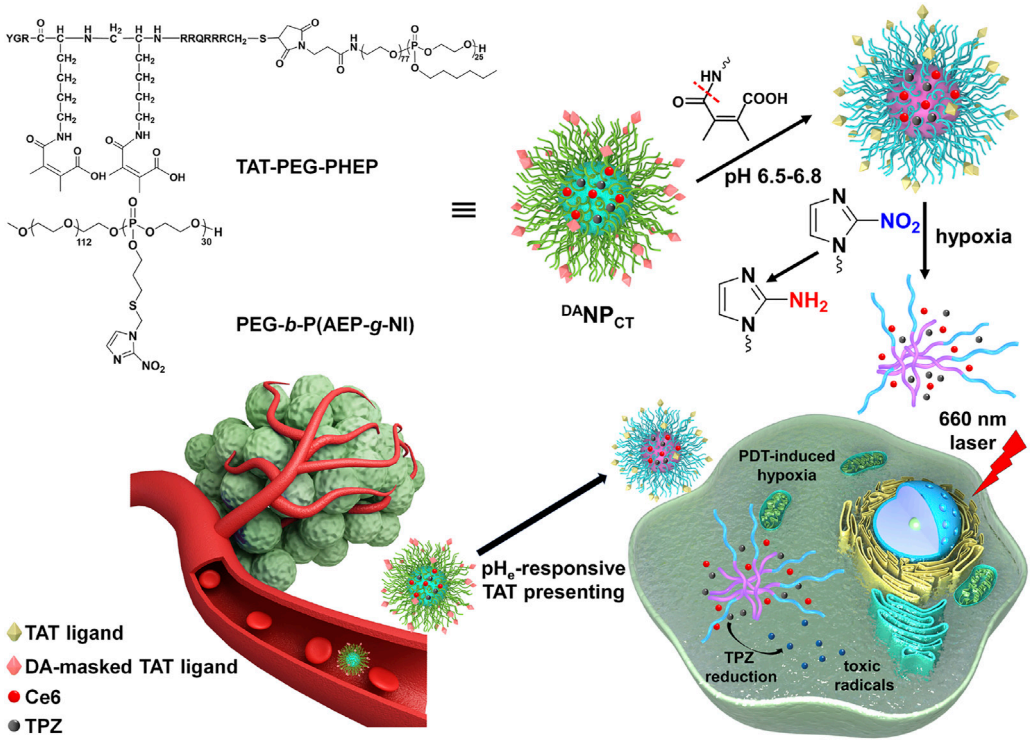

FIGURE 1
Scheme of $^{DA}NP_{CT}$ design and pH_e-sensitive TAT presenting and PDT-induced hypoxia-activated chemotherapy.

1-yl) methanethiol (NI-SH), the diblock copolymer of PEG-*b*-PAEP, and TAT-PEG-PHEP as described previously (Li et al., 2017; Ma and Sun, 2020). The cell counting kit-8 (CCK-8) was obtained from Shanghai Saint-Bio. Dulbecco's modified Eagle's medium (DMEM) and fetal bovine serum (FBS) were purchased from Gibco (Gibco, United States). Phalloidin-Alexa Fluor 488 and DAPI were obtained from Beyotime Biotechnology. All other reagents were of analytical grade and used as received.

Synthesis of diblock PEG-*b*-P (AEP-*g*-NI)

NI-SH (292.8 mg; 1.84 mmol) and DMPA (14.1 mg) were mixed in THF (16 mL) containing 287.2 mg PEG-*b*-PAEP and purged with Ar_2 for 25 min. The reaction was incubated for 60 min at room temperature under a 365-nm UV light, then transferred to a dialysis tube (MWCO 3500 Da), and dialyzed against ddH_2O at 4°C. The solution was lyophilized to obtain PEG-*b*-P (AEP-*g*-NI).

Preparation of Ce6 and TPZ-loaded nanocarriers

TAT-PEG-PHEP, PEG-*b*-P (AEP-*g*-NI), Ce6, and TPZ were mixed at a weight ratio of 3:7:1:1 in DMF. The organic solution was then added slowly to ddH_2O under gentle stirring. After stirring overnight, DMF and unencapsulated Ce6 and TPZ were removed by dialysis against ddH_2O. After centrifugation at 800 *g* for 15 min, the nanoparticles (NP_{CT}) were collected. To fabricate pH_e-sensitive $^{DA}NP_{CT}$, NP_{CT} was reacted with excess 2,3-dimethylmaleic anhydride in ddH_2O at pH 8–9 and 4°C for 6 h and then purified by ultrafiltration. A similar method was used to prepare pH_e-insensitive $^{SA}NP_{CT}$ with succinic anhydride instead of 2,3-dimethylmaleic anhydride.

Cellular uptake of nanocarriers at different pH conditions

MCF-7 cells were seeded in 24-well plates and incubated with fresh DMEM containing NP_{CT}, $^{SA}NP_{CT}$, or $^{DA}NP_{CT}$ (pretreated at pH 7.4 or 6.5) at 37°C for 6 h. The cells were washed with cold PBS, fixed with paraformaldehyde, and analyzed by FACS. Total protein and Ce6 concentrations in the cell lysate were analyzed using a bicinchoninic acid kit and spectrofluorimetry, respectively.

MCF-7 cells were seeded on coverslips in 12-well plates and incubated with NP_{CT}, $^{SA}NP_{CT}$, or $^{DA}NP_{CT}$ (pretreated at pH 7.4 or 6.5) at 37°C for 6 h. The cells were washed with PBS, fixed with 4% paraformaldehyde, and then stained with phalloidin-Alexa Fluor 488 and DAPI, according to standard protocols. The cells were then visualized on a Zeiss LSM 810 confocal laser scanning microscope.

Cell killing by ^{DA}TAT-NP_{Ce6} *in vitro*

To study the biocompatibility of nanoparticles that have not been loaded with Ce6 or TPZ, MCF-7 cells were seeded in 96-well plates (10,000 cells per well) and incubated with NP, ^{SA}NP, or ^{DA}NP for 72 h. To study the therapeutic efficacy of PDT and hypoxia-activated chemotherapy, MCF-7 cells were seeded in 96-well plates (10,000 cells per well). The normoxic (21% O_2 pressure) or hypoxic condition (2% O_2 pressure) was generated in a three-gas incubator, while the partial pressure of CO_2 was maintained at 5%. NP_{CT}, $^{SA}NP_{CT}$, or $^{DA}NP_{CT}$ was added at pH 7.4 or 6.5, incubated for 4 h, and then incubated with MCF-7 cells under normoxic conditions at different Ce6 concentrations for 24 h. The medium was replaced with DMEM (10% FBS) without nanoparticles, and then, the cells were exposed to a 660-nm laser (100 mW/cm^2; 15 min). After incubation for another 48 h under normoxic or hypoxic conditions, viability was measured using a standard CCK-8 assay.

Pharmacokinetics and biodistribution of $^{DA}NP_{CT}$ *in vivo*

Female BALB/c mice were randomly divided into four groups and treated with free Ce6, NP_{CT}, $^{SA}NP_{CT}$, or $^{DA}NP_{CT}$ via tail vein injection (Ce6 10 mg/kg). At 10 min, 30 min, 1 h, 2 h, 4 h, 8 h, 12 h, 24 h, and 48 h post-injection, blood samples were collected from the retro-orbital plexus. The plasma was obtained by centrifugation, and Ce6 content was quantified by high-performance liquid chromatography (HPLC).

To study the accumulation of $^{DA}NP_{CT}$ in the major organs and tumor tissues, 1×10^7 MCF-7 cell suspension (200 μL) was injected into the mammary fat pad of female BALB/c nude mice to develop a tumor model. Mice bearing MCF-7 xenografts were treated with an intravenous (i.v.) injection of free Ce6, NP_{CT}, $^{SA}NP_{CT}$, or $^{DA}NP_{CT}$ (Ce6 10 mg/kg). At 6 h, 12 h, and 24 h, tumor tissues and other organs were excised and homogenized, and Ce6 content was quantified by HPLC.

Antitumor efficacy *in vivo*

Female MCF-7 tumor-bearing BALB/c nude mice were randomly divided into five groups (n = 6), and, once the tumor volume reached ~100 mm^3, the mice were treated with 0.9% NaCl, free Ce6 + TPZ, NP_{CT}, $^{SA}NP_{CT}$, or $^{DA}NP_{CT}$ (TPZ 5 mg/kg) every week. At 12 h post-injection, the tumor sites were exposed to 660-nm light for 15 min at a power density of 200 mW/cm^2. Tumor volume (0.5 × length × width^2) and body weight were monitored every 3 days. On day 24, blood samples and the major organs were collected for ELISA analysis and hematoxylin and eosin (H&E) staining, respectively.

Results and discussion

Preparation of pH_e- and hypoxia-responsive $^{DA}NP_{CT}$

To prepare hierarchically responsive nanocarriers, TAT-PEG-PHEP and hypoxia-sensitive PEG-PAEP-NI were synthesized as described previously. The efficiency of NI modification was approximately 100% after thiol–ene "click" chemistry, as

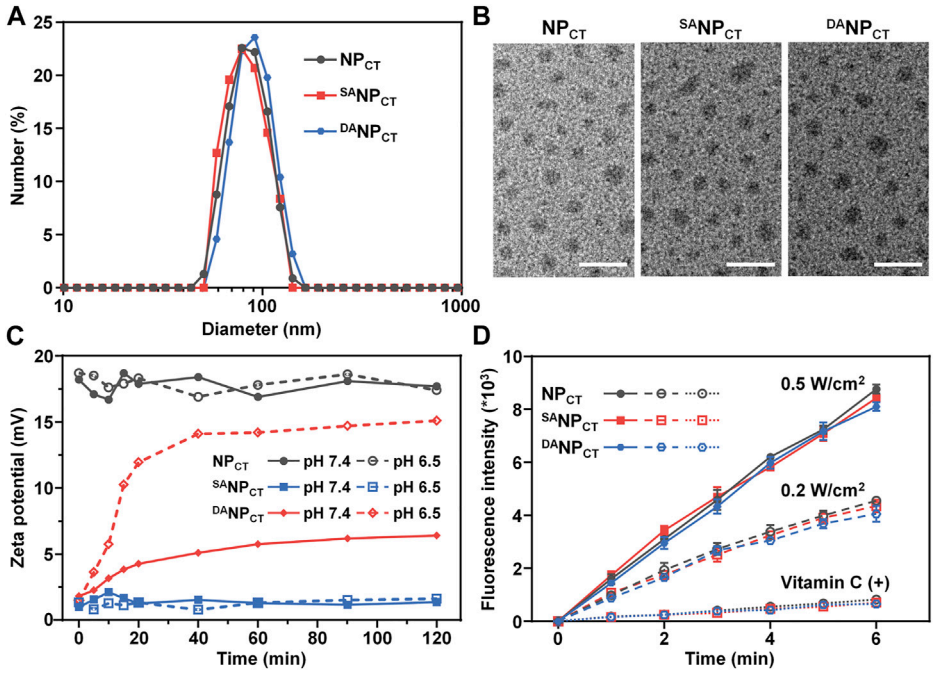

FIGURE 2
(A) Size distribution of NP_{CT}, $^{SA}NP_{CT}$, and $^{DA}NP_{CT}$ measured by DLS. **(B)** TEM observation of NP_{CT}, $^{SA}NP_{CT}$, and $^{DA}NP_{CT}$. The scale bar is 200 nm. **(C)** Zeta potential change of NP_{CT}, $^{SA}NP_{CT}$, and $^{DA}NP_{CT}$ at pH 7.4 or 6.5. **(D)** ROS production indicated by DCFH (E_m = 525 nm) of Ce6-loaded nanoparticles. Vitamin C acts as an ROS scavenger.

indicated by ^{1}H NMR spectroscopy (Supplementary Figure S1). Hydrophobic Ce6 and TPZ were encapsulated with TAT-PEG-PHEP and PEG-*b*-P (AEP-*g*-NI) at a 3:7 weight ratio to form the mixed micelle (NP_{CT}). Finally, 2,3-dimethylmaleic anhydride was introduced to react with the lysine amines of NP_{CT} to yield nanoparticles with pH_e-responsive TAT reactivation properties ($^{DA}NP_{CT}$). For comparison, pH_e-insensitive $^{SA}NP_{CT}$ was prepared by decoration with succinic anhydride. The hydrodynamic diameter of NP_{CT}, $^{SA}NP_{CT}$, and $^{DA}NP_{CT}$ was measured by dynamic light scattering and transmission electron microscopy. The various nanoparticles had a diameter of ~80 nm and a uniform, spherical morphology (Figures 2A,B). According to the UV-vis absorbance at 642 and 698 nm, the encapsulation efficacies of the mixed micelles were 2.31% (Ce6) and 2.69% (TPZ), respectively. The average size of the nanoparticles, regardless of TAT modification, remained unchanged in PBS over 168 h (Supplementary Figure S2), verifying the outstanding colloidal stability provided by the outer PEG layer.

As expected, the TAT amine groups are exposed to enable cell penetration following degradation at an acidic tumor pH. We monitored the zeta potential at pH 6.5 or 7.4 and found that NP_{CT} maintained its original zeta potential at both pH values, comparable to that of TAT-decorated nanocarriers reported elsewhere (Figure 2C) (Li et al., 2017; Zhang et al., 2020). However, the zeta potential of $^{DA}NP_{CT}$ increased dramatically from +1.4 mV to +15.1 mV at pH 6.5. Meanwhile, the slight zeta potential elevation of $^{DA}NP_{CT}$ at pH 7.4 could be explained as the partial breakage of unstable amide bonds within the DA moieties. With SA modification, $^{SA}NP_{CT}$ masked the TAT ligand, and a minimal zeta potential change was observed at both pH levels. The fluorescamine method was used to quantify the exposed amine groups. Compared to the control groups, the DA degradation efficiency of $^{DA}NP_{CT}$ reached 85.78% ± 4.65% at pH 6.5 (Supplementary Figure S3), and only 22.36% ± 2.58% of DA moieties broke at neutral pH.

The PDT effect at 660 nm was measured using a 2′,7′-dichlorodihydrofluorescein diacetate probe because it was oxidized by ROS to obtain fluorescent DCFH (Eruslanov and Kusmartsev, 2010; Kim and Xue, 2020). Emission fluorescence measurements of NP_{CT}, $^{SA}NP_{CT}$, and $^{DA}NP_{CT}$ at 525 nm (excitation = 488 nm) revealed comparable laser power-dependent ROS production rates (Figure 2D). The fluorescence intensity of DCFH induced by NP_{CT}, $^{SA}NP_{CT}$, and $^{DA}NP_{CT}$ was reduced by nearly ~11.6-fold after adding an ROS scavenger (vitamin C). ROS generated by Ce6 was mainly derived from singlet oxygen via the Type 1 mechanism. The abundant ROS generation confirmed that Ce6-encapsulated nanoparticles are efficient for PDT application and accelerated hypoxia-boosted TPZ release.

According to our design, the hypoxic conditions created by PDT facilitate hydrophobic NI conversion to hydrophilic AI and boost micelle disassembly and cargo release. Therefore, we measured the variability in the diameter of NI-containing nanoparticles after 660-nm laser exposure. The diameters of NP_{CT}, $^{SA}NP_{CT}$, and $^{DA}NP_{CT}$ significantly decreased to ~45 nm following photosensitization (Figure 3A), and negligible changes were observed in the dark.

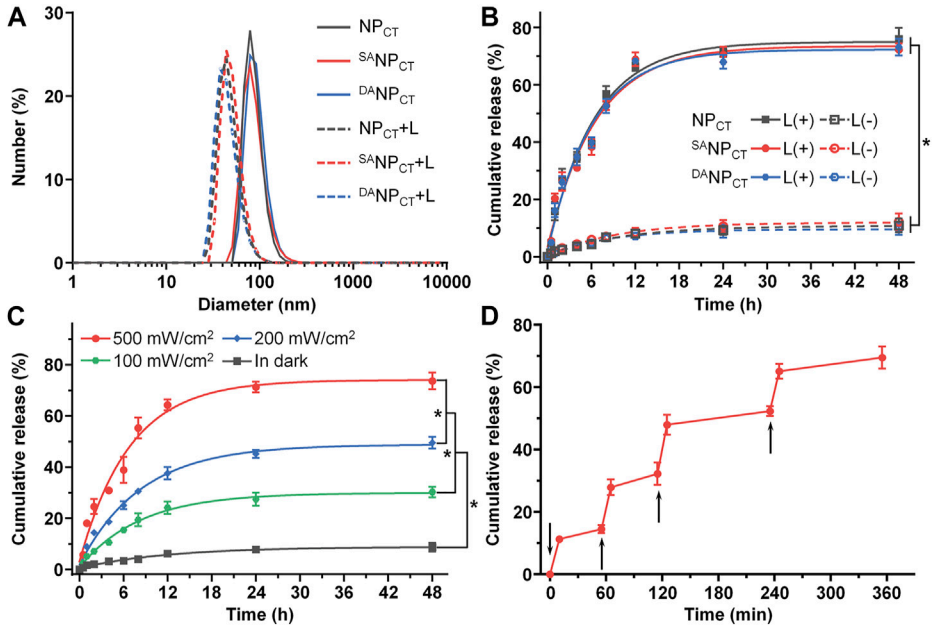

FIGURE 3
(A) Diameter change in NP_{CT}, $^{SA}NP_{CT}$, and $^{DA}NP_{CT}$ after exposure to 660-nm near infrared light. **(B)** Cumulative TPZ release profile of NP_{CT}, $^{SA}NP_{CT}$, and $^{DA}NP_{CT}$. The power density of 660-nm laser was 500 mW/cm^2. *$p < 0.05$. **(C)** Cumulative TPZ release profile of $^{DA}NP_{CT}$ at 500 mW/cm^2, 200 mW/cm^2, and 100 mW/cm^2 or in the dark. *$p < 0.05$. **(D)** Pulsed 660-nm laser-triggered TPZ release from $^{DA}NP_{CT}$. The samples were exposed to laser at the predetermined time intervals indicated by the black arrows.

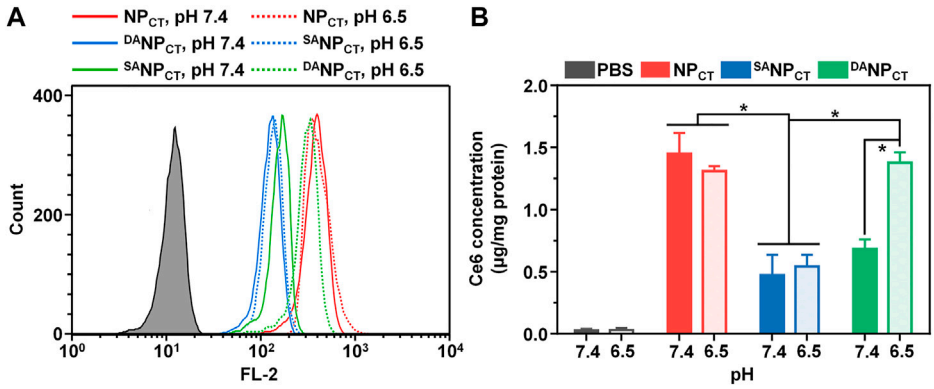

FIGURE 4
(A) Intracellular fluorescence of NP_{CT}, $^{SA}NP_{CT}$, and $^{DA}NP_{CT}$ in MCF-7 cells at pH 7.4 or 6.5. **(B)** Intracellular Ce6 concentration in MCF-7 cells at different pH conditions. *$p < 0.05$.

We quantified the TPZ release profiles with or without PDT via fluorescence spectrometry. At 48 h, there were 75.96% ± 3.94%, 72.31% ± 2.14%, and 73.14% ± 2.96% TPZ leakages from NP_{CT}, $^{SA}NP_{CT}$, and $^{DA}NP_{CT}$ after laser treatment, respectively (Figure 3B). In contrast, less than 12.50% of the total TPZ was detected without laser irradiation, and there was no significant difference in TPZ release rates. TPZ release from $^{DA}NP_{CT}$ exhibited a power density-dependent pattern, and PDT resulted in 73.66% ± 3.34%, 49.53% ± 2.34%, and 30.21% ± 2.09% of TPZ liberation at different power densities (Figure 3C). The 660-nm laser on/off cycle induced controlled pulses of TPZ release from $^{DA}NP_{CT}$ (Figure 3D). The hierarchy of pH_e and hypoxic conditions enabled TAT ligand presentation and cargo release, promoting the accumulation of active drug content at the target site.

Cellular uptake of $^{DA}NP_{CT}$ at pH 6.5

To track the TAT presentation of $^{DA}NP_{CT}$ under acidic conditions to facilitate cellular internalization, MCF-7 cells were

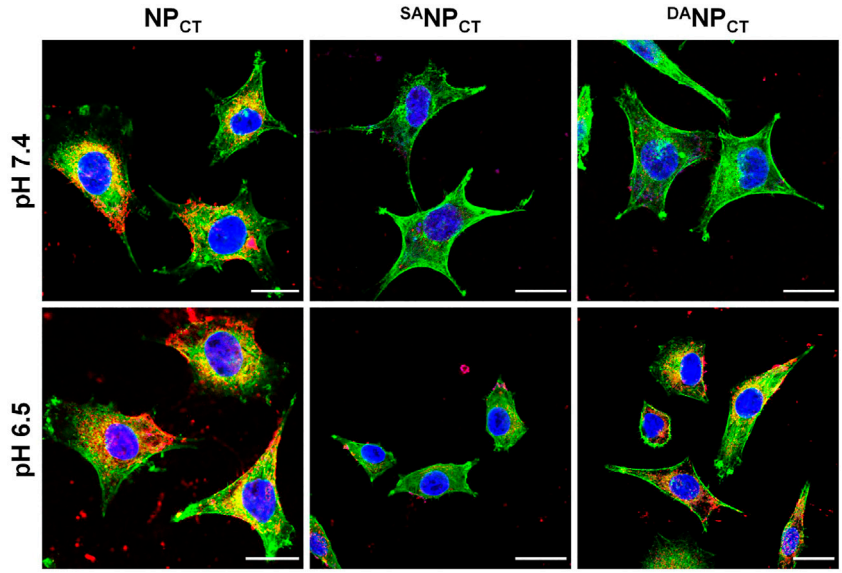

FIGURE 5
CLSM observation of NP_{CT}, $^{SA}NP_{CT}$, and $^{DA}NP_{CT}$ on MCF-7 cells at either pH 7.4 or 6.5. Cell nuclei and F-actin were stained by DAPI (blue) and phalloidin-Alexa Fluor 488 (green), respectively. The scale bar is 20 μm.

cultured and treated with NP_{CT}, $^{SA}NP_{CT}$, and $^{DA}NP_{CT}$ for 4 h. The internalized NP content was analyzed by FACS, which revealed limited cellular uptake with $^{SA}NP_{CT}$ pretreatment at pH 7.4 and 6.5, suggesting reduced interaction between masked TAT-induced and targeted cells (Figure 4A). Due to the pH_e-sensitive TAT, the intracellular $^{DA}NP_{CT}$ content was significantly higher at pH 6.5 than at pH 7.4, comparable to that of NP_{CT}. Following cell lysis, we used HPLC to detect intracellular TPZ concentration and found that the internalized TPZ of $^{DA}NP_{CT}$ increased from 0.69 ± 0.07 μg/mg protein (pH 7.4) to 1.39 ± 0.09 μg/mg protein (pH 6.5) (Figure 4B). However, there was no noticeable change in the NP_{CT} and $^{SA}NP_{CT}$ groups at neutral or acidic pH. The pH-induced $^{DA}NP_{CT}$ pattern was confirmed by confocal imaging. Compared to the weakened signals in the $^{SA}NP_{CT}$ groups, significantly stronger fluorescence was observed when cells were incubated with $^{DA}NP_{CT}$ pretreated at pH 6.5 (Figure 5). These results verified that the penetration capacity of masked TAT was specifically activated by the extracellular pH microenvironment.

Cell killing *in vitro*

The biocompatibility of non-loaded NP, ^{SA}NP, and ^{DA}NP was evaluated by CCK-8 assay, which showed no notable cytotoxicity in MCF-7 cells at the highest concentration of 500 μg/mL (Supplementary Figure S4). For chemo-PDT effectiveness, cells were incubated with NP_{CT}, $^{SA}NP_{CT}$, or $^{DA}NP_{CT}$, exposed to 660-nm light for 20 min, and then cultured at different O_2 concentrations. Without laser exposure, NP_{CT}, $^{SA}NP_{CT}$, and $^{DA}NP_{CT}$ induced low toxicity even under hypoxic conditions because of the absence of the PDT effect and TPZ (HAP) release (Figures 6A,B). However, laser irradiation-triggered cell killing occurred in all groups at comparable levels regardless of pH or O_2 conditions. Hypoxic culture reduced cell viability, indicating that TPZ was reduced to cytotoxic radicals that interacted with the nuclear DNA. Compared to the viability of MCF-7 cells treated with $^{DA}NP_{CT}$ at pH 7.4, acidic treatment promoted cell killing with 51.07% ± 6.98% cell viability (Ce6 4.0 μg/mL) under normoxic conditions. This difference is attributable to the reactivable TAT ligands and improved Ce6 and TPZ internalization. Under hypoxic conditions, the viabilities of NP_{CT} + L and $^{DA}NP_{CT}$ + L groups at acidic pH were 21.90% ± 2.30% and 26.67% ± 4.29%, respectively, 0.50- and 0.61-fold lower than those of $^{SA}NP_{CT}$ + L. Accordingly, the interactions between PDT and hypoxia-activated chemotherapy indicate that $^{DA}NP_{CT}$ could serve as a robust delivery platform for precise cancer therapy.

Pharmacokinetic and biodistribution of $^{DA}TAT\text{-}NP_{Ce6}$ *in vivo*

With pH_e-sensitive DA masking, the penetrating ability of the TAT ligand in $^{DA}NP_{CT}$ was temporally blocked in the bloodstream, limiting phagocytosis. We measured the plasma concentrations of Ce6 following the intravenous injection of different formulations (Figure 7A). NP_{CT} with bare TAT ligands was rapidly cleared from the circulation, yielding a Ce6 concentration of 0.63 ± 0.45 μg/mL at 72 h post-injection. In contrast, both $^{SA}NP_{CT}$ and $^{DA}NP_{CT}$ substantially prolonged the Ce6 circulation, consistent with prior reports (Gao et al., 2017; Zhang et al., 2022). Compared to $^{SA}NP_{CT}$ administration, the Ce6 plasma concentration in the $^{DA}NP_{CT}$ group at 72 h post-injection was reduced from 2.71 ± 1.06 to 1.81 ± 0.54 μg/mL. The pharmacokinetic difference between $^{SA}NP_{CT}$ and

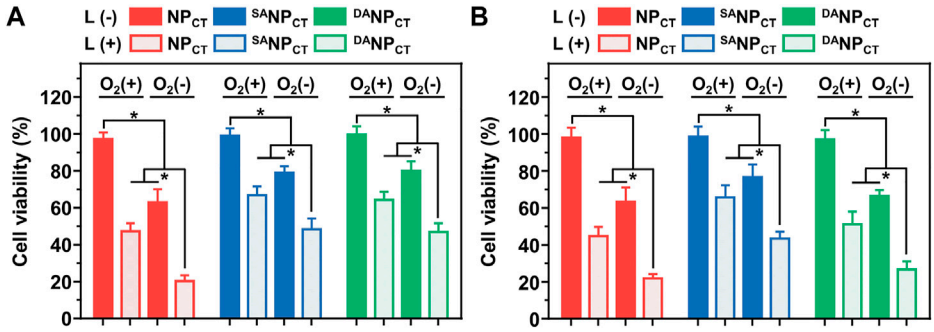

FIGURE 6
Relative MCF-7 cell viabilities after incubation with NP_{CT}, $^{SA}NP_{CT}$, or $^{DA}NP_{CT}$ at pH 7.4 **(A)** or 6.5 **(B)**. *$p < 0.05$.

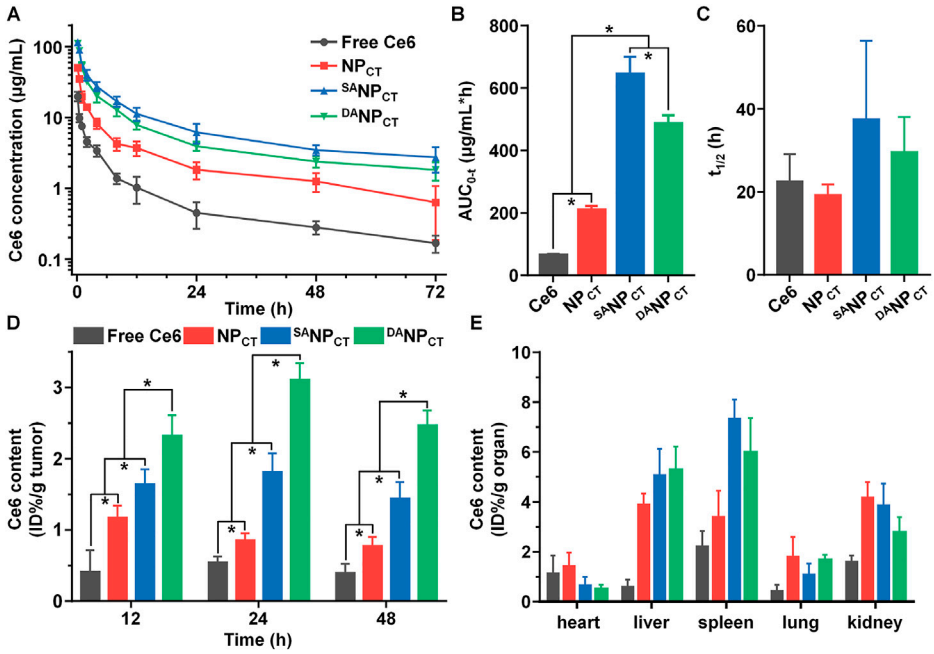

FIGURE 7
(A) Ce6 content in plasma vs. time, following *i.v.* injection of free Ce6, NP_{CT}, $^{SA}NP_{CT}$, or $^{DA}NP_{CT}$ (n = 4). The area under the curve **(B)** and half-life **(C)** of free Ce6, NP_{CT}, $^{SA}NP_{CT}$, or $^{DA}NP_{CT}$ calculated using a non-compartmental model. *$p < 0.05$. **(D)** Ce6 accumulation in MCF-7 tumor at 12, 24, and 48 h post-injection. *$p < 0.05$. **(E)** Ce6 distribution in major organs of MCF-7 tumor-bearing mice at 48 h post-injection.

$^{DA}NP_{CT}$ could be explained by the slight DA degradation at pH 7.4 (Supplementary Figure S4). We calculated the pharmacokinetic parameters of these nanocarriers using a non-compartmental model (Figures 7B,C) and found that the $AUC_{0\text{-}t}$ values of $^{SA}NP_{CT}$ and $^{DA}NP_{CT}$ were 3.08- and 2.32-fold higher than those of NP_{CT}, respectively.

Next, NP_{CT}, $^{SA}NP_{CT}$, or $^{DA}NP_{CT}$ were *i.v.* injected into BALB/c nude mice bearing MCF-7 xenografts to evaluate their biodistribution, especially toward tumor tissues. After administration, the mice were euthanized at predetermined timepoints, and the Ce6 content in different organs was analyzed by HPLC. $^{DA}NP_{CT}$ had the most preferential retention in tumor tissues at 48 h compared to NP_{CT} and $^{SA}NP_{CT}$ due to the pH_e-triggered TAT-presenting effect (Figure 7D). Although $^{SA}NP_{CT}$ showed more advanced tumor extravasation via EPR based on the best circulation pattern, stable SA modification impeded TAT ligand interaction and function in the tumor cells, resulting in insufficient tumor accumulation. The amounts of $^{DA}NP_{CT}$ quantified by Ce6 content were 2.32% ± 0.29%, 3.11% ± 0.23%, and 2.47% ± 0.21% ID per gram of tumor at 12, 24, and 48 h, respectively. The nano-sized delivery systems NP_{CT}, $^{SA}NP_{CT}$, and $^{DA}NP_{CT}$ accumulated in the liver and spleen, both components of the reticuloendothelial system (Figure 7E).

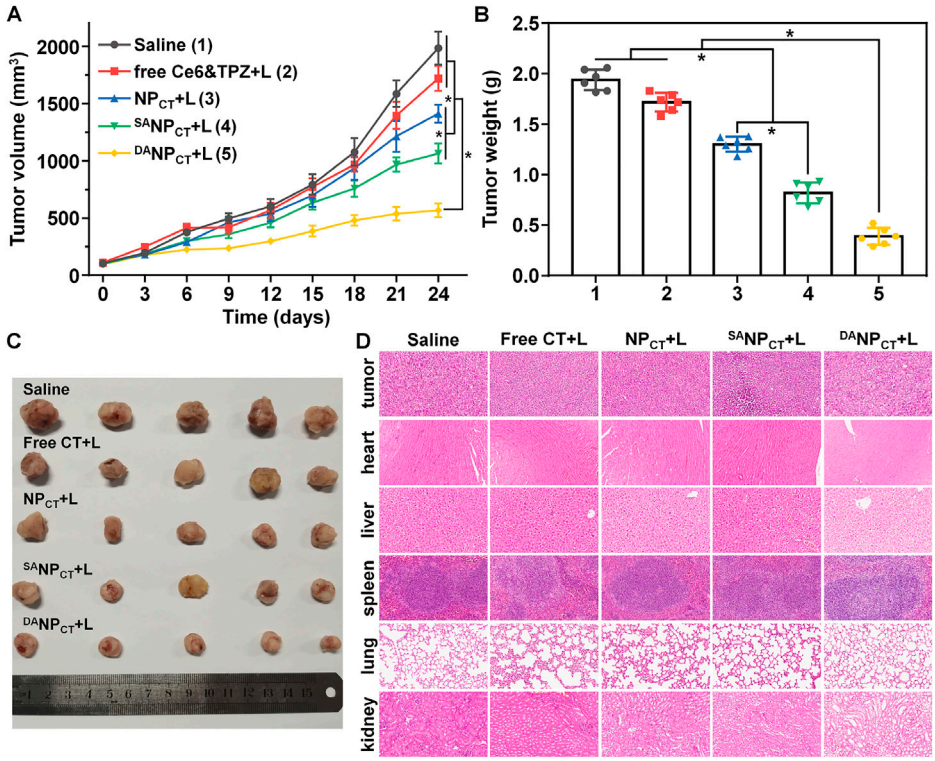

FIGURE 8
(A) Tumor growth curve of the MCF-7 tumor-bearing BALB/c nude mice treated with various formulations. The mice bearing intravenous injections were performed on days 0, 7, 14, and 21. *$p < 0.05$. **(B)** MCF-7 tumor mass after the treatment. *$p < 0.05$. **(C)** Tumor images at the end of the treatment. **(D)** H&E staining of tumors and major organs at the end of the tumor treatment.

Therapeutic efficacy of $^{DA}NP_{CT}$ *in vivo*

Encouraged by the excellent *in vitro* performance, we evaluated the *in vivo* antitumor efficacy of $^{DA}NP_{CT}$. MCF-7 tumor-bearing mice were randomly divided and treated via i.v. injection with (1) 0.9% NaCl, (2) free Ce6 + TPZ + PDT, (3) NP_{CT} + PDT, (4) $^{SA}NP_{CT}$ + PDT, and (5) $^{DA}NP_{CT}$ + PDT. The equivalent TPZ dose was 5.0 mg/kg, and the tumor size was recorded every 3 days. Tumor volume in the saline group rapidly increased to 1986.15 mm^3 at the end of treatment (Figure 8A). Because of their prolonged blood circulation and improved biodistribution, NP_{CT} and $^{SA}NP_{CT}$ significantly inhibited tumor growth after PDT compared to the free Ce6 + TPZ + PDT. Notably, the smallest tumor volumes in the $^{DA}NP_{CT}$ + L group revealed that this treatment yielded the best therapeutic effect, with an average tumor volume of only 567.78 mm^3 on day 24. The tumor weight after euthanizing confirmed these results (Figure 8B). Tumor mass in the $^{DA}NP_{CT}$ + PDT group was 0.70- and 0.52-fold lower than that in the NP_{CT} + L and $^{SA}NP_{CT}$ + L groups, respectively. In addition, the body weight curves in Supplementary Figure S5 show that the $^{DA}NP_{CT}$ + L group did not experience a decline in the body weight, suggesting the biosafety of $^{DA}NP_{CT}$ *in vivo*. H&E staining (Figure 8C), routine blood count (Supplementary Table S1), and ELISA tests (Supplementary Figure S6) for liver/kidney damage after treatment showed no significant lesions or inflammation in any groups, validating the biocompatibility of the $^{DA}NP_{CT}$ system.

Conclusion

In this work, a hierarchically responsive nanocarrier $^{DA}NP_{CT}$ was fabricated to spatially control TAT presentation in tumor sites for PDT-initiated, hypoxia-activated cancer therapy. $^{DA}NP_{CT}$ exhibited advanced stability at neutral pH and rapidly reactivated TAT function in response to pH_e, specifically accelerating internalization by tumor cells. Upon 660-nm laser irradiation, Ce6-based PDT produced cell-killing ROS and consumed surrounding O_2 to generate hypoxic conditions that stimulated $^{DA}NP_{CT}$ disassembly and TPZ liberation. Chemotherapy with TPZ was enhanced by the aggravated hypoxia in tumor tissues. The biosafety studies of $^{DA}NP_{CT}$ showed excellent *in vivo* biocompatibility with healthy organs. On the other hand, further studies on the feeding ratio of TAT-PEG-*b*-PHEP, PEG-*b*-P (AEP-*g*-NI), Ce6, and TPZ during the preparation of $^{DA}NP_{CT}$ is necessary for optimal therapeutical efficacy *in vivo*. This work contributes to the rational design of tumor microenvironment-responsive nanocarriers for precise and cascade cancer therapies.

Data availability statement

The original contributions presented in the study are included in the article/Supplementary Material; further inquiries can be directed to the corresponding authors.

Ethics statement

The animal study was reviewed and approved by the Institutional Animal Care and Use Committee at Tianjin Medical University General Hospital.

Author contributions

Conceptualization, ZZ, AG, and CS; methodology, ZZ and JF; validation, ZZ, JF, and TZ; formal analysis, TZ and AG; investigation, ZZ and JF; data curation, AG; writing—original draft preparation, ZZ, JF, and AG; writing—review and editing, AG and CS; supervision, CS; funding acquisition, ZZ and CS. All authors contributed to the article and approved the submitted version.

Funding

This work was supported by the National Natural Science Foundation of China (82071907 and 82271937), Natural Science Foundation of Tianjin (18JCYBJC25100), Health science and Technology Project of Tianjin (MS20022), Tianjin Key Medical Discipline (Specialty) Construction Project (TJYXZDXK-001A), and Wu Jieping Medical Foundation-Special Fund for Clinical Research (320.6750.2022-3-5).

Conflict of interest

The authors declare that the research was conducted in the absence of any commercial or financial relationships that could be construed as a potential conflict of interest.

Publisher's note

All claims expressed in this article are solely those of the authors and do not necessarily represent those of their affiliated organizations, or those of the publisher, the editors, and the reviewers. Any product that may be evaluated in this article, or claim that may be made by its manufacturer, is not guaranteed or endorsed by the publisher.

Supplementary material

The Supplementary Material for this article can be found online at: https://www.frontiersin.org/articles/10.3389/fbioe.2023.1197404/full#supplementary-material

References

Abrahamse, H., and Hamblin, M. R. (2016). New photosensitizers for photodynamic therapy. *Biochem. J.* 473 (4), 347–364. doi:10.1042/BJ20150942

Cairns, R. A., Harris, I. S., and Mak, T. W. (2011). Regulation of cancer cell metabolism. *Nat. Rev. Cancer* 11 (2), 85–95. doi:10.1038/nrc2981

Cheng, Y. J., Hu, J. J., Qin, S. Y., Zhang, A. Q., and Zhang, X. Z. (2020). Recent advances in functional mesoporous silica-based nanoplatforms for combinational photo-chemotherapy of cancer. *Biomaterials* 232, 119738. doi:10.1016/j.biomaterials.2019.119738

Conte, C., Maiolino, S., Pellosi, D. S., Miro, A., Ungaro, F., and Quaglia, F. (2016). Polymeric nanoparticles for cancer photodynamic therapy. *Top. Curr. Chem.* 370, 61–112. doi:10.1007/978-3-319-22942-3_3

Deshpande, P. P., Biswas, S., and Torchilin, V. P. (2013). Current trends in the use of liposomes for tumor targeting. *Nanomedicine* 8 (9), 1509–1528. doi:10.2217/NNM.13.118

Dohmen, C., and Wagner, E. (2011). Multifunctional CPP polymer system for tumor-targeted pDNA and siRNA delivery. *Methods Mol. Biol.* 683, 453–463. doi:10.1007/978-1-60761-919-2_32

Du, J. Z., Du, X. J., Mao, C. Q., and Wang, J. (2011). Tailor-made dual pH-sensitive polymer-doxorubicin nanoparticles for efficient anticancer drug delivery. *J. Am. Chem. Soc.* 133 (44), 17560–17563. doi:10.1021/ja207150n

El-Hussein, A., Manoto, S. L., Ombinda-Lemboumba, S., Alrowaili, Z. A., and Mthunzi-Kufa, P. (2021). A review of chemotherapy and photodynamic therapy for lung cancer treatment. *Anticancer Agents Med. Chem.* 21 (2), 149–161. doi:10.2174/1871520620666200403144945

Eruslanov, E., and Kusmartsev, S. (2010). Identification of ROS using oxidized DCFDA and flow-cytometry. *Methods Mol. Biol.* 594, 57–72. doi:10.1007/978-1-60761-411-1_4

Feng, L. Z., Cheng, L., Dong, Z. L., Tao, D. L., Barnhart, T. E., Cai, W. B., et al. (2017). Theranostic liposomes with hypoxia-activated prodrug to effectively destruct hypoxic tumors post-photodynamic therapy. *ACS Nano* 11 (1), 927–937. doi:10.1021/acsnano.6b07525

Futaki, S., and Nakase, I. (2017). Cell-surface interactions on arginine-rich cell-penetrating peptides allow for multiplex modes of internalization. *Acc. Chem. Res.* 50 (10), 2449–2456. doi:10.1021/acs.accounts.7b00221

Gao, M., Fan, F., Li, D. D., Yu, Y., Mao, K. R., Sun, T. M., et al. (2017). Tumor acidity-activatable TAT targeted nanomedicine for enlarged fluorescence/magnetic resonance imaging-guided photodynamic therapy. *Biomaterials* 133, 165–175. doi:10.1016/j.biomaterials.2017.04.013

Guidotti, G., Brambilla, L., and Rossi, D. (2017). Cell-penetrating peptides: From basic research to clinics. *Trends Pharmacol. Sci.* 38 (4), 406–424. doi:10.1016/j.tips.2017.01.003

Han, S. R. Y., Jeong, E., Cheon, S. Y., Lee, D. H. Y., Lee, Y., Lee, S. Y., et al. (2022). Perfluorooctylbromide-loaded fucoidan-chlorin e6 nanoparticles for tumor-targeted photodynamic therapy. *Int. J. Biol. Macromol.* 223, 77–86. doi:10.1016/j.ijbiomac.2022.10.254

Huang, S., Shao, K., Kuang, Y., Liu, Y., Li, J., An, S., et al. (2013). Tumor targeting and microenvironment-responsive nanoparticles for gene delivery. *Biomaterials* 34 (21), 5294–5302. doi:10.1016/j.biomaterials.2013.03.043

Jiang, M., Liu, Y., Dong, Y., Wang, K., and Yuan, Y. (2022). Bioorthogonal chemistry and illumination controlled programmed size-changeable nanomedicine for synergistic photodynamic and hypoxia-activated therapy. *Biomaterials* 284, 121480. doi:10.1016/j.biomaterials.2022.121480

Jing, X., Yang, F., Shao, C., Wei, K., Xie, M., Shen, H., et al. (2019). Role of hypoxia in cancer therapy by regulating the tumor microenvironment. *Mol. Cancer* 18 (1), 157. doi:10.1186/s12943-019-1089-9

Jing, Y. T., Xiong, X., Ming, Y., Zhao, J. Y., Guo, X., Yang, G., et al. (2018). A multifunctional micellar nanoplatform with pH-triggered cell penetration and nuclear targeting for effective cancer therapy and inhibition to lung metastasis. *Adv. Healthc. Mater* 7 (7), e1700974. doi:10.1002/adhm.201700974

Kim, H., and Xue, X. (2020). Detection of total reactive oxygen species in adherent cells by 2',7'-dichlorodihydrofluorescein diacetate staining. *J. Vis. Exp.* 160. doi:10.3791/60682

Kim, J., Cho, H. R., Jeon, H., Kim, D., Song, C., Lee, N., et al. (2017). Continuous O-2-Evolving MnFe2O4 nanoparticle-anchored mesoporous silica nanoparticles for efficient photodynamic therapy in hypoxic cancer. *J. Am. Chem. Soc.* 139 (32), 10992–10995. doi:10.1021/jacs.7b05559

Kopecka, J., Salaroglio, I. C., Perez-Ruiz, E., Sarmento-Ribeiro, A. B., Saponara, S., De Las Rivas, J., et al. (2021). Hypoxia as a driver of resistance to immunotherapy. *Drug Resist Updat* 59, 100787. doi:10.1016/j.drup.2021.100787

Li, D. D., Ma, Y. C., Du, J. Z., Tao, W., Du, X. J., and YangWang, X. Z. J. (2017). Tumor acidity/NIR controlled interaction of transformable nanoparticle with biological systems for cancer therapy. *Nano Lett.* 17 (5), 2871–2878. doi:10.1021/acs.nanolett.6b05396

Li, J. M., Liu, F., Shao, Q., Min, Y. Z., Costa, M., Yeow, E. K. L., et al. (2014). Enzyme-responsive cell-penetrating peptide conjugated mesoporous silica quantum dot nanocarriers for controlled release of nucleus-targeted drug molecules and real-time intracellular fluorescence imaging of tumor cells. *Adv. Healthc. Mater* 3 (8), 1230–1239. doi:10.1002/adhm.201300613

Li, Y., Zhao, L., and Li, X. F. (2021). Targeting hypoxia: Hypoxia-activated prodrugs in cancer therapy. *Front. Oncol.* 11, 700407. doi:10.3389/fonc.2021.700407

Ma, B. A., and Sun, C. Y. (2020). Tumor pH-triggered "charge conversion" nanocarriers with on-demand drug release for precise cancer therapy. *J. Mater Chem. B* 8 (40), 9351–9361. doi:10.1039/d0tb01692f

Ma, S., Zhao, Y., Lee, W. C., Ong, L. T., Lee, P. L., Jiang, Z., et al. (2022). Hypoxia induces HIF1α-dependent epigenetic vulnerability in triple negative breast cancer to confer immune effector dysfunction and resistance to anti-PD-1 immunotherapy. *Nat. Commun.* 13 (1), 4118. doi:10.1038/s41467-022-31764-9

Majerník, M., Jendželovský, R., Vargová, J., Jendželovská, Z., and Fedoročko, P. (2022). Multifunctional nanoplatforms as a novel effective approach in photodynamic therapy and chemotherapy, to overcome multidrug resistance in cancer. *Pharmaceutics* 14 (5), 1075. doi:10.3390/pharmaceutics14051075

Majmundar, A. J., Wong, W. H. J., and Simon, M. C. (2010). Hypoxia-inducible factors and the response to hypoxic stress. *Mol. Cell* 40 (2), 294–309. doi:10.1016/j.molcel.2010.09.022

Mohammed, F., Ke, W. D., Mukerabigwi, J. F., Japir, A. M. M., Ibrahim, A., Wang, Y. H., et al. (2019). ROS-responsive polymeric nanocarriers with photoinduced exposure of cell-penetrating moieties for specific intracellular drug delivery. *ACS Appl. Mater Interfaces* 11 (35), 31681–31692. doi:10.1021/acsami.9b10950

Pei, P., Sun, C. Y., Tao, W., Li, J., Yang, X. Z., and Wang, J. (2019). ROS-sensitive thioketal-linked polyphosphoester-doxorubicin conjugate for precise phototriggered locoregional chemotherapy. *Biomaterials* 188, 74–82. doi:10.1016/j.biomaterials.2018.10.010

Ruoslahti, E. (2017). Tumor penetrating peptides for improved drug delivery. *Adv. Drug Deliv. Rev.* 110, 3–12. doi:10.1016/j.addr.2016.03.008

Sun, X. K., Sun, J., Lv, J. K., Dong, B., Liu, M., Liu, J. S., et al. (2019). Ce6-C6-TPZ co-loaded albumin nanoparticles for synergistic combined PDT-chemotherapy of cancer. *J. Mater. Chem. B* 7 (38), 5797–5807. doi:10.1039/c9tb01346f

Tang, M. H., Lin, K., Ramachandran, M., Li, L. M., Zou, H. Y., Zheng, H. Z., et al. (2022). A mitochondria-targeting lipid-small molecule hybrid nanoparticle for imaging and therapy in an orthotopic glioma model. *Acta Pharm. Sin. B* 12 (6), 2672–2682. doi:10.1016/j.apsb.2022.04.005

Wang, Y. Z., Xie, Y., Li, J., Peng, Z. H., Sheinin, Y., Zhou, J. P., et al. (2017). Tumor-penetrating nanoparticles for enhanced anticancer activity of combined photodynamic and hypoxia-activated therapy. *ACS Nano* 11 (2), 2227–2238. doi:10.1021/acsnano.6b08731

Yang, D. C., Wen, L. F., Du, L. Y., Luo, C. M., Lu, Z. Y., Liu, J. Y., et al. (2022). A hypoxia-activated prodrug conjugated with a BODIPY-based photothermal agent for imaging-guided chemo-photothermal combination therapy. *ACS Appl. Mater Interfaces* 14 (36), 40546–40558. doi:10.1021/acsami.2c09071

Yang, Y. L., Lin, K., and Yang, L. (2021). Progress in nanocarriers codelivery system to enhance the anticancer effect of photodynamic therapy. *Pharmaceutics* 13 (11). doi:10.3390/pharmaceutics13111951

Yu, M., Cao, R., Ma, Z., and Zhu, M. (2023). Development of "smart" drug delivery systems for chemo/PDT synergistic treatment. *J. Mater Chem. B* 11 (7), 1416–1433. doi:10.1039/d2tb02248f

Zhang, B. B., Xue, R., Lyu, J. S., Gao, A., and Sun, C. Y. (2022). Tumor acidity/redox hierarchical-activable nanoparticles for precise combination of X-ray-induced photodynamic therapy and hypoxia-activated chemotherapy. *J. Mater Chem. B* 10 (20), 3849–3860. doi:10.1039/d2tb00303a

Zhang, Y., Xiao, Y., Huang, Y., He, Y., Xu, Y., Lu, W., et al. (2020). Poly(ethylene glycol) shell-sheddable TAT-modified core cross-linked nano-micelles: TAT-enhanced cellular uptake and lysosomal pH-triggered doxorubicin release. *Colloids Surf. B Biointerfaces* 188, 110772. doi:10.1016/j.colsurfb.2020.110772

Zhu, L., Wang, T., Perche, F., Taigind, A., and Torchilin, V. P. (2013). Enhanced anticancer activity of nanopreparation containing an MMP2-sensitive PEG-drug conjugate and cell-penetrating moiety. *Proc. Natl. Acad. Sci. U. S. A.* 110 (42), 17047–17052. doi:10.1073/pnas.1304987110

Zhu, R. Y., He, H., Liu, Y., Cao, D. S., Yan, J., Duan, S. Z., et al. (2019). Cancer-selective bioreductive chemotherapy mediated by dual hypoxia-responsive nanomedicine upon photodynamic therapy-induced hypoxia aggravation. *Biomacromolecules* 20 (7), 2649–2656. doi:10.1021/acs.biomac.9b00428

Zorko, M., Jones, S., and Langel, Ü. (2022). Cell-penetrating peptides in protein mimicry and cancer therapeutics. *Adv. Drug Deliv. Rev.* 180, 114044. doi:10.1016/j.addr.2021.114044

Frontiers in
Bioengineering and Biotechnology

Accelerates the development of therapies, devices, and technologies to improve our lives

A multidisciplinary journal that accelerates the development of biological therapies, devices, processes and technologies to improve our lives by bridging the gap between discoveries and their application.

Discover the latest Research Topics

See more →

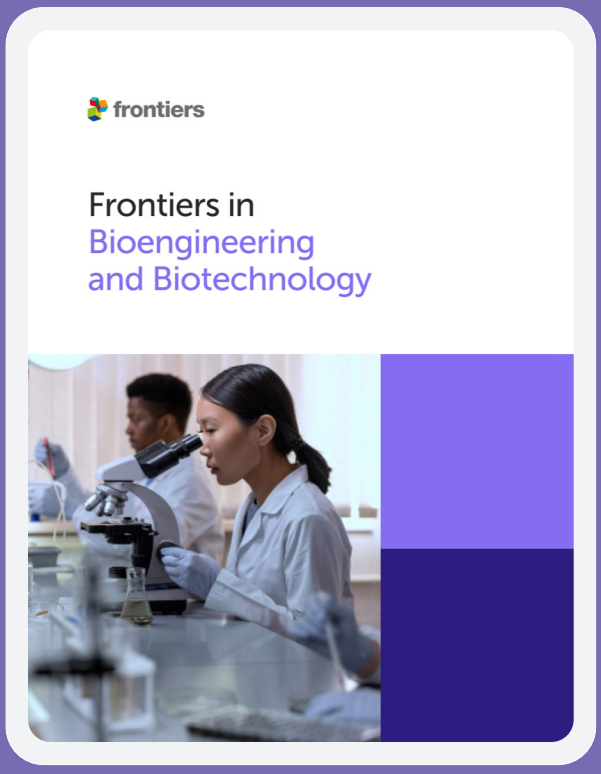

Frontiers

Avenue du Tribunal-Fédéral 34
1005 Lausanne, Switzerland
frontiersin.org

Contact us

+41 (0)21 510 17 00
frontiersin.org/about/contact